Stimuli-responsive magnetic coordination polymers:

from crystals to nanoparticles

Instituto de Ciencia Molecular

Universitat de València

…

Memoria presentada por Mónica Giménez Marqués para aspirar al grado de Doctor en Nanociencia y Nanotecnología (programa ref. I0121-01)

…

Dirigida por el Dr Eugenio Coronado Miralles y el Dr Guillermo Mínguez Espallargas

D. EUGENIO CORONADO MIRALLES, catedrático del Departamento de Química Inorgánica de la Universitat de València y D. GUILLERMO MÍNGUEZ ESPALLARGAS, doctor por la University of Sheffield y actualmente investigador del Instituto de Ciencia Molecular, de la Universitat de València

CERTIFICAN:

Que la memoria presentada por Dña. Mónica Giménez Marqués con título "Stimuli-responsive magnetic coordination polymers: from crystals to nanoparticles" corresponde a su Tesis Doctoral y ha sido realizada bajo su dirección en el Instituto de Ciencia Molecular, autorizando mediante este escrito la presentación de la misma para optar al grado de Doctor.

En Paterna, a 8 de octubre de 2013.

Dr. Eugenio Coronado Miralles

Dr. Guillermo Mínguez Espallargas

Mónica Giménez Marqués

AGRADECIMIENTOS

En primer lugar, quisiera agradecerle a Eugenio por haberme brindado la oportunidad de realizar este trabajo en su grupo. No siempre fue fácil, pero se que he crecido con tu manera de transmitir la ciencia, y me voy formada para superar cualquier reto. Siempre te agradeceré el haber confiado en mí. También quisiera aprovechar esta sección especial, para darle las gracias a Guillermo. Trabajar contigo es una constante de aprendizaje, y junto con tu entusiasmo, ha resultado el marco ideal para realizar esta tesis. Sin lugar a dudas, formamos el mejor de los equipos. Mi más sincera admiración a tu trabajo.

También le estoy muy agradecida a JR y nuestro PICLab. Fueron unos años especiales, en los que aprendí que hacer ciencia podía ser muy divertido, desde un riguroso y brillante buen hacer.

Debo de agradecer a todas aquellas personas que han colaborado en esta investigación. Al Prof. Lee Brammer, pues gracias a su aportación pudimos completar un interesante trabajo. Y a Íñigo, por prestarnos su tiempo en el sincrotrón. También al Prof. Fernando Rey, por las medidas de adsorción que tan buenos resultados nos han dado. Al Prof. van der Zant, y su grupo en Delft, agradecerle sus esfuerzos con las nanopartículas, confío en que pronto veremos los frutos.

Y llega el turno de los que me habéis acompañado todos los días, compañeros del UIMM. Primero gracias a mis chicas, Alicia, Marian, Alejandra, Sam, Elena y Helena. Habéis aportado el toque personal a esta tesis. Gracias por no olvidar ningún cumpleaños, siempre atentas a mis historias, los cafés con vosotras sí que han sido una recarga de energía. Gracias por vuestros abrazos tan llenos de positivismo.

Mauri, gracias por ser tan especial, *ja ho saps*.

Agradecer a los compis de inicio, Mauri, Salva, Pini, Concha, Julia y Efrén, juntos estrenamos el máster y disfrutamos descubriendo las escuelas. Fueron unos años divertidos, y los recuerdo con mucho cariño. También a Jose, pues a diario te he

necesitado. Y Ángel, por esas cosas que sólo tu sabes arreglar. También decirle a Néstor que mucho ánimo, y que disfrute día a día que así es como mejor se trabaja. A mis compis de ofi, sobre todo Alex y Yan, que son los que más tiempo me han aguantado. Gracias a los profes del grupo, bien por haber atendido mis consultas o por dedicarme un minuto simplemente preguntando cómo iban las cosas. Gracias Modesto por resolver tantas dudas, y lo que nos hemos reído con el ELFOS. Y Henk, te agradezco tu siempre agradable "Hallo". Al señor catedrático, Carlos, el que siempre está disponible y dispuesto, me has dado muy buenos consejos, gracias.

También importantes habéis sido los "secres", Paco, Marian, Estela y Manu. Sois el equipo más eficiente que el UIMM puede tener. GRACIAS. No me puedo dejar a la más "aseada", Amparo, pues nadie mejor que tú nos organiza el despacho.

Agradecer a los demás miembros del ICMol, con los que a diario me he cruzado, pues también formáis parte de esta tesis.

No podría dejarme a mis kimikolokas, que me acompañan en mis éxitos y en los no tan buenos momentos; tenemos toda la vida para seguir acompañándonos, y doy gracias porque formáis parte de mi vida.

A Julio y a Lola, gracias por vuestro apoyo. Y los *parisiens*, AyA(yC), espero que disfrutéis con este resultado pues también formáis parte de él.

A ti, qué te digo que no sepas. Simplemente 8.

Y como en toda obra maestra, lo mejor llega al final. El pilar que sostiene mi vida, sin los que nada tendría sentido. Gracias por regalarme las horas que os he robado, y por confiar ciegamente en mi. A mis abuelitos, que siempre han estado ahí para escucharme. Sister y Fernando, dais luz a mi vida. Bueno, y también a Fernandito, mi Sol. Papis, si estáis orgullosos, que sepáis que soy quien soy gracias a vosotros.

Esto va por vosotros.

A mi hermana

SUMMARY

The work described in this thesis is motivated by the intention of developing new stimuli-responsive magnetic coordination polymers, and through them learn about the insights of dynamic behaviour. Two different areas, which refer to the scale at which the systems are obtained, have been explored. In this sense, the thesis has been divided in two parts: the first one deals with the preparation of crystalline stimuli-responsive magnetic CPs, and the second part refers to the synthesis of responsive magnetic nanoparticles (NP). Hence, macroscopic crystals or nanoparticles of CPs have been obtained following different methodologies: for the preparation of CPs, methods of crystal engineering based in soft-chemistry have been applied, whereas typical sol-gel methods have been adjusted to obtain nanostructured CPs.

From a general point of view, both parts of the thesis have in common the use of coordination chemistry as the key driving force to obtain new magnetic materials with interesting dynamic and responsive behaviour. A rational ligand design has been developed in order to provide different properties to the final frameworks. In this sense, the ligands of use have promoted magnetic exchange interactions and/or flexibility to the structure. Four different ligands have been used and are presented in the following table:

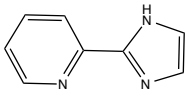

2-(imidazol-2-yl)pyridine

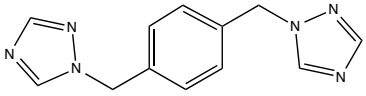

1,4-bis(triazol-1-ylmethyl)benzene

1H-1,2,4-triazole

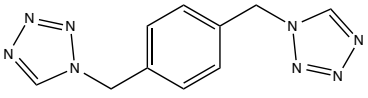

1,4-bis(tetrazol-1-ylmethyl)benzene

The ligand 2-(imidazol-2-yl)pyridine, pyimH, has been used to obtain magnetic CPs, since it is capable of promoting magnetic exchange interactions; the flexible ligand 1,4-bis(triazol-1-ylmethyl)benzene, btix, can adopt different conformations by the effect of an external stimulus resulting in dynamic frameworks; and finally, the ligands 1,4-bis(tetrazol-1-ylmethyl)benzene, btzx, and *1H*-1,2,4-triazole provide a suitable ligand field for the appearance of spin-crossover phenomena.

The first part extends to *Chapters 1–5,* and deals with the preparation of the responsive CPs as crystalline solids. To pursuit this objective, two different approaches have been followed. The first method has used an imidazolate based ligand that can promote magnetic exchange interactions to obtain magnetic CP. The second approach refers to the use of flexible ligands which can respond to an external stimulus and are capable to adapt to structural modifications.

After a general introduction to stimuli responsive magnetic MOFs in *Chapter 1*, *Chapter 2* presents a non-porous CP based on an imidazolate ligand, which can modulate the physical properties by chemisorption of gas molecules. Upon chemisorption of 3 equivalents of HCl molecules, the crystalline coordination polymer undergo a severe structure transformation and converts to ionic solid, which is able to extrude 2 equivalents of HCl yielding a molecular compound. The remarkable concerted reorganization of covalent bonds that occurs during the sorption/desorption processes results in significant changes in the magnetic properties of the materials, from strong antiferromagnetic interactions to weak ferro- or antiferromagnetic interactions.

Chapter 3 deals with the preparation of SCO coordination polymers whose spin transition has shown to be strongly sensitive to physisorption of gas molecules (CO_2) despite the lack of permanent channels. These SCO-CPs remarkably sorb gas molecules despite the absence of permanent pores due to the presence of a flexible ligand. In addition, a selective sorption of CO_2 over N_2 is observed. Importantly, structural evidence of the CO_2 molecules located in the discrete voids of the

frameworks has permitted the unequivocal description of the nature of the interaction between the gas molecule and the host framework. Magnetic properties before and after physisorption have been carried out to study the gas-mediated SCO modulation. In this sense, magnetic properties are for the first time modulated upon sorption of gas molecules in SCO systems.

Chapter 4 and *Chapter 5* show examples of magnetic CPs that undergo structural changes under physical and chemical stimuli, respectively. In *Chapter 4* a physical stimulus is able to induce motions in the bridging ligands, promoting a *syn-anti* isomerism upon heating. *Chapter 5* presents the study of flexible magnetic CPs that suffer structural and magnetic modifications upon anion exchange.

The second part of the work moves towards the study of nanostructured SCO-CP. This section deals with the synthesis, characterization and later processing of the nano-objects and covers *Chapters 6–9*.

In *Chapter 7* a detailed description of the synthetic protocol is described. Then, essential analysis of the parameters that exert an influence on the particle size is presented, with particular interest focused on the key parameter that can control the particle size. Finally, the study of the size effect in the magnetic properties has been also developed.

Chapter 8 deals with the preparation of a chemically modulated family of SCO-NPs conducted by a successive ligand substitution. The effect of this chemical perturbation has been studied by means of magnetic susceptibility measurements, since ligand substitution provokes a clear modification in the transition temperature of the SCO.

Finally *Chapter 9* focuses in the potential processing of SCO-NPs for their possible integration in electronic nano-devices. Thus, NPs have been deposited onto different substrates with the aim of understanding a possible preferentiality. In addition, stable and homogeneous thin films of SCO-NPs with a few nanometers thickness have been prepared following the spin-coating method. Finally, the controlled deposition of SCO-NPs through conformal contact has been demonstrated.

The work described in this dissertation has given rise to the following publications:

"*Tuning the magneto-structural properties in non-porous coordination polymers through HCl chemisorption*". E. Coronado, M. Giménez-Marqués, G. Mínguez Espallargas, L. Brammer. *Nature Commun.* **2012**, *3*, 828.

"*Dynamic magnetic materials based on the cationic coordination polymer* $[Cu(btix)_2]^{2n+}$ *(btix = 1,4-bis(triazol-1-ylmethyl)benzene): tuning the structural and magnetic properties through anion exchange*". E. Coronado, M. Giménez-Marqués, C. J. Gómez-García, G. Mínguez Espallargas. *Inorg. Chem.* **2012**, *51*, 12938–12947.

"*Combination of magnetic susceptibility and electron paramagnetic resonance to monitor the 1D to 2D solid state transformation in flexible metal−organic frameworks of Co(II) and Zn(II) with 1,4-bis(triazol-1-ylmethyl)benzene*". E. Coronado, M. Giménez-Marqués, G. Mínguez Espallargas. *Inorg. Chem.* **2012***, 51,* 4403−4410.

"*Combination of superconductivity and spin crossover phenomena in hybrid materials*". E. Coronado, M. Giménez-Marqués, C. Martí-Gastaldo, G. Mínguez Espallargas, E. Navarro-Moratalla, J. Waerenborgh. *Inorg. Chem.* **2013**, *52*, 8451−8460.

"*Spin-crossover modification through selective* CO_2 *sorption*". E. Coronado, M. Giménez-Marqués, G. Mínguez Espallargas, F. Rey, I. J. Vitórica-Yrezábal. *J. Am. Chem. Soc.* **2013**, DOI: 10.1021/ja407135k.

"*Synthesis of bistable spin crossover nanoparticles based on the system* $[Fe(Htrz)_2(trz)](BF_4)$". E. Coronado, M. Giménez-Marqués. *Submitted.*

"*Controlling size and deposition of spin crossover nanoparticles"*. E. Coronado, A. Forment-Aliaga, M. Giménez-Marqués. *Manuscript in preparation*.

CONTENTS

SUMMARY ..... **i**

LIST OF PUBLICATIONS ..... **v**

PART I

1 Introduction to dynamic magnetic MOFs **3**

2 Chemisorption in non-porous magnetic coordination polymers **29**

2.1 Introduction 31

2.2 Results and discussion 33

2.2.1 Description of the structures 33

2.2.2 X-ray powder diffraction studies 37

2.2.3 Chemisorption/desorption of gaseous HCl molecules 38

2.2.4 Magnetic response to HCl chemisorption 41

2.2.5 EPR response to HCl chemisorption and monitoring 46

2.3 Conclusions 52

2.4 Methods 53

2.4.1 Synthesis 53

2.4.2 Structural characterization 55

2.4.3 Physical measurements 59

2.5 References 60

3 Physisorption in non-porous Fe^{II} spin-crossover coordination polymers **63**

3.1 Introduction 65

3.2 Results and discussion 66

3.2.1 Description of the structures 66

3.2.2 X-ray powder diffraction studies 71

3.2.3 Gas adsorption properties 75

3.2.4 Magnetic properties 80

3.2.5 Magnetic response to CO_2 sorption 81

3.2.6 *In situ* structural determination upon CO_2 loading 85

3.3 Conclusions 89

3.4 Methods 90

3.4.1 Synthesis....90
3.4.2 Structural characterization....91
3.4.3 Physical measurements....95
3.5 References....97
4 Physically-driven solid-state transformation in coordination polymers....101
4.1 Introduction....103
4.2 Results and discussion....105
4.2.1 Description of the structures....105
4.2.2 Thermogravimetric analysis....109
4.2.3 X-ray powder diffraction studies....111
4.2.4 Sorption studies....114
4.2.5 Magnetic properties....115
4.2.4 EPR studies....116
4.3 Conclusions....119
4.4 Methods....120
4.4.1 Synthesis....120
4.4.2 Structural characterization....121
4.4.3 Physical measurements....124
4.5 References....125
5 Chemically-driven solid-state transformation in coordination polymers....129
5.1 Introduction....131
5.2 Results and discussion....133
5.2.1 Description of the structures....133
5.2.2 Anion exchange....137
5.2.3 Structural transformations upon anion exchange....140
5.2.4 X-ray powder diffraction studies....143
5.2.5 Magnetic properties....146
5.2.6 EPR studies....151
5.3 Conclusions....152
5.4 Methods....153
5.4.1 Synthesis....153
5.4.2 Structural characterization....154
5.4.3 Physical measurements....159
5.5 References....160

PART II

6 Introduction to spin-crossover phenomenon 165

6.1 The spin-crossover phenomenon 167

6.1.1 Ligand field considerations 167

6.1.2 Classification of spin-crossover systems 170

6.2 Spin-crossover at the nanometer scale 171

6.3 References 175

7 Synthesis of bistable SCO NPs based on the system $[Fe(Htrz)_2(trz)](BF_4)$ 177

7.1 Introduction 179

7.1.1 Generalities about the compound $[Fe(Htrz)_2(trz)](BF_4)$ 179

7.1.2 $[Fe(Htrz)_2(trz)](BF_4)$ at the nanometre scale 182

7.1.3 Generalities about the micellar systems 183

7.2 Nanoparticles of $[Fe(Htrz)_2(trz)](BF_4)$ 186

7.2.1 Experimental protocol 186

7.2.2 Selection of synthetic parameters 188

7.3 Control over the size in $[Fe(Htrz)_2(trz)](BF_4)$ NPs 194

7.3.1 Effect of ω_0 variation on the nanoparticle size 194

7.3.2 Effect of size variation on the spin transition 199

7.4 Conclusions 202

7.5 Methods 203

7.5.1 General synthesis 203

7.5.2 Physical measurements 204

7.6 References 205

8 Tuning the transition temperature in SCO NPs by ligand substitution 207

8.1 Introduction 209

8.2 Results and discussion 211

8.2.1 Optical properties 213

8.2.2 Magnetic properties 215

8.3 Conclusions 217

8.4 Methods 218

8.4.1 General synthesis 218

8.4.2 Physical measurements 219

8.5 References....220
9 Processing of spin-crossover nanoparticles....221
9.1 Introduction....223
9.2 Preferential and controlled deposition onto surfaces....224
9.3 Controlled two-dimensional distribution on NPs in thin films....228
9.4 SCO-NPs patterned on SiO_2 surfaces....233
9.5 Conclusions....234
9.6 Methods....235
9.7 References....237

PART III

Resumen....241

Compounds reference....247

I

1

INTRODUCTION TO DYNAMIC MAGNETIC MOFS

Coordination Polymers (CPs) represent an important area in material science with foremost applications in catalysis, magnetism, electronics and optics.[1,2] The term CP was first used by Bailar *et al*. in 1964,[3] who described and classified the synthesis and structures of inorganic chain compounds. In the last two decades the study of CPs has experienced a substantial progress and enormous research effort has focused on the synthesis and study of novel CPs with singular chemical and physical properties. CPs consists of metal and organic ligands connected via coordination bonds that extend infinitely in 1, 2 or 3 dimensions (1D, 2D or 3D, respectively) (figure 1.1).[1] The structure and properties of CPs vary depending on the type of metal and ligand used. Therefore, the adaptable nature of the organic ligands and their variety of coordination modes, together with the geometry of the constitutive metal ions, provide an assortment of topologies and different architectures that can be intended by chemical design.[4] In addition, their regular frameworks can be easily prepared with inorganic crystal engineering by self-assembly of their components, resulting in highly potential versatile materials.[5] Thus, a variety of CPs can be foreseen ranging from robust frameworks of enhanced stability to flexible solids able to respond to external stimuli given their dynamic structures.

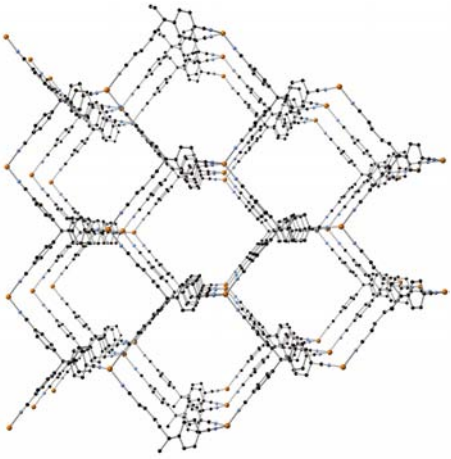

Figure 1.1 Crystal stucture of the first CP by B.F. Hoskins and R. Robson.[7a]

Porous Coordination Polymers (PCPs) or metal-organic frameworks (MOFs) are a specific type of hybrid inorganic-organic solid which present permanent pores in their structure. MOFs are built up from the assembly of inorganic sub-units (metals, clusters, or chains) and easily tunable multitopic organic linkers.[6] Since their discovery a few decades ago,[7] a large number of studies have been devoted to the synthesis and structural characterization of novel hybrid materials and also to their potential applications in catalysis, separations of mixtures, energy storage media, sensors, electronic devices and biomedicine.[8] As a consequence, the number of articles published in the last 10 years has been rapidly increased as shown in figure 1.2.

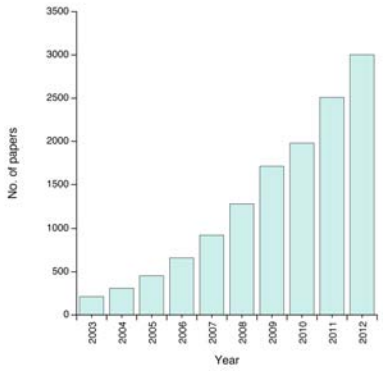

Figure 1.2 Rapid increase of papers dealing with porous CPs or MOFs in the period 2003-2012 (source: ISI-web of knowledge).

MOFs possess unique characteristics such as highly regular frameworks, high porosity and high specific surface area offering plausible tuneability of pore surface. In comparison to their analogous inorganic porous materials zeolites, MOFs are of remarkable significance due to their enhanced dynamic structures and the extensive possibilities upon reasonable design. Upon appropriate variation of the metal nodes and/or the organic ligands (primary building units), a wide range of MOFs structures can be obtained. Transition-metal ions are often used as versatile connectors given their different possibilities in coordination numbers and coordination geometries (see figure 1.3). The organic ligands used for MOF construction contain coordinating functional groups such as carboxylate, azolate, sulfonate, phosphonate or amine.

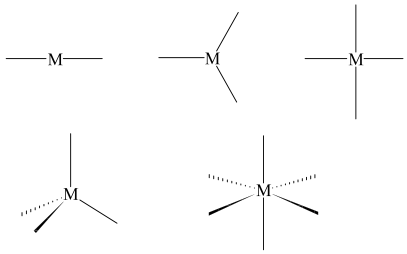

Figure 1.3 Common coordination geometries of metal ions used in network synthesis.

In this sense, multifunctional nanoporous materials can be obtained by incorporating specific functionalities for magnetic,[9] electric,[10] optical[11] and chiral[12] properties. This approximation, based on reasonable design, opens the possibility for coexistence of sorption behaviour with an additional functionality, or even more fascinating, can promote the interplay between different properties in the same material. In the following paragraphs, barely a limited number of well-known MOF structures will be presented in a chronological order, focusing on their peculiarities and/or applications.

Milestone MOFs

In 1999 Williams and co-workers published a microporous 3D structure of formula $[Cu_3(BTC)_2(H_2O)_3]$ commonly known as CuBTC or HKUST-1 (HKUST = Hong Kong University of Science and Technology).[13] This MOF comprises interconnected units of Cu^{II} acetate showing a paddle-wheel structure $[Cu_2(O_2CR)_4]$, which creates a 3D structure with internal channels with accessible pores (8.6 x 8.6 $Å^2$ pore window) representing 40 % of the total volume, affording a Langmuir surface > 900 m^2g^{-1} (see figure 1.4a). This CuBTC material presents coordinated water molecules to the axial sites of the paddle-wheel, which can be reversible removed upon thermal activation, affording open metal sites for plausible functionalization.

The same year, Yaghi and co-workers published the well-known MOF-5 material $[Zn_4(O)(BDT)_3]$ (figure 1.4b).[14] This MOF is based on regular Zn_4O tetrahedra that form supertetrahedral cluster motifs $[Zn_4(O)(CO_2)_6]$ with the central μ_4-oxide coordination. The significance of this solid relies on its unprecedented chemical

stability and its sorption properties: Langmuir surface area of 2900 m^2g^{-1} and pore volumes of 0.61 – 0.54 $cm^3 \cdot cm^{-3}$

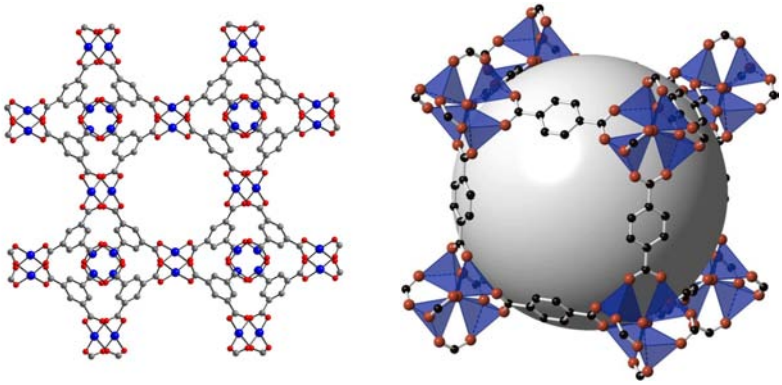

(a) (b)

Figure 1.4 (a) Crystal structure with the cubic unit cell of $[Cu_3(BTC)_2(H_2O)_3]$, HKUST-1 illustrating its highly symmetric and porous framework. Neither the disordered water molecules in the pores nor the H atoms on the aqua ligands and on carbon are shown. (b) The cubic repeat unit of MOF-5, $Zn_4O(BDC)_3$. The grey sphere represents the large cavity.

In 2000, Kitagawa and co-workers reported a porous 3D CP based on $[Cu(SiF_6)_2(4,4\text{-bipy})_2]_n$ (figure 1.5a).[15] The 3s-dimensionality results from bridging of 2D-$\{Cu(4,4'\text{-bipy})_2\}^{2+}$ nets by the SiF_6^{2-} dianions, displaying square channels of 8 × 8 Å. This solid exhibits a high adsorption capacity for CH_4 gas significantly better than zeolite 5A, which is the zeolite with the highest methane adsorption capacity. This porous solid opened a new dimension in the study of adsorbent materials based on CPs.

Later in 2002, the group of Férey obtained the MIL-53 series (MIL = Materials of Institute Lavoisier), (MIL-53 = $M^{III}(OH)\cdot\{O_2C\text{-}C_6H_4\text{-}CO_2\}\cdot\{HO_2C\text{-}C_6H_4\text{-}CO_2H\}_{0.75}$), the first nanoporous solids based on trivalent metal ions exhibiting zeolitic behaviour (figure 1.5b). These solids present a very large breathing effect, a high thermal stability, magnetic properties and sorption capacities.[16] The 3D structure displays 1D large pore channels filled with hosted molecules, which can be removed leading to a nanoporous solid with Langmuir surface area over 1500 m^2g^{-1}. The flexibility of these solids upon removal and reversible hydration affords a high breathing effect (more than 5 Å). The solid can therefore assume different shapes and porosities depending

on the guest's presence or absence. Few years later, two new cubic zeotypic metal carboxylates, MIL-100 and MIL-101, were reported by the same research group.[17]

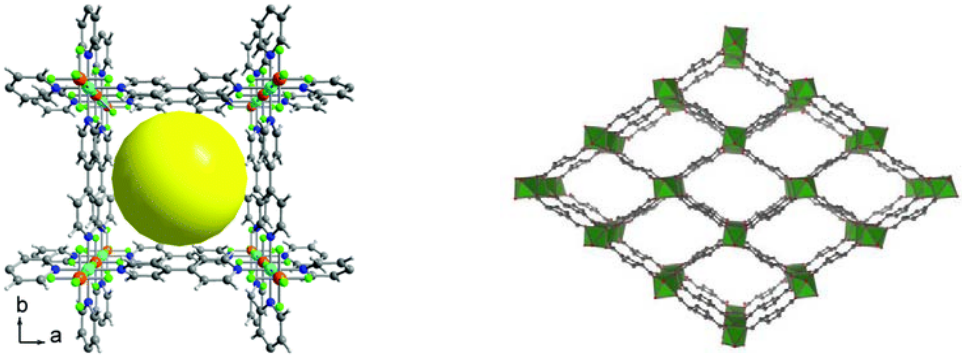

(a) (b)

Figure 1.5 (a) Crystal structure of [Cu(μ-SiF_6)(μ-4,4′-bipy)$_2$] along the *ab* direction. The yellow sphere with a radius of 4.5 Å takes into account the van der Waals radii of the framework walls. (b) Crystal structure of [Al(BDC)(μ-OH)], MIL-53(Al) with a flexible, 'breathing' network adapting to guest molecules.

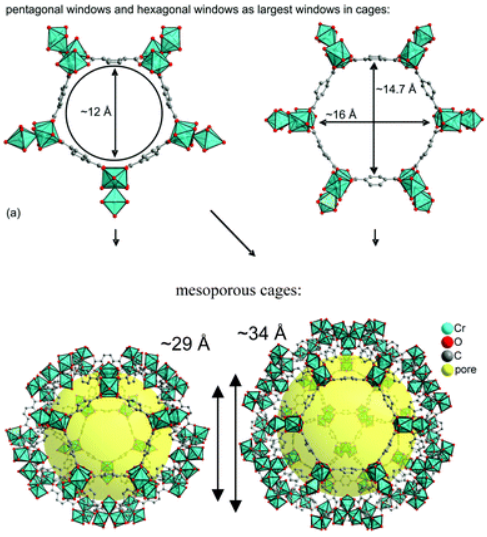

Figure 1.6 Structures of MIL100 and MIL-101. Reproduced form reference 17.

These systems are cubic zeotipic metal carboxylates, built up from trimers of octahedral chromium and di- or tricarboxylic acids. In particular, crystalline 3D mesoporous material MIL-101, $[Cr_3O(BDC)_3(F,OH)(H_2O)_2]$, is a Cr-terephthalate with inner free cage diameters up to 34 Å and pore aperture windows up to 16 Å (figure 1.6). This CP has shown to be the most water-stable carboxylate MOFs. These MIL porous solids have been recently investigated for its use as plausible drug controlled delivery systems.[18,19]

Another significant category of hybrid materials comprises the family of zeolitic imidazolate frameworks (ZIFs). ZIFs are special cases of MOFs in which transition metal ions are linked by substituted imidazolate ions into frameworks with a topology that is either that of a known zeolite or a zeolite-like topology. Thus, the ZIFs' crystal structures are based in the aluminosilicate zeolites where the tetrahedral Si(Al) and the bridging O are replaced by Zn ion and imidazolate link, respectively (figure 1.7). These ZIFs are characterized by a high thermal and chemical stability and permanent porosity with a wide range of functional groups because of the ready availability of substituted imidazoles. ZIFs are excellent candidates for selective absorption of carbon dioxide from gas streams. The most relevant work dealing with this class of solids was published in 2006 by Yaghi and co-workers.[20]

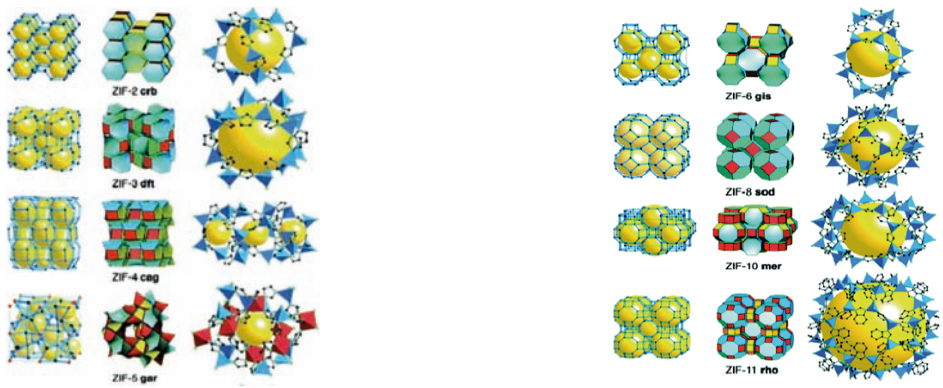

Figure 1.7. Crystal structures of ZIFs. In each row, the net is shown as a stick diagram (left) and as tiling (center). (Right) The largest cage in each ZIF is shown with ZnN_4 tetrahedra in blue, and, for ZIF-5, InN_6 octahedra in red. H atoms are omitted for clarity. Reproduced from ref 200.

STIMULI-RESPONSIVE MAGNETIC MOFS

One of the most exciting findings in this field is that some MOFs present flexible or dynamic structures,[21] which are intrinsically related to the structural flexibility of the ligand,[22] or to the ability of the coordination sites to accept, release and/or exchange coordinating molecules. These dynamic materials undergo reversible structural changes to respond to an applied stimulus, being exceptionally useful in the preparation of functional materials with tunable or switching physical properties. This is particularly interesting for magnetic materials since their physical properties are extremely sensitive to minor structural changes provoked by an external stimulus.

Magnetic CPs are a class of magnetic materials of particular interest due to their potential applications in the development of low-density magnetic materials, magnetic sensors and intelligent or multifunctional materials.[23] Magnetism is based on individual spin carriers, which are paramagnetic metal centres or organic radicals. Thus, depending on the origin of the coupling between therse spin carriers, two different magnetic MOFs can be distinguished: i) magnetic MOFs presenting long-range magnetic ordering, as it occurs in general magnets; and ii) spin transition based MOFs. In the former, magnetic ordering is derived from the cooperative exchange interactions between the paramagnetic metal cations through superexchange pathways of (typically) diamagnetic entities. Consequently, magnetic centres need to be necessarily organized in specific topologies and linked by ligands that efficiently promote magnetic exchange interactions to achieve a long-range control of the magnetic interaction. The target is to control the magnetic exchange interactions by regulating bridging distances, angles and electronic configuration of magnetic centres. As a result, the ligand design is crucial, often resulting an intricate issue to merge porosity and long-range magnetic ordering. To tackle this problem, one plausible solution is the use of organic radicals as ligands, which possess individual spins and may promote effective magnetic exchange interactions, thus alleviating the necessity of short distances between metal centers.[24] Notice that, even in the favourable cases, the exchange interactions are in general weak and hence, the magnetic cooperativity is

only observed at very low temperatures. The second type of magnetic CPs encloses MOF based in spin transition complexes. Spin-crossover (SCO) is a phenomenon in which electronic configurations of a transition metal ion can be switched between high-spin (HS) and low-spin (LS) states in response to external stimuli (temperature, pressure light irradiation, magnetic field, electric field, guest sorption), producing changes in magnetism, colour and structure. In particular, Fe^{II} compounds exhibit a remarkable magnetic change between the paramagnetic HS (S = 2) and the diamagnetic LS (S = 0) states.[25-27] In this last case, exchange interactions between the neighbouring magnetic centers is not needed. However, cooperative effects are required to make this SCO phenomenon useful, and they appear from the elastic forces present in the solid and not from the magnetic exchange interactions. Hence, this approximation seems to be better adapted to obtain stimuli-responsive magnetic MOFs responding at high temperatures. A more detailed description of the SCO phenomena is given in *Chapter 6*.

Stimuli-responsive magnetic MOFs have attracted considerable attention in recent years, and interesting examples with appealing magnetic properties have been observed including guest-modulated magnetic ordering,[28] guest sensitive spin crossover,[29] and guest-induced switching between different magnetic states.[30] In these systems, magnetic properties can be dramatically modified by the structural changes provoked by an external chemical or physical stimulus such as guest molecules, temperature or pressure. The structural changes can also be chemically induced by the exchange of anion or guest molecules. In the following paragraphs, a general overview of the different sources that induce structural modifications in dynamic magnetic MOFs will be illustrated, showing interesting examples with appealing magnetic properties.

Chemically-induced transformations in magnetic MOFs

The use of a chemical stimulus such as guest inclusion to affect the magnetic properties of a porous CP has been extensively explored.[31] In the following paragraphs, some representative examples of chemically-driven magnetic modulations

in MOFs are presented. The first 5 examples are MOFs presenting long-range magnetic ordering which undergo magnetic transformation, followed by 6 representative examples of chemically-induced transformations in SCO-based MOFs. Finally, special attention will be focused on examples of gas-mediated magnetic transformations.

Solvent-mediated magnetic transformations

In 1999, Kahn and co-workers introduced the concept of "magnetic sponge'',[32] a magnetic material which can reversibly release and reabsorb both noncoordinated and coordinated solvent molecules upon a reversible dehydration and polymerization process, which is accompanied by a dramatic change of structure and of magnetic properties. The discrete paramagnetic compound $[CoCu(obbz)(H_2O)_4]\cdot{}_2H_2O$ (obbz = *N*,*N*'-bis(2-carboxyphenyl)oxamido) is converted to a 1-D ferrimagnet $[CoCu(obbz)(H_2O)_3]$ (with $T_c < 2$ K) and 2-D ferrimagnet $[CoCu(obbz)(H_2O)]$ (with $T_c = 30$ K) upon heating.[32] Therefore, this dynamic system transforms from a nonmagnetic state to a magnetically ordered state through a simple chemical process such as dehydration and rehydration. However, the lack of structural data after the transformation limits the information of the changes that take place in both the metal centres and the ligands.

Another example of magnetic sponge-like behaviour was later published by Veciana and co-workers in 2003.[24] In this work, the open-framework structure $\{[Cu_3(ptmtc)_2(py)_6(EtOH)_2(H_2O)]\}$ (ptmtc = polychlorinated triphenylmethyl tricarboxylic acid radical), known as MOROF-1 (MOROF = metal-organic radical open-framework), undergoes a reversible and highly selective solvent-induced 'shrinking–breathing' process involving large volume changes (25–35 %) that strongly influence the magnetic properties of the material (figure 1.8). Thus, a reversible change from a 2-D ferrimagnet (with $T_c < 2$ K) to an amorphous paramagnet occurs by a desolvation/resolvation process.

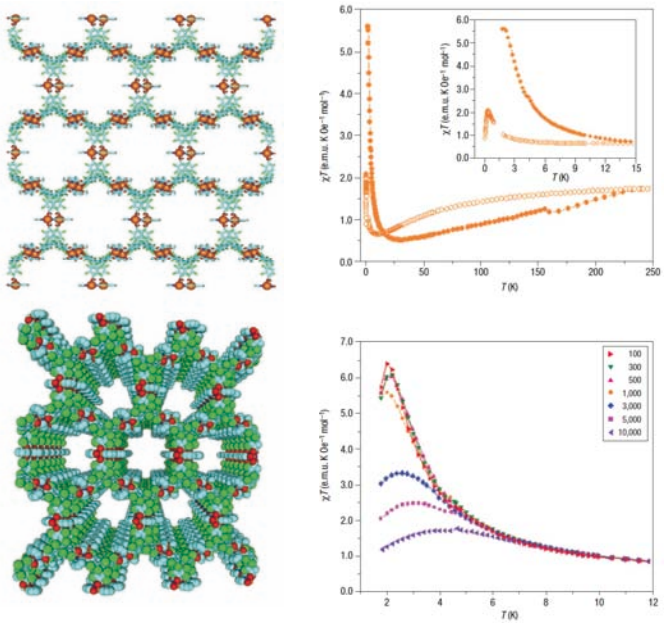

(a) (b)

Figure 1.8 (a) Structure of $\{[Cu_3(ptmtc)_2(py)_6(EtOH)_2(H_2O)]\}$ showing the open-framework. (b) DC magnetic susceptibility measurements.

The adsorption/desorption of coordinated water molecules was also shown to promote a reversible magnetic conversion of the ferromagnetic Prussian blue analogue, $Co^{II}_3[Cr^{III}(CN)_6]_2 \cdot xH_2O$, from a ferromagnet ($T_c$ = 28 K) to a ferrimagnet (T_c = 22 K) depending on humidity. In this work reported by Ohkoshi and Hashimoto and co-workers,[33] the humidity-induced variation in the present material changes the coordination geometry of the Co ion from pseudo-octahedral to pseudo-tetrahedral, (6-Co^{II} ↔ 4-Co^{II}) and switches the magnetic interaction from ferromagnetic coupling with a magnetic pathway of 6-Co^{II}–NC–Cr^{III} in the hydrated solid to antiferromagnetic coupling with a magnetic pathway of 4-Co^{II}–NC–Cr^{III} (figure 1.9).

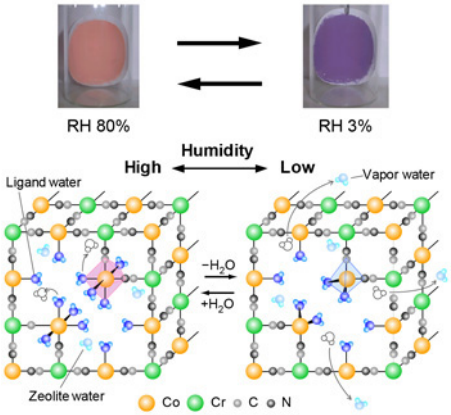

Figure 1.9 Colour change and structural modifications upon reversible dehydration of $Co_3[Cr(CN)_6]_2{\cdot}xH_2O$

Later in 2007, also Ohkoshi, Hashimoto and co-workers[34] reported the heterometallic porous CP $Cu_3[W(CN)_8]_2(pyrimidine)_2{\cdot}8H_2O$ whose magnetic properties can be tuned by *n*-propanol vapours (figure 1.10). This CP is composed by alternated Cu and W ions linked by cyanide groups. The two independent Cu^{2+} ions present a pseudo-octahedral geometry with the coordination sphere completed either by pyrimidine ligands or water molecules. The two types of Cu centres result in two different Cu–NC–W exchange couplings, one ferromagnetic and one antiferromagnetic. The exposure of this MOF to vapours of *n*-propanol produces an exchange of the solvent molecules, yielding a material of formula $Cu_3[W(CN)_8]_2(pyrimidine)_2{\cdot}3/2PrOH{\cdot}9/4H_2O$, where the non-coordinated water molecules have been replaced by propanol molecules. More interestingly, however, is the elimination of one of the Cu-coordinated water molecules, yielding two distinct geometries: one Cu atom is 5-coordinated square pyramidal and other Cu atom is 6-coordinated pseudo-octahedron. This change of coordination of one Cu centre produces a change in the Cu–NC–W antiferromagnetic exchange coupling, whereas the ferromagnetic exchange coupling involving the 6-coordinate Cu centre remains the same. Thus, spontaneous magnetization is shifted from T_c = 9.5 K to T_c = 12.0 K, and an increase of the coercive field (from 30 G to 1000 G) is observed.

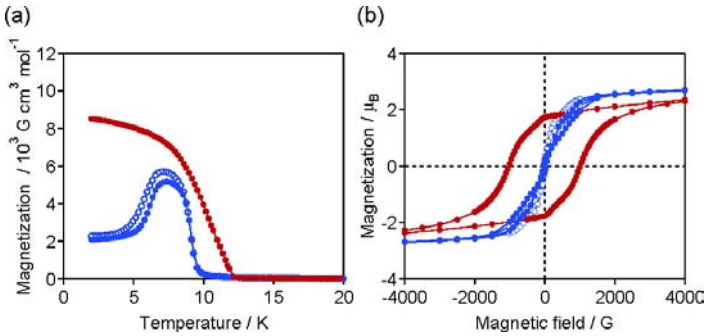

Figure 1.10 Magnetic properties for $Cu_3[W(CN)_8]_2(pyrimidine)_2 \cdot 8H_2O$ (blue closed circle), $Cu_3[W(CN)_8]_2(pyrimidine)_2 \cdot 3/2PrOH \cdot 9/4H_2O$ (red closed circle), and the recovered sample (blue open circle). (a) Field-cooled magnetization curves in an applied field of 50 G; (b) magnetic hysteresis loops at 2 K.

Another example of reversible magnetic conversions by a solvation/desolvation process was reported by Ohba and Kitagawa in the same year.[28a] A reversible single-crystal-to-single-crystal (SCSC) transformation occurs in the compound $[Mn(HL)(H_2O)][Cr(CN)_6] \cdot H_2O$ (L = N,N-dimethylethylenediamine) between a 2-D ferrimagnet (T_c = 35.2 K) and a 3-D ferrimagnet (T_c = 60.4 K) through release and uptake of lattice and coordinated water molecules (figure 1.11).

All these magnetic CPs showing dynamic magnetic ordering could be potentially developed for guest-responsive switching sensors and memory devices. However, this approach is actually not very practical for sensing applications since the thermal induced desorption/sorption of molecules takes place at relatively high temperature while the magnetic ordering occurs at very low temperature. The spin-crossover (SCO) phenomenon is one of the solutions to implement the combination of porous and magnetic properties while overcoming the above-mentioned temperature gap. MOFs based on SCO complexes may serve to defeat this difficulty in combining magnetic cooperativity and porosity, since magnetic cooperativity is not required to obtain a modulation on the magnetic properties. In addition, the SCO phenomenon can occur near room temperature, being these paramagnetic complexes particularly sensitive to the structural changes provoked by an external stimulus. MOFs based on

these molecular complexes can also exhibit magnetic switching via a chemical stimulus. Typically, the high sensitivity of these porous materials is evidenced by the modification of the transition temperature upon physisorption of guest molecules within the porous framework,[29,35-39] or even upon oxidative addition reactions following gas sorption at metal sites that are far from the magnetic centres.[40,41]

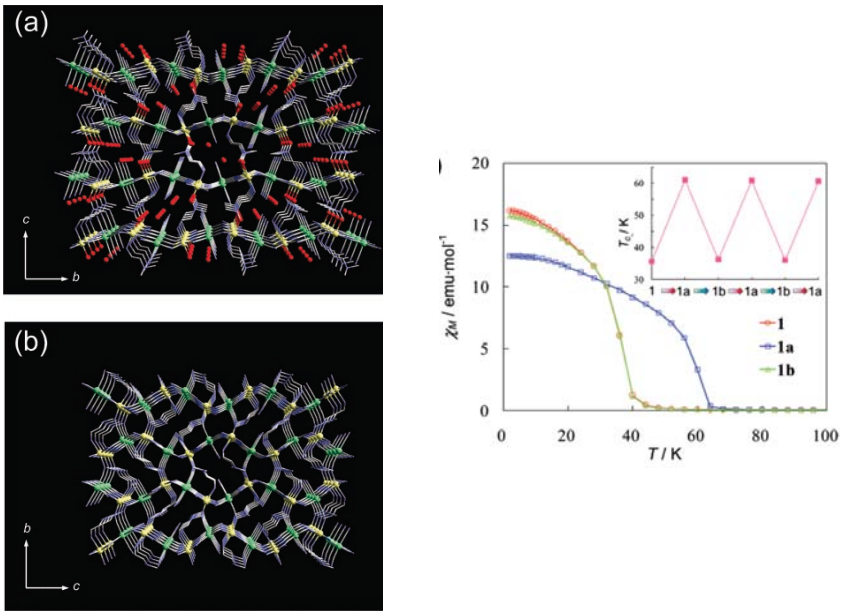

Figure 1.11 Projections of hydrated $[Mn(HL)(H_2O)][Cr(CN)_6]\cdot H_2O$ (a) and dehydrated (b) form onto the *bc* plane. (c) Temperature dependence of molar magnetic susceptibility χ_M for as-synthesized form (red), dehydrated form (blue), and rehydrated form (green) in an applied dc field of 500 Oe. The insert demonstrates the reversible TC switching by dehydration/hydration treatments. Reproduced from reference 27a.

Guest modulated spin-crossover

The first example in which the SCO phenomenon was modulated by guest sorption in a MOF was published by Kepert and co-workers.[29a] The solid $Fe_2(azpy)_4(NCS)_4\cdot$(guest) (azpy = *trans*-4,4'-azopyridine) exhibits reversible uptake and release of guest molecules (MeOH, EtOH, *n*-PrOH). The framework displays a considerable flexibility with the guest uptake and release (figure 1.12), causing substantial changes in the local geometry of the Fe^{II} centres. The as-synthesized

compound displays a broad half-SCO transition between 50 and 150 K, whereas the desolvated form shows no SCO. The initial half-SCO behaviour is recovered by immersion in alcohol solvent. In the synthetic procedure, the azopyridine ligand can be replaced by different *bis*-pyridyl ligands producing the most extensive class of porous SCO materials,[36-39] in which the desorption/adsorption of guest molecules into the 1-D channels produces the variation of SCO temperature as a consequence of the structural transformations associated to the guest sorption.

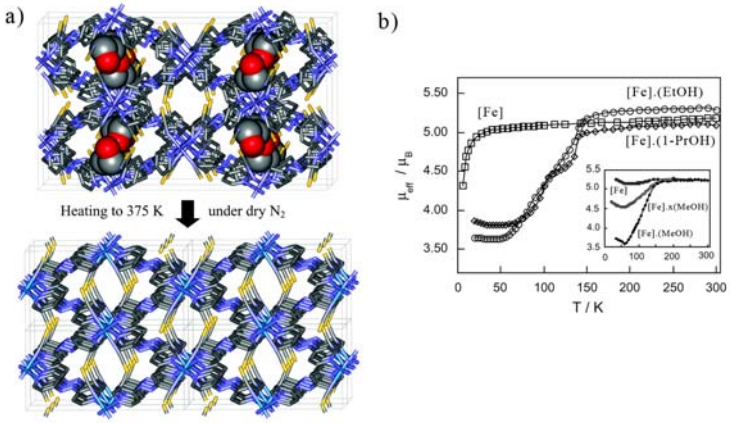

Figure 1.12 a) Reversible guest extrusion/uptake in $Fe_2(azpy)_4(NCS)_4 \cdot$(guest) provokes subtle changes that affect the network; b) effects of the guest extrusion/uptake in the magnetic moment. Reproduced from reference 29a.

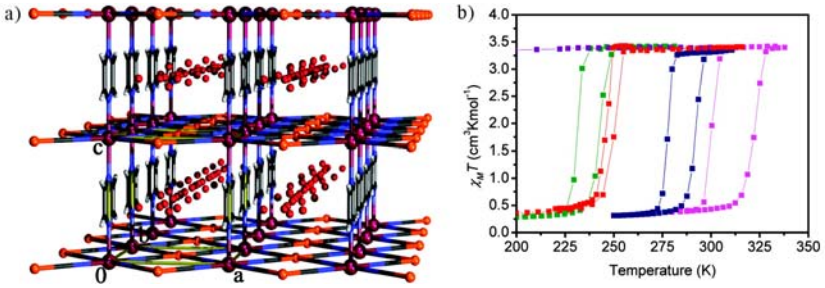

Figure 1.13 a) Crystal structure of $\{Fe(pz)[M(CN)_4]\} \cdot 2H_2O$ showing the 1-D channels which are filled with removable water molecules in the as-synthesised phase; b) temperature dependence of X_MT for $[Fe^{II}(pz)Ni^{II}(CN)_4] \cdot x$Guest; guest = toluene (purple), acetone (green), ethanol (red), methanol (blue), and acetonitrile (pink). Reproduced from reference 38.

Later, in two independent studies, Ohba *et al.* and Southon *et al*. have shown the effects of guest molecules in pillared Hofmann systems {Fe(pz)[M(CN)$_4$]} (M = Ni,[38] Pt[39]) (figure 1.13) exhibiting hysteretic spin-crossover at ambient conditions. In these systems, the stabilization of either the high spin (HS) or the low spin (LS) states of the porous framework upon sorption of guest molecules has been demonstrated.

Another example published by Real and co-workers proved how changes in the coordination environment of the SCO centres induce a modulation in the spin transition.[40] The cyanide-based bimetallic 3D CP {Fe(pmd)(H_2O)[M(CN)$_2$]$_2$}·H_2O (M = Ag, Au; pmd = pyrimidine), displays cooperative half-SCO with hysteresis (8 K wide) centred at $T_{1/2}$ = 219 K for M = Ag and 167 K for M = Au. After elimination of the coordinated and lattice water molecules, a large structural change is induced as a result of a topochemical solid-state reaction, in which the pmd ligands coordinate to the nearest Fe^{II} acting as a bridge. In the case of M = Ag, this structural transformation results in shifting the $T_{1/2}$ to 132.5 K with a larger hysteresis (17 K wide) while the isostructural Au system completely loses the SCO behaviour after dehydration. The initial half-SCO behaviour is recovered by rehydration upon exposure to air.

Another possibility to promote changes in the spin-crossover properties consists on the modification of the coordination sphere of the SCO centres. A beautiful example is the work published by Aromí, Gamez and co-workers, in which a 1D CP, [Fe_3(dpyatriz)$_2$(CH_3CH_2CN)$_4$(BF_4)$_2$](BF_4)$_4$·4CH_3CH_2CN, is capable of replacing the coordinated propionitrile molecules upon immersion into different solvents.[41] Thus, a decrease of the transition temperature from 300 K to 273 K (acetonitrile) or suppression of the spin-crossover properties is observed, with retention of the overall crystal structure (figure 1.14). However, replacement with water molecules from the atmosphere results in reversible structural change. This transformation involves suppression of the spin-crossover properties, presumably due to a reduction of the ligand field around the Fe^{II}.

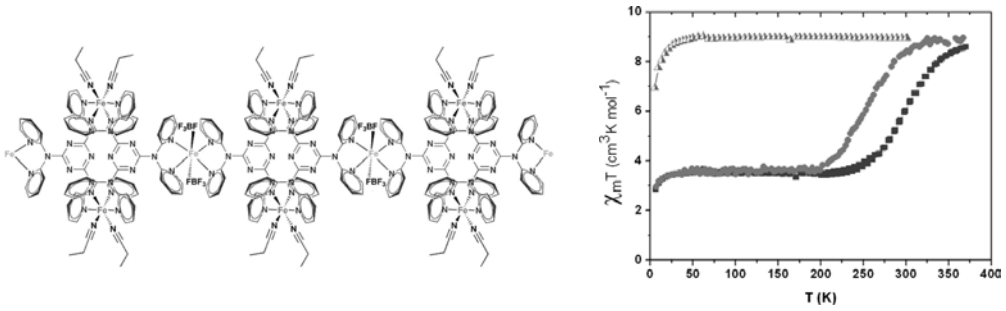

Figure 1.14 a) 1D CP $[Fe_3(dpyatriz)_2(CH_3CH_2CN)_4(BF_4)_2](BF_4)_4 \cdot 4CH_3CH_2CN$ showing the coordinated propionitrile molecules that can be replaced (non-coordinated molecules omitted for clarity); (b) temperature-dependent DC magnetic susceptibilities of pristine material (squares), after acetonitrile exchange (circles) and after 1-propanole exchange (triangles). Reproduced from reference 41.

Finally, one last example of dynamic porous CP showing a modulation of the transition temperature is given by the oxidative chemisorption in Hofmann chlatrates obtained by Real, Ohba and co-workers. In this system, exposure to dihalogens promotes an oxidation of Pt^{II} to Pt^{IV} with a reduction of the dihalogen to the corresponding halide resulting in the formation of $\{Fe(pz)[Pt(CN)_4(X)_p]\}$ [X=Cl^- (p=1), Br^- (p=1), I^- (0<p<1)].[42-43] This oxidative chemisorption (figure 1.15) modifies the σ-donor capability of the nitrogen atom of the Pt–CN group, provoking a change of $T_{1/2}$ in a way that the more electronegative halogen induces a decrease of the ligand field, and so $T_{1/2}$ is decreased.

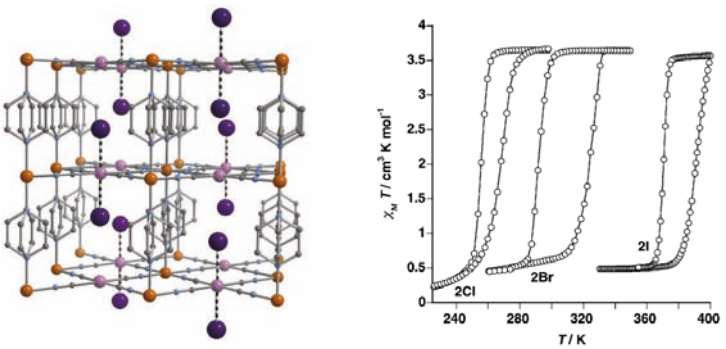

(a) (b)

Figure 1.15 (a) Crystal structure of $\{Fe(pz)[Pt(CN)_4(X)_p]\}$. (b) $\chi_M T$ versus T plot for 2Cl, 2Br and 2I α-phase.

Gas-mediated magnetic transformations

Especially interesting are those systems in which magnetic properties are modulated upon sorption of gas molecules. Most commonly, adsorbed gas molecules (H_2, N_2, CO_2…) do not appreciably interact with the magnetic host network, thus provoking no effects on the magnetic ordering or the spin transition temperatures. Indeed, the observed gas sensitive, long-range magnetic ordering in a porous material has been solely observed in two examples in magnetically ordered systems. In the following paragraphs these two examples will be explained.

In 2008, Long and co-workers[44] published the first example in which sorption of paramagnetic gas molecules produced a magnetic transformation in microporous magnets with high ordering temperatures. In this work, desolvation of the Prussian blue analogues $Cr_3[Cr(CN)_6]_2{\cdot}10H_2O$ and $CsNi[Cr(CN)_6]{\cdot}2H_2O$ afforded $Cr_3[Cr(CN)_6]_2{\cdot}6H_2O$ and $CsNi[Cr(CN)_6]$, respectively, which resulted to be microporous magnets with BET surface areas of 360 and 400 m^2g^{-1} and magnetic ordering temperatures of 75 and 219 K, respectively. Unexpectedly, both materials were found to exhibit changes in their magnetic properties upon adsorption of O_2 but not N_2, indicating the presence of magnetic exchange coupling between the paramagnetic O_2 guest molecules and the frameworks. The adsorption of O_2 results in a net antiferromagnetic interaction with the ferrimagnetic nickel framework. Interestingly, this exchange interaction switches to ferromagnetic for O_2 adsorbed within the ferromagnet $CsNi[Cr(CN)_6]$, suggesting that ferromagnetic coupling between O_2 and the $[Cr(CN)_6]^{3-}$ units provides the predominate exchange pathway in each material.

The same year, Navarro, Parra, Sironi and co-workers[45] reported a gismondine-like magnetic MOF, $[Cu(F\text{-}pymo)_2(H_2O)_{1.25}]_n$ (F-pymo = 5-fluoropyrimidin-2-olate), which suffers reversible changes in the ligand structure upon insertion of gas molecules in the pores. This compound presents helical channels of *ca*. 2.9 Å diameter which are filled with water molecules that can be removed upon heating (figure 1.16). The activated solid behaves as a molecular sieve and preferentially adsorbs H_2 over

N_2, in addition to CO_2. The as-synthesized solid shows antiferromagnetic interactions and it orders as a canted antiferromagnet below T_N = 24 K. Such temperature is reduced to 22 K upon activation. Interestingly, the ordering temperature is increased to 29 K when the material is loaded with CO_2 (figure 1.16b), presumably due to the structural perturbation exerted by the CO_2 guests, which affect the exchange interaction pathways through the ligands. This structural perturbation can tune the magnetic properties of the $[Cu(F\text{-}pymo)_2]_n$ network.

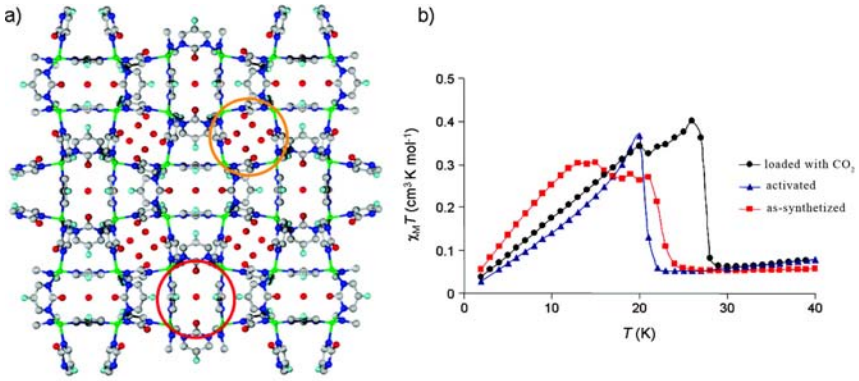

Figure 1.16 (a) Crystal structure of $[Cu(F\text{-}pymo)_2(H_2O)_{1.25}]_n$ highlighting the water filled channels. (b) Effects of the guest molecules in the magnetic behaviour of the Cu MOF at an external magnetic field of 100 Oe.

There is a special case comprising a SCO system in which the spin state of the host has a substantial effect on the gas sorption. This example, published by Kepert and co-workers,[38] explains the different adsorption capacity depending on the spin state of a robust pillared Hofmann-type SCO system. Therefore, the adsorption capacity for the system towards sorption of N_2 and O_2 gas molecules in the HS is greater than that for the LS. For CO_2 adsorption the effect of spin state on adsorption capacity is pressure dependent, at higher pressures the behaviour is similar to N_2 and O_2, but at lower pressures (<0.5 bar) the system in the LS has a slightly higher adsorption capacity. Importantly, there is a lack of examples in the literature for which gas-mediated magnetic transformations occur in a SCO system, which has been one of the aims of this thesis.

Physically-induced transformations

Responsive magnetic MOFs responding to a physical stimulus are scarce in comparison to the above-mentioned chemically-driven transformations. The vast majority of such materials present a structural modification promoted by thermal activation. In this sense, some of the materials presented in the previous section are also thermally-driven, although the physisorption or chemisorption of molecules is common to all of them.

A beautiful example of this category of dynamic MOFs was published in our group in 2005.[46a] In this work the non-symmetric cyanide ligand undergoes a rotation induced by pressure when it is connecting Fe^{II} to Cr^{III} in a Prussian blue analogue.

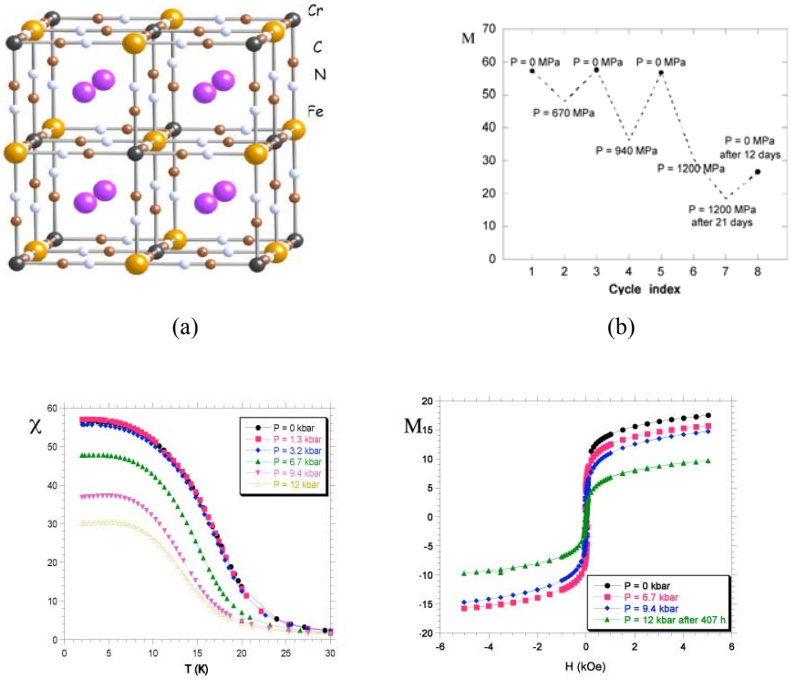

Figure 1.17 (a) Crystal structure of $K_{0.4}Fe_4[Cr(CN)_6]_{2.8}\cdot 16H_2O$. (b) Reversibility plot: magnetization changes induced upon alternating pressure application and release. (c) Thermal dependence of the magnetization of $K_{0.4}Fe_4[Cr(CN)_6]_{2.8}\cdot 16H_2O$ (applied field = 0.1 T) at different pressures; (d) field dependence of the magnetization of $K_{0.4}Fe_4[Cr(CN)_6]_{2.8}\cdot 16H_2O$ ($T = 2$ K) at different applied pressures.

This molecular magnet, formulated as $K_{0.4}Fe_4[Cr(CN)_6]_{2.8}\cdot 16H_2O$, presents structural features typical of a Prussian blue analogue (figure x) and behaves as a soft ferromagnet ordering at T_c = 19 K. Upon application of external pressure (*P*) in the 0-1200 MPa range, the magnetization decreases considerably and the Curie temperature shifts to lower temperatures in a reversible manner (figure 1.17). An additional and irreversible decrease of the magnetization and ordering temperature (T_c = 8 K) is observed after prolonged treatment (21 days) at 1200 MPa. This piezomagnetic behaviour has been attributed to the linkage isomerism of the cyanide. In fact, under pressure some of the Cr^{III}–CN–Fe^{II} linkages present in the compound isomerize to the more compressed Cr^{III}–NC–Fe^{II} form.[46b] This results in an increase of the ligand field around the iron^{II} centres, which undergo spin crossover to the diamagnetic LS state. This molecular process explains that, as the pressure increases, the number of paramagnetic centres in the cubic lattice decreases, as do the net magnetization and the critical temperature of the material. At the local level, the rotational movement of the cyanide anions can be considered as a molecular switch of the magnetic interaction between nearest neighbours.

REFERENCES

1. Janiak, C. *Dalton Trans*., **2003**, 2781.
2. Batten, S. R., Turner, D. R. and Neville, M. S. "Coordination Polymers: Design, Analysis and Application", The Royal Society of Chemistry, Cambridge, **2009**.
3. Bailar Jr., J. C. *Preparative Inorganic Reactions*, ed. W. L. Jolly, Interscience, New York, **1964**,*1*,1.
4. Kitagawa, S., Kitaura, R. and Noro, S. *Angew. Chem., Int. Ed.* **2004**, *43*, 2334.
5. Blake, A. J., Champness, N. R., Hubberstey, P., Li, W.-S., Withersby, M. A. and Schröder, M. *Coord. Chem. Rev.* **1999**, *183*, 117.
6. Férey, G. *Chem. Soc. Rev.* **2008**, *37*, 191.
7. (a) Hoskins, B. F. and Robson, R. *J. Am. Chem. Soc.* **1989**, *111*, 5962. (b) Hoskins, B. F. and Robson, R. *J. Am. Chem. Soc.* **1990**, *112*, 1546.
8. Special issues: *Chem. Soc. Rev.* **2009**, *42*, 3277, and *Chem. Rev*. **2012**, *112*, 673.
9. (a) Ohba, M., Kaneko, W., Kitagawa, S., Maeda, T. and Mito, M. *J. Am. Chem. Soc*. **2008**, *130*, 4475. (b) Larionova, J., Chavan, S. A., Yakhmi, J. V., Frøystein, A. G., Sletten, J., Sourisseau, C. and Kahn, O. *Inorg. Chem.* **1997**, *36*, 6374. (c) Miyasaka, H., Matsumoto, N., Re, N., Gallo, E. and Floriani, C. *Inorg. Chem*. **1997**, *36*, 670.
10. (a) Miyasaka, H., Ieda, H., Matsumoto, N., Re, N., Crescenzi, R. and Floriani, C. *Inorg. Chem.* **1998**, *37*, 255. (b) Kahn, O., Larionova, J. and Yakhmi, J. V. *Chem.-Eur. J.* **1999**, *5*, 3443.
11. Usuki, N., Ohba, M. and Okawa, H. *Bull. Chem. Soc. Jpn*. **2002**, 75, 1693.
12. Wang, C., Zhang, T. and Lin, W. *Chem. Rev*. **2012**, *112*, 1084.
13. Chui, S. S.-Y., Lo, S. M.-F., Charmant, J. P. H., Orpen, A. G. and Williams, I. D. *Science* **1999**, *283*, 1148.
14. Li, H., Eddaoudi, M., O'Keeffe, M. and Yaghi, O. M. *Nature* **1999**, *402*, 276.
15. Noro, S., Kitagawa, S., Kondo, M. and Seki, K. *Angew. Chem., Int. Ed.* **2000**, *39*, 2081.
16. Serre, C., Millange, F., Thouvenot, C., Noguès, M., Marsolier, G., Louër, D. and Férey, G. *J. Am. Chem. Soc.* **2002**, *124*, 13519.
17. (a) Férey, G., Serre, C., Mellot-Draznieks, C., Millange, F., Surbé, S., Dutour, J. and Margiolaki, I. *Angew. Chem. Int. Ed*. **2004**, 43, 6296. (b) Férey, G., Mellot-Draznieks, C., Serre, C., Millange, F., Dutour, J., Surbé, S. and Margiolaki, I. *Science* **2005**, *309*, 2040.
18. Horcajada, P., Serre, C., Vallet-Regí, M., Sebban, M., Taulelle, F. and Férey, G. *Angew. Chem. Int. Ed.* **2006**, 45, 5974.
19. (a) Horcajada, P., Chalati, T., Serre, C., Gillet, B., Sebrie, C., Baati, T., Eubank, J. F., Heurtaux, D., Clayette, P., Kreuz, C., Chang, J.-S., Hwang, Y. K., Marsaud, V., Bories, P.-N., Cynober, L., Gil, S., Férey, G., Couvreur, P. and Gref, R. *Nat. Mater.* **2010**, *9*, 172. (b) Horcajada, P., Gref, R., Baati, T., Allan, P. K., Maurin, G., Couvreur, P., Férey, G., Morris, R. E. and Serre, C. *Chem. Rev.* **2012**, *112*, 1232.

20. Banerjee, R., Phan, A., Wang, B., Knobler, C. B., Furukawa, H., O'Keeffe, M. and Yaghi, O. M. *Science* **2008**, *319*, 939.

21. (a) Kitagawa, S. and Uemura, K. *Chem. Soc. Rev*. **2005**, *34*, 109. (c) Férey, G. and Serre, C. *Chem. Soc. Rev*. **2009**, *38*, 1380.

22. (a) Kole, G. K. and Vittal, J. J. *Chem. Soc. Rev*. **2013**, 42, 1755. (b) Hawxwell, S. M., Mínguez Espallargas, G., Bradshaw, D., Rosseinsky, M. J., Prior, T. J., Florence, A. J., van de Streek, J. and Brammer, L. *Chem. Commun*. **2007**, 1532. (c) Pigge, F. C. *CrystEngComm* **2011**, *13*, 1733. (d) Fletcher, A. J., Thomas, K. M. and Rosseinsky, M. J. *J. Solid State Chem.* **2005**, *178*, 2491.

23. Coronado, E. and Mínguez Espallargas, G. *Chem. Soc. Rev.* **2013**, *42*, 1525.

24. Maspoch, D., Ruiz-Molina, D., Wurst, K., Domingo, N., Cavallini, M., Biscarini, F., Tejada, J., Rovira, C. and Veciana, J. *Nature Mat.* **2003**, *2*, 190.

25. Kahn, O. and Martinez, C. J. *Science* **1998**, *279*, 44.

26. "Spin Crossover in Transition Metal Compounds" (Eds: P. Gütlich, H. A. Goodwin), *Top. Curr. Chem*. **2004**, 233. (b) Spiering, H., Kohlhaas, T., Romstedt, H., Hauser, A., Bruns-Yilmaz, C., Kusz, J. and Gütlich, P. *Coord. Chem. Rev.* **1999**, *629*, 190. (c) Gütlich, P., Hauser, A. and Spiering, H. *Angew. Chem. Int. Ed*. **1994**, *33*, 2024. (d) Gütlich, P., Garcia, Y. and Woike, T. *Coord. Chem. Rev*. **2001**, 219, 839.

27. (a) Real, J. A., Gaspar, A. B., Niel, V. and Muñoz, M. C. *Coord. Chem. Rev.* **2003**, *236*, 121. (b) Hauser, A., Jeftic, J., Romstedt, H., Hinek, R. and Spiering, H. *Coord. Chem. Rev.* **1999**, *190-192*, 471. (c) Gaspar , A. B., Seredyuk, M. and Gütlich, P. *J. Mol. Struct*. **2009**, *9*, 924.

28. (a) Kaneko, W., Ohba, M. and Kitagawa, S. *J. Am. Chem. Soc.* **2007**, *129*, 13706. (b) Milon, J., Daniel, M. C., Kaiba, A., Guionneau, P., Brandes, S. and Sutter, J. P. *J. Am. Chem. Soc*. **2007**, *129*, 13872. (c) Navarro, J. A. R., Barea, E., Rodríguez-Diéguez, A., Salas, J. M., Ania, C. O., Parra, J. B., Masciocchi, N., Galli, S. and Sironi, A. *J. Am. Chem. Soc*. **2008**, *130,* 3978. (d) Sun, W. W., Tian, C. Y., Jing, X. H., Wang, Y. Q. and Gao, E. Q. *Chem. Commun*. **2009**, 4741. (e) Wang, Z. M., Zhang, B., Fujiwara, H., Kobayashi, H. and Kurmoo, M. *Chem. Commun*. **2004**, 416.

29. (a) Halder, G. J., Kepert, C. J., Moubaraki, B., Murray, K. S. and Cashion, J. D. *Science* **2002**, *298*, 1762. (b) Neville, S. M., Halder, G. J., Chapman, K. W., Duriska, M. B., Southon, P. D., Cashion, J. D., Létard, J. F., Moubaraki, B., Murray, K. S. and Kepert, C. J. *J. Am. Chem. Soc.* **2008**, *130*, 2869.

30. (a) Kurmoo, M., Kumagai, H., Chapman, K. W. and Kepert, C. J. *Chem. Commun.* **2005**, 3012. (b) Zhang, X. M., Hao, Z. M., Zhang, W. X. and Chen, X. M. *Angew. Chem., Int. Ed.* **2007**, *46*, 3456. (c) Cheng, X. N., Zhang, W. X., Lin, Y. Y., Zheng, Y. Z. and Chen, X. M. *Adv. Mater*. **2007**, *19*, 1494. (d) Motokawa, N., Matsunaga, S., Takaishi, S., Miyasaka, H., Yamashita, M. and Dunbar, K. R. *J. Am. Chem. Soc.* **2010**, *132*, 11943.

31. Maspoch, D., Ruiz-Molina, D. and Veciana, J. *Chem. Soc. Rev*. **2007**, *36*, 770. (b) Dechambenoit, P. and Long, J. R. *Chem. Soc. Rev.* **2011**, *40*, 3249. (c) Kurmoo, M. *Chem. Soc. Rev.* **2009**, *38*, 1353. (d) Roques, N., Mugnaini, V. and Veciana, J. *Top. Curr. Chem.* **2010**, *293*, 207. (e) Hao, Z.-M. and Zhang, X.-M. *Dalton Trans.* **2011**, *40*, 2092.

32. (a) Larionova, J., Chavan, S. A., Yakhmi, J. V., Frøystein, A. G., Sletten, J., Sourisseau, C. and Kahn, O. *Inorg. Chem*. **1997**, *36*, 6374. (b) Kahn, O., Larionova, J. and Yakhmi, J. V. *Chem. -Eur. J*. **1999,** *5*, 3443.

33. Ohkoshi, S., Arai, K., Sato, Y. and Hashimoto, K. *Nature Mater*. **2004**, 3, 857.

34. Ohkoshi, S.-i., Tsunobuchi, Y., Takahashi, H., Hozumi, T., Shiro, M. and Hashimoto, K.*J. Am. Chem. Soc.* **2007**, *129*, 3084.

35 Neville, S. M., Moubaraki, B., Murray, K. S. and Kepert, C. J. *Angew. Chem., Int. Ed.* **2007**, *46*, 2059.

36 Halder, G. J., Chapman, K. W., Neville, S. M., Moubaraki, B., Murray, K. S., Létard, J. F. and Kepert, C. J. *J. Am. Chem. Soc.* **2008**, *130*, 17552.

37 Neville, S. M., Halder, G. J., Chapman, K. W., Duriska, M. B., Moubaraki, B., Murray, K. S. and Kepert, C. J. *J. Am. Chem. Soc*. **2009**, *131*, 12106.

38 Southon, P. D., Liu, L., Fellows, E. A., Price, D. J., Halder, G. J., Chapman, K. W., Moubaraki, B., Murray,| K. S., Létard, J.-F. and Kepert, C. J. *J. Am. Chem. Soc.* **2009**, *131*, 10998.

39 Ohba, M., Yoneda, K., Agustí, G., Muñoz, M. C., Gaspar, A. B., Real, J. A., Yamasaki, M., Ando, H., Nakao, Y., Sakaki, S. and Kitagawa, S. *Angew. Chem. Int. Ed.* **2009**, *48*, 4767.

40. Niel, V., Thompson, A. L., Muñoz, M. C., Galet, A., Goeta, A. E. and Real, J. A. *Angew. Chem. Int. Ed.* **2003**, *42*, 3760.

41. Quesada, M., de la Peña-O'Shea, V. A., Aromí, G., Geremia, S., Massera, C., Roubeau, O., Gamez, P. and J. Reedijk, *Adv. Mater.* **2007**, *19,* 1397.

42 Agustí, G., Ohtani, R., Yoneda, K., Gaspar, A. B., Ohba, M., Sánchez-Royo, J. F., Muñoz, M. C., Kitagawa, S. and Real, J. A. *Angew. Chem. Int. Ed*. **2009**, *48*, 8944.

43 Ohtani, R., Yoneda, K., Furukawa, S., Horike, N., Kitagawa, S., Gaspar, A. B., Muñoz, M. C., Real, J. A. and Ohba, M. *J. Am. Chem. Soc*. **2011**, *133*, 8600.

44. Kaye, S. S., Choi, H. J. and Long, J. L. *J. Am. Chem. Soc*. **2008**, *130*, 1692.

45. Navarro, J. A. R.; Barea, E.; Rodríguez-Diéguez, A.; Salas, J. M.; Ania, C. O.; Parra, J. B.; Masciocchi, N.; Galli, S.; Sironi, *J. Am. Chem. Soc.* **2008**, *130*, 3978.

46 (a) Coronado, E., Giménez-López, M. C., Levchenko, G., Romero, F. M., García-Baonza, V., Milner, A. and Paz-Pasternak, M. *J. Am. Chem. Soc*. **2005**, *127*, 4580. (b) Coronado, E., Giménez-López, M. C., Korzeniak, T., Levchenko, G., Romero, F. M., Segura, A., García-Baonza, V., Cezar, J. C., de Groot, F. H. F., Milner, A. and Paz-Pasternak, M. *J. Am. Chem. Soc.* **2008***, 130*, 15519.

2

CHEMISORPTION IN NON-POROUS MAGNETIC COORDINATION POLYMERS

2.1 INTRODUCTION

The design of responsive magnetic materials has recently attracted considerable attention in the field of molecular magnetism. In this sense, coordination chemistry has resulted essential for the preparation of molecule-based materials in which magnetic properties can be reversibly tuned at low temperatures through a physical stimulus such as light[1,2] or pressure.[3,4] In addition, the recent explosion in research on MOFs[5-11] has opened the use of chemical stimulus such as gas sorption to affect the magnetic properties of a porous coordination polymer. There are many examples of magnetic MOFs in which the physisorption of guest molecules provoke subtle changes in the framework that affect their magnetic properties.[12,13] However, the synthesis of magnetic MOFs remains a challenging issue since long range magnetic ordering and porosity are two properties inimical to one another: magnetic cooperativity requires short distances to promote strong exchange interactions while porosity is improved with long linkers which result in large distances between metal centres. Several possible approaches can be taken to overcome this challenge. It is possible to take advantage of the sensitivity of spin-crossover complexes to subtle structural changes in metal coordination environments, which do not require magnetic cooperativity.[14-16] Thus, it has been shown that MOFs based on spin crossover metal ions exhibit magnetic switching at room temperature upon physisorption of specific molecules within the porous framework.[17,18] The high sensitivity of these materials is also evidenced by the modification of the transition temperature upon oxidative addition reactions following gas sorption at metal sites that are far from the magnetic centres.[19,20] Special attention will be paid to these spin crossover MOFs in *Chapter 3*.

A different approach to tune the magnetic properties of porous solids consists on the modification of the magnetic ground state of the MOF, which can be achieved through gas sorption processes that subtly affects the geometry of either the bridge between metal centres[21] or the ligand substituents.[22] The change of the oxidation state of the metal centre[23] or the variation of the coordination number[24] upon hydration/dehydration have also been used to modify the magnetic properties of

porous materials. In all these cases the presence of pores is essential to accommodate the gas molecules that induce the minor structural changes in the framework provoking major changes in the magnetic properties. And, as mentioned before, porosity and magnetism are often difficult to combine.

Interestingly, it has been shown that changes in the metal coordination environment might also be feasible in non-porous materials through the chemisorption of some molecular species (see figure 2.1).[25] Chemisorption consists on the reversible incorporation of gases in the framework, commonly involving covalent bond breaking and formation. A particular example of such a dramatic transformation involves the reaction of molecular solids with gaseous HX (X = Cl, Br) leading to profound structural changes,[26,27] where porosity is not necessary since the chemisorption process involves the removal/addition of HX from/to the framework.

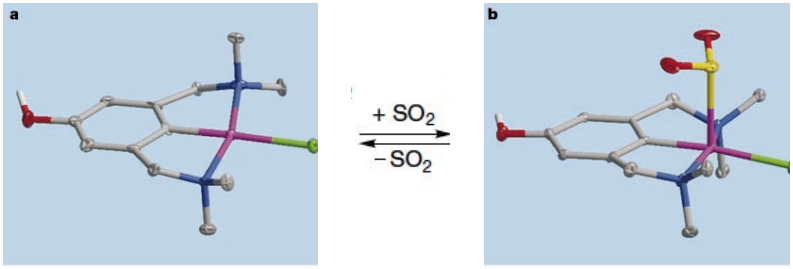

Figure 2.1 Scheme of the controlled and fully reversible crystalline-state reaction of gaseous SO_2 with a non-porous crystalline materials consisting of organoplatinum molecules. Adapted from reference 25.

The observation that non-porous molecular complexes are able to sorb HX has been the motivation to explore whether this chemisorption process could be used as an approach to design responsive molecular materials with tunable magnetic properties. Basically, this chemisorption would permit the uptake of gases in the absence of pores, thus alleviating the difficulty in combining porosity and magnetic cooperativity.

In this *Chapter* is shown that upon chemisorption of 3 equivalents of HCl molecules, the crystalline coordination compound [Cu(pyim)(Cl)(MeOH)] (**1**, where pyimH = 2-(imidazol-2-yl)pyridine) changes its structure from a polymeric chain of

pentacoordinated square-pyramidal Cu centres to an ionic solid, $(H_2pyimH)[CuCl_4]$ (**2**), containing discrete distorted tetrahedral $[CuCl_4]^{2-}$ anions. Compound **2** is able to extrude 2 equivalents of HCl yielding the molecular compound *cis*-$[CuCl_2(pyimH)]$ (**3**) in which the Cu centres present a square-planar geometry. The remarkable concerted reorganization of covalent bonds that occurs during the sorption/desorption processes results in significant changes in the magnetic properties of the materials, from strong antiferromagnetic interactions in **1** to weak ferro- or antiferromagnetic interactions in **2** and **3**, respectively. This can be precisely understood because of the retention of crystallinity of the materials. The single-crystal nature of compounds **1** and **2** provides direct structural evidence of the profound structural changes as a result of the sorption process, while complete structure determination for compound **3** was carried out by *ab initio* synchrotron X-ray powder diffraction (XPRD) analysis, since the removal of the gas molecules yields a uniform microcrystalline powder.

2.2 RESULTS AND DISCUSSION

2.2.1 Description of the structures

[Cu(pyim)(Cl)(MeOH)] (1). Structural analysis by X-ray single-crystal diffraction at 120 K revealed that **1** is composed of helical one-dimensional chains that run parallel to the crystallographic *c*-axis (figure 2.2). Individual crystals are chiral, but single crystals of both chiralities (space groups $P3_2$ and $P3_1$) are found in the product, which is a racemic mixture. Fully deprotonated $[pyim]^-$ ligands connect adjacent Cu centres via the imidazolate moieties within the ligands, forming a Cu–NCN–Cu bridge which is reminiscent of that found in the recently discovered zeolitic imidazolate frameworks (ZIFs)[28,29] and that has been exploited to promote magnetic interactions in Cu^{II} dimmers (figure 2.3).[30] The ligand pyimH has been previously used in the synthesis of mononuclear spin-crossover complexes acting as a bidentate ligand,[31] but its deprotonation to act as a tridentate ligand for the formation of a coordination polymer is unprecedented. The Cu–N distances are 1.969(7), 1.979(7) and 2.034(7) Å. The

coordination sphere of the metal centres is completed with terminal Cl and MeOH ligands [Cu–Cl: 2.274(2), Cu–O: 2.277(7) Å], resulting in a distorted square pyramidal pentacoordinated Cu centre. Each helical chain interacts with six neighbouring independent chains via O–H···Cl hydrogen bonds[32] between the methanol and chloride ligands.

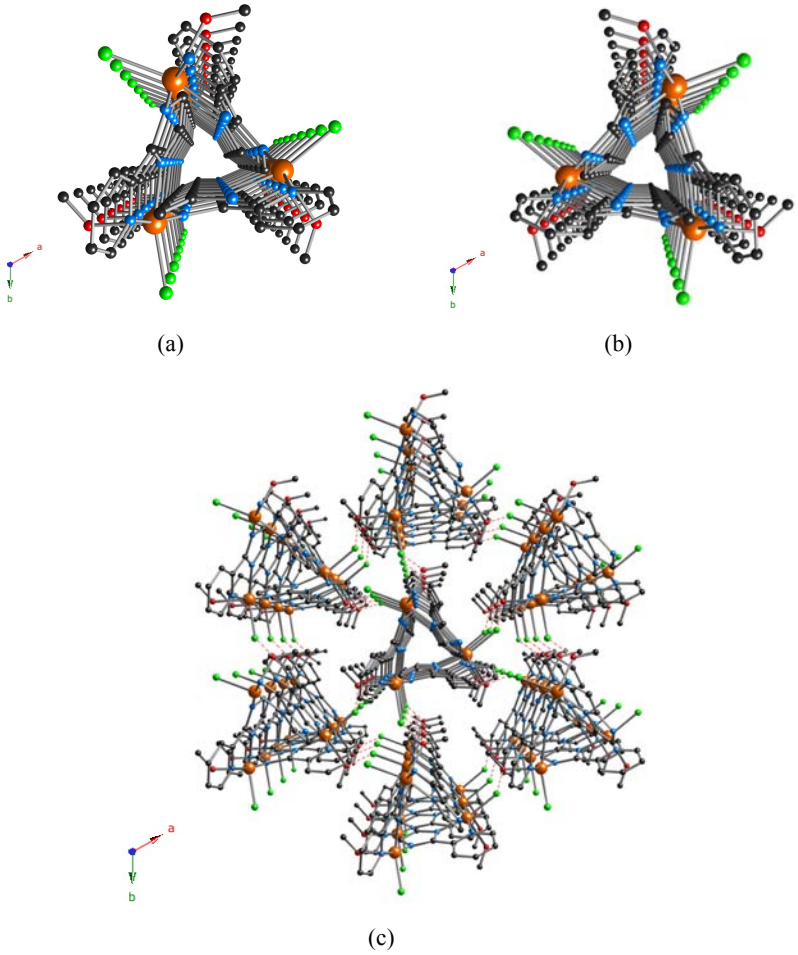

(a) (b)

(c)

Figure 2.2 (a,b) Helical one-dimensional chains of compounds **1+** (a, space group $P3_2$), and **1–** (b, space group $P3_1$) viewed along the *c* axis. (c) Crystal structure of compound **1+** showing the interaction of one chain with six neighbouring independent chains via O–H···Cl hydrogen bonds (dashed red lines) between the methanol and chloride ligands. Hydrogen atoms have been omitted for clarity.

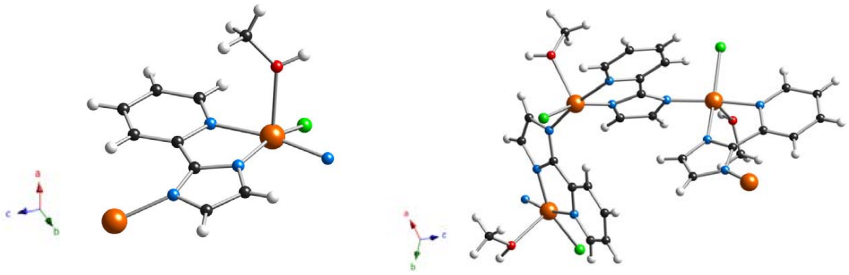

(a) (b)

Figure 2.3 (a) Structural unit of **1** showing the distorted square pyramidal pentacoordinated Cu centre and the bridging $[pyim]^-$ ligand. (b) View of the helical one-dimensional coordination polymer **1** which runs parallel to the crystallographic *c*-axis. The Cu–NCN–Cu bridge provides the closest contacts between the Cu centres. Key: Cu, orange; Cl, green; N, blue; O, red; C, black; H, white.

$(H_2pyimH)[CuCl_4]$ (2). After the HCl chemisorption of **1** we were able to isolate one single crystal from a polycrystalline powder that has permitted the structural analysis of the product $(H_2pyimH)[CuCl_4]$, **2**.

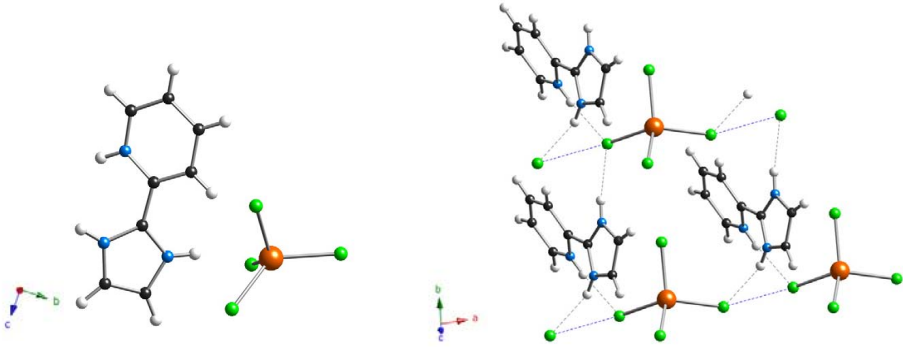

(a) (b)

Figure 2.4 (a) Structural unit of salt **2** showing the distorted tetrahedral $[CuCl_4]^{2-}$ anion and $[H_2pyimH]^{2+}$ cation. (b) Crystal structure of **2** showing the 2D hydrogen-bonded network formed by N–H···Cl–Cu hydrogen bonds. Key: Cu, orange; Cl, green; N, blue; O, red; C, black; H, white. Black dotted lines represent non-covalent interactions.

Compound **2** is a hydrogen bonded salt that comprises distorted tetrahedral $[CuCl_4]^{2-}$ anions and $(H_2pyimH)^{2+}$ cations that form a 2D network of (6,3) topology. In the

network each cation interacts with three anions via two N–H···Cl–Cu hydrogen bonds (H···Cl 2.162 and 2.184 Å) and one asymmetrically bifurcated N–H···Cl_2Cu (H···Cl 2.383 and 2.798 Å) (figure 2.4). Intermolecular Cu–Cl···Cl–Cu interactions [3.631(2) Å] provide the closest contacts between $[CuCl_4]^{2-}$ anions, which form supramolecular chains along the *a*-axis.

***cis*-[$CuCl_2$(pyimH)] (3).** Crystal structure of compound **3** (figure 2.5) has been determined *ab initio* by X-ray powder diffraction and subsequent refinement by Rietveld analysis (figure 2.6) since all attempts to recrystallize it from solution yield a microcrystalline powder. Synchrotron data was collected by Prof. L. Brammer (University of Sheffield) at the Diamond Light Source, UK. The structure of **3** consists of neutral [$CuCl_2$(pyimH)] units in which the copper atoms adopt a *cis* square-planar geometry coordinated by two nitrogen atoms from pyimH and two chloride ligands (figure 2.5) [Cu–N distances: 1.951(5) and 2.117(5)Å; Cu–Cl distances: 2.195(5) and 2.255(5) Å]. A one-dimensional coordination network structure is formed through a weak apical interaction with one of the chlorine atoms of a neighbouring complex [Cu–Cl···Cu 2.846(5) Å]. These chains are linked into 2D layers through N–H···Cl hydrogen bonds involving the imidazole group and chloride ligand and weaker C–H···Cl hydrogen bonds provide intermolecular links in the 3rd dimension.

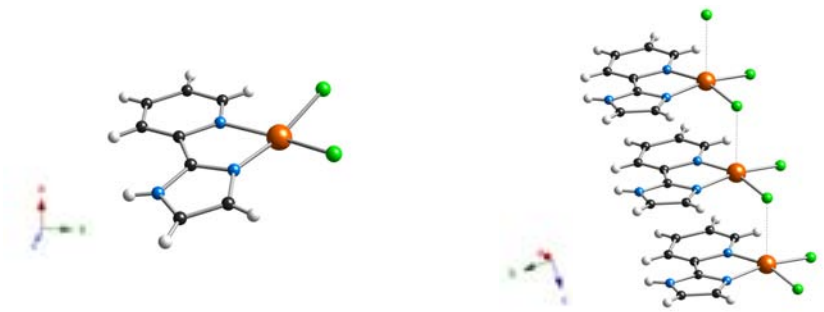

(a) (b)

Figure 2.5 (a) Structural unit of **3** in which the Cu centres adopt a *cis* square-planar geometry and the chelating ligand [pyimH] remains neutral. (b) One-dimensional coordination network structure of **3**. Black dotted lines represent a weak apical interaction with one of the chlorine atoms of a neighbouring complex [Cu–Cl···Cu Key: Cu, orange; Cl, green; N, blue; O, red; C, black; H.

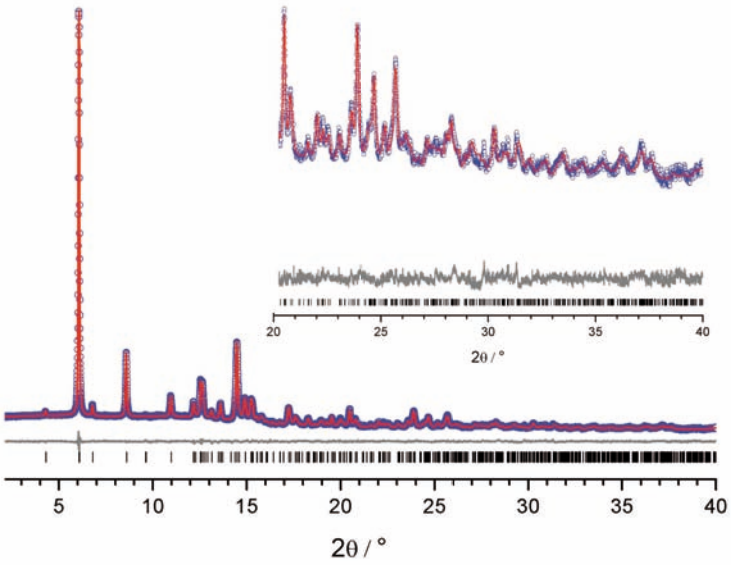

Figure 2.6 X-ray powder pattern and Rietveld refinement of compound **3.** Observed (blue) and calculated (red) powder XRD pattern profiles and difference plot [(I_{obs} - I_{calcd})] (grey) of the Rietveld refinement of a polycrystalline sample of **3** collected at room temperature in the 2θ range 2.0–40.0 ° using λ = 0.826134 Å. Rietveld refinement after ab initio structure solution converged to R_{wp} = 0.02267, R_{wp}' = 0.07678 (R_{wp}' is the background subtracted R_{wp}). The inset shows an expansion of the high angle region.

2.2.2 X-ray powder diffraction studies

Phase purity. To confirm the phase purity of the samples, X-ray powder diffraction (XRPD) studies have been performed on a crystalline powder of samples **1** and **2**. A comparison of the experimental diffraction pattern obtained for each compound and the simulated pattern calculated from single crystal diffraction data is presented in figure 2.7. The perfect match between the two patterns (experimental and calculated) reveals the purity of the sample. In addition, X-ray powder diffraction and Rietveld refinement of compound **3** have been performed and are detailed on section 2.3.2.

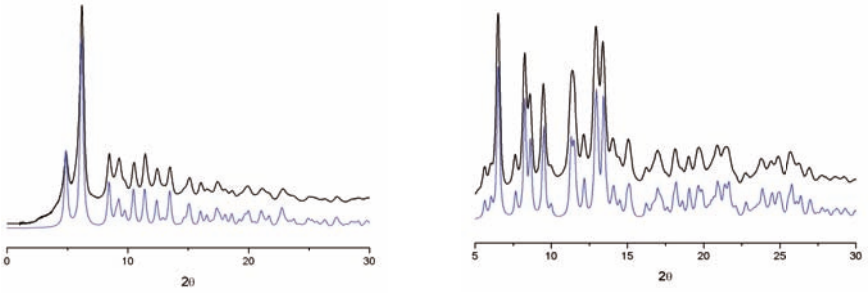

(a) (b)

Figure 2.7 X-ray powder diffraction patterns. Observed and calculated powder diffraction patterns of compounds **1** (left) and **2** (right) (λ = 0.71073 Å). The observed pattern is shown in black and the calculated pattern with full width at half maximum set to 0.25° is shown in blue.

2.2.3 Chemisorption/desorption of gaseous HCl molecules

Coordination polymer **1** is stable under ambient conditions, but possesses reactive Cu centres that undergo ligand substitution when crystalline **1** is exposed to an atmosphere of hydrochloric acid vapour in a sealed vessel despite the lack of pores in the structure. Since there is no possibility of a "guest molecule" being accommodated within pores, the gas molecules react with the material promoting significant chemical changes and atomic motions within the crystalline solid. As a result, the gas molecules are incorporated as part of the network. Thus, this process requires the cooperative movement of atoms in the solid state. The sorption process leads to protonation of the imidazolate ligand and modifies the geometry around the Cu centres as indicated by a dramatic colour change from dark green to yellow within a few minutes (see figure 2.8). The chemisorption of HCl occurs in 100 % yield within one hour, as demonstrated unequivocally by X-ray powder diffraction and EPR spectroscopy (figures 2.7 and 2.17, *vide infra*). Three equivalents of HCl molecules are inserted into all Cu–N bonds requiring rupture of the covalent bond of the gaseous molecules (H–Cl) and of the coordination bonds of the polymeric compound in order that new N–H and Cu–Cl bonds can be formed (figure 2.9). In addition, the MeOH molecules that complete the coordination sphere in **1** are displaced during the sorption process.

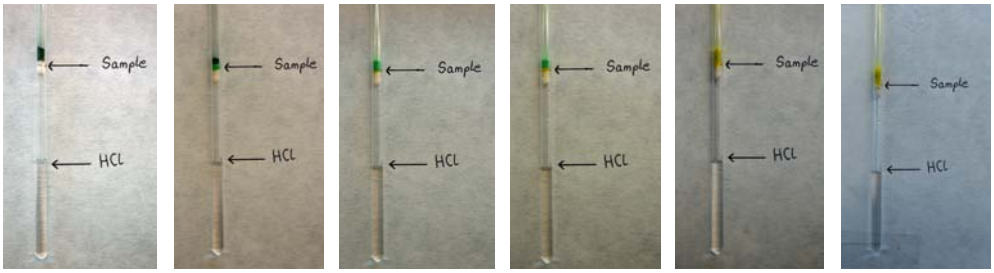

0 min 45 min 80 min 160 min 20 h 45 h

Figure 2.8 Pictures of the sample preparation for the magnetic measurements of compound **2** under HCl atmosphere. It should be noted that the reaction is surface area dependent, and well-packed sample used in this experiment results in an increase in the reaction time for completion.

When left to stand in air at room temperature, **2** is able to release two equivalents of HCl gas leading to conversion into *cis*-[$CuCl_2$(pyimH)], **3**. The complete deprotonation of the ligand pyimH requires the use of basic conditions. The HCl molecules that are liberated are part of the components of the framework, which implies that porosity is not needed for the release reaction to take place. Rather, a complete rearrangement of the solid takes place (figure 2.9). Interestingly, only the least acidic of the three N–H groups (pK_a = 13.4(1) in water),[33] which also forms the longest N–H···Cl hydrogen bond, does not participate in the dehydrochlorination process. This clearly confirms the significant role played by the N–H···Cl hydrogen bonds in this type of reaction.[34] This hydrogen bond donor capacity of chelated pyimH has been previously reported in mononuclear Fe^{II} spin-crossover systems.[35] Remarkably, when subjected to an atmosphere of HCl vapour, compound **3** is able to incorporate two equivalents of this gas and the resulting crystalline product was confirmed to be salt **2**, showing that the molecular coordination compound **3** and the salt **2** can be interconverted as crystalline solids at room temperature. The sorption behaviour of compound **3** is therefore analogous to that of compound **1** with the proviso that only 2 equivalents of HCl are incorporated. Thus, compound **3** can be seen as a likely intermediate in the uptake of 3 equivalents of HCl by **1** to yield **2** via a

2-step process: an irreversible sorption of 1 equivalent of HCl (**1→3**) followed by a reversible sorption of 2 equivalents of HCl (**3 ⇄ 2**).

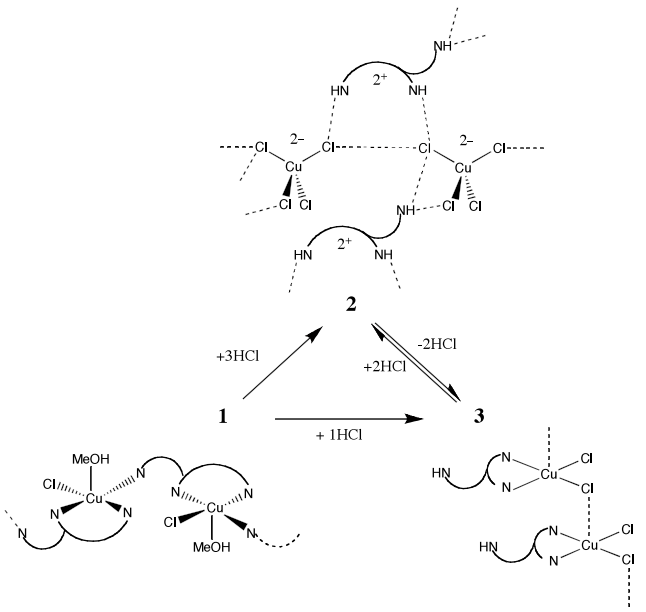

Figure 2.9 Rearrangement of covalent bonds upon chemisorption and release of HCl. When crystalline [Cu(pyim)(Cl)(MeOH)] **1** is exposed to an atmosphere of hydrochloric acid vapour an irreversible sorption of 3 equivalent of HCl (**1→2**) results into the hydrogen bonded salt (H_2pyimH)[$CuCl_4$], **2**, which is able to release two equivalents of HCl gas in a complete rearrangement of the solid, leading to conversion into *cis*-[$CuCl_2$(pyimH)], **3**, which is capable of reversibly incorporate 2 equivalents of HCl affording **2** (**2 ⇄ 3**). Alternatively, **3** can also be obtained by direct exposition of **1** to 1 equivalent of HCl (**1→3**). Chemisorption of HCl molecules involves insertion into Cu–N bonds requiring rupture and formation of new covalent bonds.

Upon exposure of **1** to HCl vapours in the magnetic sample holder (*vide infra*), the material closer to the vapours of HCl began to change colour from dark green to light green (figure 2.8). This colour front moved along the capillary over time providing a visual indication of the reaction front, which is completed in less than 1 hour. Upon further exposure, a second colour front (light green-to-yellow) is observed, and indicates completion in 1 day. This strongly suggests that the chemisorption process

1→2 is a two-step process that occurs via the formation of **3**. Interestingly, all attempts to prepare crystalline **2** from aqueous solution by reaction of $CuCl_2$ with one equivalent of pyimH in concentrated HCl afforded only a microcrystalline powder of **3**. Thus, the synthesis of **2** is only achievable by a gas-solid reaction with either **1** or **3** as the starting material. We speculate that this is due to this process being a gas–solid equilibrium reaction analogous to previous studies,[36] but the chelating effect of the ligand pyimH affects the position of the equilibrium.

2.2.4 Magnetic response to HCl chemisorption

Upon HCl chemisorption/desorption major changes take place in the magnetic properties as a consequence of the structural changes experienced by the compounds, which modify the magnetic exchange paths between the copper centres (figure 2.10). Thus, the magneto-structural switching of these materials arises from the presence of labile copper(II) centres which are capable of reacting with gaseous HCl or releasing HCl in a cyclic manner without loss of effectiveness.

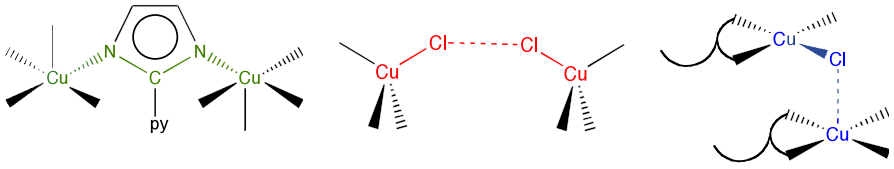

(a) (b) (c)

Figure 2.10 Different magnetic path for each compound: the Cu–NCN–Cu imidazolate bridge in **1** (a) is shown in green; the two-halide Cu–Cl···Cl–Cu exchange pathway in **2** (b) is shown in red; the Cu–Cl···Cu chloride bridge in **3** (c) is shown in blue.

The magnetic characterization of compound **1** shows that the product of the molar magnetic susceptibility and temperature, $\chi_M T$, has a value of 0.38 emu.K.mol^{-1} at room temperature (figure 2.11a). As the system is cooled, the $\chi_M T$ product decreases continuously, indicating the presence of strong antiferromagnetic Cu···Cu interactions through the imidazolate bridges. The spin Hamiltonian to describe the isotropic interaction between nearest neighbour ions is presented in equation 1.[37]

$$H = -J\sum_{N=1}^{\infty} S_1 S_{1+N} \qquad \text{Eq. 1}$$

The expression for the magnetic susceptibility of antiferromagnetic linear chains of S = 1/2 ions is obtained from the numerical results of Bonner and Fisher[37a] and is presented below:

$$\chi_m = \frac{Ng^2\mu_\beta{}^2}{kT}\frac{0.25 + 0.074975x + 0.075235x^2}{1.0 + 0.9931x + 0.172135x^2 + 0.757825x^3} \qquad \text{Eq. 2}$$

where x = (| J | /kT)

This fit leads to a magnetic coupling J = –45.7 cm^{-1} (figure 2.11a), using a Landé-factor g = 2.13 as measured by EPR (figure 2.14, *vide infra*). A small fraction of the paramagnetic monomer is also detected at low temperatures (contribution of *ca*. 8%).

HCl chemisorption results in the protonation of the [pyim]$^-$ ligand, which switches off the efficient Cu···Cu exchange pathway present in **1**, and therefore the Cu^{II} spins do not show any interaction down to 20 K in compound **2**, as demonstrated by the constant χ_MT value of 0.45 emu.K.mol^{-1} observed from 300 to 20 K. Upon further cooling χ_MT increases to reach a value of 0.83 emu.K.mol^{-1} at 2.0 K (figure 2.11b), indicating the presence of a weak ferromagnetic interactions. The magnetic data have been analyzed using a model comprising a uniformly spaced linear ferromagnetic chain of spin S = ½ as proposed by Baker *et al*.[38] (see equation 3) affording an exchange coupling of J = +0.76 cm^{-1} with a Landé-factor g = 2.07.

$$\chi_m = \frac{Ng^2\mu_\beta{}^2}{kT}\left[\frac{A}{D}\right]^{2/3} \qquad \text{Eq. 3}$$

$$A = 1.0 + 5.7979916y + 16.902653y^2 + 29.376885y^3 + 29.832959y^4 + 14.036918y^5$$
$$D = 1.0 + 2.7979916y + 7.0086780y^2 + 8.6538644y^3 + 4.5743114y^4$$
$$y = J/2kT$$

The susceptibility data of compound **2** has been fitted to a Curie-Weiss law (equation 4) where C is the Curie constant and θ is the Weiss constant (or Weiss temperature). A positive value of θ indicates ferromagnetic exchange interactions whereas negative θ indicates antiferromagnetic interactions. Representation of χ^{-1} gives a straight line of which the slope is C^{-1}. The intercept with the T axis yields both the sign and the value of θ. Figure 2.12 shows the best fitting of the χ^{-1} affording a Weiss constant of +2 K.

$$\chi = \frac{C}{(T - \theta)} \qquad \text{Eq. 4}$$

The most plausible exchange pathway in **2** involves a two-halide Cu–Cl···Cl–Cu interaction (figure 2.10),[39,40] although it may also contain some influence from other potential superexchange mechanisms such as Cu–Cl···Cu non-bonding interactions or N–H···Cl–Cu hydrogen bonds. Due to the rapid release of HCl by **2** (conversion to **3**), magnetic measurements were performed under HCl atmosphere to guarantee homogeneity during the magnetic measurements.

After release of HCl, the magnetic behaviour of **3** indicates that the Cu···Cu interactions are also very weak (figure 2.11c), which is due to the fact that after the release of two equivalents of HCl (**2** → **3**) the imidazole ligand remains neutral and does not act as a bridging ligand in the product. Instead, a chloride ligand bridges the square-planar Cu^{II} units. Similar to **2**, exchange interactions are only detected in the low temperature magnetic behaviour. Below 20 K, $\chi_M T$ increases slightly to reach a maximum value of 0.45 emu.K.mol^{-1} at 13 K and then decreases at lower temperatures. This behaviour is indicative of weak ferromagnetic interactions coexisting with a dominant antiferromagnetic coupling. All these features have been modeled by treating this compound as a uniformly spaced antiferromagnetic regular chain, *J*, (equation 2).[37b] plus an additional inter-chain interaction (*J′*), modelled with the molecular field approximation.[41] The bridging chloride ligand provides the magnetic pathway for the antiferromagnetic exchange (J = –4.46 cm^{-1}) and the N–H···Cl and C–H···Cl hydrogen bonds might be responsible for the weak ferromagnetic

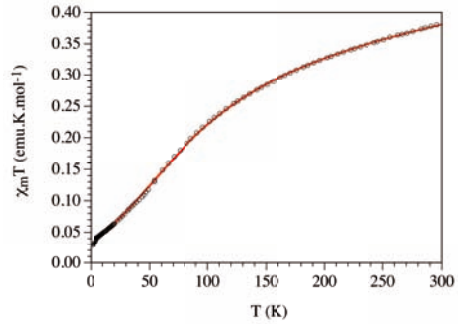

(a)

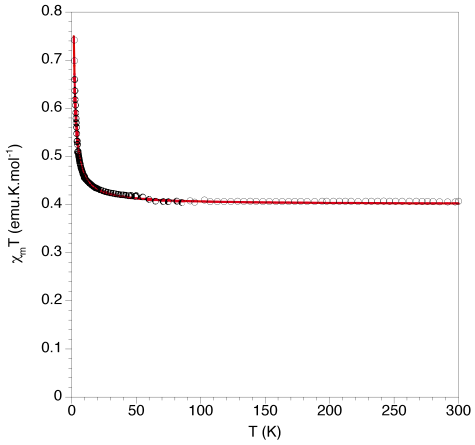

(b)

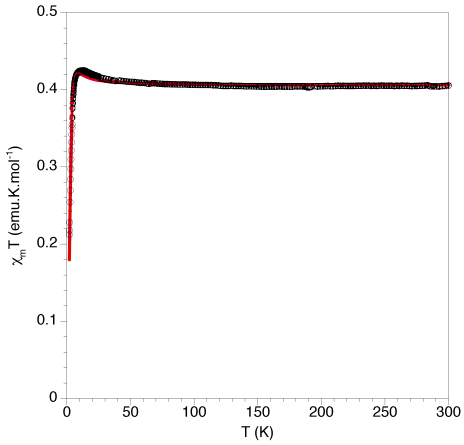

(c)

Figure 2.11 Thermal dependence of the $\chi_M T$ product of **1** (a), **2** (b) and **3** (c) including the fit (red line).

coupling (J' =+1.70). The small value of J is consistent with the structural features. The out-of-plane bridging framework created by the packing of the square-planar Cu^{II} units linked through the chloride ligand is not favourable to promote any exchange interaction since the magnetic orbital of the Cu^{II} is mainly delocalized in the equatorial plane and a very weak spin density is expected on its axial position.

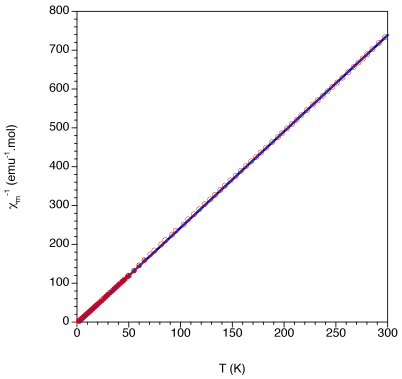

Figure 2.12 Best fitting (blue line) of the susceptibility data of compound **2** from 300 to 200 K to a Curie-Weiss law (Weiss constant θ = +2 K).

The different magnetic response upon HCl chemisorption/desorption (see table 2.1) is confirmed by the field dependence of the magnetization measured at 2 K (figure 2.13). The strong antiferromagnetic nature of coordination polymer **1** is evident due to the linear increase of the weak signal which is much below the calculated Brillouin curve (Bη(x), see equation 5) for non-interacting spin S = ½ (M_{sat} = 1 μ_B). Thus, antiferromagnetic intrachain interactions are present in compound **1**. For compound **2** the magnetization increase is sharper than that of the Brillouin function and saturates at 5 T, whereas for **3** the magnetization values are always below the Brillouin function and does not reach saturation, which agrees with the weak ferromagnetic (**2**) and weak antiferromagnetic (**3**) exchange interactions in these compounds.

The Brillouin function Bη(x):

$$B\eta(x) = \frac{1}{S}\left[\left(S+\frac{1}{2}\right)\coth\left[\left(S+\frac{1}{2}\right)x\right] - \frac{1}{2}\coth\frac{x}{2}\right] \qquad \text{Eq. 5}$$

Where $x = \frac{g\mu_B H}{kT}$

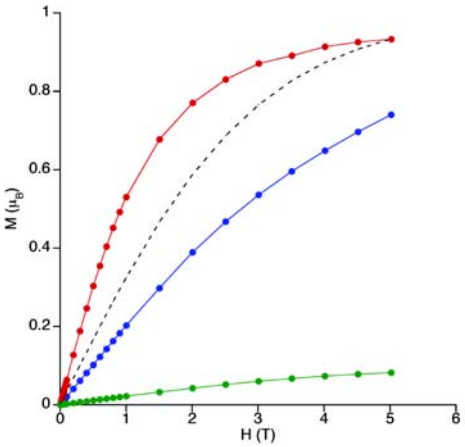

Figure 2.13 Field dependence of the magnetization, M, measured at 2 K of compounds **1** (green), **2** (red) and **3** (blue) and the Brillouin function for non-interacting S=1/2 (black dashed line).

Table 2.1 Fitting parameters for magnetic data according to different models and magnetic pathways.

	Fitting model	ref	*S*	*J* (cm^{-1})	*J'* (cm^{-1})	Magnetic pathway
1	1D linear-chain	37	1/2	−45.7	-	Cu–NCN–Cu
2	1D linear-chain	38	1/2	+0.76	-	Cu–Cl···Cl–Cu
3	1D linear-chain and intermolecular interaction	39, 40	1/2	−4.46	+1.70	Cu–Cl···Cu

2.2.5 EPR response to HCl chemisorption and monitoring

The substantial changes in coordination environments of the copper centres due to the sorption/desorption processes permit the use of electron paramagnetic resonance (EPR) spectroscopy, which is strongly sensitive to the coordination environment of

the metal centres and lead to clear differences in the EPR spectra of these compounds. EPR spectra of compounds **1**, **3** and **2** will be discussed below in this order.

EPR spectra of compound **1** have been measured at different temperatures (300, 200, 100, 50, 25, 10 and 4 K). An axial spectrum is obtained for all temperatures (g values can be modeled to $g_{\parallel} = 2.25$ and $g_{\perp} = 2.08$; $g_{average} = 2.13$). These values (with $g_{\parallel} > g_{\perp}$) are in agreement with the coordination environment of the Cu, which presents a pentacoordinated square-pyramidal geometry and a $d_{x^2-y^2}$ magnetic orbital (see table 2.2). The $\Delta m_s = \pm 2$ transition characteristic of dimeric species[42] is not observed at the half-field region, in agreement with the dimensionality of the system (J-uniform magnetic chains).

In order to demonstrate that the observed EPR signal does not correspond to the monomer impurity, the variation of the intensity of the signal with temperature has been studied (figure 2.14). The intensity of the EPR signal (I) is proportional to the magnetic susceptibility, and is in agreement with the magnetic properties: the product IT decreases with T, which demonstrates that the observed EPR signal corresponds to the Cu chain. The signal intensities have been normalized such that the value of the IT product at 300 K matches the observed χ_MT value. With this normalization, it is observed that the IT product at 50 K matches also the observed χ_MT value.

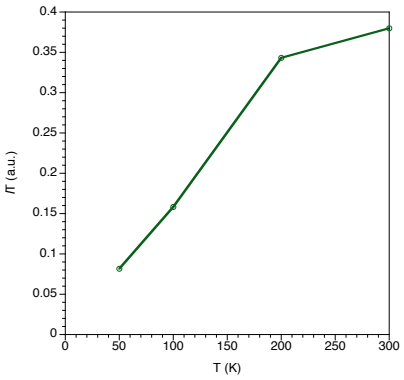

Figure 2.14 Thermal dependence of the product of the normalized intensity of the EPR signal with temperature of compound **1** (green) in the temperature range 50-300 K.

EPR spectra of compound **3** have been measured at different temperatures (300, 200, 100, 50, 25, 10 and 4 K). An axial spectrum is observed at all temperatures (g values can be modeled to $g_{||} = 2.28$ and $g_{\perp} = 2.08$; $g_{average} = 2.14$). These values (with $g_{||} > g_{\perp}$) are in agreement with the coordination environment of the Cu which indicates a $d_{x^2-y^2}$ magnetic orbital.

EPR spectra of compound **2** at different temperatures (figure 2.15) shows that a split of the signal occurs below 100 K. At 300 K an isotropic spectra can be observed with g = 2.20, which fully agrees with an unresolved spectra with a distorted tetrahedral environment exhibited by the Cu site (figure 2.4a). However, at low temperatures an inverse axial spectrum with $g_{||} < g_{\perp}$ is found (modeled values $g_{||} = 2.100$ and $g_{\perp} = 2.255$; $g_{average} = 2.20$), indicating a d_{z^2} magnetic orbital, which is unusual for distorted tetrahedral environments but typical for penta-coordinated Cu^{II} complexes with trigonal bipyramid geometries.[43] This might be due to the presence of a Cu–Cl···Cu non-bonding interaction (figure 2.16) that results in a pseudo-pentacoordination of the Cu atom which is closer to a trigonal bipiramid than to a square pyramidal geometry. Hence, the anisotropy of the EPR spectra below 100 K can be seen as the result of an intermediate situation between trigonal bipyramid (from the pseudopentacoordination of the Cu) and distorted tetrahedral (from the real tetracoordination of the Cu), which implies a ground state described by a mixture of the $d_{x^2-y^2}$ and d_{z^2} Cu(II) orbitals and explains that $g_{||} < g_{\perp}$. Previous studies on the variation of the EPR spectra of $[CuCl_5]^{3-}$ with temperature support this point of view.[44] In that work, Reinen and Friebel show that the g anisotropy increases considerably upon decrease of temperature due to a change of geometry of the $[CuCl_5]^{3-}$ polyhedra due to a second-order Jahn-Teller effect. The situation in compound **2** is somewhat similar: at room temperature there are isolated $[CuCl_4]^{2-}$ anions with isotropic g values; upon decrease of temperature, weak Cu–Cl···Cu interactions produce a splitting of the EPR signal, which can be achieved due to the high plasticity of the $[CuCl_4]^{2-}$ anions. Nevertheless, this small g-anisotropy has no effect on the magnetic description of compound **2,** which has been demonstrated by calculating the magnetic susceptibility of a ferromagnetic S = 1/2

Heisenberg chain with a fixed J value of 0.7 cm^{-1} as a function of the degree of anisotropy of the g tensor, with $0.8 < g_{\|}/g_{\perp} < 1.2$ maintaining in all cases $g_{av} = 2.20$. All $g_{\|}/g_{\perp}$ values yield the same magnetic susceptibilities, i.e. several fits with $g_{\|}/g_{\perp}$ values in the range 0.8–1.2 and the same *J* value can reproduce the experimental magnetic susceptibility of compound **2**.

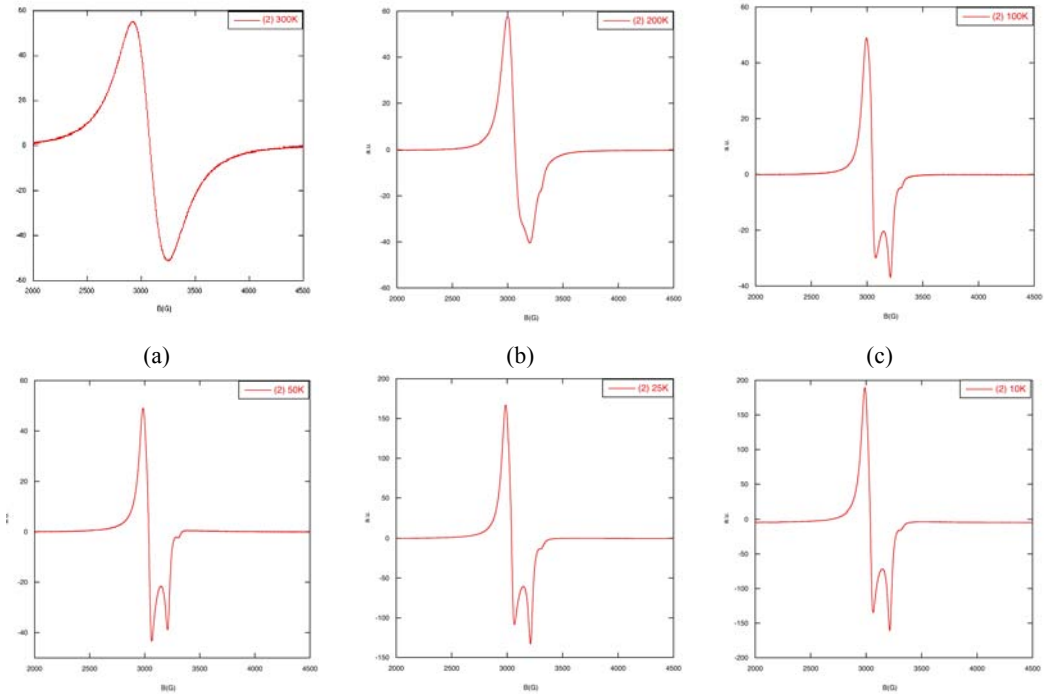

Figure 2.15 X-band EPR spectra of compound **2** at different temperatures: 300 (a), 200 (b), 100 (c), 50 (d), 25 (e), and 10 K (f).

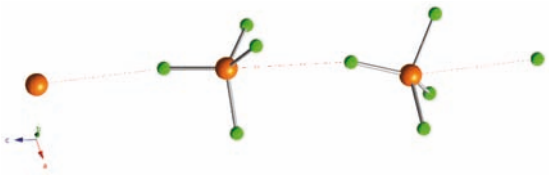

Figure 2.16 View of crystal structure of compound **2.** The environment of Cu centre in **2** shows a Cu–Cl···Cu non-bonding interaction (dashed red line) which results in a pseudo-pentacoordination of the Cu atom.

Table 2.2 EPR spectral parameters and magnetic orbitals.

	$g_{\parallel}$	$g_{\perp}$	$g_{average}$	Magnetic orbital
1	2.25	2.08	2.13	$d_{x^2-y^2}$
2	2.10*	2.26*	2.20	$d_{x^2-y^2}$ and d_{z^2}
3	2.28	2.08	2.14	$d_{x^2-y^2}$

* Values for spectra recorded at T <100 K.

Table 2.3 Values of EPR signals for **2** and **3** at 3079 G and 3209 G.

	Value at 3079 G	Value at 3208.5 G	% **2**	% **3**
Compound **2**	0	–2030	0	100
Compound **3**	8150	0	100	0
EPR_0	8146	–	100	0
EPR_1	–	–1768	12.9	87.1
EPR_2	8158	–	100	0
EPR_3	–	–2016	0.7	99.3
EPR_4	8149	–	100	0
EPR_5	–	–2006	1.2	98.8
EPR_6	8108	–	99.5	0.5
EPR_7	–	–2031	0	100
EPR_8	8132	–	99.8	0.2
EPR_9	–	–1840	9.4	90.6
EPR_10	8190	–	100	0
EPR_11	–	–2017	0.6	99.4
EPR_12	8134	–	99.8	0.2
EPR_13	–	–1862	8.3	91.7
EPR_14	8155	–	100	0

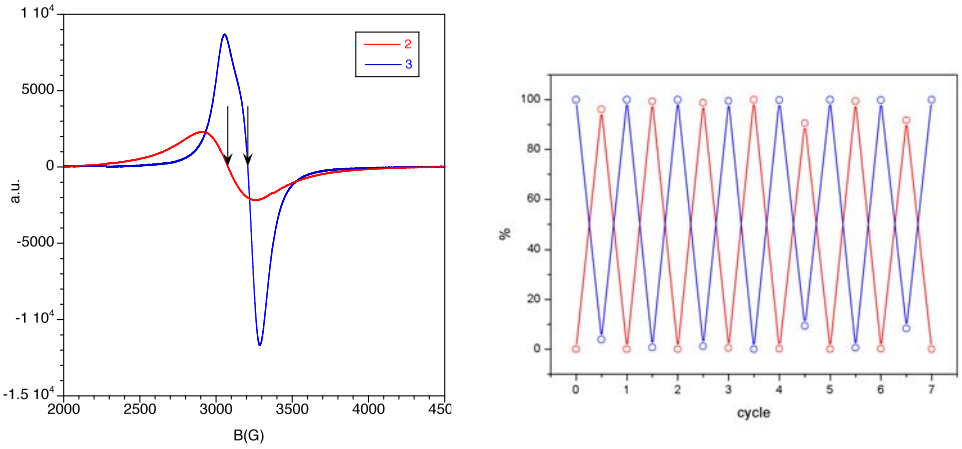

(a) (b)

Figure 2.17 Monitored EPR signals at room temperature. (a) X-band EPR spectra of compounds **2** (red) and **3** (blue) showing broad signals at 300 K for both compounds. Arrows indicate the resonance fields at which their EPR signals are zero, centred at different values (3079 G for **2** and 3209 G for **3**). (b) "On/off" switching between crystalline **2** and **3** monitored at room temperature.

The changes from the distorted tetrahedral geometry in **2** to a square-planar copper centre in **3** lead to clear differences in the room-temperature EPR spectra of these two compounds, as shown in figure 2.19a. Although both compounds present broad signals at room temperature, they are clearly distinct. More important than their difference in shape is that their resonance fields, at which their EPR signals are zero, are centred at different values (3079 G for **2** and 3209 G for **3**, see arrows in figure 2.19a). This provides with the opportunity to monitor the position of the switch and the ratio of **2** and **3** at a given point by measuring the EPR signals at these two fields. The resonance fields of compounds **2** and **3** are centred at different values, at which their EPR signals are zero (3079 G for **2** and at 3209 G for **3**). Thus, the signals measured at these two fields can be used to monitor the position of the switch and the ratio of **2** and **3** at a given point. Hence, by fixing the field at 3079 G we can quantify the amount of **3**, whereas by fixing the field at 3209 G we quantify the amount of **2**. Note that the signal at 3079 G cannot be used to quantify **3** since this region corresponds to the maximum slope of the spectra of **3**, and a small variation of the

field corresponds to a large variation of the signal. Similarly, the signal at 3209 G cannot be used to quantify **2** (Table 2.3). Therefore, these two signals afford a good estimation of the composition of a mixture of **2** and **3** at room temperature. Interestingly, we show that the uptake-release of HCl is totally reversible and can be repetitively switched "on" and "off" (Figure 2.19b), demonstrating the responsive behaviour of this magnetic molecular material.

2.3 CONCLUSIONS

In this *Chapter* the possibility of modulating the magnetic properties through chemisorption of a gas in the absence of pores has been presented.

The preparation of a non-porous coordination polymer [Cu(pyim)(Cl)(MeOH)] (**1**) capable of modifying the magnetic properties upon sorption of HCl gas despite the lack of porosity is described. The process can be illustrated as a two-step irreversible-reversible chemisorption (**1→3 ⇄ 2)**: **1** forms *antiferromagnetic* chains of square pyramidal Cu centres and is able to incorporate 3 equivalents of HCl molecules resulting in the ionic solid **2** $(H_2pyimH)[CuCl_4]$; **2** presents *ferromagnetic* interactions between the distorted tetrahedral $[CuCl_4]^{2-}$ anions and is able to extrude 2 equivalents of HCl yielding the molecular compound **3** *cis*-$[CuCl_2(pyimH)]$ where the square planar Cu centres show *antiferromagnetic* interactions.

Importantly, these non-porous frameworks display a considerable flexibility with the guest uptake and release, which do not disrupt the crystallinity of the compounds. Thus, structural analysis from single crystal diffraction and *ab initio* structure determination from powder diffraction have been performed and resulted essential to rationalize the changes in the physical properties of these compounds.

The magnetic changes caused by the structural transformations in these compounds are only observable in the low temperature region (below 10 K) except for compound **1**, since the magnetic susceptibility is primarily sensitive to the magnetic interactions,

which are quite weak in both **2** and **3**. In spite of this, the substantial changes in coordination environments due to the sorption/desorption processes have permitted the use of electron paramagnetic resonance (EPR) spectroscopy to monitor the reaction at room temperature due to its high sensitivity to the coordination environment of the metal centres. Monitoring of the switch observed in the magnetic properties upon HCl chemisorption has been explored, in particular, the reversible inter-conversion **2** ⇄ **3**.

To conclude, in this *Chapter* is shown that chemisorption of HCl by a non-porous coordination polymer can be used as a novel approach to design responsive molecular materials with tunable magnetic properties.

2.4 METHODS

2.4.1 Synthesis

All reagents were purchased from Aldrich and used as received.

Synthesis of 2-(1H-Imidazol-2-yl)pyridine L1. The ligand 2-(1H-Imidazol-2-yl)pyridine (L1) was synthesized by the general method of Radziszewskias described by Chiswell, Lions and Morris.[45] Ice-cold solutions of pyridine-2-aldehyde (22.65 g, 0.21 mol) in ethanol (20 mL) and glyoxal (29 mL of 40% aqueous solution) in ethanol (20 mL) were mixed and then, ice-cold concentrated aqueous ammonia solution (85 mL of 20 N) was rapidly added. The yellow-brown solution was stirred at 0ºC for 1 h, then allowed to stand overnight at room temperature. Most of the ethanol was distilled off and the cold residue extracted with ether (10 x 100 mL). The solvent was removed from the combined, dried (Na_2SO_4) ether extracts and the residual oil distilled *in vacuo*. A pale yellow oil was collected and recrystallization from ethyl acetate and methanol afforded the desired compound as yellow prisms. ^{1}H-NMR (300 MHz, D6-CD_3CN): 8.54 (*d*, ^3J = 5, 1H); 8.07 (*d*, ^3J = 8, 1H); 7.81 (*td*, *J* = 7.8, 1.5, 1H); 7.30 (*ddd*, ^3J = 7.5, 4.8, 1.5, 1H); 7.13 (*s*, 1H); Analysis (calcd., found for $C_8H_7N_3$): C

(66.19, 66.32), H (4.86, 4.92), N (28.95, 28.81). ESI-MS: (146, $M–H^+$).

Synthesis of [Cu(pyim)Cl(MeOH)] (1). Single crystals of **1** were grown in a methanol solution by a slow diffusion method using an H-shaped tube at room temperature. A solution of $CuCl_2·2H_2O$ (34 mg, 0.2 mmol) in MeOH (2 mL) was placed in one arm, and a solution of 2-(1H-Imidazol-2-yl)pyridine (29 mg, 0.2 mmol) in MeOH (2 mL) and NEt_3 (28 µL, 0.2 mmol) were added to the other arm. Methanol was added to connect the two arms. Needle-shaped dark green single crystals of both chiralities (noted as **1+** and **1-**) were obtained after several weeks in quantitative yield in the product, which is a racemic mixture with no dichroic signal in the solid state (figure 2.20, *vide infra*). Phase purity was established by X-ray powder diffraction and EPR spectroscopy. Analysis (calcd., found for $C_9H_{10}N_3Cl_1O_1Cu_1$): C (39.28, 39.59), H (3.66, 3.58), N (15.27, 15.01).

Synthesis of $(H_2pyimH)[CuCl_4]$ (2): uptake of HCl from aqueous HCl vapour by 1. 30 mg (0.1 mmol) of crystalline powder **1** was placed in a vial in the presence of vapours of concentrated aqueous HCl (37%). A change of colour of the powder from dark green to yellow occurred within minutes, but the sample was allowed to react for 1 day to ensure completion of the reaction. A small single crystal suitable for X-ray single crystal diffraction was found among the crystalline powder. Phase purity was established by X-ray powder diffraction and EPR spectroscopy.

Synthesis of *cis*-$[CuCl_2(pyimH)]$ (3): release of HCl by 2. Crystalline powder **2** was left uncovered and a change in colour was observed after 2 hours (from yellow to bright green). Completion of the reaction was obtained within 1 day. No single crystals suitable for X-ray diffraction were found, and the structure was established by X-ray powder diffraction. Phase purity was confirmed by EPR spectroscopy. Analysis (calcd., found for $C_8H_7N_3Cl_2Cu$): C (34.36, 33.79), H (2.52, 2.55), N (15.03, 15.01).

2.4.2 Structural characterization

2.4.2.I Single crystal diffraction for 1 and 2

Single crystals of compounds **1**+, **1**– and **2** were mounted on glass fibres using a viscous hydrocarbon oil to coat the crystal and then transferred directly to the cold nitrogen stream for data collection. X-ray data were collected at 120 K on a Supernova diffractometer equipped with a graphite-monochromated Enhance (Mo) X-ray Source (λ = 0.71073 Å) at ICMol (University of Valencia). The program CrysAlisPro, Oxford Diffraction Ltd., was used for unit cell determinations and data reduction. Empirical absorption correction was performed using spherical harmonics, implemented in the SCALE3 ABSPACK scaling algorithm. Crystal structures were solved and refined against all F^2 values using the SHELXTL suite of programs.[46] Non-hydrogen atoms were refined anisotropically and hydrogen atoms were placed in calculated positions that were refined using idealized geometries (riding model) and assigned fixed isotropic displacement parameters. In **1**+ and **1**–, the coordinated methanol molecules have the CH_3 group disordered over two sites and have been modeled with 51(2):49(2) and 66.6:33.3 ratios respectively. The single crystal of compound **2** was found to be twinned as two domains related by a rotation of 180º about the *a* axis [0.709(2):0.291(2)]. Crystal structure solution and refinement of the model was performed using the major component with corrected intensities for the contribution of the minor component to the overlapped reflexions. A summary of the data collection and structure refinements is provided in table 2.4.

2.4.2.II X-ray powder diffraction. Phase purity

Polycrystalline samples of **1** and **3** were lightly ground in an agate mortar and pestle and filled into 0.5 mm borosilicate capillaries. Data were collected at room temperature in the 2θ range 2–30 º on an Supernova diffractometer at ICMol (University of Valencia), using Mo K_α radiation.

Table 2.4 Crystallographic data for compounds **1+**, **1-** and **2**.

Compound	**1+**	**1-**	**2**
Empirical formula	$C_9H_{10}N_3OClCu$	$C_9H_{10}N_3OClCu$	$C_8H_9N_3Cl_4Cu$
Formula weight	275.19	275.19	352.52
Crystal colour	Dark green	Dark green	Yellow
Crystal size	0.21×0.06×0.04	0.08×0.07×0.03	0.06×0.03×0.03
Temperature (K)	120(2)	120(2)	120(2)
Wavelength (Å)	0.71073	0.71073	0.71073
Crystal system, *Z*	Trigonal, 3	Trigonal, 3	Monoclinic, 2
Space group	$P3_2$	$P3_1$	*Pc*
a (Å)	9.6491(3)	9.6388(5)	6.9831(10)
b (Å)	9.6491(3)	9.6388(5)	7.2397(9)
c (Å)	10.7075(6)	10.6890(8)	12.931(2)
α (°)	90	90	90
b (°)	90	90	105.067(15)
γ (°)	120	120	90
V (Å^3)	863.36(6)	860.03(9)	631.28(15)
ρ_{calc} (Mg/m^3)	1.588	1.594	1.855
$\mu(Mo_{K\alpha})$ (mm^{-1})	2.105	2.114	2.550
θ range (°)	3.09 – 27.48	3.10 – 27.48	2.81 – 27.54
Reflns collected	4663	4303	9442
Independent reflns (R_{int})	2640 (0.0458)	2611(0.0631)	1558 (0.090)
Reflns used in refinement, *n*	2640	2611	9442
L. S. parameters, *p*/ restraints, *r*	137 / 2	140 / 2	146 / 2
Absolute structure parameter	0.06(4)	0.03(3)	0.001(19)
$R1(F)$,[a] $I>2\sigma(I)$]	0.0699	0.0651	0.0546
$wR2(F^2)$,[b] all data	0.1647	0.1166	0.1506
$S(F^2)$,[c] all data	1.098	1.037	0.966

[a] $R1(F) = \Sigma(||F_o| - |F_c||)/\Sigma|F_o|$; [b] $wR2(F^2) = [\Sigma w(F_o^2 - F_c^2)^2/\Sigma wF_o^4]^{1/2}$; [c] $S(F^2) = [\Sigma w(F_o^2 - F_c^2)^2/((n + r - p)]^{1/2}$

2.4.2.III X-ray powder diffraction and Rietveld refinement for 3

A polycrystalline sample of **3** was lightly ground in an agate mortar and pestle and filled into a 0.7 mm borosilicate capillary. Data were collected at room temperature in

the 2θ range 0 – 40 º on beam line I11 at Diamond Light Source, UK, using λ = 0.826134 Å and a wide angle (90º) PSD detector comprising multiple Mythen-2 modules.[49,50] A series of 6 pairs of scans were conducted at room temperature, each pair related by a 0.25º detector offset to account for gaps between detector modules. The resulting 12 patterns were summed to give the final pattern for structural analysis. The diffraction pattern was indexed using DICVOL91[51] to a monoclinic cell [F(18) = 71.0, M(18) = 19.8] and space group $P2_1/n$ was assigned from volume considerations and a statistical consideration of the systematic absences. The dataset was background-subtracted and truncated to d = 2.795 Å (2θ = 17.00º), for Pawley refinement[47] and the structure was solved *ab initio* using the simulated annealing (SA) global optimization procedure implemented in the DASH computer program.[52,53] The SA structure solution involved the optimization of four independent fragments in the asymmetric unit (one Cu atom, two Cl atom and one pyimH ligand), totalling 16 degrees of freedom. Z matrices describing the molecular topology of the fragments in each compound were generated automatically for all fragments using DASH. Global optimization of all external (rotational and translational) degrees of freedom against the extracted intensities was carried out with all DASH SA control parameters set to default values. 10 runs with 5×10^7 SA moves per run were implemented for each structure determination. The best SA solutions had a chemically reasonable packing arrangement, and exhibited no significant misfit to the data. The solved structure was used as starting model for Rietveld refinement, conducted using TOPAS.[48] All atomic positions and displacement parameters, U_{iso}, of non-hydrogen atoms were refined (one for Cu atom, one for all Cl atoms and one for all C and N atoms; H atoms were fixed at idealised positions and the atomic displacement parameters were set as 1.2 times those of non-hydrogen atoms), subject to a series of restraints on bond lengths, bond angles and planarity of the aromatic rings. A March-Dollase correction of the intensities for preferred orientation was applied in the final stage of refinement. Rietveld refinement[54] converged to R_{wp} = 0.02267, R_{wp}' = 0.07678 (R_{wp}' is the background subtracted R_{wp}). The observed and calculated diffraction patterns for the

refined crystal structures are shown in Figure 2.6. A summary of the data collection and structure refinements is provided in Table 2.5.

Table 2.5 Data collection, structure solution and refinement parameters of **3**.

Compound	**3**
Empirical formula	$C_8H_7N_3Cl_2Cu$
Formula weight	279.62
Specimen colour	Bright green
Specimen shape (mm)	Cylinder 12 × 0.7 × 0.7
Wavelength, λ (Å)	0.826134
Crystal system	Monoclinic
Space group, *Z*	$P2_1/n$, 4
a (Å)	15.6450(2)
b (Å)	15.5700(3)
c (Å)	3.91545(8)
a (°)	90
b (°)	94.722(2)
γ (°)	90
V (Å^3)	950.54(3)
Density (Mg/m^3)	1.954
Temperature (K)	298
μ (mm^{-1})	4.248
2θ range ((°)	2.0 to 40.0
Increment in 2θ (°)	0.004
Reflns measured, n	565
Specimen mounting	0.7 mm borosilicate capillary
Mode	transmission
Detector	90 ° PSD
Parameters refined, p	116
Restraints, r	25
R_p [a]	0.01697
R_{wp} [b]	0.02267
R_{exp} [c]	0.188
GoF [d], all data	12.086

[a] $R_p = \Sigma|y_o - y_c|/\Sigma y_o$; [b] $R_{wp} = [\Sigma w(y_o - y_c)^2/\Sigma w(y_o)^2]^{1/2}$; [c] $R_{exp} = R_{wp}/GoF$; [d] $GoF = [\Sigma w(y_o - y_c)^2/(n - p + r)]^{1/2}$

2.4.3 Physical measurements

^{1}H NMR spectra was recorded on a Bruker DPX300 (300 MHz) spectrometer. Proton (^{1}H) chemical shifts are reported in parts per million (δ) and referenced internally with respect to the protic solvent impurity. Elemental analysis was carried out at the Centro de Microanálisis Elemental, Universidad Complutense de Madrid. Circular dichroism of compound **1** was measured with a JASCO J-810 circular dichroism spectrometer (with a 150 W Xe lamp) at the Central Services of the University of Alicante.

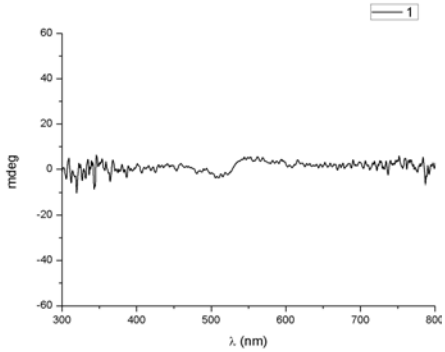

Figure 2.18 Dichroic spectra of compound **1** (racemic mixture of **1+** and **1-**) in KBr.

Magnetic measurements. Magnetic susceptibility measurements were performed on single-phased polycrystalline samples with a Quantum Design SQUID magnetometer at ICMol (University of Valencia). The susceptibility data were corrected from the diamagnetic contributions as deduced by using Pascal's constant tables. The d.c. data were collected in the range 2–300 K for decreasing temperatures with an applied field of 0.1 T and field dependent magnetization were collected at 2 K with an applied magnetic field increased from 0 to 5 T. Electron paramagnetic resonance spectroscopy was recorded with a Bruker ELEXYS E580 spectrometer operating in the X-band (9.47 GHz).

2.5 REFERENCES

1. Gütlich, P., Hauser, A. and Spiering, H. *Angew. Chem. Int. Ed*. **1994**, *33*, 2024.
2. Sato, O., Iyoda, T., Fujishima, A. and Hashimoto, K. *Science* **1996**, *272*, 704.
3. Coronado, E., Giménez-López, M.C., Levchenko, G., Romero, F. M., García-Baonza, V., Milner, A. and Paz-Pasternak, M. *J. Am. Chem. Soc.* **2005**, *127*, 4580.
4. Egan, L., Kamenev, K., Papanikolaou, D., Takabayashi, Y. and Margadonna, S. *J. Am. Chem. Soc.* **2006,** *128*, 6034.
5. Hoskins, B. F. and Robson, R. *J. Am. Chem. Soc.* **1989**, *111*, 5962.
6. Kitagawa, S., Kitaura, R. and Noro, S.-i. *Angew. Chem. Int. Ed.* **2004**, *43*, 2334.
7. Férey, G. *Chem. Soc. Rev*. **2008**, *37*, 191.
8. Furukawa, H., Cordova, K. E., O'Keeffe, M. and Yaghi. O. M. *Science* **2013**, 341, 974.
9. Horike, S., Shimomura, S. and Kitagawa, S. *Nature Chem*. **2009**, *1*, 695.
10. Czaja, A. U., Trukhan, N. and Müller, U. *Chem. Soc. Rev*. **2009**, *38*, 1284.
11. Cohen, S. M. *Chem. Sci*. **2010**, *1*, 32.
12. Dechambenoit, P. and Long, J. R. *Chem. Soc. Rev.* **2011**, *40*, 3249.
13. Coronado, E. and Mínguez Espallargas, G. *Chem. Soc. Rev.* **2013**, *42*, 1525.
14. Halcrow, M. A. *Chem. Soc. Rev.* **2011**, *40*, 4119.
15. Real, J. A., Gaspar, A. B. and Muñoz, M. C. *Dalton Trans.* **2005**, 2062.
16. Bousseksou, A., Molnár, G., Salmon, L. and Nicolazzi, W. *Chem. Soc. Rev.* **2011,** *40*, 3313.
17. Halder, G. J., Kepert, C. J., Moubaraki, B., Murray, K. S. and Cashion, J. D. *Science* **2002**, *298*, 1762.
18. Ohba, M., Yoneda, K., Agustí, G., Muñoz, M. C., Gaspar, A. B., Real, J. A., Yamasaki, M., Ando, H., Nakao, Y., Sakaki, S. and Kitagawa, S. *Angew. Chem. Int. Ed.* **2009**, *48*, 4767.
19. Agustí, G., Ohtani, R., Yoneda, K., Gaspar, A. B., Ohba, M., Sánchez-Royo, J. F., Muñoz, M. C., Kitagawa, S. and Real, J. A. *Angew. Chem. Int. Ed*. **2009**, *48*, 8944.
20. Ohtani, R., Yoneda, K., Furukawa, S., Horike, N., Kitagawa, S., Gaspar, A. B., Muñoz, M. C., Real, J. A. and Ohba, M. *J. Am. Chem. Soc*. **2011**, *133*, 8600.
21. Kurmoo, M., Kumagai, H., Chapman, K. W. and Kepert, C. J. *Chem. Commun.* **2005**, 3012.
22. Motokawa, N., Matsunaga, S., Takaishi, S., Miyasaka, H., Yamashita, M. and Dunbar, K. R. *J. Am. Chem. Soc*. **2010**, *132*, 11943.
23. Bao, S.-S., Liao, Y., Su, Y.-H., Liang, X., Hu, F.-C., Sun, Z., Zheng, L.-M., Wei, S., Alberto, R., Li, Y.-Z. and Ma, J. *Angew. Chem. Int. Ed*. **2011,** *50*, 5504.
24. Ohkoshi, S., Arai, K., Sato, Y. and Hashimoto, K. *Nat. Mater.* **2004**, *3*, 857.
25. Albrecht, M., Lutz, M., Spek, A. L. and van Koten, G. *Nature* **2000**, *406*, 970.
26. Mínguez Espallargas, G., Brammer, L. van de Streek, J., Shankland, K., Florence, A. J. and Adams,

H. *J. Am. Chem. Soc.* **2006**, *128*, 9584.

27. Adams, C. J., Colquhoun, H. M., Crawford, P. C., Lusi, M. and Orpen, A. G. *Angew. Chem. Int. Ed.* **2007**, *46*, 1124.
28. Park, K. S., Ni, Z., Côté, A. P., Choi, J. Y., Huang, R., Uribe-Romo, F. J., Chae, H. K., O'Keeffe, M. and Yaghi, O. M. *Proc. Nat. Acad. Sci*. **2006**, *103*, 10186.
29. Wang, B., Côté, A. P., Furukawa, H., O'Keeffe, M. and Yaghi, O. M. *Nature* **2008**, *453*, 207.
30. Bechlars, B., D'Alessandro, D. M., Jenkins, D. M., Iavarone, A. T., Glover, S. D., Kubiak, C. P. and Long, J. R. *Nature Chem*. **2010**, *2*, 362.
31. Sasaki, Y. and Shigematsu, T. *Bull. Chem. Soc. Jap.* **1973**, *46*, 3438.
32. Brammer, L., Bruton, E. A. and Sherwood, P. *Cryst. Growth Des*. **2001**, *1*, 277.
33. Boggess, R. K. and Martin, R. B. *Inorg. Chem*. **1974**, *13*, 1525.
34. Mínguez Espallargas, G., van de Streek, J., Fernandes, P., Florence, A. J., Brunelli, M., Shankland, K., Brammer, L. *Angew. Chem. Int. Ed.* **2010**, *49*, 8892.
35. Leita, B. A., Moubaraki, B., Murray, K. S. and Smith, J. P. *Polyhedron* **2005**, *24*, 2165.
36. Mínguez Espallargas, G., Hippler, M., Florence, A. J., Fernandes, P., van de Streek, J., Brunelli, M., David, W. I. F., Shankland, K., Brammer, L. *J. Am. Chem. Soc.* **2007**, *129*, 15606.
37. (a) Bonner, J. C. and Fisher, M. E. *Phys. Rev.* **1964**, *135*, 640. (b) Brown, D. B., Donner, J. A., Hall, J. W., Wilson, S. R., Wilson, R. B., Hodgson, D. J. and Hatfield, W. E. *Inorg. Chem.* **1979**, *18*, 2635. (c) Swank, D. D., Landee, C. P. and Willet, R. D. *Phys. Rev. B* **1979**, *20*, 2154.
38. Baker, G. A. Jr, Rushbrooke, G. S. and Gilbert, H. E. *Phys. Rev.* **1964**, *135*, AI272.
39. Snively, L. O., Tuthill, G. F. and Drumheller, J. E. *Phys. Rev. B* **1981**, *24*, 5349.
40. Woodward, F. M., Albrecht, A. S., Wynn, C. M., Landee, C. P. and Turnbull, M. M. *Phys. Rev. B* **2002**, *65*, 144412.
41. O'Connor, C. J. *Prog. Inorg. Chem*. **1982**, *29*, 203.
42. (a) Estes, W. E., Wasson, J. W., Hall, W. E. and Hatfield, W. E. *Inorg. Chem*. **1978**, *17*, 3657. (b) Aggarwal, R. C., Singh, N. K. and Singh, R. P. *Inorg. Chem*. **1981**, *20*, 2794. (c) Alves, W. A., Almeida-Folho, S. A., Santos, R. H. A. and Ferreira, A. M. D. C. *Inorg. Chem. Commun*. **2003**, *6*, 294.
43. Slade, R. C., Tomlinson, A. A. G., Hathaway, B. J. and Billing D. E. *J. Chem. Soc. A* **1968**, 61.
44. Reinen, D. and Friebel, C. *Inorg. Chem*. **1984**, *23*, 791.
45. Chiswell, B., Lions, F. and Morris, B. S. *Inorg. Chem.* **1964**, *3*, 110.
46. Sheldrick, G. M. *Acta Crystallogr., Sect. A: Found. Crystallogr*. **2008**, *64*, 112.
47. Pawley, G. S. *J. Appl. Cryst*. **1981**, *14*, 357.
48. Coelho, A. A. TOPAS-Academic, Version 4.1, **2007**, see: http:// www.topas-academic.net.
49. Thompson, S. P., Parker, J. E., Potter, J., Hill, T. P., Birt, A., Cobb, T. M., Yuan, F. and Tang, C. C. *Rev. Sci. Instrum.* **2009**, *80*, 075107.

50. Thompson, S. P., Parker, J. E., Marchal, J., Potter, J., Birt, A., Yuan, F., Fearn, R. D., Lennie, A. R., Street, S. R. and Tang, C. C. *J. Synchrotron Rad.* **2011**, *18*, 637.
51. Boultif, A. and Louër, D. *J. Appl. Cryst*. **1991**, *24*, 987.
52. David, W. I. F., Shankland, K. and Shankland, N. *Chem. Commun*. **1998**, 931.
53. David, W. I. F., Shankland, K., van de Streek, J., Pidcock, E., Motherwell, S., Cole, J. C. *J. Appl. Crystallogr*. **2006**, *39*, 910.
54. Rietveld, H. M. *J. Appl. Crystallogr*. **1969**, *2*, 65.

3

PHYSISORPTION IN NON-POROUS Fe^{II} SPIN CROSSOVER COORDINATION POLYMERS

3.1 INTRODUCTION

The use of an external stimulus to affect the magnetic properties of a magnetic MOF has been recently explored,[1-4] specially the effects of chemical stimuli. Most commonly this involves the use of solvent molecules (H_2O, MeOH, aromatic molecules…) that can penetrate the pores producing changes in the crystal structures.[5-9] However, adsorbed gas molecules (H_2, N_2, CO_2…) do not appreciably interact with the magnetic host network, thus provoking no effects on the magnetic ordering or the spin transition temperature. In fact, modification of the magnetic ordering of a porous magnet through gas sorption has only been achieved in a Cu MOF in which the presence of CO_2 molecules in the pores provokes an increase in T_N from 22 K to 29 K,[10] whereas no effects have been reported in spin-crossover MOFs. The latter materials are more interesting from an application point of view, since the spin-crossover phenomenon can occur at temperatures of gas sorption, and even at room temperature, which can cause a synergy in the properties.[11,12]

This *Chapter* presents a new strategy to obtain a SCO coordination polymer whose properties can be affected by gas sorption by using flexible organic ligands which can respond to an external stimulus (figure 3.1). This contrasts to the most common strategy that involves the use of rigid ligands to bridge between the metal nodes, which leads to robust and rigid frameworks with the formation of pores.[13-15] The main disadvantage of the use of flexible linkers arises from the difficulty in the formation of porous materials. However, as presented in *Chapter 2*, the presence of pores is not a requirement to tune magnetic properties through gas sorption.[16]

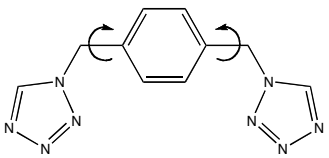

Figure 3.1 1,4-bis(tetrazol-1-ylmethyl)benzene (btzx) ligand. Arrows indicate the possible rotational motion of the phenyl ring.

In this *Chapter* a family of SCO coordination polymers whose spin transition has shown to be sensitive to gas sorption (CO_2) despite the lack of permanent channels is presented. In particular, two non-porous coordination polymers are shown to selectively trap CO_2 over N_2 gas molecules, which cause a modification in the transition temperatures. To fully characterize this selectivity, gravimetric adsorption measurements of single-component and binary mixtures of gases have been addressed to one of the systems. The gas molecules are incorporated into the internal cavities in the absence of permanent pores given the existence of a dynamic framework, which is mainly provided by the flexibility of the ligand. Magnetic measurements prior and after gas loading have been performed to characterize the spin transition phenomena and the perturbation exerted by the gas molecules. Finally, *in situ* powder X-ray diffraction has been used to locate the binding sites of the CO_2 molecules and permits the examination of the nature of the interaction with the framework.

3.2 RESULTS AND DISCUSSION

3.2.1 Description of the structures

$[Fe(btzx)_3](ClO_4)_2$ (4). The controlled reaction of $Fe(ClO_4)_2 \cdot xH_2O$ with 1,4-bis(tetrazol-1-ylmethyl)benzene (btzx, figure 3.1) affords blocked-shaped crystals of $[Fe(btzx)_3](ClO_4)_2$ (**4**) after several hours. The crystal structure of **4** was determined in the low-spin (LS) and the high-spin (HS) states using the same single crystal at 120 K and 240 K, respectively (see section 3.4.2.I). In both states, **4** crystallizes in the $P6_3/m$ space group and is composed of $[Fe(btzx)_3]^{2+}$ units that form linear chains that run parallel to the crystallographic *c*-axis (figure 3.2). Each Fe^{II} ion lies on the 3–fold axis and is surrounded by six crystallographically related tetrazole rings coordinated through nitrogen atoms from six btzx ligands in an almost perfect octahedral environment. The N-Fe-N angles are of 90.2(2) and 89.8(2) º at 120 K and 90.4(2) and 89.6(2) º at 240 K (see table 3.1) affording an octahedral distortion parameter (Σ) of 2.4 and 4.8 º for LS and HS respectively (Σ = 0 ° for an ideal octahedron). Structural parameters for **4** at 120 K and 240 K are shown in table 3.2. At 120 K, all Fe–N

distances are 1.996(4) Å, while these are 2.160(6) Å at 240 K, which are in the expected range for Fe–N distances at LS and HS, respectively, in Fe–tetrazolate systems.[17] This change in distance corresponds to a 8 % decrease of the bond length upon the transition. In addition, the change in bond distances is accompanied by a colour change of the crystal from pink (120 K) to colourless (240 K), further confirming the different spin states of the Fe^{II} centres. The most severe structural change caused by the spin transition occurs along the *c*-axis, although the overall structure remains practically identical (see section 3.2.2.II).

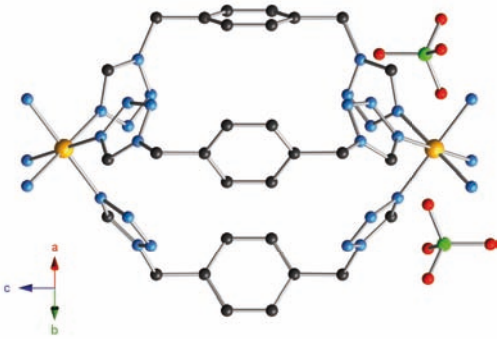

(a)

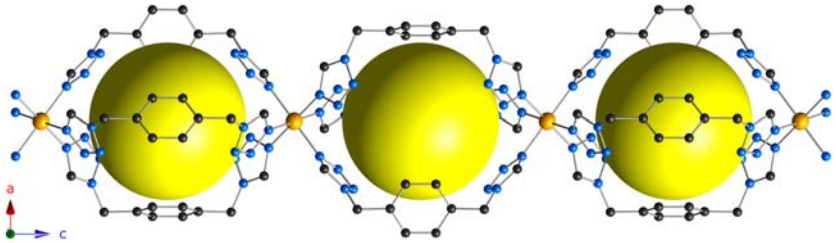

(b)

Figure 3.2 (a) Coordination environment of the Fe^{II} centres in **4**, showing the connection to three *anti*-btix ligands and the two ClO_4^- anions. (b) Crystal structure of compound **4** viewed along the *b*-axis. The ClO_4^- anions and hydrogen atoms have been removed for clarity. Key: Fe, orange; C, gray; N, blue, Cl, green and O, red. The yellow spheres (diameter of 9 Å) are placed in the structure as a visual indication of the empty space of the internal voids.

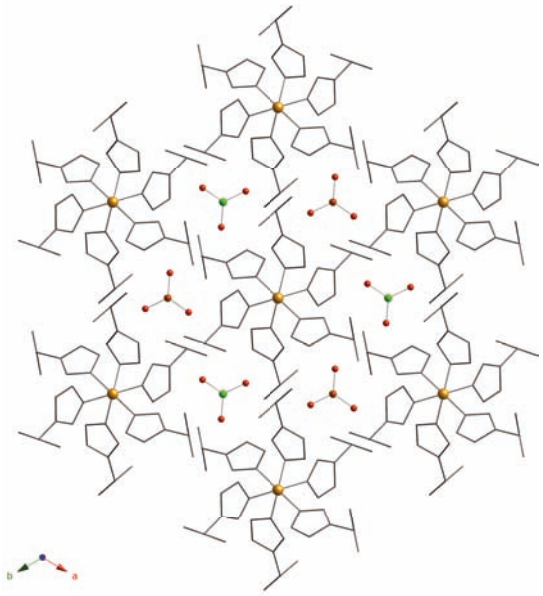

(a)

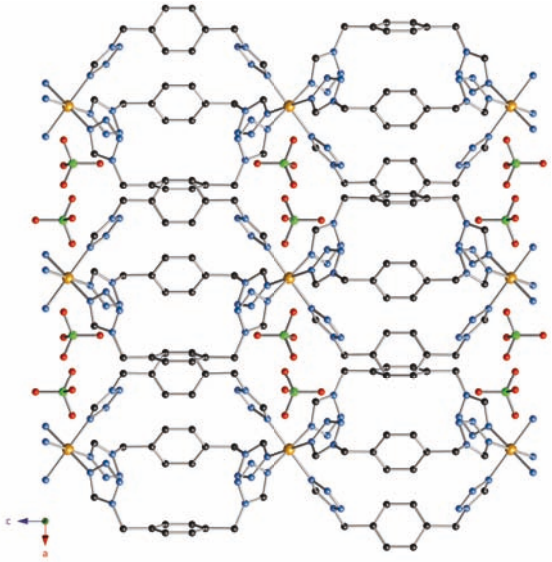

(b)

Figure 3.3 Crystal structure of **4.** (a) View along the chain direction (*c*-axis) showing that the chains are packed as would be expected for close packing of cylinders. Key: Fe, orange; C, gray; N, blue, Cl, green and O, red. (b) View along the *b*-axis showing the position of the ClO_4^- anions, which are coplanar to the Fe centers. Key: Fe, orange; Cl, green; O, red; C and N, gray; H, omitted for clarity. Analogous structures are found for **5**.

The ligands arrange in a *syn* conformation acting as bridges between neighbouring Fe^{II} ions lying in a common plane, with Fe···Fe distances of 11.5752(9) Å at 120 K and 11.7881(12) Å at 240 K. Interestingly, propagation of this bridging mode leads to cationic chains which display internal cavities with no permanent channels. The void volumes were estimated using PLATON to be 10.8 % (at 120 K) and 11.7 % (at 240 K) of the unit cell (discrete voids of 117 $Å^3$ and 132 $Å^3$, respectively). Remarkably, no solvent molecules are present in these cavities, as demonstrated by SQUEEZE[18] and thermogravimetric analysis (TGA) (figure 3.24). This contrasts with analogous systems where solvent molecules are found in the voids of the as-synthetized materials.[19] The chains are packed in a hexagonal arrangement separated by ClO_4^- counterions which are coplanar to the Fe centers (figure 3.3). The Fe···Fe distance between chains is of 10.3668(4) Å at 120K and 10.5117(7) Å at 240 K. Each ClO_4^- anion interacts with three different chains through weak C–H···O hydrogen bonds.

$[Fe(btzx)_3](BF_4)_2$ (5). 5 is obtained in a procedure analogous to that of **4** except that $Fe(BF_4)_2 \cdot 6H_2O$ was used. Crystal structure of **5** was determined in the low-spin (LS) and the high-spin (HS) states at 120 K and 240 K, respectively (see section 3.4.2.I). Compound **5** is isostructural to **4**, thus, it also crystallizes in the $P6_3/m$ space group for the two spin states and is composed of $[Fe(btzx)_3]^{2+}$ units. The N-Fe-N angles are of 90.4(6) and 89.6(5) º at 120 K and 91.2(5) and 88.8(5) º at 240 K, affording an octahedral distortion parameter (Σ) of 4.8 and 9.6 º for LS and HS respectively (structural parameters for **5** at 120 K and 240 K are shown in table 3.2). Fe–N distances are 1.985(13) Å at 120 K and 2.1156(15) Å at 240 K (table 3.1), which are also in the expected range for in Fe–tetrazolate systems.[17] This change in distance corresponds to a 7.4 % decrease of the bond length upon the transition. A colour change of the crystal from pink (120 K) to colourless (240 K) is observed. Structural changes caused by the spin transition are summarized in section 3.2.2.II. The intrachain Fe···Fe distances are 11.4814(7) Å at 120 K and 11.6924(16) Å at 240 K and the Fe···Fe distance between chains is of 10.3690(5) Å at 120K and 10.5265(12) Å at 240 K. No solvent molecules are present in the internal cavities along the chains

and the void volumes were estimated using PLATON to be 11.3 % (at 120 K) and 12.4 % (at 240 K) of the unit cell (discrete voids of 121 $Å^3$ and 140 $Å^3$, respectively. See table 3.2). The BF_4^- counterions separate the chains, which are packed in a hexagonal arrangement (figure 3.4). Each BF_4^- anion interacts with three different chains through weak C–H···O hydrogen bonds.

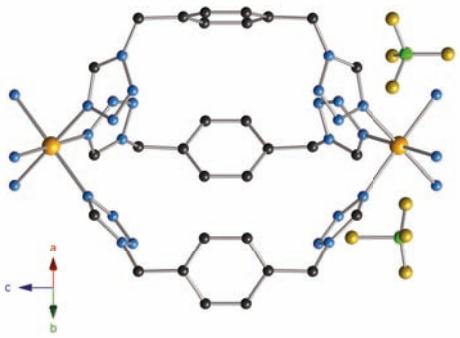

(a)

Figure 3.4 (a) Coordination environment of the Fe^{II} centres in **5**, showing the connection to three *anti*-btix ligands and the two BF_4^- anions. Key: Fe, orange; B, green; F, yellow; C and N, gray; H, omitted for clarity.

Table 3.1 Selected bond lengths (Å), angles (º) and metal-metal distances for **4** and **5** in the HS (240 K) and LS (120 K) states.

	4–LS	**4–HS**	**5–LS**	**5–HS**
Fe–N	1.996(4)	2.160(6)	1.985(13)	2.156(15)
N–Fe–N	90.18(16)	90.4(2)	90.4(6)	91.2(5)
	89.82(16)	89.6(2)	89.6(5)	88.8(5)
	180.00	180.0	180.00(3)	180.0(8)
Fe···Fe $_{intra}$	11.5752(9)	11.7881(12)	11.4814(7)	11.6924(16)
Fe···Fe $_{inter}$	10.3668(4)	10.5117(7)	10.3690(5)	10.5265(12)

Table 3.2 Octahedral distortion parameters and voids for **4** and **5** in the HS (240 K) and LS (120 K) states.

	4–LS	**4–HS**	**5–LS**	**5–HS**
Σ [a]	2.4	4.8	4.8	9.6
Discrete void ($Å^3$) [b]	117	132	121	140
Voids % [c]	10.8	11.7	11.3	12.4

[a] Octahedral distortion parameter $\Sigma = \Sigma_1^{12}(|90–\varphi i|)$ [$\Sigma = 0°$ for an ideal octahedron; φi represents the twelve smallest L–M–L angles]

[b] Solvent accessible area ($Å^3$)

[c] Total potential solvent area volume per unit cell volume

3.2.2 X-ray powder diffraction studies

3.2.2.I Phase purity. XRPD studies have served to establish the phase purity of polycrystalline samples **4** and **5**.

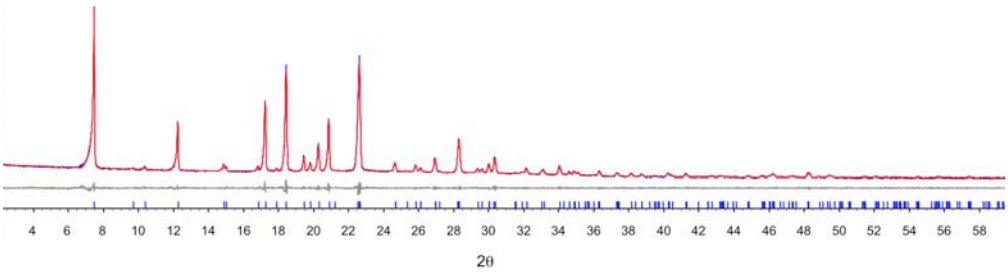

(a)

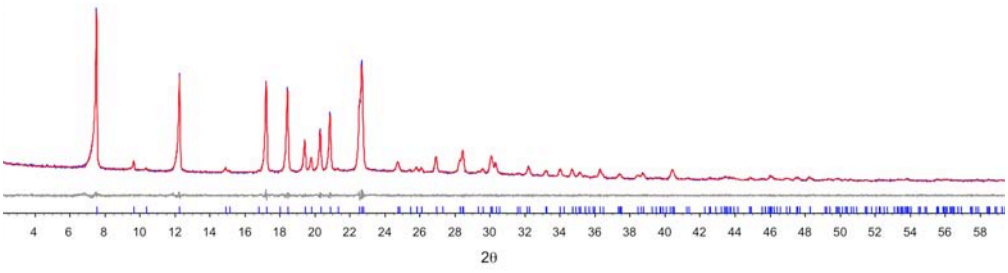

(b)

Figure 3.5 Observed (blue) and calculated (red) profiles and difference plot [($I_{obs} – I_{calcd}$)] (grey) of the Pawley refinements for compounds **4** (a) and **5** (b) (2θ range 2.0–60.0 °; maximum resolution 1.54 Å).

Pawley refinements have been applied to the experimental powder patterns of polycrystalline samples **4** and **5**. The observed and calculated diffraction patterns for the refined crystal structures are shown in figure 3.5. Pawley refinement converged to R_{wp} = 0.0270, R_{wp}' = 0.0933 with a gof = 1.206 for **4** and R_{wp} = 0.0264, R_{wp}' = 0.0961 and gof = 1.461 for **5** (R_{wp}' is the background subtracted R_{wp}).

3.2.2.II Variation of the lattice parameters along the hysteresis loop. Temperature-dependent XRPD data from temperature-dependent studies can be extremely useful in the characterization of the spin transition and for determining changes of the lattice parameters. In order to examine these parameters, X-ray variable temperature experiments have been performed on crystalline powdered samples of **4** and **5**. Powder patterns were collected at 300, 210, 205, 200, 195, 190 and 150 K both in the cooling and the heating mode. A detailed view of the most intense diffraction peak (7.2–8.0 º in 2θ range) is presented in figure 3.6 for **4** and **5**. Upon cooling (diffractograms 1–7), the maximum of the peak successively appears at higher values of 2θ as a consequence of the thermal contraction but mainly due to the spin transition from the high spin to the low spin. The subsequent warming mode (diffractograms 7–13) results in a reversible decrease of the maximum to lower 2θ values indicating a spin transition from the low spin to the high spin. In figure 3.7 the variation of the 2θ position of the intense peak as a function of the temperature is presented. For both systems, a reversible variation of *ca.* 0.16 º is observed. No hysteresis is found in this experiment.

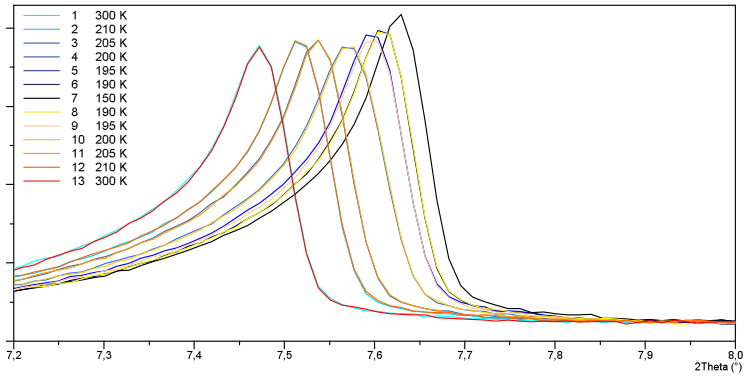

(a)

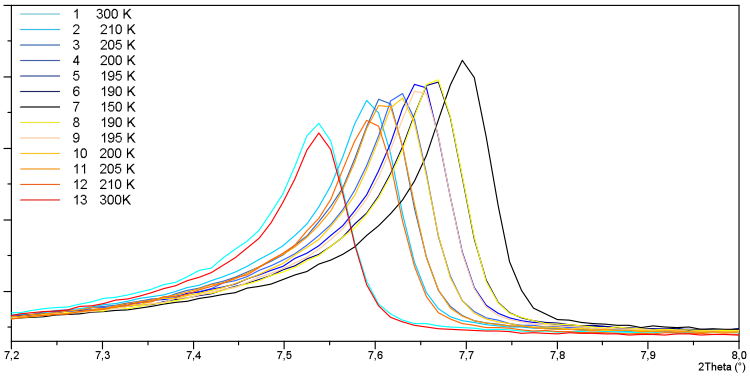

(b)

Figure 3.6 View of the most intense diffracted peak at different temperatures for **4** (a) and **5** (b) (2θ range 7.2–8.0 º).

A Pawley refinement was carried out on each individual scan, in which profile parameters, background and unit-cell parameters were refined. Consequently, refined unit cell parameters were extracted for each temperature scan. The unit-cell temperature dependence shows that the spin transition corresponds to a reversible modification of the unit cell volume of 5.1 and 4.6 % for **4** and **5** respectively. This difference in volume variation can be discussed in terms of anisotropy of the unit cell modification at the spin transition (figure 3.8). Several considerations can be highlighted: i) for each compound the *c* parameter presents a larger variation (−2.0 and −2.1 % for **4** and **5** respectively) than the *a* and *b* parameters (−1.6 % and −1.3 % for **4** and **5** respectively); ii) the *c* parameter decreases similarly in both systems from

HS to LS; iii) *a* and *b* parameters in each system are affected slightly different by the transition. These facts can be explained by careful analysis of the crystal structures. For **4** and **5** the higher variation along the *c* parameter compared with the *a* and *b* parameters is essentially a consequence of the linear arrangement of the chains, which run parallel to the crystallographic *c*-axis. As expected, the major change of the unit cell upon spin transition occurs along the chains where all the Fe–N bonds are propagated. For Fe^{II} complexes the t_{2g} orbitals are of non-bonding character, whereas the e_g orbitals are anti-bonding. Therefore, the metal-ligand bond length is significantly higher in the HS state than in the LS state, because in the former the anti-bonding orbitals are populated. In addition, the variation of the *c* parameter is equivalent in the two compounds, which is unsurprising given the similarity of the chains. However, both *a* and *b* parameters vary in a different manner for each system. This can be explained since the *a* and *b* parameters form the plane in which the anions are located and each anion interacts differently with the framework.

X-ray variable temperature experiments support the absence of a structural phase transition accompanying the spin crossover phenomenon as previously determined by single crystal X-ray diffraction studies. Additionally, these experiments further confirm the different spin states of the Fe^{II} centres by means of unit cell variation.

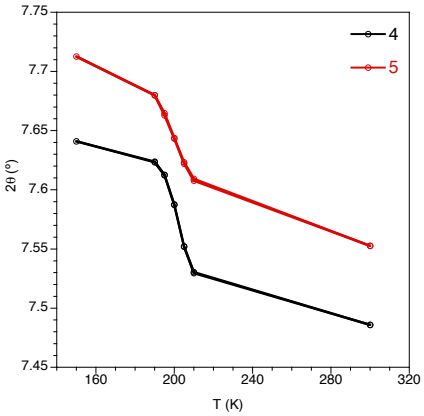

Figure 3.7 2θ position displacement of the most intense diffracted peak at different temperatures for **4** (black) and **5** (red).

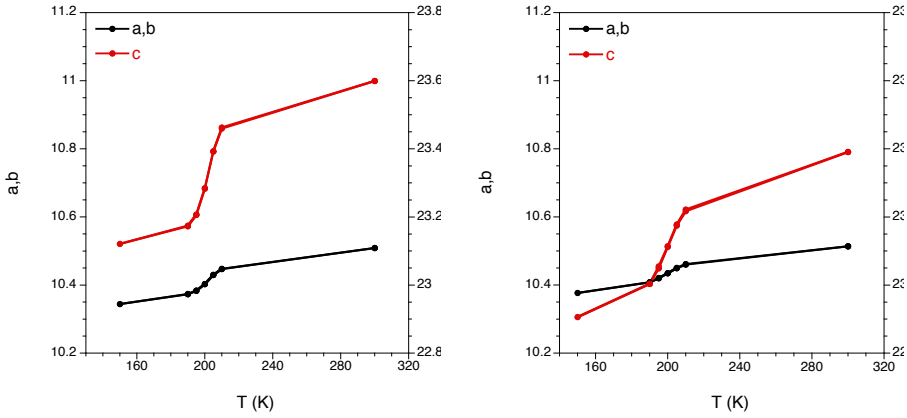

Figure 3.8 Variation of unit cell parameters for **4** (a) and **5** (b).

3.2.3 Gas adsorption properties

Since the frameworks of **4** and **5** possess flexibility in rotation through the $C_{aromatic}$–$C_{methylene}$ bonds of the btzx ligand, their solid-gas adsorption properties toward N_2 (77 K) and CO_2 (273 K) have been evaluated despite the lack of gas-accessible channels. This has been performed in collaboration with Prof. F. Rey from the Instituto de Tecnología Química of Valencia. As shown in figure 3.9, significant differences can be observed between these two single component isotherms. Importantly, **4** and **5** exhibit a preferential adsorption of CO_2 over N_2. In fact, N_2 molecules remain practically unadsorbed in **4** at 100 kPa, whereas almost one CO_2 molecule is adsorbed per void. In **5**, less than 0.2 molecules of N_2 are adsorbed while one CO_2 molecule is adsorbed per void. This is likely due to the larger kinetic diameter of N_2 compared to CO_2 (3.64 vs. 3.30 Å), and the large polarizability and quadrupolar moment of the CO_2 molecules, which results in a stronger interaction with the cationic framework (see table 3.3).[20] In addition, the facilitated diffusion of CO_2 at 273 K versus N_2 at 77 K must be also a factor in this phenomenon. An additional factor to take into account, although unlikely to have an important role in this case, is the different spin states of the frameworks at the sorption temperatures, which modifies the volume voids (from

132 to 117 $Å^3$ in **4** and from 121 to 140 $Å^3$ in **5**). However, this should not have an important effect in the gas sorption, as the smaller void is still large enough to accommodate gas molecules. This sorption behaviour is of remarkable relevance due to the lack of permanent channels connecting the internal voids. However, gas adsorption studies on organic molecular solids[21] and metallocycles[22] containing constrained internal voids have shown that gas molecules can enter the solids through molecular motion of the host,[23] which is likely to occur in this case.

Table 3.3 Physical properties of CO_2 and N_2 gases.

	CO_2	N_2
Kinetic diameter [Å]	3.30	3.64
Quadrupolar moment [$C \cdot m^2$]	$13.4 \cdot 10^{-40}$	$4.7 \cdot 10^{-40}$
Polarizability [cm^3]	$26.3 \cdot 10^{-25}$	$17.6 \cdot 10^{-25}$

Gases listed in the above table do not have a permanent dipole moment.

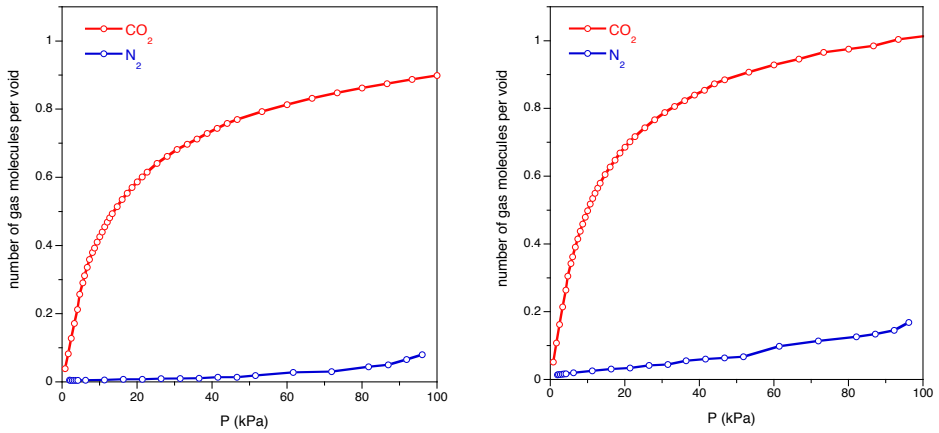

(a) (b)

Figure 3.9 CO_2 (red) and N_2 (blue) adsorption isotherm at 273 K and 77 K, respectively of **4** (a) and **5** (b).

To further demonstrate the preferential adsorption of CO_2 over N_2 and dismiss the possible facilitated diffusion effect due to the different temperatures, single-component adsorptions of CO_2 and N_2 for **4**, and CO_2 for **5**, have been measured at the same temperature (298 K, see figure 3.10) up to 10 bar. In these gravimetric adsorptions the previous preferentiality is also observed even at higher pressures. The unambiguously confirmation that **4** selectively sorbs CO_2 over N_2 has been performed by evaluating the actual sorption capacity in a mixture of gases, which can provide experimental evidence of the sorption preference.[24] Figure 3.11 shows the binary gas-adsorption isotherm for a 20/80 partial pressure mixture of CO_2/N_2 (black) compared to pure CO_2 isotherm (red) at 298 K up to 10 bar. The gas sorption in the mixture is in perfect agreement with CO_2 being the unique molecule sorbed, as the sorption isotherm in the mixture is equivalent to that of pure CO_2 when comparing the partial pressure of CO_2 (figure 3.11b), indicating that CO_2 uptake is a function of P_{CO_2} rather than the total pressure (P_{tot}) for these mixtures. Hence, we can unequivocally conclude that **4** preferentially absorbs CO_2 over N_2 with selectivity close to 100 %, and the presence of N_2 just acts as a diluting agent.

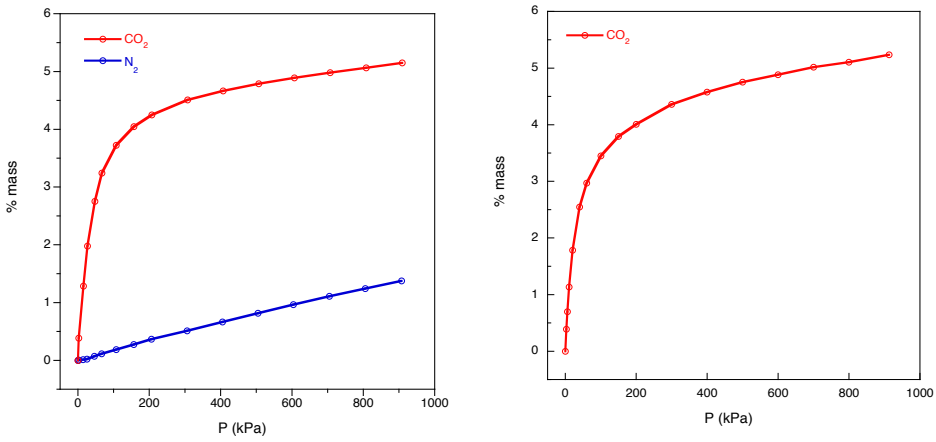

(a) (b)

Figure 3.10 (a) Single-component adsorptions isotherms at 298 K of CO_2 (red) and N_2 (blue) for **4** (a) and for CO_2 for **5**.

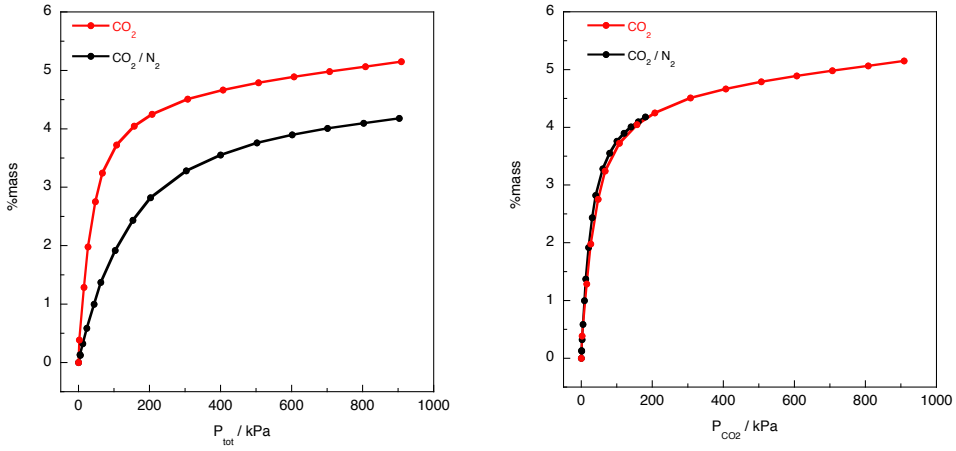

(a) (b)

Figure 3.11 (a). Adsorption isotherms at 298 K of a 20/80 binary mixture of CO_2/N_2 (black) and pure CO_2 (red) for **4**. Figure (b) is plotted versus total pressure (P_{tot}) while figure (c) is plotted versus CO_2 partial pressure (P_{CO_2}).

The Virial isotherm for fitting experimental data points has been applied. This approach is just a polynomial fitting without any starting assumption about the adsorption process, but which provides a precise extrapolation of the adsorption constant at zero coverage (see equation 1).

$$\ln\left(\frac{P}{Q}\right) = a_0 + \frac{a_1}{T} + \left(b_0 + \frac{b_1}{T}\right)\cdot Q + \left(c_0 + \frac{c_1}{T}\right)\cdot Q^2 + \left(d_0 + \frac{d_1}{T}\right)\cdot Q^3 + \cdots \qquad \text{Eq. 1}$$

$$q_{st} = R\cdot T^2 \cdot \left[\frac{\partial(\ln P)}{\partial T}\right]_{Q=cte} \equiv R\cdot \left[-\frac{\partial(\ln P)}{\partial\left(1/T\right)}\right]_{Q=cte} \qquad \text{Eq. 2}$$

It has been found that a fourth grade polynomial is able to properly describe the CO_2 isotherms studied in this work at the different temperatures (figure 3.13). Then, the isosteric heat of adsorption for CO_2 (figure 3.14) was calculated from the Clausius-Clapeyron equation (see equation 2) using adsorption data collected at 273, 283, 298, 313 and 333 K for **4** and **5**. The isosteric heat of adsorption at zero coverage was estimated to be 21.2 and 22.0 $kJ\cdot mol^{-1}$ for **4** and **5** respectively and remains nearly

constant upon increasing CO_2 uptake (20-25 kJ·mol^{-1} for **4** and 22-27 kJ·mol^{-1} for **5**). The calculated heat of adsorption in the two systems is within the typical range for physisorption of CO_2 on a MOF.[25,26] Thus, as expected, the **4**–CO_2 and **5**–CO_2 interaction is mainly physisorptive in nature, without significant chemical association. In addition, this low value might result from the compensation for the rearrangement of the framework for the CO_2 molecules to enter the crystal. Thus, although the energy of the system decreases when guest molecules are accommodated in the framework, the required deformation of the host implies an energetic penalty.

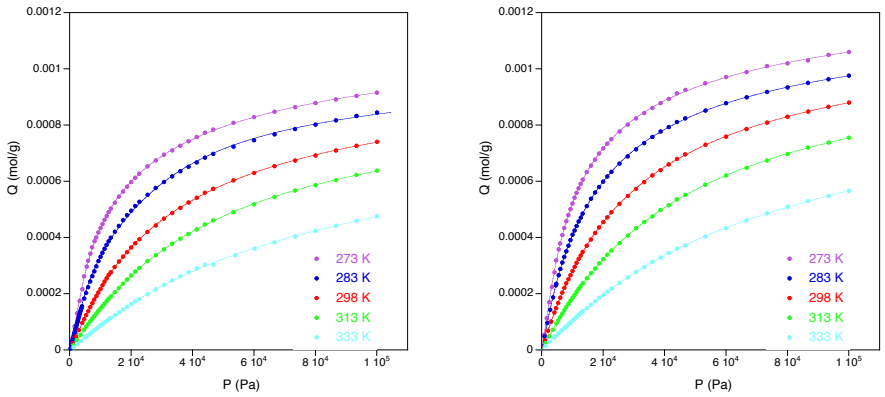

(a) (b)

Figure 3.12 CO_2 adsorption isotherms for **4** (a) and **5** (b) collected at 273, 283, 298, 313 and 333 K (lines correspond to the best fits).

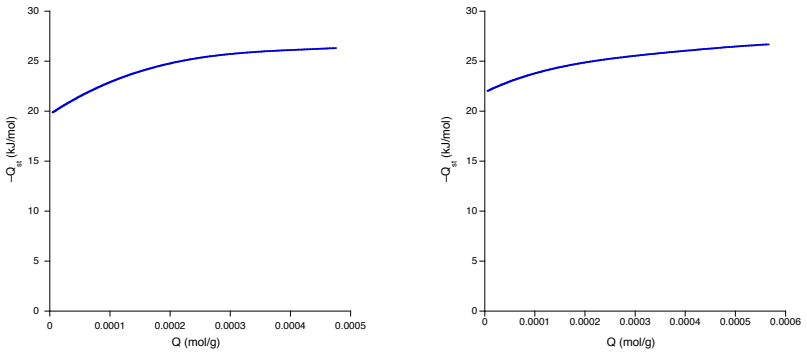

(a) (b)

Figure 3.13 Plot of the isosteric heat of adsorption of CO_2 in **4** (left) and **5** (right).

3.2.4 Magnetic properties

Magnetic susceptibility measurements were performed on polycrystalline powders of **4** and **5** in the temperature range 2–300 K at 1 $K \cdot min^{-1}$ under an applied magnetic field of 0.1 T. Compounds **4** and **5** exhibit analogous magnetic and chromatic thermal–induced spin transition centred both at 200 K (Figure 3.14) with the remarkable peculiarity that **4** displays in addition a hysteretic transition. At room temperature the $\chi_M T$ value for both **4** and **5** is typical of Fe^{II} compounds in the HS state (3.7 $emu \cdot mol^{-1} \cdot K$), whereas at low temperature a remanent $\chi_M T$ value of 0.3 $emu \cdot mol^{-1} \cdot K$ is observed in both, corresponding to a small fraction (*ca*. 8 %) of residual HS Fe^{II}. Thus, the two systems display a complete spin transition from the HS to the LS state. Significantly, the degree of completion and the transition temperature are not affected by the choice of the counterion. This contrasts with previous studies performed with analogous spin-crossover systems in which the counterion plays a crucial role in both the degree of completion and the transition temperature.[19] However, it must be stated that the two anions here studied are very similar in size and chemical behaviour. The synthesis of analogous systems with bulkier anions was tried, but unsuccessful results were obtained.

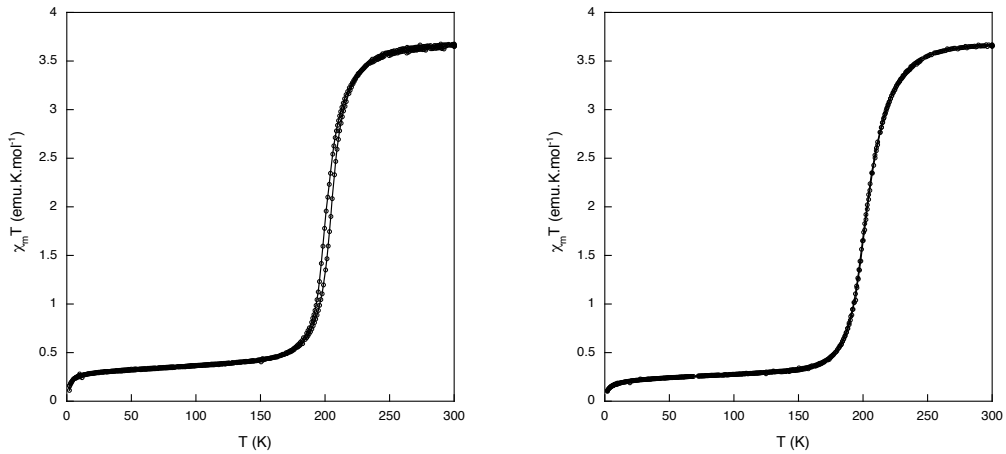

(a) (b)

Figure 3.14 Temperature dependence of $\chi_M T$ for **4** (a) and **5** (b) in the temperature range 2–300 K at 0.1 T.

The subsequent warming mode reveals the occurrence of a thermal hysteresis loop of 4 K wide in compound **4** (transition temperatures: $T_{1/2}\downarrow$ = 200 K and $T_{1/2}\uparrow$ = 204 K) whilst in compound **5** the $\chi_M T$ product overlays that of the cooling mode and consequently no hysteresis is observed. Hence, the hysteretic spin transition observed in **4** is of remarkable significance for several reasons: i) the relatively large distance between Fe centres (>10 Å) hinders feasible intra- or inter-chain interactions; ii) cooperativity mediated via counterion is reduced since permanent disorder of the anion leads to weak interactions among the transition temperature.

3.2.5 Magnetic response to CO_2 sorption

We have studied the effect of the perturbation exerted by the CO_2 molecules on the magnetic properties of **4** and **5**. The response to gas molecules of SCO materials has been previously studied in porous MOFs,[5-7] but they produced no influence on the magnetic properties. Since coordination polymers **4** and **5** posses more restricted accessible space than a typical porous material, we expect an interplay between the gas sorption and the spin-crossover behaviour. The magnetic response of compounds **4** and **5** upon CO_2 physisorption is presented in figure 3.15. These two analogous compounds display similar gas–responsive behaviour. Indeed, loading of CO_2 gas molecules onto **4** and **5** induces an increase of the $T_{1/2}$ in both systems. **CO_2@4** (which refers to compound **4** loaded with CO_2) experiences an increase in the $T_{1/2}$ from 200 K to 209 K, with retention of the hysteresis, whereas in **CO_2@5** the $T_{1/2}$ is modified from 200 K to 205 K. This difference may be related with minor dissimilarity presented in the interaction between the CO_2 gas in each framework, and will be discussed in section 3.2.6. Thus, physisorption of CO_2 gas molecules into the cavities of the two frameworks serve to stabilize the LS state. Interestingly, apart from the spin-crossover modulation in **CO_2@5** a hysteretic transition also appears as a consequence of the inserted gas molecules.

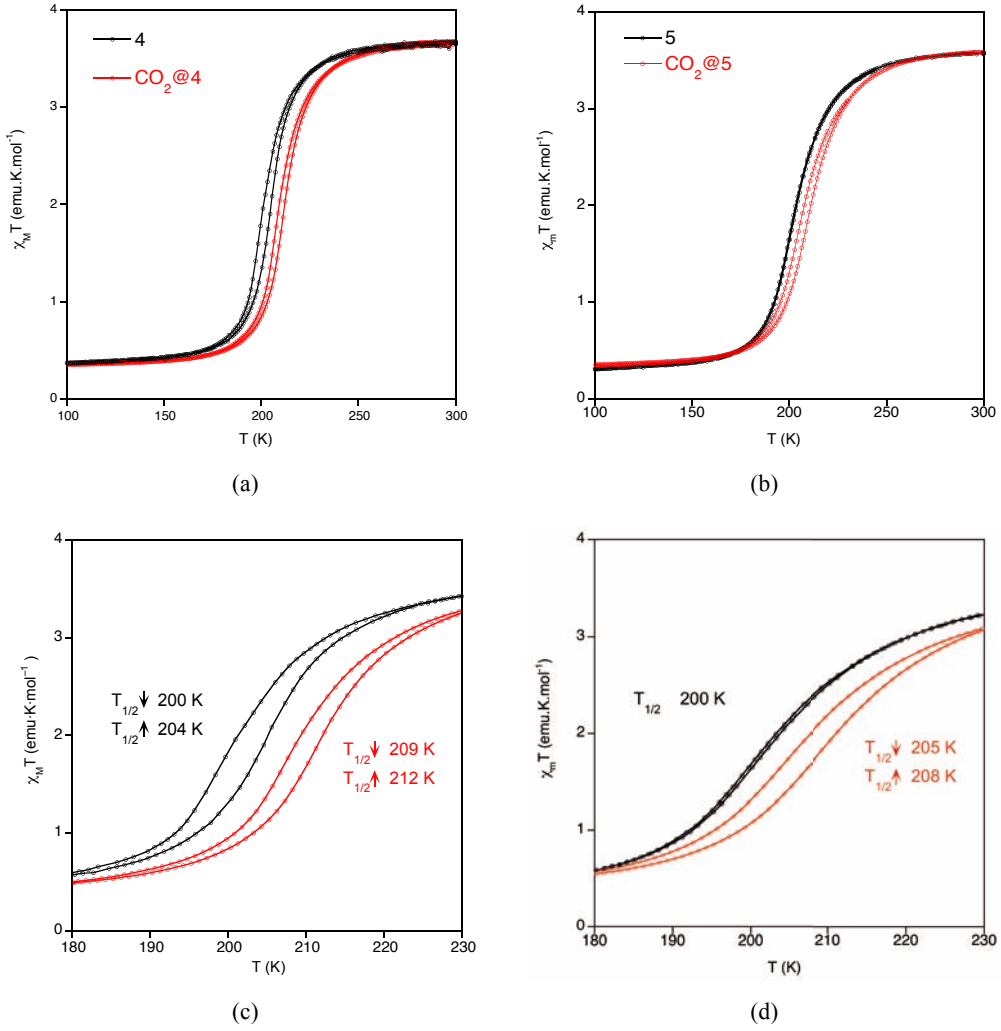

Figure 3.15 (a,b) Temperature dependence of $\chi_M T$ for **4** and **CO_2@4** and **5** and **CO_2@5**, respectively. (c,d) Detailed view of the spin transition region. As-synthesized **4** and **5** shown in black and loaded with CO_2 (**CO_2@4** and **CO_2@5**) shown in red. Measured at 1 K·min^{-1} with an applied field of 0.1 T.

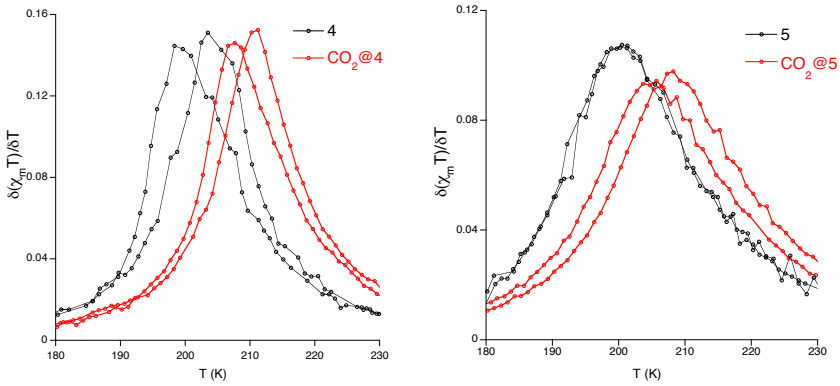

(a) (b)

Figure 3.16 Derivative of the product $\chi_M T$ for **4** (a), **5** (b) (black) and CO_2@**4**, CO_2@**5** (red), showing the increase in $T_{1/2}$ upon CO_2 sorption.

This gas–responsive behaviour can be modulated depending on the number of CO_2 gas molecules incorporated in the framework. Figure 3.17 shows the magnetic response of **4** and **5** with partial loading of CO_2 (*ca*. 0.3 per void). A shift of $T_{1/2}$ towards higher temperatures is also observed, although this increase is only partial when compared to the fully loaded sample. Furthermore, upon removal of the CO_2 molecules $T_{1/2}$ is shifted back to lower temperatures, which perfectly matches with the spin transition of the activated **4'** and **5'** (after heating at 150 ºC for 3h), thus showing the reversibility of this process.

In order to guarantee that modulation of the spin transition is due to the number of CO_2 gas molecules incorporated in the framework, additional experiments have been performed. Thus, the magnetic response of **4** under N_2 and under several CO_2/N_2 gas mixtures at 1 bar (figure 3.18) has been measured. As expected, the presence of N_2 does not influence the spin transition temperature, since N_2 is not adsorbed as demonstrated in the sorption experiments. Interestingly, in the gas mixtures the transition temperature increases as if only the same amount of CO_2 was present. This indicates the possibility of using spin-crossover for sensing CO_2 in the presence of N_2.

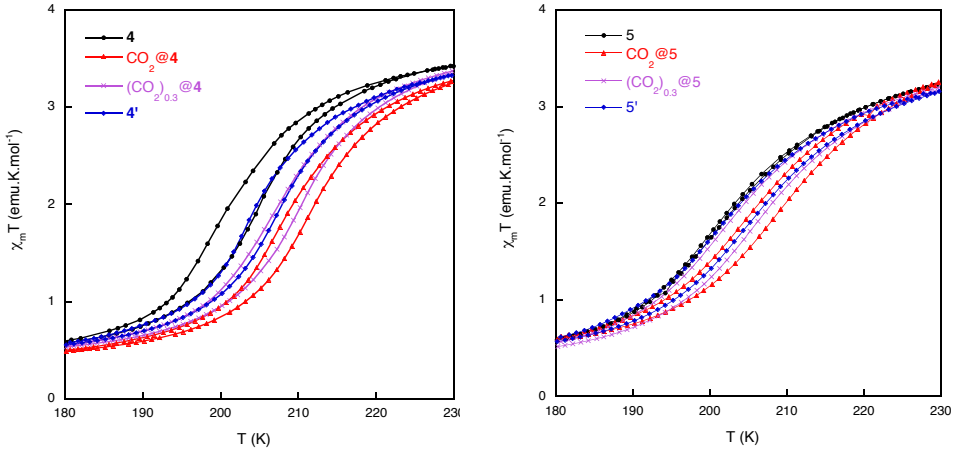

(a) (b)

Figure 3.17 Magnetic response to CO_2 sorption for **4** (a) and **5** (b). Thermal dependence of the $\chi_M T$ product in the temperature range 180–230 K of as-synthesised **4** and **5** (black); partially loaded $(CO_2)_{0.3}$@**4** and $(CO_2)_{0.3}$@**5** (violet); fully loaded CO_2@**4** and CO_2@**5** (red); and after CO_2 removal **4'** and **5**' (blue). Measured at 1 K·min^{-1} with an applied field of 0.1 T.

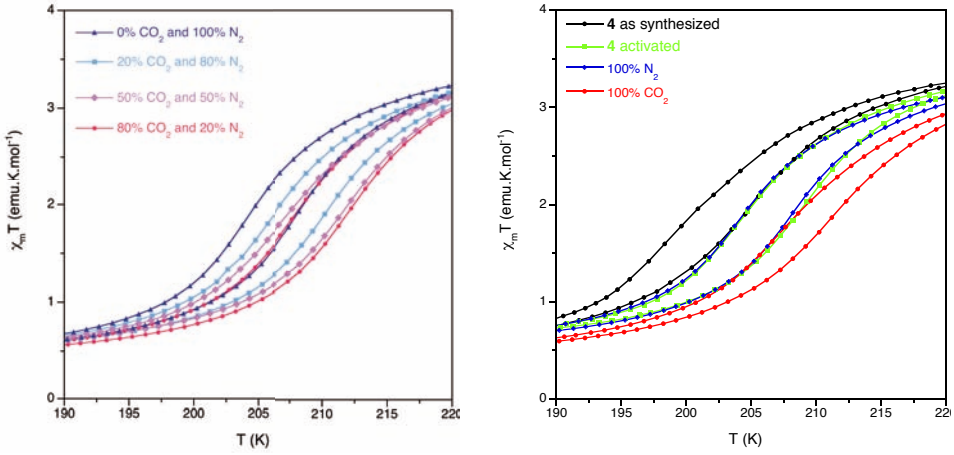

(a) (b)

Figure 3.18 (a) Magnetic response of **4** under N_2 (blue) and under 20/80 (light blue), 50/50 (purple) and 80/20 (pink) CO_2/N_2 gas mixtures at 1 bar. (b) Magnetic response of **4**–as synthesized (black), **4**–activated (green), **4**–under 1 bar of N_2 (blue) and **4**–under 1 bar of CO_2 (red). Measured at 1 K·min^{-1} with an applied field of 1 T.

3.2.6 *In situ* structural determination upon CO_2 loading

In order to investigate the CO_2 sorption sites in **4** and **5**, we have determined *in situ* both structures with adsorbed CO_2 molecules by Rietveld analysis[27] using synchrotron X-ray powder diffraction data (figure 3.19).[28] Data was collected by Dr. I. J. Vitórica-Yrezábal, from the University of Sheffield (UK), at Diamond SRS (Oxford, UK). The gas molecules were refined as a rigid body and their occupancies were freely refined with a constraint thermal parameter. The structures of **CO_2@4** (figures 3.20 and 3.21) reveals that the framework remains unchanged, with the CO_2 molecules located in the internal cavities. Analogous structure is obtained for **CO_2@5**. The gas molecules are disordered over six symmetry related positions, with a total refined occupancy of 0.93(1) CO_2 molecules per void in **CO_2@4**, which agrees well with the calculated loading of 0.90 CO_2 molecules per void from the adsorption isotherms at 100 kPa and 273 K (which are comparable conditions to those of the powder diffraction experiments, see section 3.4.2.III). The refined occupancy in **CO_2@5** results of 0.94(1) CO_2 molecules per void and also correspond with the adsorption isotherms at 100 kPa and 273 K. Interestingly, in the two structures the CO_2 molecules interact with the cationic framework in an end-on mode through the nucleophilic oxygen atom, as previously established in other porous solids,[29-33] with a $O{=}C{=}O(\delta^-)\cdots\pi_{N-N}$ distance of 2.591 and 2.608 Å for **CO_2@4** and 2.925 and 2.746 Å in **CO_2@5**, an interaction which is analogous in nature to the well established anion-π interactions.[34] No interaction between the framework and the electrophilic carbon atom is found.[29,35-37] The end-on binding of the CO_2 molecules is in agreement with the increase in $T_{1/2}$, as donation of electron density stabilizes the low-spin state.

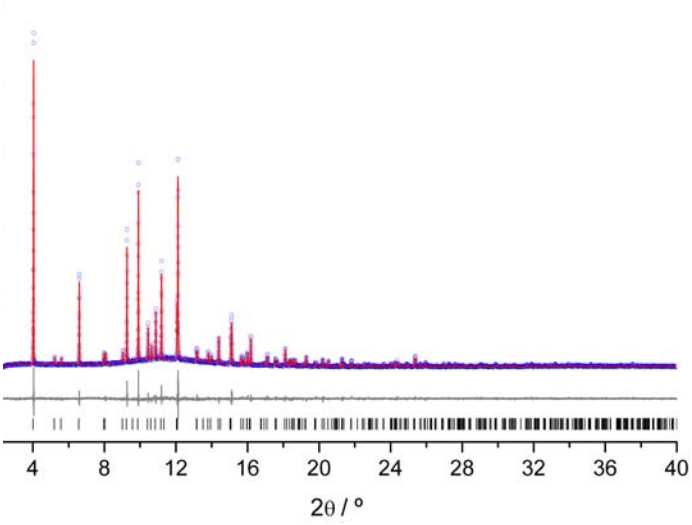

(a)

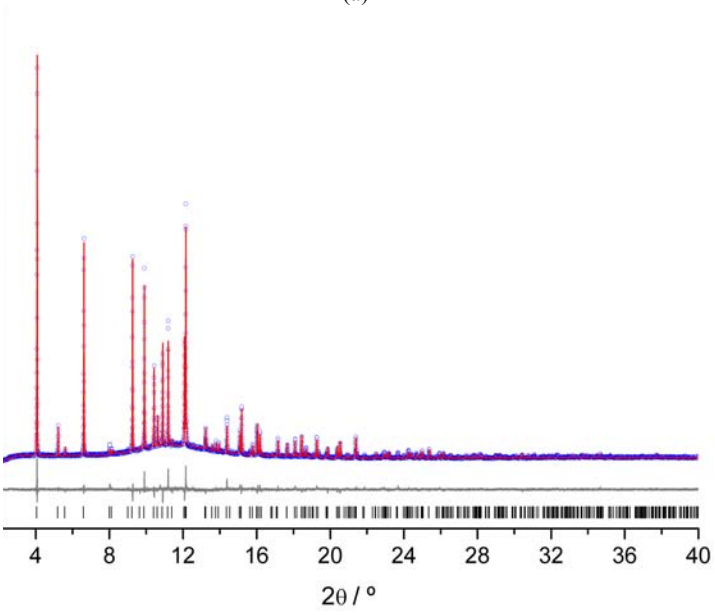

(b)

Figure 3.19 (a) Observed (blue) and calculated (red) profiles and difference plot [($I_{obs} - I_{calcd}$)] (grey) of the Rietveld refinement of compound **CO_2@4** (a) and **CO_2@5** (b) (2θ range 2.0–40.0 °, maximum resolution of 1.21 Å).

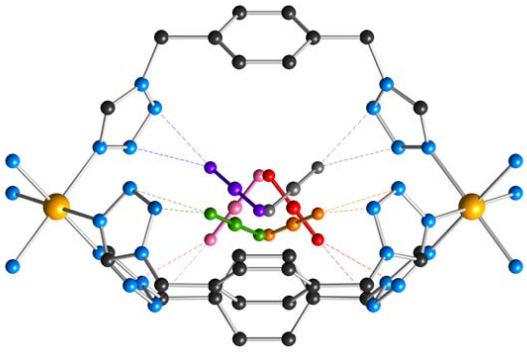

Figure 3.20 Crystal structure of **CO_2@4** showing the end-on interactions between the gas molecules and the framework (O···N distances of 2.591 and 2.608 Å). The symmetry related CO_2 molecules have been coloured differently for clarity. Hydrogen atoms and anions omitted for clarity. Key: Fe, orange; C, gray; N, blue. The same figure may be attributed to **CO_2@5**, where O···N distances are of 2.925 and 2.746 Å.

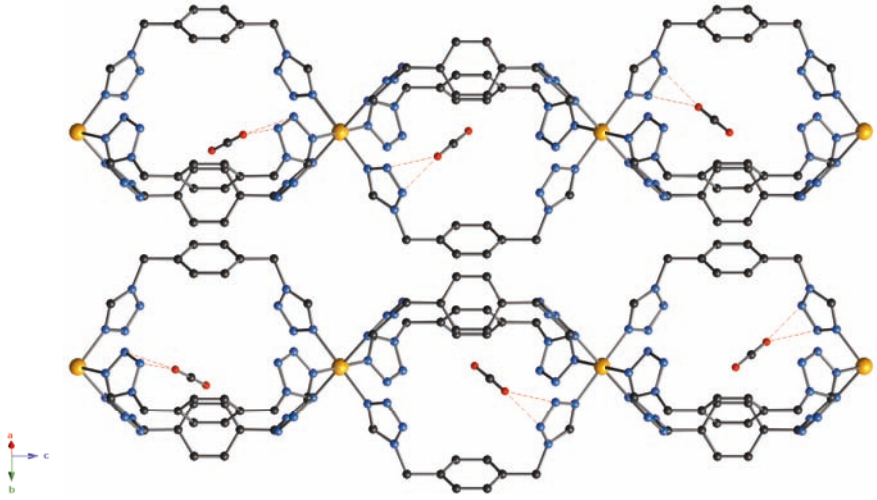

Figure 3.21 Crystal structure of **CO_2@4** showing six different cavities each with a different orientation of the disordered CO_2 molecules. Hydrogen atoms and anions omitted for clarity. Key: Fe, orange; C, gray; N, blue. The same figure may be attributed to **CO_2@5**.

The most plausible mechanism for CO_2 sorption consists on the rotation of the phenyl rings of the btzx through the $C_{aromatic}$–$C_{methylene}$ bonds, as this would permit the connection between voids of different chains along the (100) and (010) directions (figures 3.22 and 3.23). In addition, the extraframework ClO_4^- and BF_4^- anions required to balance the framework charge are located at the planes formed by the Fe^{II} centres (figure 3.3b), without interfering with the sorption process. Thus, the aromatic rings can be viewed as flexible barriers to CO_2 transport within the crystals acting in a similar way to a rotary door.

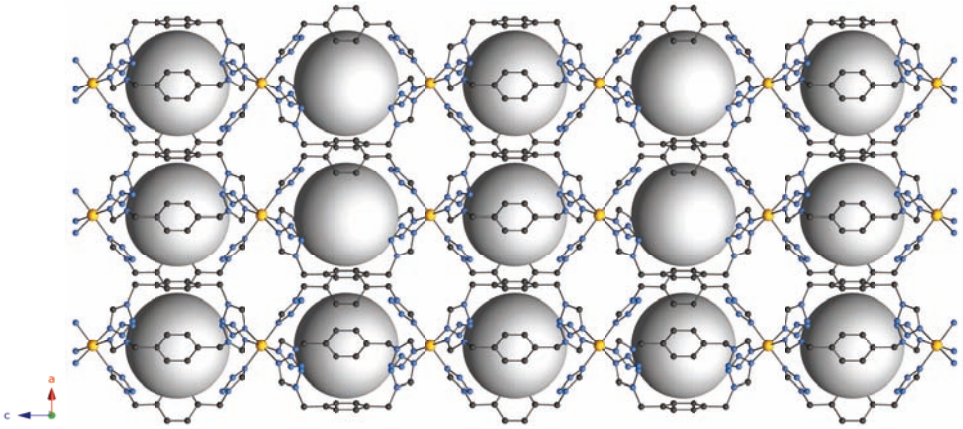

Figure 3.22 Crystal structure of **4** viewed along the *b*-axis showing three different chains. Rotation of the phenyl rings could permit the connection of discrete voids along the *a*-axis. The ClO_4^- anions and hydrogen atoms have been removed for clarity. Key: Fe, orange; C, gray; N, blue. The gray spheres (diameter of 9 Å) are placed in the structure as a visual indication of the empty space of the internal voids, which are blocked by the phenyl rings.

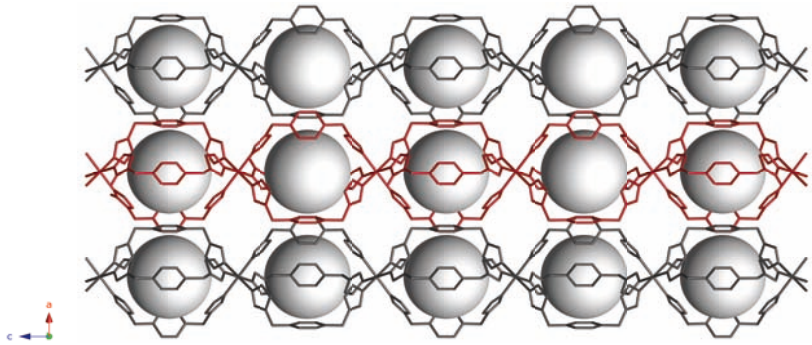

(a)

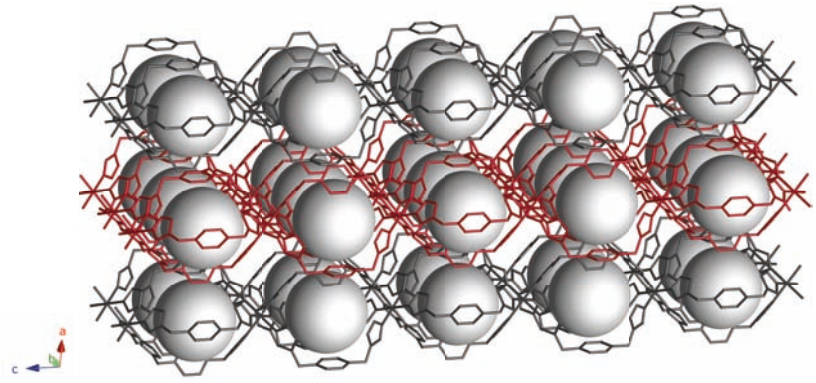

(b)

Figure 3.23 (a) Crystal structure of **4** viewed along the *b*-axis showing three different chains. (b) Rotated view along the *a*-axis to show that rotation of the phenyl rings could also permit the connection of discrete voids along the *b*-axis. The central chains have been coloured in red for clarity. The ClO_4^- anions (and hydrogen atoms) have been removed for clarity.

3.3 CONCLUSIONS

In this *Chapter*, the synthesis of two tetrazolate based Fe^{II} spin crossover coordination polymers is presented. These non-porous coordination polymers are able to incorporate gas molecules in their internal cavities albeit the absence of pores. This is possible given the existence of a dynamic framework that permits the connection between voids of different chains.

This chapter shows the first example in which a modification in the spin transition of SCO CP is achieved through gas sorption. The presented SCO CPs have been designed to present multifaceted properties: i) they posses a sharp SCO transition at 200 K; ii) gas molecules can enter the crystals despite the lack of permanent pores due to the presence of a flexible ligand; iii) a selective sorption of CO_2 over N_2 is observed, with the CO_2 molecules located in the discrete voids of the framework through O=C=O···π interactions; iv) the physisorption of CO_2 in the cavities produces an increase in the SCO temperature. The confined space of the voids seems to be essential for this unusual response to gas molecules.[38] In future work, the rotation of phenyl rings[39] and the insertion of other gas molecules in the voids will be studied for better understanding the response of this nonporous SCO coordination polymer toward gas sorption. This will permit the design of other multifunctional materials with larger response occurring near room temperature.

3.4 METHODS

3.4.1 Synthesis

All reagents and solvents were commercially available and used without further purification. **Caution!** Perchlorate salts are explosive (especially if they are dry) and should be handled with extreme caution.

Synthesis of 1,4-bis(tetrazol-1-ylmethyl)benzene (btzx). This ligand was prepared adapting a literature method,[19] which is based on Fujisawa's patent for the preparation of R-tetrazoles.[40] *p*-xylylenediamine (5 g, 0.037 mol), triethylortoformate (54 g, 0.363 mol) and sodium azide (4.79 g, 0.074 mol) were dissolved in acetic acid (90 mL) and heated at 90 ºC for 2 days. After cooling down to room temperature, the solvent was evaporated at reduced pressure. The remaining yellow solid was washed with methanol and water yielding the ligand as a white powder. Yield = 68 %; ^{1}H NMR (300 MHz, [D6]DMSO): d=5.7 (s, 4H; ttz-CH_2-ph), 7.4 (s, 4H; ph), 9.5 ppm (s, 2H; ttz); IR: = 3118 cm^{-1} (Cttz-H).

Synthesis of [Fe(btzx)$_3$](ClO$_4$)$_2$ (4). A solution of Fe(ClO$_4$)$_2$·xH$_2$O (112 mg) in 5 mL of MeCN was added into a suspension of btzx (152 mg, 0.8 mmol) in 40 mL of MeCN containing ascorbic acid (*ca*. 10 mg). The resulting milky suspension was refluxed and stirred for 4 h. A white crystalline precipitate appeared during the reaction. After cooling down to room temperature, the white powder was filtered and washed with MeCN. Phase purity was established by X-ray powder diffraction. Yield = 71 %. Anal. calc. $C_{30}H_{30}FeN_{24}Cl_2O_8$ (981.47): C, 36.71; H, 3.08; N, 34.25 %. Found: C, 36.98; H, 3.16; N, 34.03 %. IR: = 3147, 3118 (Cttz-H), 637 and 625 cm^{-1} (ClO_4^-).

Synthesis of [Fe(btzx)$_3$](BF$_4$)$_2$ (5). 5 was synthesized in a procedure analogous to that of **1** except that Fe(BF$_4$)$_2$·6H$_2$O (135 mg, 0.4 mmol) was used. A white crystalline precipitate was collected and washed with MeCN. Phase purity was established by X-ray powder diffraction. Yield = 52 %. Anal. calc. $C_{30}H_{30}FeN_{24}B_2F_8$ (956.18): C, 37.68; H, 3.16; N, 35.16 %. Found: C, 38.81; H, 3.37; N, 35.34 %. IR: = 3148, 3117 (Cttz-H), 1078 cm^{-1} (BF_4^-).

3.4.2 Structural characterization

3.4.2.I Single crystal X-ray diffraction for 4 and 5

Single crystals of compounds **4** and **5** were mounted on glass fibres using a viscous hydrocarbon oil to coat the crystals and then transferred directly to the cold nitrogen stream for data collection. X-ray data was collected at 240 K **(4–HS, 5–HS)** and then at 120 K (**4–LS, 5–LS**) on a Supernova diffractometer equipped with a graphite-monochromated Enhance (Mo) X-ray Source (λ = 0.71073 Å) at ICMol (University of Valencia). The program CrysAlisPro, Oxford Diffraction Ltd., was used for unit cell determinations and data reduction. Empirical absorption correction was performed using spherical harmonics, implemented in the SCALE3 ABSPACK scaling algorithm. Crystal structures were solved and refined against all F^2 values using the SHELXTL suite of programs.[41] Non-hydrogen atoms were refined anisotropically (except the disordered anions, which were modelled over two orientations) in **4–HS**, **4–LS** and **5–LS**. However, in **5–HS** only the Fe centre was refined anisotropically due to the bad quality of the data. Hydrogen atoms were placed in calculated positions that

were refined using idealized geometries (riding model) and assigned fixed isotropic displacement parameters. Restraints in **5–LS** were necessary to model the tetrazole ring, and atom distances for these restraints were assigned from the structural model of **4–LS**. In addition, a planarity restraint on the tetrazole ring was also needed. A summary of the data collection and structure refinements is provided in table 3.4.

Table 3.4 Crystallographic data for compounds **4** (**4–HS** and **4–LS**) and **5** (**5–HS** and **5–LS)**.

Compound	**4–HS**	**4–LS**	**5–HS**	**5–LS**
Empirical formula	$C_{30}H_{30}N_{24}Cl_2O_8Fe$		$C_{30}H_{30}N_{24}B_2F_8Fe$	
Formula weight	981.53	981.53	956.25	956.25
Crystal colour	Colourless	Pink	Colourless	Pink
Crystal size (mm^3)	0.07×0.05×0.05		0.07×0.07×0.06	
Temperature (K)	240(2)	120(2)	240(2)	120(2)
Crystal system, Z	Hexagonal, 2	Hexagonal, 2	Hexagonal, 2	Hexagonal, 2
Space group	$P6_3/m$	$P6_3/m$	$P6_3/m$	$P6_3/m$
a (Å)	10.5117(7)	10.3668(4)	10.5265(12)	10.3690(5)
b (Å)	10.5117(7)	10.3668(4)	10.5265(12)	10.3690(5)
c (Å)	23.576(2)	23.1504(17)	23.385(3)	22.9628(15)
α (°)	90.00	90.00	90.00	90.00
β (°)	90.00	90.00	90.00	90.00
γ (°)	120.00	120.00	120.00	120.00
V ($Å^3$)	2256.1(3)	2154.7(2)	2244.0(5)	2138.1(2)
ρ_{calc} (Mg/m^3)	1.445	1.513	1.415	1.485
$\mu(Mo_{K\alpha})$ (mm^{-1})	0.527	0.551	0.423	0.444
θ range (°)	3.42 – 25.04	3.48 – 25.05	2.83 – 25.11	3.50 – 25.01
Reflns collected	8181	15986	4614	9643
Independent reflns	1377	1308	1371	1300
(R_{int})	(0.1962)	(0.1870)	(0.1645)	(0.1235)
Reflns used in refinement, n	1377	1308	1371	1300
L. S. parameters, p/ restraints, r	97/0	100/0	50/8	95/13
$R1(F)$,[a] $I>2\sigma(I)$	0.0984	0.0669	0.2383	0.2137
$wR2(F^2)$,[b] all data	0.2975	0.1943	0.6084	0.5254
$S(F^2)$,[c] all data	1.009	1.062	1.758	1.128

[a] $R1(F) = \Sigma(|F_o| - |F_c|)/\Sigma|F_o|$; [b] $wR2(F^2) = [\Sigma w(F_o^2 - F_c^2)^2/\Sigma wF_o^4]^{1/2}$; [c] $S(F^2) = [\Sigma w(F_o^2 - F_c^2)^2/((n + r - p)]^{1/2}$

3.4.2.II X-ray powder diffraction. Phase purity

Polycrystalline samples of **4** and **5** were lightly ground in an agate mortar and pestle and filled into 0.5 mm borosilicate capillaries. Data were powder collected at room temperature in the 2θ range 2–60 º on an Empyrean PANalytical diffractometer, using Cu K_α radiation, at ICMol (University of Valencia). Pawley refinements[42] were performed using the TOPAS computer program[43] and revealed an excellent fit to a one-phase model, indicating the absence of any other detectable crystalline phases.

3.4.2.III X-ray powder diffraction and Rietveld refinement under CO_2 pressure

Polycrystalline samples of **4** and **5** were lightly ground in an agate mortar and pestle and filled into a 0.7 mm borosilicate capillaries. Data were collected at room temperature in the 2θ range 0 – 40 º on beam line I11 at Diamond Light Source (UK) using λ = 0.826179 Å and a multi-analysing crystals (MAC) detector comprising five arms with 45 MAC channels. The sample was pumped at a pressure of 1×10^{-5} mbar for 30 minutes, after which the CO_2 pressure was increased to 1.04 bar. The capillary was allowed for stabilization for 30 minutes before data collection. A Rietveld refinement[27] was undertaken with the program TOPAS,[43] using as the starting point the structure determined at 240 K for **4** and **5**. A CO_2 molecule was included in the refinement, and refined as a rigid body with rotational and translational freedom. In addition, the occupancy of the CO_2 molecule was also refined maintaining a fixed thermal parameter. Atomic positions and displacement parameters of the non-hydrogen atoms of framework were refined subject to a series of restraints on bond lengths, bond angles and planarity of the aromatic rings. For **4** and **5,** the perchlorate and the tetrafluoroborate anions were modelled as disorder over two positions, as in the single crystal experiment. A March-Dollase correction of the intensities for preferred orientation was applied in the final stage of refinement. Rietveld refinement converged to R_{wp} = 0.0846 and R_{wp}' = 0.2241 for **4** and R_{wp} = 0.0644 and R_{wp}' = 0.1903 for **5** (R_{wp}' is the background subtracted R_{wp}). The observed and calculated diffraction patterns for the refined crystal structures are shown in figure 3.19. A summary of the data collection and structure refinements is provided in table 3.5.

Table 3.5 Data collection, structure solution and refinement parameters of compound **CO_2@4** and **CO_2@5.**

Compound	**CO_2@4**	**CO_2@5**
Empirical formula	$C_{30.93}H_{30}N_{24}Cl_2O_{9.86}Fe$	$C_{30.94}H_{30}N_{24}B_2F_8O_{1.86}Fe$
Formula weight	1122.83	1099.05
Specimen colour	White	White
Specimen shape (mm)	Cylinder	Cylinder
	12 × 0.7 × 0.7 mm	12 × 0.7 × 0.7 mm
Wavelength, λ (Å)	0.826179	0.826179
Crystal system	Hexagonal	Hexagonal
Space group, *Z*	$P6_3/m$, 2	$P6_3/m$, 2
a (Å)	10.51427(6)	10.52516(5)
b (Å)	10.51427(6)	10.52516(5)
c (Å)	23.58103(29)	23.3805(2)
a (°)	90	90
b (°)	90	90
γ (°)	120	120
V (Å^3)	2257.48(2)	2243.07(3)
Density (Mg/m^3)	1.504	1.477
Temperature (K)	295	295
μ (mm^{-1})	0.796	0.430
2θ range ((°)	2.0 to 40.0	2.0 to 40.0
Increment in 2θ (°)	0.003	0.003
Reflns measured, n	487	487
Specimen mounting	0.7 mm borosilicate capillary	0.7 mm borosilicate capillary
Mode	transmission	transmission
Detector	MAC	MAC
Parameters refined, p	78	78
Restraints, r	32	32
R_p[a]	0.0668	0.0499
R_{wp}[b]	0.0846	0.0644
R_{exp}[c]	0.0519	0.0391
GoF [d], all data	1.630	1.647

[a] $R_p = \Sigma|y_O - y_C|/\Sigma y_O$; [b] $R_{wp} = [\Sigma w(y_O - y_C)^2/\Sigma w(y_O)^2]^{½}$; [c] $R_{exp} = R_{wp}/GoF$; [d] $GoF = [\Sigma w(y_O - y_C)^2/(n - p + r)]^{½}$

3.4.3 Physical measurements

^{1}H NMR spectra was recorded on a Bruker DPX300 (300 MHz) spectrometer at the Central Services of University of Valencia. Proton (^{1}H) chemical shifts are reported in parts per million (δ) and referenced internally with respect to the protic solvent impurity. Elemental analysis was carried out at the Centro de Microanálisis Elemental, Universidad Complutense de Madrid. Thermogravimetric analysis (TGA) of **4** and **5** were carried out with a Mettler Toledo TGA/SDTA 851 apparatus at ICMol (University of Valencia) in the 25–270 °C temperature range under a 10 °C·min^{-1} scan rate and an air flow of 30 mL·min^{-1}.

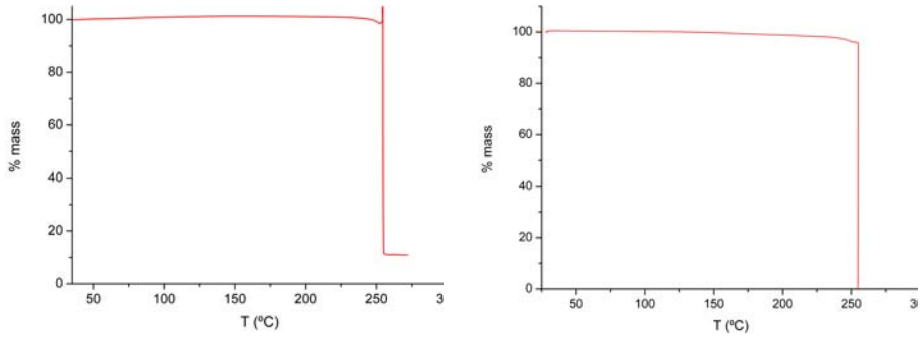

Figure 3.24 Thermogravimetric analysis (TGA) of compounds **4** (a) and **5** (b) reveal the thermal stability of the compounds which remain stable until 250 °C indicating the absence of solvent molecules. At 250 ºC the **4** and **5** rapidly decompose in a drastic manner, which is typical for tetrazolate compounds.

Magnetic measurements. Magnetic susceptibility measurements were performed on single-phased polycrystalline samples with a Quantum Design MPMS-XL-5 SQUID susceptometer at ICMol (University of Valencia). The susceptibility data were corrected from the diamagnetic contributions as deduced by using Pascal's constant tables. The susceptibility data were collected at 1 K·min^{-1} with an applied field of 0.1 T for **4,** $(CO_2)_{0.3}$@**4**, CO_2@**4**, **4'** and **5**, $(CO_2)_{0.3}$@**5**, CO_2@**5** and **5'**, while were collected at 1 T for **4'**, CO_2/N_2 gas mixtures in **4**. Magnetic susceptibility measurements of gas loaded samples were performed by sealing a glass tube with 10 mg of **4** or **5** and a known amount of CO_2 (0.3 and 1 mol CO_2/mol), N_2, or after

heating a loaded sample to remove all CO_2 molecules (**4'** or **5'**). Prior to the gas loading, the sample was heated in situ at 150 °C for 3 h under vacuum.

Gas sorption studies. High-resolution isotherms were measured at a series of temperatures in a Micromeritics ASAP 2010 volumetric instrument at ITQ (Polytechnique University of Valencia) using approximately 150 mg of sample as a powder. We have applied the Virial isotherm for fitting experimental data points and it was found that a fourth grade polynomial is able to properly describe the CO_2 isotherms. The heat of adsorption was calculated accordingly to the Clausius-Clapeyron equation from the isotherms taken at different temperatures. High-Pressure Isotherms and competitive CO_2/N_2 adsorption experiments were performed in an IGA-3 gravimetric analyzer (Hiden Isochema). Approximately 50 mg of the sample were placed in the balance. Adsorption measurements were performed by introducing gas to build up the desired pressures.

3.5 REFERENCES

1. Coronado, E. and Mínguez Espallargas, G. *Chem. Soc. Rev*. **2013**, *42*, 1525.
2. Kepert, C. J. *Chem. Commun*. **2006**, 695.
3. Maspoch, D., Ruiz-Molina, D. and Veciana, J. *Chem. Soc. Rev*., **2007**, *36*, 770.
4. Dechambenoit, P. and Long, J. R. *Chem. Soc. Rev*. **2011**, *40*, 3249.
5. Neville, S. M., Halder, G. J., Chapman, K. W., Duriska, M. B., Moubaraki, B., Murray, K. S. and Kepert, C. J. *J. Am. Chem. Soc.* **2009**, *131*, 12106.
6. Southon, P. D., Liu, L., Fellows, E. A., Price, D. J., Halder, G. J., Chapman, K. W., Moubaraki, B., Murray, K. S., Létard, J.-F. and Kepert, C. J. *J. Am. Chem. Soc*. **2009**, *131*, 10998.
7. Ohba, M., Yoneda, K., Agustí, G., Muñoz, M. C., Gaspar, A. B., Real, J. A., Yamasaki, M., Ando, H., Nakao, Y., Sakaki, S. and Kitagawa, S. *Angew. Chem. Int. Ed.* **2009**, *48*, 4767.
8. Wriedt, M., Yakovenko, A. A., Halder, G. J., Prosvirin, A. V., Dunbar, K. R. and Zhou, H.-C. *J. Am. Chem. Soc*. **2013**, *135*, 4040.
9. Ferrando-Soria, J., Serra-Crespo, P., de Lange, M., Gascon, J., Kapteijn, F., Julve, M., Cano, J., Lloret, F., Pasán, J., Ruiz-Pérez, C., Journaux, Y. and Pardo, E. *J. Am. Chem. Soc.* **2012**, *134*, 15301.
10. Navarro, J. A. R., Barea, E., Rodríguez-Diéguez, A., Salas, J. M., Ania, C. O., Parra, J. B., Masciocchi, N., Galli, S. and Sironi, *J. Am. Chem. Soc.* **2008**, *130*, 3978.
11. Kahn, O. and Martinez, C. J. *Science*, **1998**, *279*, 44.
12. Bousseksou, A., Molnár, G., Salmon, L. and Nicolazzi, W. *Chem. Soc. Rev.* **2011**, *40*, 3313.
13. Eddaoudi, M., Kim, J., Rosi, N., Vodak, D., Wachter, J., O'Keeffe, M. and Yaghi, O. M. *Science* **2002**, *295*, 469.
14. Férey, G., Mellot-Draznieks, C., Serre, C., Millange, F., Dutour, J., Surblé. S. and Margiolaki, I. *Science* **2005**, *309*, 2040.
15. Chui, S. S. Y., Lo, S. M. F., Charmant, J. P. H., Orpen, A. G. and Williams, I. D. *Science* **1999**, *283*, 1148.
16. Coronado, E., Giménez-Marqués, M., Mínguez Espallargas, G. and Brammer, L. *Nature Commun*. **2012**, *3*, 828. *Chapter 2* of this thesis.
17. Aromí, G., Barrios, L. A., Roubeau, O. and Gamez, P. *Coord. Chem. Rev.* **2011**, *255*, 485.
18. Spek, A. L. *J. Appl. Cryst*. **2003**, *36*, 7.
19. Quesada, M., Prins, F., Bill, E., Kooijman, H., Gamez, P., Roubeau, O., Spek, A. L., Haasnoot, J. G. and Reedijk, J. *Chem. Eur. J*. **2008**, *14*, 8486.
20. (a) D'Alessandro, D. M., Smit, B. and Long, J. R. *Angew. Chem. Int. Ed*. **2010**, *49*, 6058. (b) Chowdhury, P., Bikkina, C. and Gumma, S. J. *Phys. Chem. C*, **2009**, *113*, 6616.
21. Atwood, J. L., Barbour, L. J., Jerga, A. and Schottel, B. L. *Science* **2002**, *298*, 1000.

22. Jacobs, T., Lloyd, G. O., Gertenbach, J.-A., Müller-Nedebock, K. K., Esterhuysen, C. and Barbour, L. J. *Angew. Chem. Int. Ed*. **2012**, *51*, 4913.
23. Dalgarno, S. J., Thallapally, P. K., Barbour, L. J. and Atwood, J. L. *Chem. Soc. Rev*. **2007**, *36*, 236.
24. Kauffman, K. L., Culp, J. T., Allen, A. J., Espinal, L., Wong-Ng, W., Brown, T. D., Goodman, A., Bernardo, M. P., Pancoast, R. J., Chirdon, D. and Matranga, C. *Angew. Chem. Int. Ed.* **2011**, *50*, 10888.
25. Sumida, K., Rogow, D. L., Mason, J. A., McDonald, T. M., Bloch, E. D., Herm, Z. R., Bae, T.-H. and Long, J. R. *Chem. Rev*. **2012**, *112*, 724.
26. Li, J.-R., Ma, Y., McCarthy, M. C., Sculley, J., Yu, J., Jeong, H.-K., Balbuena, P. B. and Zhou, H.-C. *Coord. Chem. Rev*. **2011**, *255*, 1791.
27. Rietveld, H. M. *J. Appl. Crystallogr*. **1969**, *2*, 65.
28. Thompson, S. P., Parker, J. E., Potter, J., Hill, T. P., Birt, A., Cobb, T. M., Yuan, F. and Tang, C. *Rev. Sci. Instrum*. **2009**, *80*, 075107.
29. Dietzel, P. D. C., Johnsen, R. E., Fjellvåg, H., Bordiga, S., Groppo, E., Chavan, S. and Blom, R. *Chem. Commun*. **2008**, 5125.
30. Zhang, J-P. and Chen, X-M. *J. Am. Chem. Soc.* **2009**, *131*, 5516.
31. Kim, H., Kim, Y., Yoon, M., Lim, S., Park, S. M., Seo, G. and Kim, K. *J. Am Chem. Soc*. **2010**, *132*, 12200.
32. Takamizawa, S., Nataka, E.-i., Akatsuka, T., Miyake, R., Kakizaki, Y., Takeuchi, H., Maruta, G. and Takeda, S. *J. Am. Chem. Soc.* **2010**, *132*, 3783.
33. Yang, S., Sun, J., Ramirez-Cuesta, A. J., Callear, S. K., David, W. I. F., Anderson, D. P., Newby, R., Blake, A. J., Parker, J. E., Tang, C. C. and Schröder, M. *Nature Chem*. **2012**, *4*, 887.
34. Frontera, A., Gamez, P., Mascal, M., Mooibroek, T.J. and Reedijk, J. *Angew. Chem. Int. Ed.* **2011**, *50*, 9564.
35. Vaidhyanathan, R., Iremonger, S. S., Shimizu, G. K. H., Boyd, P. G., Alavi, S. and Woo, T. K. *Science* **2010**, *330*, 650.
36. Liao, P.-Q., Zhou, D.-D., Zhu, A.-X., Jiang, L., Lin, R.-B., Zhang, J.-P. and Chen, X.-M. *J. Am. Chem. Soc.* **2012**, *134*, 17380.
37. Plonka, A. M., Banerjee, D., Woerner, W. R., Zhang, Z., Nijem, N., Chabal, Y. J., Li, J. and Parise, J. B. *Angew. Chem. Int. Ed.* **2013**, *52*, 1692.
38. Wriedt, M., Sculley, J. P., Yakovenko, A. A., Ma, Y., Halder, G. J., Balbuena, P. B. and Zhou, H.-C. *Angew. Chem. Int. Ed.* **2012**, *51*, 9804.
39. Rodríguez-Velamazán, J. A., González, M. A., Real, J. A., Castro, M., Muñoz, M. C., Gaspar, A. B., Ohtani, R., Ohba, M., Yoneda, K., Hijikata, Y., Yanai, N., Mizuno, M., Ando, H. and Kitagawa, S. *J. Am. Chem. Soc*. **2012**, *134*, 5083.
40. Pharmaceutical, F. BDR patent:BRD, 1973 Vol. 2147023.

41. Sheldrick, G. M. *Sect. A: Found. Crystallogr*. **2008**, *64*, 112.
42. Pawley, G. S. *J. Appl. Cryst.* **1981**, *14*, 357.
43. Coelho, A. A. TOPAS-Academic, Version 4.1, 2007, see: http:// www.topas-academic.net.

4

PHYSICALLY-DRIVEN SOLID-STATE TRANSFORMATION IN COORDINATION POLYMERS

4.1 INTRODUCTION

Over the past decades, the most commonly used strategy for the synthesis of MOFs has consisted on the use of rigid ligands to bridge between the metal nodes leading to robust frameworks.[1] However, there is recently a growing interest in the search for flexible and dynamic MOFs owing to their potential applications as functional materials.[2,3] These soft porous crystals[4] are porous solids that possess both a highly ordered network and a dynamic structure. Therefore, they can be regarded as bistable crystalline solids with long-range structural ordering.

Dynamic MOFs are susceptible of modifying their framework upon the effect of external stimuli.[5] As a result, a large variety of transformations that take place in the crystalline state exist as a consequence of applied physical or chemical stimuli. Several examples of 'breathing' MOFs are known, in which structural changes occur upon guest removal/inclusion without bond cleavage, implying that the framework retains the same (or similar) topology.[6,7] Even more extraordinary result those examples of solid-state transformations that involve formation and cleavage of covalent bonds, while maintaining the crystallinity.[8] In these cases a drastic rearrangement of the network connectivity can occur, with changes in ligand coordination which affect the dimensionality of the network and can influence the physical properties of the coordination polymer.[9,10] Single-crystal-to-single-crystal transformations (SCSC) are the most desirable of these reactions, since they permit the unequivocal structural characterization of the product.[11,12] Actually, large atomic motions can provoke breaks in the single crystals and often yields a polycrystalline powder that can hinder the structural characterization, thus disabling complete comprehension of the changes in the properties of the material. Recent improvements on X-ray powder diffraction analysis (XRPD) have permitted the *ab initio* structural determination of MOFs after structural transformation,[3b,13] although it can result very challenging due to the high complexity of these systems. In *Chapter 5,* an example of *ab initio* structural determination after structural transformation in a coordination polymer will be presented. Spectroscopic techniques and thermoanalytical methods

also provide useful information on the structural rearrangement, and molecular dynamic simulations have also been reported to confirm the movement of a flexible fragment for which a suitable model from X-ray powder data could not be obtained.[14]

Incorporation of magnetic metal ions into these frameworks opens the possibility to obtain magnetic porous materials with multifaceted properties, which can coexist in the material or interplay in a more sophisticated device. As pointed out in *Chapter* 1, there are different types of magnetic MOFs, those based on bistable molecules and the ones that incorporate exchange coupled systems. They represent a versatile family of systems since magnetic properties can be for example switched by an external stimulus or triggered by light. For instance, as shown in previous *Chapter 3*, these magnetic properties can be modified by the structural changes provoked by the uptake of molecular species in the pores, making them suitable candidates for potential application as switches or sensors.[5] An additional plausible mechanism to induce a change in the magnetic properties of a flexible MOF is to provoke a structural transformation. In particular, those transformation involving dimensionality changes often generate tunable magnetic systems. Another relevant issue to take into account is the degree of solvation of magnetic MOFs which has been proved to promote direct effect on the magnetic properties.[15]

The scope of this *Chapter* is the study of two families of dynamic magnetic coordination polymers based on the flexible ligand 1,4-bis(triazol-1-ylmethyl)benzene) (btix). This ligand can adopt different conformations, *syn* and *anti*, as shown in figure 5.1.

(a) (b)

Figure 4.1 Diferent conformations of the flexible ligand btix: (a) *syn*; (b) *anti.*

As previously seen in *Chapter 3*, dynamic frameworks based on an analogous ligand are likely to develop structural transformations occurring in the crystalline state upon sorption/release of gases. In this *Chapter* we will investigate in detail such possibility. Thus, we will explore the different structures provided by the flexibility of an organic ligand upon release of water molecules. We will show that the presence of magnetic centres permits the application of electron paramagnetic resonance (EPR) and magnetic susceptibility to gather information on structural features. Thus, EPR can provide information on the changes of the coordination sphere of the metal, whereas magnetic susceptibility measurements can help to elucidate the connectivity between the metal centres. This kind of magneto-structural correlations has been extensively applied to molecular coordination complexes in the early years of molecular magnetism,[16] but its application in flexible MOFs is novel.

4.2 RESULTS AND DISCUSSION

4.2.1 Description of the structures

$\{[M(btix)_2(OH_2)_2]\cdot 2NO_3\cdot 2H_2O\}_n$ (6–8). The reaction of $M(NO_3)_2\cdot 6H_2O$ (M = Co^{II}, Zn^{II}) and btix in a EtOH/H_2O solution results in the formation of block-shaped crystals of formula $\{[M(btix)_2(OH_2)_2]\cdot 2NO_3\cdot 2H_2O\}_n$ [M= Co (**6**),[17] Zn (**7**), Co-Zn (**8**)]. Crystallographic analysis reveals that compounds **6**, **7**, and **8** are composed of 1D chains that run parallel to the crystallographic (10 $\bar{1}$) direction (figure 4.2).

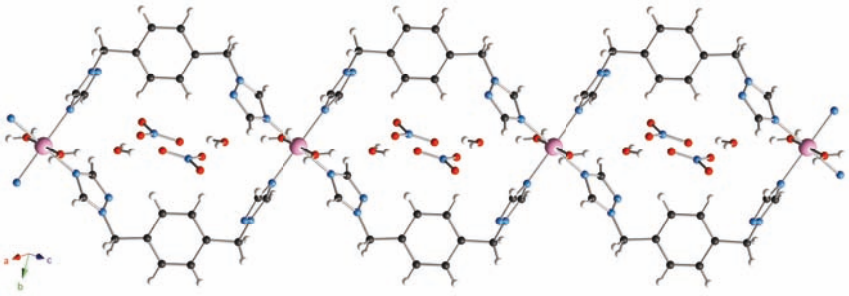

Figure 4.2 Crystal structure of **6** showing the one-dimensional chains that run parallel to the crystallographic (10 $\bar{1}$) direction. Cobalt, nitrogen, oxygen, carbon and hydrogen are coloured pink, blue, red, black and white, respectively. Compounds **7** and **8** are isostructural to **6**.

They crystallize in the triclinic $P\bar{1}$ space group. The asymmetric unit consists of one crystallographycally independent M^{II} that lies in the inversion centre with *trans*-N_4O_2 coordination octahedron mode. Each metal is coordinated by four triazole nitrogen atoms derived from four *syn*-btix ligands in the equatorial positions and two oxygen atoms from water molecules in the apical positions. The coordination environment of the M^{II} ions features a slightly distorted octahedron with Co–N distances of 2.137(3) and 2.162(3) Å and Co–O distance of 2.094(2) Å for compound **6**, and Zn–N distances of 2.140(2) and 2.173(2) Å and Zn–O distances of 2.1295(14) Å for compound **7**, and angles that slightly deviate from idealized octahedron geometry (see table 4.1). Two *syn*-btix ligands act as bridges between adjacent metal centres leading to M···M distances of 12.1087(17) and 12.1134(11) Å for **6** and **7** respectively.

Table 4.1 Selected bond lengths (Å), angles (º) and metal-metal distances for **4** and **5** in the HS (240 K) and LS (120 K) states.

	6	**7**	**9**	**10**
M–N (Å)	2.137(3)	2.140(2)	2.121(2)	2.143(2)
	2.162(3)	2.173(2)	2.137(2)	2.119(2)
M–O (Å)	2.094(2)	2.1295(14)	2.192(3)[a]	2.223(4)[c]
			2.154(3)[b]	2.190(3)[d]
N–M–N (º)	92.72(10)	93.39(6)	90.35(6)	90.18(7)
	180	180	180	180
N–M–O (º)	92.07(10)	92.15(6)	91.32(9)[a]	90.90(12)[c]
	92.08(9)	91.93(6)	102.08(10)[a]	102.29(13)[c]
			97.25(8)[b]	97.67(10)[d]
			102.26(10)[b]	102.22(12)[d]
O–M–O (º)	180	180	180[a]	180[c]
			180[b]	180[d]

[a] This value corresponds to the NO_3^- anion with 48.1(3) % occupancy. [b] This value corresponds to the NO_3^- anion with 51.9(3) % occupancy. [c] This value corresponds to the NO_3^- anion with 51.2(4) % occupancy. [d] This value corresponds to the NO_3^- anion with 48.8(4) % occupancy.

The one-dimensional networks are cationic and the charge is compensated by the presence of NO_3^- anions in the voids (figure 4.3). In addition, the voids are filled with water molecules which complete a hydrogen bonding network that involves both the coordinated and non-coordinated water molecules and the nitrate anions.

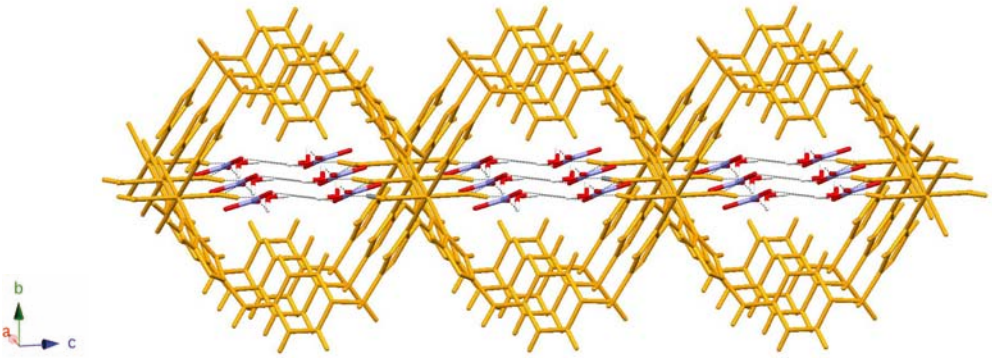

(a)

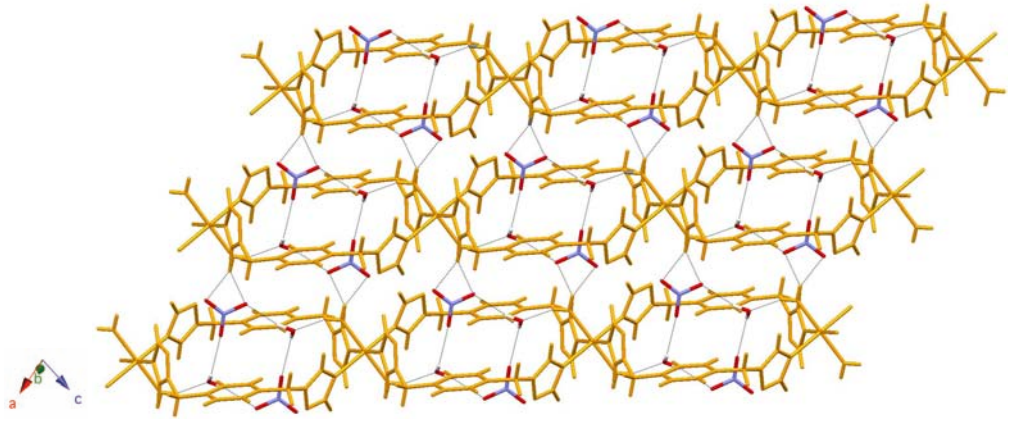

(b)

Figure 4.3 (a) One-dimensional chains formed by **6** and **7** that run parallel to the crystallographic (10 $\bar{1}$) direction showing the non-coordinated water molecules and nitrate anions that fill the voids. (b) Hydrogen bonding network formed by both the coordinated and non-coordinated water molecules and the nitrate anions. The cationic one-dimensional networks are represented in orange while nitrogen, oxygen and hydrogen from nitrate and non-coordinated water molecules are coloured blue, red and white, respectively. Black dotted lines represent hydrogen bonds.

$\{[M(btix)_2(NO_3)_2]\}_n$ (9–11). The reaction of $M(NO_3)_2{\cdot}6H_2O$ (M = Co^{II}, Zn^{II}) and btix in MeOH results in the formation of block-shaped crystals of formula

$\{[M(btix)_2(NO_3)_2]\}_n$ [M= Co (**9**),[17] Zn (**10**), Co-Zn (**11**)]. Compounds **9**, **10** and **11** crystallize in the monoclinic $P2_1/c$ space group. Each metal lies in an inversion centre and is coordinated by four triazole nitrogen atoms from four *anti*-btix ligands and two oxygen atoms from two nitrate ions in the apical positions. Thus, the coordination sphere of each M^{II} ion is very similar to those of **6-7**, with *trans*-N4O2 coordination octahedron mode. The Co–N distances are 2.121(2) and 2.137(2) Å and the Co–O distances are 2.192(3) and 2.154(3) Å for the two disordered NO_3^- anions for compound **9**, and the Zn–N distances are 2.143(2) and 2.119(2) Å and the Zn–O distances are 2.223(4) and 2.190(3) Å for the two disordered NO_3^- anions for compound **10**. The angles slightly deviate from idealized octahedron geometry (see table 4.1). The *anti*-btix ligands act as bidentate linkers generating a 2D grid with (4,4) topology with M···M distances of 14.5346(6) and 14.5193(4) Å for **9** and **10** respectively. Theses layers stack along the (101) direction in an ABCABC fashion (figure 4.5). Weak C–H···O interlayer interactions are observed between the three oxygen atoms of the nitrate anions from one sheet and aromatic and aliphatic C–H groups of the ligand from the next sheet.

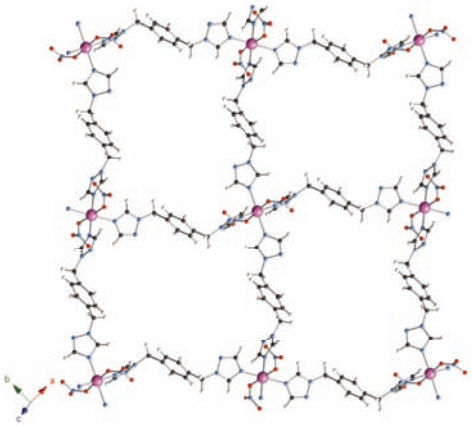

Figure 4.4 Crystal structure of **9** showing the 2D grids with (4,4) topology. Cobalt, nitrogen, oxygen, carbon and hydrogen are coloured pink, blue, red, black and white, respectively. Hydrogen atoms have been omitted for clarity. Compounds **10** and **11** are isostructural to **9**.

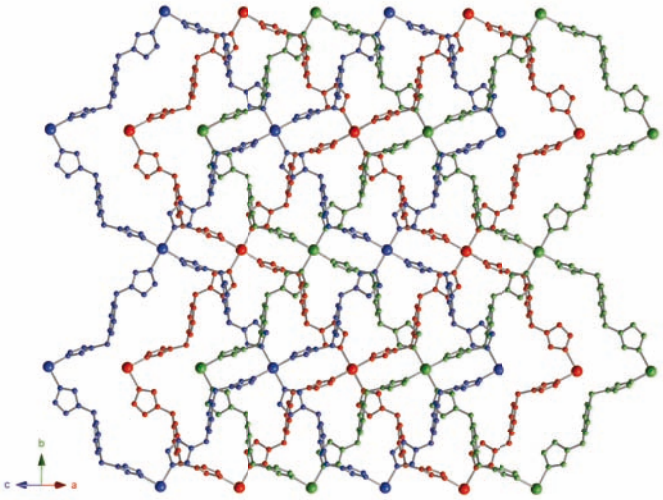

(a)

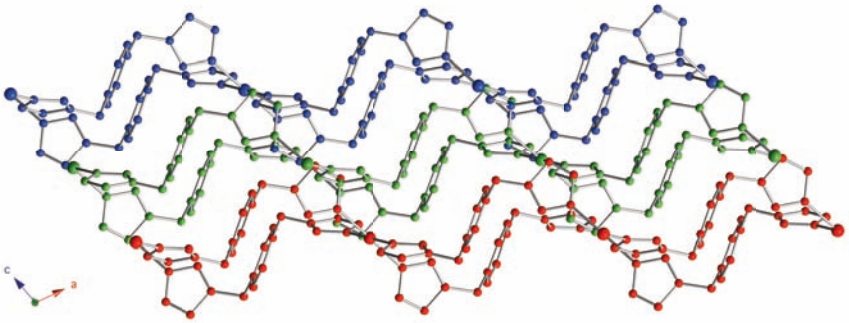

(b)

Figure 4.5 Crystal structure of compounds **9** showing the 2D grids with (4,4) topology stacking along the 101 axis in an ABCABC fashion, shown in two orientations which are related by rotation of 90 º about the 101 axis. Red, green and blue represent three different ABC layers. Hydrogen atoms and nitrate ligands have been omitted for clarity.

4.2.2 Thermogravimetric analysis

Compounds **6-8** present internal cavities that in principle result attractive for adsorption of guest molecules. However, these voids are occupied by anions and solvent molecules as seen in figure 4.2. The presence of the anions in the cationic

framework is not necessarily an inconvenience since, in principle, non-coordinating ions (which are permanent dipoles) could interact with guests molecules inducing a temporary dipole, thus facilitating the diffusion of these guest molecules into the ionic framework.[18]

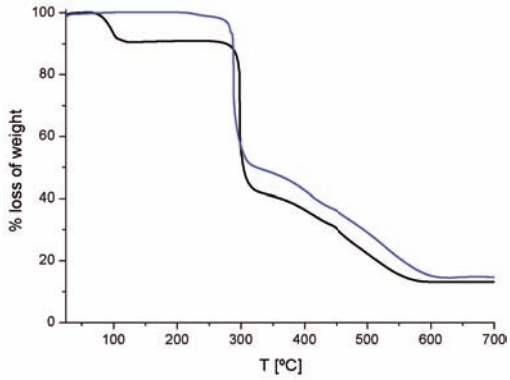

Figure 4.6 Thermogravimetric analysis of compounds **6** (black line) and **9** (blue line). TGA of compound **6** reveals that a continuous loss of 10.6% occurs from 25 to 100 °C, which can be attributed to the loss of both coordinating and non-coordinating water molecules (calc. 11.5%). TGA of compound **9** shows the thermal stability of the compound which remains stable until 280 °C and gradually decomposes until 700 °C.

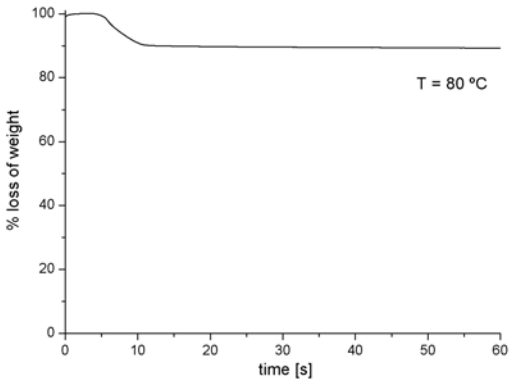

Figure 4.7 Gravimetric analysis of compound **6** exposed under a constant temperature of 80 ºC shows a total loss of weight of 10.9% after 10 minutes of heating, which corresponds to the loss of all the water molecules (calc. 11.5%) and remains stable for hours.

To increase the effective void volume of the framework and thus obtain a porous system suitable for gas uptake, it is necessary to remove the solvent molecules from the cavities. Thus, thermal stability of the compounds has been explored. Thermogravimetric analysis performed on **6** shows a mass loss of 10.6 % between 70 and 120 ºC, which corresponds to removal of four water molecules per formula unit (expected 11.5 %), revealing that both the solvated and coordinated water molecules in **6** are liberated below 120 ºC (figure 4.6). In fact, this loss of water molecules can be achieved by heating **6** at only 80 ºC for 1 h (Figure 4.7). Several experiments were performed at different temperatures and heating times in order to differentiate the elimination of both the solvated and coordinated water molecules. However, discrimination of both types of water molecules resulted unsuccessful. As a result, both solvated and coordinated solvent molecules are therefore eliminated from the coordination polymer at the same time. The final mass loss, between 100 and 700 °C, corresponds to the decomposition of the complex. The same thermogravimetric analysis has been applied to **9**, showing that the compound remains stable up to 280 ºC, where gradually decomposes until 700 ºC, indicating the lack of solvent molecules as previously established by structural characterization.

4.2.3 X-ray powder diffraction studies

4.2.3.I Phase purity. XRPD studies have served to establish the phase purity of the as-synthesized polycrystalline samples **7** and **10**. Note that XRPD of samples **6** and **9** present a very poor resolution given a high background, which is due to the fluorescence effect typical of cobalt-containing samples when measured with Cu X-ray radiation. Therefore, instead of Co compounds **6** and **9,** analogous Zn compounds **7** and **10** will be used in further experiments involving XRPD studies. A Pawley refinement has been applied to the experimental powder patterns of polycrystalline samples **7** and **10**. The observed and calculated diffraction patterns for the refined crystal structures are shown in figure 4.8. Pawley refinement converged to R_{wp} = 0.0368, R_{wp}' = 0.0641 and gof = 2.397 for **7** and R_{wp} = 0.0287, R_{wp}' = 0.0501 with a gof = 1.944 for **10** (R_{wp}' is the background subtracted R_{wp}).

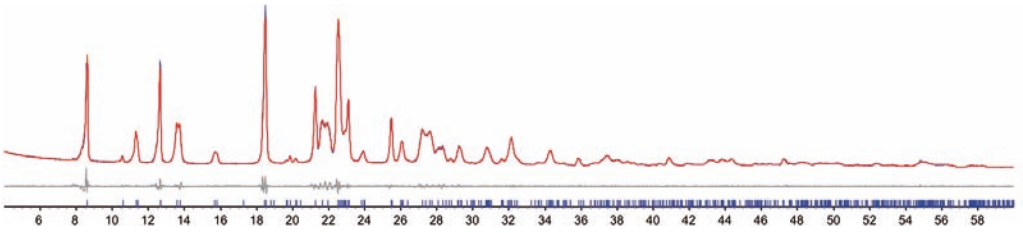

(a)

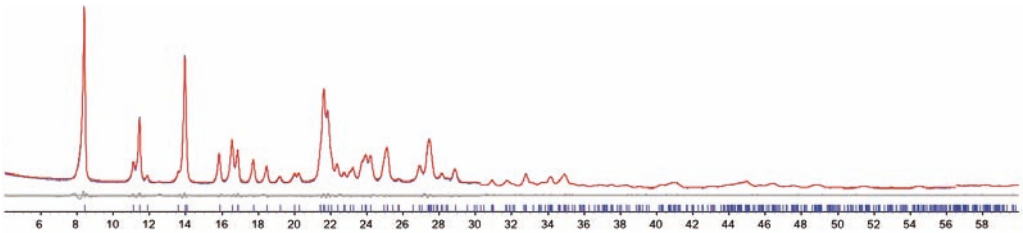

(b)

Figure 4.8 Observed (blue) and calculated (red) profiles and difference plot [(I_{obs} – I_{calcd})] (grey) of the Pawley refinements for compound **7** (a) and **10** (b) (2θ range 4.0–60.0 °; maximum resolution 1.54 Å).

After thermal treatment of **7**, it is necessary to confirm that crystallinity is preserved, since desolvation processes commonly end with an amorphous phase. Thus, X-ray powder diffraction (XRPD) experiment performed on crystalline powder after thermal treatment **7'** has established the maintenance of crystallinity. This implies that the removal of both the solvated and the coordinated water molecules in **7'** occurs without disrupting the long-range order. However, the diffraction pattern is clearly different from that of the original compound **7** indicating a totally different crystalline phase (figure 4.9). A solid-state transformation has occurred during the evacuation process, leading to a different compound. Interestingly, the XRPD pattern of the dehydrated sample **7'** corresponds exactly to the XRPD pattern of compound **10**, meaning that the dehydration process is a solid-state reaction in which **7** is transformed into **10**.

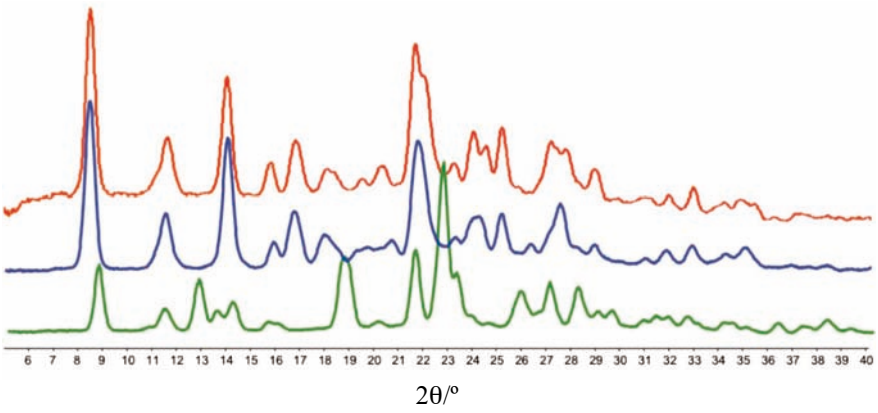

Figure 4.9 Observed X-ray powder diffraction patterns of **7** before heating (green) and **7'** after heating at 350 K for 2h (blue), and compound **10** as synthesized (red). Selected 2θ range 4–40 °.

Solid-state transformation. This conversion of the chain compound into the 2D system is of remarkable significance, given the drastic rearrangement of coordination bonds that occurs in the solid-sate. This structural transformation consists on a conformational change of the btix ligand from *syn*-conformation in **6-8** to *anti*-conformation in **9-11**. The conformational change implies: i) the cleavage of coordination bonds between M^{II} ions and btix ligands; ii) the rotation of btix ligand through the methylene groups to adopt the anti conformation and iii) the subsequent re-formation of M–N bonds. Additionally to this conformational change, a ligand substitution takes place since the loss of coordinated water molecules is followed by coordination of the NO_3^- anions. As a result, this rearrangement ends with an increase of the dimensionality of the network from 1D to 2D. Importantly, immersion of compoundS **9-11** into water to induce the reversible process, that is reconversion into **6-8**, resulted unsuccessful.

4.2.3.II XRPD monitoring of the solid-state transformation

Temperature-dependent XRPD data from temperature-dependent studies have been applied to monitor the solid-state transformation. X-ray variable temperature experiments have been performed on crystalline powdered samples of **7**. Powder patterns were collected at 300, 320, 340, and finally at 350 K, remaining at this

temperature and collecting a pattern every 20 minutes. A detailed view of a selected 2θ range (7.5–14.5 º) is presented in figure 4.10. Upon heating from 300 to 340 K, the intensity of the peaks corresponding to **7** successively diminishes. At 350 K new peaks appear indicating that the solid-state transformation is initiated. Subsequent measurements collected at 350 K show how new peaks corresponding to **10** grow in intensity while the peaks corresponding to **7** disappear.

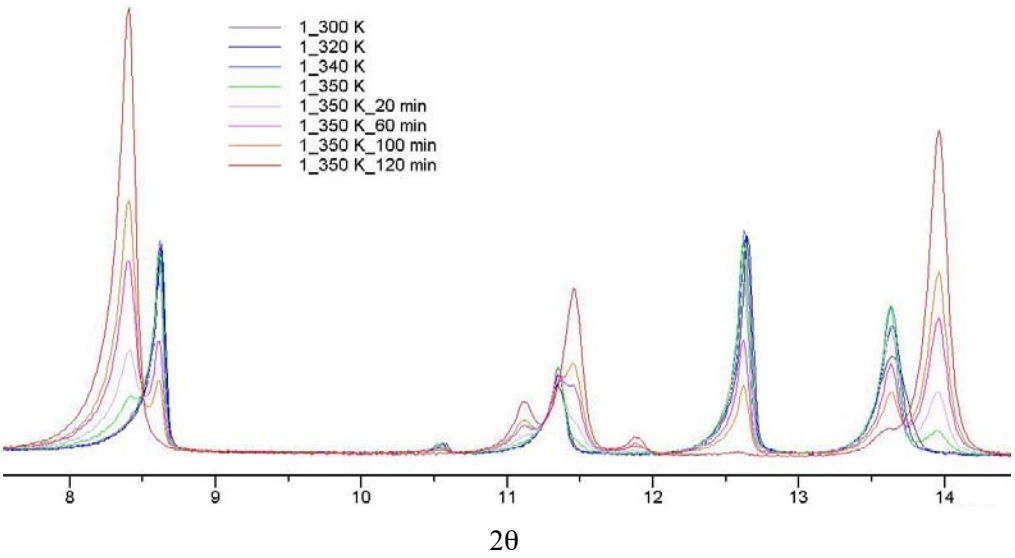

Figure 4.10 View of the selected 2θ range 4–60 ° for **7** at different temperatures and reaction times.

4.2.4 Sorption studies

Thermogravimetric analysis of coordination polymers **6-8** (section 4.4.2) have served to established that the internal cavities that could in principle result attractive for adsorption of guest molecules are not available once the solvent molecules are eliminated. In spite of this, coordination polymers **9-11** could be considered as the thermodynamic favourable system. Importantly, the morphology and structural flexibility of coordination polymers **9-11** make them plausible candidates for guest-induced "gate opening" behaviour. This phenomenon, first enunciated by Kitagawa *et al.*,[19] describes the gate effect that occurs when the framework structure of a coordination polymer changes during the adsorption process from a closed structure to

an open one at a specific pressure. As described in the structural section 4.2.1, the 2D systems are formed of layers which stack in an ABCABC fashion and are weakly connected through C–H···O interlayer interactions. Each layer presents individual 2D windows of *ca*. 10 $Å^2$, which are not connected in the third direction (thus ending with a closed structure). These windows could be connected in an opened structure if a concrete displacement of the layers is achieved by gas sorption at high pressures (see figure 4.5). Solid-gas adsorption properties of **9** towards N_2 (298 K) have been evaluated at high pressure (60 bar). The adsorption isotherm of **9**, shown in figure 4.11, reveals that N_2 molecules remain unadsorbed even at 60 bar. This clearly confirms the incapability of **9** to change its conformation from a closed to an opened structure upon high pressure exposure of N_2 gas.

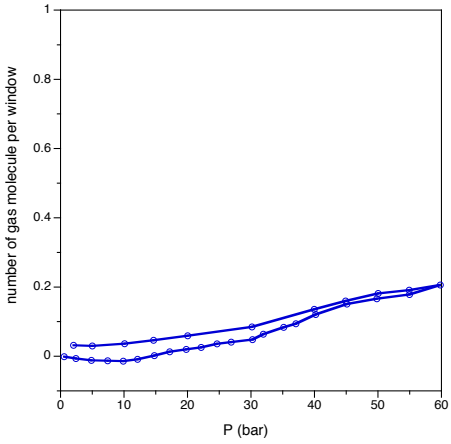

Figure 4.11 N_2 adsorption isotherm of **9** at 298 K.

4.2.5 Magnetic properties

The presence of magnetic centers in these families of coordination polymers has been exploited to study the structural changes experienced by these solids. More precisely, magnetic susceptibility measurements have been used to study whether the change in metal connectivity (from 1D to 2D) has some influence on the magnetic dimensionality. This could result very useful in the characterization of more complex

systems that also suffer structural transformations. The product of the molar magnetic susceptibility and temperature, $\chi_M T$, of the Co^{II} compounds (**6** and **9**) are shown in figure 4.12. At room temperature $\chi_M T$ has a value of 3.12 and 3.38 emu.K.mol^{-1} for **6** and **9** respectively, and decreases on cooling reaching a minimum value at 2 K of 2.17 and 1.90 emu.K.mol^{-1} for **6** and **9**, respectively. This decrease is similar in both cases and indicates that the Co-Co exchange interactions are very weak in both compounds, being totally insensitive to the different conformations adopted by the bridging btix ligand (*syn* vs. *anti*). The observed decrease in $\chi_M T$ down to 2 K has to be associated to the single-ion behavior and arises from the depopulation of the excited spin-orbit levels of octahedral Co^{II}. Hence, although the magnetic measurements clearly indicate that the metal centers have a similar connectivity (via the btix ligand), it is insensitive to the different dimensionality of the two networks caused by the change in conformation of the ligand.

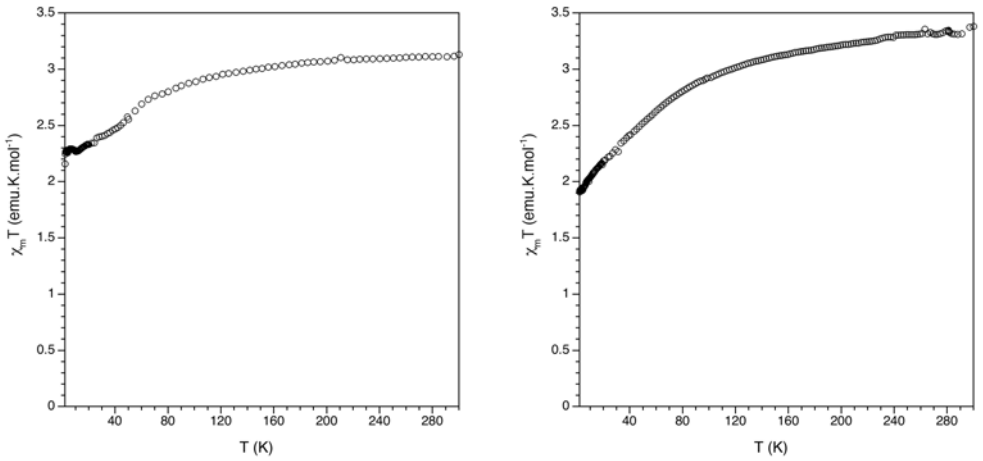

(a) (b)

Figure 4.12 Thermal dependence of the $\chi_M T$ product of **6** (a) and **9** (b) in the temperature range 2-300 K.

4.2.6 EPR studies

EPR spectroscopy has been used in solid samples of coordination polymers to detect changes in the coordination sphere of the metal ion due to its strong sensitivity to the

coordination environment of the metal centres. Magnetically diluted samples **8** and **11** have been prepared to improve the resolution of the spectra. The EPR spectrum of **8** (figure 4.13) displays a typical distorted axial pattern for high-spin Co^{II} with g-values 6.49, 3.28 and 2.31, which is in good agreement with the distorted *trans*-N_4O_2 coordination octahedron mode observed in the crystallographic analysis.[20] The hyperfine splitting is only apparent on the low-field component, and corresponds to a coupling constant of 65 G for the I = 7/2 ^{59}Co nucleus. Upon heating, the EPR spectrum stays unchanged, demonstrating that the coordination environment of the metal is not enormously modified and retains the *trans*-N_4O_2 coordination octahedron mode. After the solid-state transformation the EPR spectrum remains rhombic, but the g components slightly change to 6.70, 3.71 and 2.26, indicating the sensitivity to small changes in the coordination environment. In contrast, significant differences are observed in the hyperfine structure of the spectra, with hyperfine constants that increase from 65 (in **8**) to 100 G (in **11**). This is consistent with the modification in the nature of the oxygen ligand, which changes from (neutral) water molecules to (anionic) nitrate ligands (figure 4.14). Thus, EPR spectroscopy is able to detect these minor changes in which the coordination geometry remains similar albeit with changes in the nature of the ligands (figure 4.12).

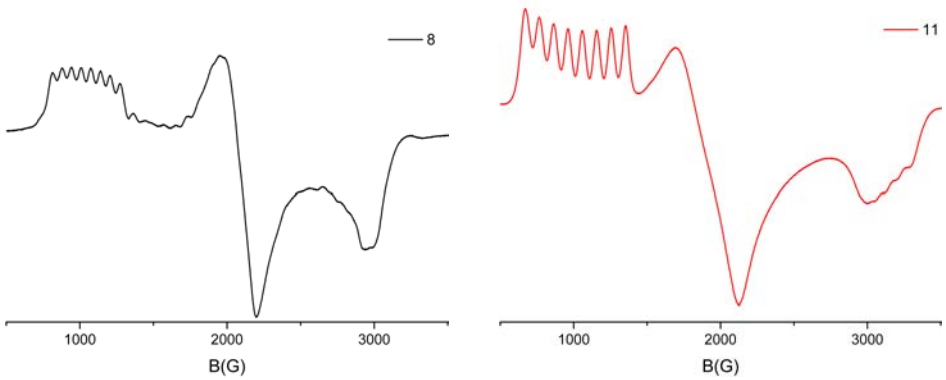

Figure 4.13 X-band EPR spectra at 4 K of compounds **8** (a)**,** and **11** (b).

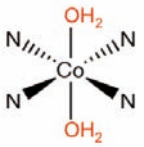

(a)

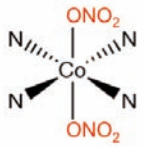

(b)

Figure 4.14 Coordination environments of cobalt(II) centres in **8** (a) and **11** (b).

EPR monitoring of the solid-state transformation. To understand the path of the reaction, we have followed the solid-state transformation **8→11** by EPR spectroscopy. A sample of **8** was placed in an open capillary and heated at 353 K for 2 hours. It should be noted that the reaction times are surface area dependent, so the well-packed sample used in this experiment results in an increase in the reaction time for completion. EPR spectra were recorded every 15 min intervals at 4 K (figure 4.15 shows a selection of the EPR spectra). Therefore, the reaction was quenched to obtain a sequence of snapshots of the reaction during its progress. It can be observed that the signal corresponding to **8** diminishes in intensity with time, whereas that corresponding to **11** increases, indicating the lack of an intermediate in the reaction. Thus, a concerted substitution reaction in which NO_3^- ligands displace the coordinated H_2O molecules is likely to occur.

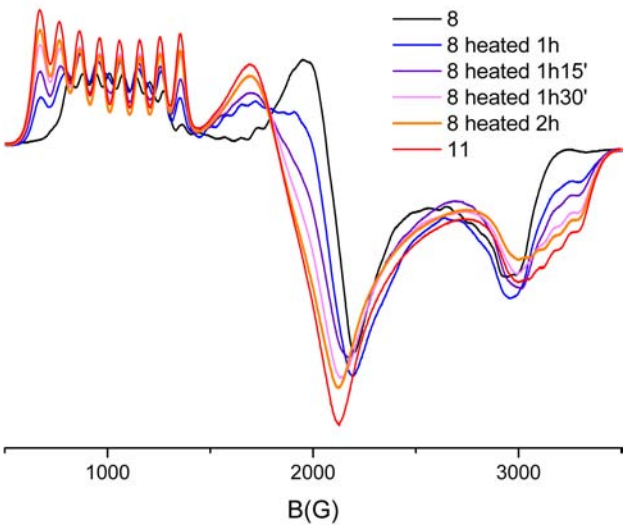

Figure 4.15 X-band EPR spectra at 4 K of compounds **8** at different times of heating and **11**.

4.3 CONCLUSIONS

In this chapter two families of coordination polymers, $\{[M(btix)_2(OH_2)_2]\cdot 2NO_3\cdot 2H_2O\}_n$ [M= Co (**6**), Zn (**7**), Co-Zn (**8**); btix = 1,4-bis(triazol-1-ylmethyl)benzene] and $\{[M(btix)_2(NO_3)_2]\}_n$ [M= Co (**9**), Zn (**10**), Co-Zn (**11**)], have been studied. These families of coordination polymers present different dimensionalities, which are related with the conformation adopted by the ligand, which can adopt a *syn* or an *anti* conformation. Thus, compounds **6-8** consist of non-interpenetrated 1D cationic chains with large cavities that are partially filled with anions and solvent molecules, whereas compounds **9-11** form a 2D neutral grid with (4,4) topology.

Given the attractiveness of **6-8** for gas sorption applications, removal of the solvent molecules trapped into the cavities has been explored. Hence, thermogravimetric and XRPD studies have been applied in **6**. Interestingly, it has been shown that the chain compounds are able to extrude both coordinated and non-bonded water molecules and transform into the layered compounds in the solid state upon heating without loosing their crystallinity, thanks to the flexibility of the btix ligand. This thermally-induced solid-state process involves a change in conformation of the flexible btix ligands (from *syn* to *anti*) and also requires a rearrangement in the metal environment with the cleavage and formation of M–N bonds.

This structural transformation can be monitored through the use of magnetic techniques as it provokes changes in the magnetic properties of these magnetic coordination polymers. In particular, the use of EPR spectroscopy to detect the minor modifications that suffer the Co^{II} coordination sphere upon transformation of the chains to the layers structures has been detailed. In addition, XRPD at variable temperature has served to monitor the solid-state transformation. Consequently, the thermally-induced solid-state process is determined to occur in a single step since no intermediate has been detected during the reaction process.

Compound **9** has been tested as a plausible system to present gas sorption through the

mechanism named “gate opening behaviour”. Exposure of **9** at high pressures of N_2 revealed the absence of any sorption process in the system.

To conclude, it has been shown that the presence of magnetic centres can provide very useful information in structural changes in coordination polymers when there is a lack of single crystal diffraction data. Thus, this methodology could be applied in more complex systems to better understand solid-state transformations.

4.4 METHODS

4.4.1 Synthesis

The ligand btix was prepared according to a literature method with some modifications.[21] All reagents and solvents were commercially available and used without further purification.

Synthesis of $\{[Co(btix)_2(OH_2)_2]\cdot 2NO_3\cdot 2H_2O\}_n$ (6): A solution of $Co(NO_3)_2\cdot 6H_2O$ (125.2 mg, 0.4 mmol) in 4 mL of H_2O was added slowly into a EtOH/H_2O solution (7:1 v/v) of btix (96.0 mg, 0.4 mmol) without stirring. The mixture was left at RT for crystallization. After several days, pink needle-shaped crystals were filtered off and washed with water. Anal. calc. $C_{24}H_{32}CoN_{14}O_{10}$ (735.54): C, 39.19; H, 4.39; N, 26.66%. Found: C, 39.11; H, 4.39; N, 25.97%.

Synthesis of $\{[Zn(btix)_2(OH_2)_2]\cdot 2NO_3\cdot 2H_2O\}_n$ (7): 7 was synthesized in a procedure analogous to that of **6** except that $Zn(NO_3)_2\cdot 6H_2O$ (120.0 mg, 0.4 mmol) was used instead of $Co(NO_3)_2\cdot 6H_2O$. Colourless block-shaped crystals were filtered off and washed with water. Anal. calc. $C_{24}H_{32}ZnN_{14}O_{10}$ (742.00): C, 38.85; H, 4.35; N, 26.43%. Found: C, 38.90; H, 4.32; N, 25.89%.

Synthesis of $\{[Zn_{(0.98)}Co_{(0.02)}(btix)_2(OH_2)_2]\cdot 2NO_3\cdot 2H_2O\}_n$ (8): 8 was synthesized in a procedure analogous to that of **6** except that a mixture of $Zn(NO_3)_2\cdot 6H_2O$ (116.6 mg, 0.392 mmol) and $Co(NO_3)_2\cdot 6H_2O$ (2.4 mg, 0.008mmol) was used. Light-pink needle-

shaped crystals were filtered off and washed with water. Phase purity was established by X-ray powder diffraction.

Synthesis of $[Co(btix)_2(NO_3)_2]_n$ (9): Different routes are available for the synthesis of **9**. Crystals of **6** were heated to 353 K for 2 h to yield **9** as pale pink crystalline powder. Alternatively, **9** can be obtained by slowly addition of a solution of $Co(NO_3)_2 \cdot 6H_2O$ (125.2 mg ,0.4 mmol) in 15 mL of MeOH into a solution of btix (96.0 mg, 0.4 mmol) in 20 mL of MeOH without stirring. The mixture was left at RT for crystallization. After filtration, pink needle-shaped crystals were obtained in 24h and washed with MeOH. Anal. calc. $C_{24}H_{24}CoN_{14}O_6$ (663.48): C, 43.45; H, 3.65; N, 29.56%. Found: C, 42.77; H, 3.84; N, 28.32%.

Synthesis of $[Zn(btix)_2(NO_3)_2]_n$ (10): 10 was synthesized in a procedure analogous to that of **9** except that $Zn(NO_3)_2 \cdot 6H_2O$ (120.0 mg, 0.4 mmol) was used instead. Colourless block-shaped crystals were filtered off and washed with MeOH. Anal. calc. $C_{24}H_{24}ZnN_{14}O_6$ (669.94): C, 42.52; H, 4.76; N, 28.92%. Found: C, 42.66; H, 3.64; N, 28.74%.

Synthesis of $[Zn_{(0.98)}Co_{(0.02)}(btix)_2(NO_3)_2]_n$ (11): 11 was synthesized in a procedure analogous to that of **9** except that a mixture of $Zn(NO_3)_2 \cdot 6H_2O$ (116.6 mg, 0.392 mmol) and $Co(NO_3)_2 \cdot 6H_2O$ (2.4 mg, 0.008mmol) was used. Light-pink block-shaped crystals were filtered off and washed with MeOH. Phase purity was established by X-ray powder diffraction.

4.4.2 Structural characterization

4.4.2.I Single crystal X-ray diffraction for 6, 7, 9 and 10.

Single crystals of compounds **6**, **7**, **9** and **10** were mounted on glass fibres using a viscous hydrocarbon oil to coat the crystal and then transferred directly to the cold nitrogen stream for data collection. X-ray data were collected at 120 K on a Supernova diffractometer equipped with a graphite-monochromated Enhance (Mo) X-ray Source

(λ = 0.71073 Å) at ICMol (University of Valencia). The program CrysAlisPro, Oxford Diffraction Ltd., was used for unit cell determinations and data reduction. Empirical absorption correction was performed using spherical harmonics, implemented in the SCALE3 ABSPACK scaling algorithm. Crystal structures were solved and refined against all F^2 values using the SHELXTL suite of programs.[22] Non-hydrogen atoms were refined anisotropically (except the disordered fragments) and hydrogen atoms were placed in calculated positions that were refined using idealized geometries (riding model) and assigned fixed isotropic displacement parameters except for those of water molecules, which were located and refined with distance restraints. In **6** and **7**, the (non-coordinated) NO_3^- anions are disordered over two sites and have been modeled with 51.2(13):48.8(13) and 62(4):38(4) ratios respectively. In **9** and **10**, the (coordinated) NO_3^- anions are disordered over two sites and have been modeled with 51.9(3):48.1(3) and 51.2(4):48.8(4) ratios respectively. In addition, the benzene moiety of the btix ligand in compound **9** is disordered over two sites and have been modeled with a 53.2(19):46.8(19) ratio. A summary of the data collection and structure refinements is provided in table 4.2.

4.4.2.II X-ray powder diffraction.

Phase purity. Polycrystalline samples of **7** and **10** were lightly ground in an agate mortar and pestle and filled into 0.7 mm borosilicate capillaries. Data were collected at room temperature in the 2θ range 2 – 50 º on an Empyrean PANalytical powder diffractometer, using Cu K_α radiation (λ = 1.54177 Å) at ICMol (University of Valencia). Pawley refinements[23] were performed using the TOPAS computer program[24]

Table 4.2 Crystallographic data for compounds for compounds **6**, **7**, **8** and **9**.

Compound	**6**	**7**	**9**	**10**
Empirical formula	$C_{24}H_{32}N_{14}O_{10}Co$	$C_{24}H_{32}N_{14}O_{10}Zn$	$C_{24}H_{24}N_{14}O_6Co$	$C_{24}H_{24}N_{14}O_6Zn$
Formula weight	735.57	742.01	663.50	669.94
Crystal colour	Pink	Colourless	Pink	Colourless
Crystal size (mm^3)	0.10 × 0.10 × 0.10	0.20 × 0.10 × 0.10	0.14 × 0.12 × 0.04	0.16 × 0.08 × 0.04
Temperature (K)	120(2)	120(2)	120(2)	120(2)
Crystal system, Z	Triclinic, 1	Triclinic, 1	Monoclinic, 2	Monoclinic, 2
Space group	$P\bar{1}$	$P\bar{1}$	$P2_1/c$	$P2_1/c$
a (Å)	9.0395(10)	9.0695(7)	8.2019(5)	8.1968(3)
b (Å)	9.3091(10)	9.3491(7)	20.7198(11)	20.7210(9)
c (Å)	10.5172(12)	10.5511(8)	8.4751(5)	8.4639(3)
α (°)	80.840(9)	80.933(6)	90	90
β (°)	76.092(10)	75.831(7)	105.604(6)	105.358(4)
γ (°)	61.651(11)	61.733(8)	90	90
V ($Å^3$)	754.99(14)	763.08(10)	1387.19(14)	1386.22(9)
ρ_{calc} (Mg/m^3)	1.618	1.615	1.588	1.605
$\mu(Mo_{K\alpha})$ (mm^{-1})	0.650	0.885	0.688	0.955
θ range (°)	2.61 – 27.57	2.48 – 29.13	2.58 – 27.53	1.97 – 27.50
Reflns collected	10922	17419	10941	9927
Independent reflns (R_{int})	3232 (0.0865)	4114 (0.0858)	3176 (0.0642)	3172 (0.00489)
Reflns used in refinement, n	3232	4114	3176	3172
L. S. parameters, p/ restraints, r	233/4	263/4	200/0	233/0
$R1(F)$,[a] $I>2\sigma(I)$	0.0538	0.0394	0.0378	0.0422
$wR2(F^2)$,[b] all data	0.1245	0.0599	0.0624	0.0860
$S(F^2)$,[c] all data	0.964	0.777	0.785	1.141

[a] $R1(F) = \Sigma(|F_O| - |F_C|)/\Sigma|F_O|$; [b] $wR2(F^2) = [\Sigma w(F_O^2 - F_C^2)^2/\Sigma wF_O^4]^{1/2}$; [c] $S(F^2) = [\Sigma w(F_O^2 - F_C^2)^2/((n + r - p)]^{1/2}$

4.4.3 Physical measurements.

Thermogravimetric analysis. Thermogravimetric analysis of **6** and **9** were carried out with a Mettler Toledo TGA/SDTA 851 apparatus at ICMol (University of Valencia) in the 25–800 °C temperature range under a 10 °C·min^{-1} scan rate and an air flow of 30 mL·min^{-1}. In addition, thermogravimetric analysis of compound **6** was also performed at a fixed temperature of 80 ºC.

Magnetic measurements. Magnetic susceptibility measurements were performed on single-phased polycrystalline samples of **6** and **9** with a Quantum Design SQUID magnetometer at ICMol (University of Valencia). The susceptibility data were corrected from the diamagnetic contributions as deduced by using Pascal's constant tables. The d.c. data were collected in the range 2–300 K for decreasing temperatures with an applied field of 1000 G. Electron paramagnetic resonance spectroscopy was recorded with a Bruker ELEXYS E580 spectrometer operating in the X-band (9.47 GHz).

4.5 REFERENCES

1. Representative examples of MOFs using rigid ligands: a) Eddaoudi, M., Kim, J., Rosi, N., Vodak, D., Wachter, J., O'Keeffe, M. and Yaghi, O. M. *Science* **2002**, *295*, 469. b) Chun, H., Dybtsev, D. N., Kim, H. and Kim, K. *Chem.–Eur. J.* **2005**, *11*, 3521. c) Moulton, B., Abourahma, H., Bradner, M. W., Lu, J., McManus, G. J. and Zaworotko, M. J. *Chem. Commun.* **2003**, 1342. d) Férey, G., Mellot-Draznieks, C., Serre, C., Millange, F., Dutour, J., Surblé. S. and Margiolaki, I. *Science*, **2005**, *309*, 2040. e) Chui, S. S. Y., Lo, S. M. F., Charmant, J. P. H., Orpen, A. G. and Williams, I. D. *Science*, **1999**, *283*, 1148. f) Bradshaw, D., Prior, T. J., Cussen, E. J., Claridge, J. B. and Rosseinsky, M. J. *J. Am. Chem. Soc*. **2004**, *126*, 6106. g) Chae, H. K., Siberio-Pérez, D. Y., Kim, J., Go, Y., Eddaoudi, M., Matzger, A. J., O'Keeffe, M. and Yaghi, O. M. *Nature*, **2004**, *427*, 523. h) Lin, X., Jia, J., Zhao, X., Thomas, K. M., Blake, A. J., Walker, G. S., Champness, N. R., Hubberstey, P. and Schröder, M. *Angew. Chem., Int. Ed*., **2006**, *45*, 7358. i) Lin, X., Blake, A. J., Wilson, C., Sun, X. Z., Champness, N. R., George, M. W., Hubberstey, P., Mokaya, R. and Schröder, M. *J. Am. Chem. Soc*. **2006**, *128*, 10745. j) Sava, D. F., Kravtsov, V., Nouar, F., Wojtas, L., Eubank, J. F. and Eddaoudi, M. *J. Am. Chem. Soc.* **2008**, *130*, 3768. k) Caskey, S. R., Wong-Foy, A. G. and Matzger, A. J. *J. Am. Chem. Soc.* **2008**, *130*, 10870.
2. a) Pigge, F. C. *CrystEngComm* **2011**, *13*, 1733. b) Fletcher, A. J., Thomas, K. M. and Rosseinsky, M. J. *J. Solid State Chem.* **2005**, *178*, 2491.
3. Representative examples of MOFs using flexible ligands: a) Zhao, X., Xiao, B., Fletcher, A. J., Thomas, K. M., Bradshaw, D. and Rosseinsky, M. J. *Science* **2004**, *306*, 1012. b) Hawxwell, S. M., Mínguez Espallargas, G., Bradshaw, D., Rosseinsky, M. J., Prior, T. J., Florence, A. J., van de Streek, J. and Brammer, L. *Chem. Commun*. **2007**, 1532. c) Yang, W., Lin, X., Blake, A. J., Wilson, C., Hubberstey, P., Champness, N. R. and Schröder, M. *Inorg. Chem.* **2009**, *48*, 11067. d) Qiu, W., Perman, J. A., Wojtas, Ł., Eddaoudi, M. and Zaworotko, M. J. *Chem. Commun.* **2010**, *46*, 8734. e) Xie, L.-H. and Suh, M. P. *Chem. Eur. J.* **2011**, *17*, 13653. f) Choi, H.-S. and Suh, M. P. *Angew. Chem. Int. Ed*. **2009**, *48*, 6865. g) Rebilly, J.-N., Bacsa, J. and Rosseinsky, M. J. *Chem. Asian J.* **2009**, *4*, 892. h) Ghosh, S. K., Azhakar, R. and Kitagawa, S. *Chem. Asian J.* **2009**, *4*, 870. i) Hauptvogel, I. M., Biedermann, R., Klein, N., Senkovska, I., Cadiau, A., Wallacher, D., Feyerherm, R. and Kaskel, S. *Inorg. Chem*. **2011**, *50*, 8367.
4. Horike, S., Shimomura, S. and Kitagawa, S. *Nature Chem*. **2009**, *1*, 695.
5. a) Maspoch, D., Ruiz-Molina, D. and Veciana, J. *J. Mater. Chem.* **2004**, *14*, 2713. b) Dechambenoit, P. and Long, J. R. *Chem. Soc. Rev.* **2011**, *40*, 3249. c) Halder, G. J., Kepert, C. J., Moubaraki, B., Murray, K. S. and Cashion, J. D. *Science* **2002**, *298*, 1762. d) Ohba, M., Yoneda, K., Agustí, G., Muñoz, M. C., Gaspar, A. B., Real, J. A., Yamasaki, M., Ando, H., Nakao, Y., Sakaki, S. and Kitagawa, S. *Angew. Chem. Int. Ed.* **2009**, *48*, 4767. e) Agustí, G., Ohtani, R., Yoneda, K., Gaspar, A. B., Ohba, M., Sánchez-Royo, J. F., Muñoz, M. C., Kitagawa, S. and Real, J.

A. *Angew. Chem. Int. Ed*. **2009**, *48*, 8944. f) Kurmoo, M., Kumagai, H., Chapman, K. W. and Kepert, C. J. *Chem. Commun.* **2005**, 3012. g) Motokawa, N., Matsunaga, S., Takaishi, S., Miyasaka, H., Yamashita, M. and Dunbar. K. R. *J. Am. Chem. Soc*. **2010**, *132*, 11943.

6. a) Ferey, G. and Serre, C. *Chem. Soc. Rev*. **2009**, *38*, 1380.
7. a) Barthelet, K., Marrot, J., Riou, D. and Férey, G. *Angew. Chem., Int. Ed*. **2002**, *41*, 281. b) Serre, C., Millange, F., Thouvenot, C., Nogues, M., Marsolier, G., Louer, D. and Ferey, G. *J. Am. Chem. Soc.* **2002**, *124*, 13519. c) Loiseau, T., Serre, C., Huguenard, C., Fink, G., Taulelle, F., Henry, M., Bataille, T. and Ferey, G. *Chem.–Eur. J.* **2004**, *10*, 1373. d) Liu, Y., Her, J. H., Dailly, A., Ramirez-Cuesta, A. J., Neumann, D. A. and Brown, C. M. *J. Am. Chem. Soc.* **2008**, *130*, 11813. e) Trung, T. K., Trens, P., Tanchoux, N., Bourrelly, S., Llewellyn, P. L., Loera-Serna, S., Serre, C., Loiseau, T., Fajula, F. and Férey, G. *J. Am. Chem. Soc*. **2008**, *130*, 16926. f) Finsy, V., Kirschhock, C. E., Vedts, G., Maes, M., Alaerts, L., De Vos, D. E., Baron, G. V. and Denayer, J. F. *Chem.–Eur. J.* **2009**, *15*, 7724. g) Walker, A. M., Civalleri, B., Slater, B., Mellot-Draznieks, C., Cora, F., Zicovich-Wilson, C. M., Roman-Perez, G., Soler, J. M. and Gale, J. D. *Angew. Chem., Int. Ed.* **2010**, *49*, 7501. h) Matsuda, R., Kitaura, R., Kitagawa, S., Kubota, Y., Kobayashi, T. C., Horike, S. and Takata, M. *J. Am. Chem. Soc.*, **2004**, *126*, 14063. i) Salles, F., Ghoufi, A., Maurin, G., Bell, R. G., Mellot-Draznieks, C. and Férey, G. *Angew. Chem. Int. Ed.* **2008**, *47*, 8487. j) Motkuri, R. K., Thallapally, P. K., Nune, S. K., Fernandez, C. A., McGrail, B. P. and Atwood, J. L. *Chem. Commun*. **2011**, *47*, 7077.
8. a) Chen, C., Sun, J.-K., Li, W., Chen, C.-N. and Zhang, J. *Chem. Commun*., **2011**, ***47***, 6683. b) Ghosh, S. K., Kaneko, W., Kiriya, D., Ohba, M. and Kitagawa, S. *Angew. Chem. Int. Ed.* **2008**, *47*, 8843. c) Libri, S., Mahler, M., Mínguez Espallargas, G., Singh, D. C. N. G., Soleimannejad, J., Adams, H., Burgard, M. D., Rath, N. P., Brunelli, M. and Brammer, L. *Angew. Chem. Int. Ed*. **2008**, *47*, 1693. d) Bradshaw, D., Warren, J. E. and Rosseinsky, M. J. *Science* **2007**, *315*, 977. e) Niel, V., Thompson, A. L., Muñoz, M. C., Galet, A., Goeta, A. E. and Real, J. A. *Angew. Chem. Int. Ed.* **2003**, *42*, 3760. f) Mínguez Espallargas, G., Brammer, L., van de Streek, J., Shankland, K., Florence, A. J. and Adams, H. *J. Am. Chem. Soc.* **2006**, *128*, 9584. g) Mínguez Espallargas, G., Hippler, M., Florence, A. J., Fernandes, P., van de Streek, J., Brunelli, M., David, W. I. F., Shankland, K. and Brammer, L. *J. Am. Chem. Soc.* **2007**, *129*, 15606. h) Mínguez Espallargas, G., van de Streek, J., Fernandes, P., Florence, A. J., Brunelli, M., Shankland, K. and Brammer, L. *Angew. Chem. Int. Ed.* **2010**, *49*, 8892.
9. a) Coronado, E., Giménez-Marqués, M., Mínguez Espallargas, G. and Brammer, L. *Nature Commun.* **2012***, 3,* 828. b) Kaneko, W., Ohba, M. and Kitagawa, S. *J. Am. Chem. Soc*. **2007**, *129*, 13706. c) Cheng, X.-N., Zhang, W.-X. and Chen, X.-M., *J. Am. Chem. Soc*. **2007**, *129*, 15738. d) Duan, Z., Zhang, Y., Zhang, B. and Zhu, D. *J. Am. Chem. Soc.* **2009**, *131*, 6934. e) Hu, C. and

Englert, U. *Angew. Chem., Int. Ed*. **2005**, *44*, 2281. f) Ghosh, S. K., Zhang, J.-P. and Kitagawa, S. *Angew. Chem., Int. Ed.* **2007**, *46*, 7965.

10. Leong, W. L.; Vittal, J. J. *Chem. Rev.* **2011**, *111*, 688.
11. a) Lauher, J. W., Fowler, F. W. and Goroff, N. S. *Acc. Chem. Res*. **2008**, *41*, 1215. b) Halder, G. J. and Kepert, C. J. *Aust. J. Chem*. **2006**, *59*, 597. c) Halasz, I. *Cryst. Growth Des*. **2010**, *10*, 2817.
12. Vittal, J. J. *Coord. Chem. Rev*. **2007**, *251*, 1781.
13. a) Matsuda, R., Kitaura, R., Kitagawa, S., Kubota, Y., Belosludov, R. V., Kobayashi, T. C., Sakamoto, H., Chiba, T., Takata, M., Kawazoe, Y. and Mita, Y. *Nature* **2005**, *436*, 238. b) Kawano, M., Haneda, T., Hashizume, D., Izumi, F. and Fujita, M. *Angew. Chem. Int. Ed*. **2008**, *47*, 1269. c) Ohara, K., Martí-Rujas, J., Haneda, T., Kawano, M., Hashizume, D., Izumi, F. and Fujita, M. *J. Am. Chem. Soc.* **2009**, *131*, 3860. d) Fujii, K., Lazuen Garay, A., Hill, J., Sbircea, E., Pan, Z., Xu, M., Apperley, D. C., James, S. L. and Harris, K. D. M. *Chem. Commun*. **2010**, *46*, 7572. e) Martí-Rujas, J., Islam, N., Hashizume, D., Izumi, F., Fujita, M., Jae Song, H., Choi, H. C. and Kawano, M. *Angew. Chem. Int. Ed*. **2011**, *50*, 6105. f) Martí-Rujas, J., Islam, N., Hashizume, D., Izumi, F., Fujita, M. and Kawano, M. *J. Am. Chem. Soc.* **2011**, *133*, 5853.
14. Rabone, J., Yue, Y.-F., Chong, S. Y., Stylianou, K. C., Bacsa, J., Bradshaw, D., Darling, G. R. Berry, N. G., Khimyak, Y. Z., Ganin, A. Y., Wiper, P., Claridge, J. B. and Rosseinsky, M. J. *Science* **2010**, *329*, 1053.
15. Y. Milon, J., Daniel, M.-C., Kaiba, A., Guionneau, P., Brandes, S. and Sutter J.-P. *J. Am. Chem. Soc.* **2007**, *129*, 13872**.**
16. *Magneto-Structural Correlations in Exchange Coupled Systems*, Willett R. D., Gatteschi D., Kahn O., Eds. Reidel, Dordrecht, **1985**, 241.
17. Zhang, S.-Y., Zhang, Z.-J., Shi, W., Zhao, B., Cheng, P., Liao, D.-Z. and Yan, S.-P. *Dalton Trans.* **2011**, *40*, 7993.
18. An, J. and Rosi, N. L. *J. Am. Chem. Soc.* **2010**, *132*, 5578
19. (a) Ghosh, S. K., Kaneko, W., Kiriya, D., Ohba, M. and Kitagawa, S. *Angew. Chem. Int. Ed*. **2008**, *47*, 8843. (b) Tanaka, D., Nakagawa, K., Higuchi, M., Horike, S., Kubota, Y., Kobayashi, T. C., Takata, M. and Kitagawa, S. *Angew. Chem. Int. Ed*. **2008**, *47*, 3914.
20. a) Banci, L., Bencini, A., Benelli, C., Gatteschi, D., and Zanchini, C. Spectral-Structural Correlations in High-Spin Cobalt(II) Complexes. Structure & Bonding, 1982, Vol. 52, 37–86, Springer-Verlag Berlin Heidelberg. b) Abragam, A., Pryce, M. H. L. *Proc. R. Soc*. *Lond. A* **1951**, *206*, 173.
21. Meng, X., Song, Y., Hou, H., Han, H., Xiao, B., Fan, Y. and Zhu, Y. *Inorg. Chem*. **2004**, *43*, 3528.
22. Sheldrick, G. M. *Acta Crystallogr., Sect. A: Found. Crystallogr*. **2008**, *64*, 112.
23. Pawley, G. S. *J. Appl. Cryst*. **1981**, *14*, 357.
24. Coelho, A. A. TOPAS-Academic, Version 4.1, **2007**, see: http:// www.topas-academic.net

5

CHEMICALLY-DRIVEN SOLID-STATE TRANSFORMATIONS IN COORDINATION POLYMERS

5.1 INTRODUCTION

Since the origin of molecular magnetism, physical stimuli, such as pressure, temperature or light, have been widely used to modulate the magnetic properties of molecules and CPs (see *Chapter 4*).[1] The use of chemical stimuli for this purpose has also been achieved.[2] The most studied solid-state transformations through chemical modifications in CPs are, among others, those involving solvent effects or post-synthetic modifications.[3] In particular, post-synthetic variation of CPs have been used as an interesting approach to produce functionalized materials. Specifically, the chemical post-synthetic modifications of extended frameworks are mainly focused on the modification of the organic ligand, with minor changes in the connectivity of the metal centres, for which examples are scarce.[4] A different type of chemical modification of particular interest is that involving ion exchange process, which is an extensively studied non-covalent post-synthetic chemical modification of CPs.[5] The first example of anion exchange in an extended network was published by Hoskins and Robson at the beginning of the 90's (see figure 5.1).[5a] It was then demonstrated that crystals of CPs could undergo ready anion exchange in the crystalline state. More recently, this chemical modification has been shown as an effective way to tune gas sorption[6] and for anion recognition in more complex smart-materials.[7] Typically, the ions are trapped in the pores of the CPs and are weakly bonded to the (ionic) framework through weak interactions. In these cases, ion exchange often occurs in a single-crystal-to-single-crystal (SCSC) manner since non-coordinated ions can be easily exchanged without massive perturbation of the network.

A particularly interesting case of anion exchange is that involving metal-coordinated anions in a CP.[8] This anion exchange is of remarkable significance since, occurring quantitatively in the solid state, gives rise to drastic changes in covalent bonds that involves the structural transformation. As expected, this exchange process often yields a polycrystalline powder since cleavage and formation of coordination bonds usually provoke breaks in the single crystals. Nevertheless, to obtain a SCSC transformation in anion exchange processes could in principle be feasible even with major changes in

covalent bonds, as it occurs with gas sorption processes of non-porous systems, as has been demonstrated in *Chapter 2*. However, no examples of SCSC transformations involving metal-coordinated anions in a CP have been reported yet.

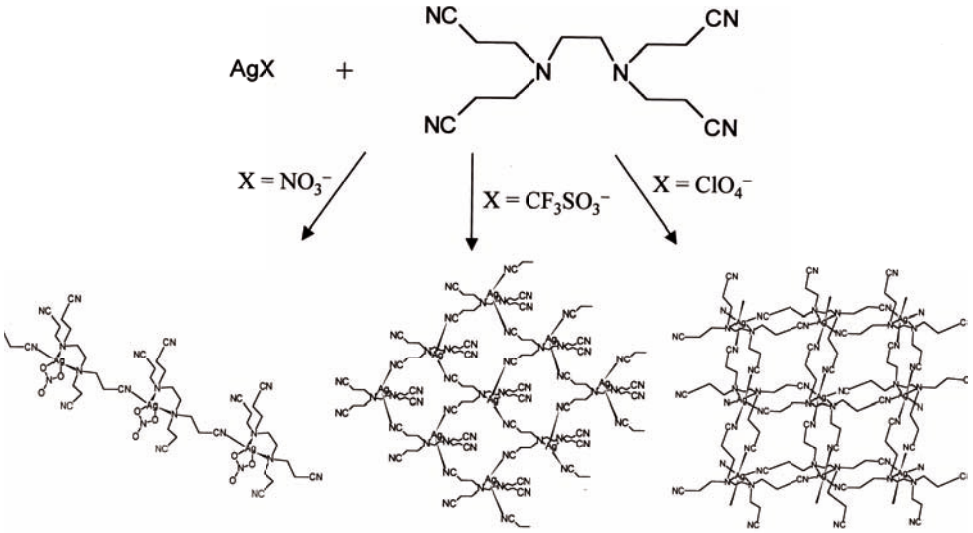

Figure 5.1 Schematic representation of the first example of ion exchange in the solid state involving metal-coordinated anions in a CP. Adapted from ref 8a.

The scope of this Chapter is to analyse the structural transformations that occur in a magnetic CP upon anion exchange and then to study the effect on the magnetic properties. In particular a flexible three-dimensional (3D) CP, $[Cu(btix)_2(BF_4)_2]_n$ (**12**) (btix = 1,4-bis(triazol-1-ylmethyl)benzene), with antiferromagnetic interactions occurring via the organic ligand has been synthesized and characterized. Coordinated BF_4^- anions can be reversibly exchanged by different anions with retention (PF_6^-, ClO_4^-) or modification (NO_3^-, Cl^-) of the network. However, an irreversible exchange occurs with N_3^- anions to generate a new CP, $[Cu(btix)(N_3)_2]_n$ (**17**), whose structure has been determined *ab initio* by X-ray powder diffraction revealing that not only a change in the configuration of the organic ligand occurs, but a totally different connectivity between the Cu^{II} centers is found, which now involves both the organic and the inorganic ligands. As expected, this structural transformation is accompanied with a change of the magnetic properties, which have been detected by EPR and magnetic susceptibility measurements.

5.2 RESULTS AND DISCUSSION

5.2.1 Description of the structures

Crystal structure of *trans*-[Cu(btix)$_2$(BF$_4$)$_2$]$_n$ (12). The reaction of Cu(BF$_4$)$_2$·xH$_2$O and btix in MeOH results in the formation of block-shaped crystals of formula *trans*-[Cu(btix)$_2$(BF$_4$)$_2$]$_n$ (**12**).[9] Single crystal X-ray analysis of compound **12** reveals that it is composed of a three-dimensional network that crystallizes in the monoclinic *C*2/*c* space group (figure 5.2). In this CP, the ligand adopts two different conformations, *syn* and *anti.* The asymmetric unit contains one crystallographycally independent Cu^{II} ion which lies on an inversion center, one *syn*-btix and one *anti*-btix ligands and a coordinated BF$_4^-$ anion. Each metal ion is coordinated by four triazole nitrogen atoms derived from two *syn*-btix and two *anti*-btix ligands in the equatorial positions and two fluor atoms from two BF$_4^-$ anions in the apical positions. The coordination environment of the Cu^{II} ions features a slightly distorted octahedron with Cu–N distances of 2.006(6) and 2.000(6) Å and a longer Cu–F distance of 2.422(5) Å, as a result of the Jahn-Teller elongation along the Cu–F bonds and of the weak coordination ability of this anion.[10] The bond angles slightly deviate from the idealized octahedron geometry (see table 5.1). All btix ligands act as bridges between adjacent metal centres leading to Cu···Cu distances of 9.940(17) and 14.112(11) Å. Thus, compound **12** consists of a neutral three-dimensional network with a very unusual coordination of BF$_4^-$ anions. The BF$_4^-$ anion is commonly described as a non-coordinated anion[10] with a coordination ability index, a^{TM}, of –1.1, indicative of a poor tendency to coordinate. Interestingly, each Cu centre is bonded to two BF$_4^-$ anions in *trans* positions by Cu−FBF$_3$ coordination bonds. The parameter a^{TM} is defined as log $(c+s)/u$,[10] where c, s and u are the number of structures with the group coordinated, semicoordinated and uncoordinated, respectively. A positive value of a^{TM} indicates that the group has more chance to coordinate to a transition metal atom than to remain uncoordinated in its presence (the larger the positive value of a, the greater its coordinating ability). On the other hand, large negative values of a indicate a poor tendency to coordinate). The three-dimensional structure can be described as chains

further linked in the other two directions. In this view, the *syn*-btix ligands link the Cu centres forming an undulating chain along the [10-1] direction (see figure 5.2b), which is connected to four neighbouring chains via the *anti*-btix ligands in an alternated fashion: each Cu centre of the undulating chain is connected to two chains, but two consecutive Cu centres do not connect the same two chains (see figures 5.2c and 5.2d).

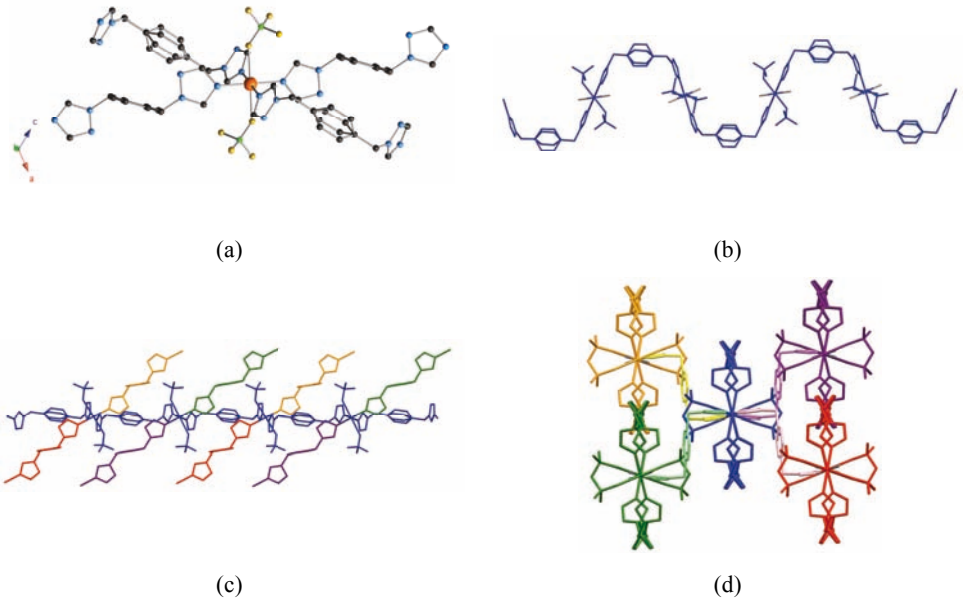

Figure 5.2 (a) Coordination environment of the Cu^{II} centres in **12**, showing the connection to two *syn*-btix, two *anti*-btix and two BF_4^- anions (copper, nitrogen, carbon, boron and fluorine are coloured orange, blue, black, green and yellow, respectively); (b) undulating chain along the [10-1] direction formed by *syn*-btix ligands; (c) top view of the undulating chain (in blue) showing the *anti*-btix ligands that connect with four adjacent chains (colours of the *anti*-btix refer to the colours of the different undulating chain in d) to which they connect); (d) front view of the central chain (in blue) and its four adjacent chains (in red, violet, green and yellow). Hydrogen atoms have been omitted in all figures for clarity.

Crystal structures of *trans*-$[Cu(btix)_2(X)_2]_n$ (13, X = ClO_4) and (14, X = PF_6). The direct anion exchange of crystalline powder samples of **12** also affords crystalline powders **13** and **14** (see section 5.2.2). XRPD analysis of the crystalline powders **13**

and **14** reveal that the crystal structures are analogous to that of **12** (see previous section for a detailed description of the networks)

Crystal structures of $[Cu(btix)_2(X)_2]_n$ (15, X = NO_3) and (16, X = Cl).[9] Crystalline powders **15** and **16** are obtained by direct anion exchange of crystalline powder samples of **12** (see section 5.2.2). XRPD studies of crystalline powders of **15** and **16** reveal that both compounds are isostructural (see section 5.2.4). Previously reported single crystal X-ray studies of **16** reveals that crystallizes in the triclinic $P2_1/c$ space group. The asymmetric unit of **16** contains one crystallographycally independent Cu^{II} ion which lies on an inversion centre, two *anti*-btix ligands and two chloride atoms (figure 5.3). Each metal centre is coordinated to four nitrogen atoms derived from four *anti*-btix ligands in the equatorial positions and two chloride ions occupying the axial positions. In **16** each *anti*-btix ligand acts as a bidentate ligand that bridges two Cu^{II} ions. All Cu^{II} are linked by four *anti*-btix ligands to four Cu^{II} neighbours thus affording a 2D network with (4,4) topology structure. The 2D layers stack in an ABCABC fashion (figure 5.3).

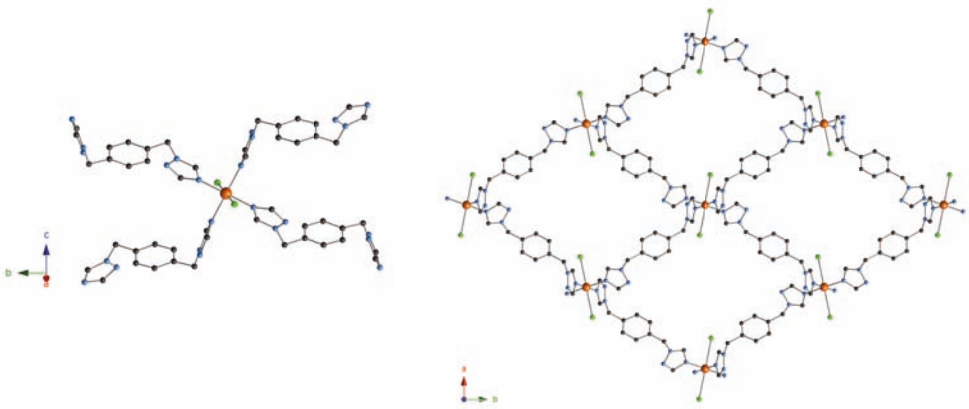

(a) (b)

Figure 5.3 (a) Coordination environment of the Cu^{II} centres in **16**. (b) Crystal structure of **16** showing the 2D grids with (4,4) topology. Copper, nitrogen and carbon, are coloured orange, blue and black, respectively; hydrogen atoms have been omitted for clarity. Compound **15** is isostructural to **16**.

Crystal structure of $[Cu(btix)(N_3)_2]_n$ (17). *Ab initio* solution from X-ray powder diffraction data and Rietveld refinement (see section 5.4.2.III, figure 5.4) show that

compound **17** consists of a two-dimensional network that crystallizes in the monoclinic group *C2/c*. The asymmetric unit contains one crystallographycally independent Cu^{II} located at the 2-fold axis, one *anti*-btix bridging ligand, and two coordinated N_3^- anions with asymmetric end-on bridging mode, resulting in a neutral two-dimensional network (figure 5.4). The metal environment is distorted octahedral: the basal plane is formed by four nitrogen atoms from two coordinated and two semicoordinated azidos, whereas the axial positions are filled by two triazole nitrogen atoms derived from two *anti*-btix (see table 5.1). The Cu–N_{btix} bond length (2.079(5) Å) is similar to those reported for other btix-containing Cu^{II} complexes.[9,11a] The values of the equatorial Cu–N_{az} are 2.036(10) and 2.886(10) Å for coordinated and semicoordinated azido, respectively, indicating an asymmetric azido bridge which leads to Cu···Cu distances of 4.342(8) Å within this chain. The Cu–N_{az}–Cu angle is 122.9(4) º. The azido groups in **17** are essentially linear with a N–N–N bond angle of 179.8(10) º. The two N–N bond distances within the azido groups are significantly different (1.095(10) and 1.113(11) Å), the longer bond involving the end which is coordinated to the metal ion, as expected. The *anti*-btix ligand acts as a bridge between adjacent metal centres leading to Cu···Cu distances of 15.334(1) Å, forming a two-dimensional layer parallel to the (101) plane.

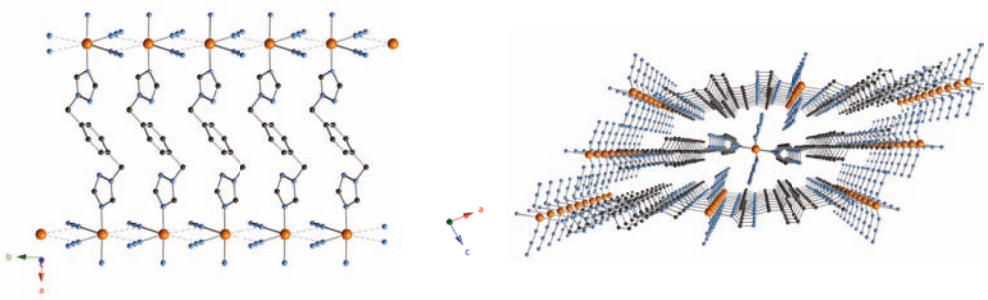

(a) (b)

Figure 5.4 Views of the crystal structure of **17**. (a) One-dimensional azido-bridged chains connected by *anti*-btix ligands showing the octahedral environment of the Cu^{II} centres; (b) two-dimensional layers viewed along the *b* axis. Copper, nitrogen and carbon, are coloured orange, blue and black, respectively; hydrogen atoms have been omitted for clarity.

Table 5.1 Selected bond lengths, distances and angles for **12** and **17**.

	12		**17**
Cu–N (Å)	2.006(6)	Cu–N_{az} (Å)	2.036(10)
	2.000(6)		2.886(10)
Cu–F (Å)	2.422(5)	Cu–N_{btix} (Å)	2.079(5)
Cu···Cu (Å)	9.940(17)	Cu···Cu (Å)	4.342(8)
	14.112(11)		15.334(1)
N–Cu–N (º)	91.90 (22)	N_{az}–Cu–N_{btix} (º)	96.2(3)
	88.10(22)		81.9(3)
	93.73 (21)		
N–Cu–F (º)	89.99 (20)		
F–Cu–F (º)	180		

5.2.2 Anion exchange

The presence of a weakly coordinated BF_4^- anion in compound **12**, together with the insolubility of this polymer in common organic solvents (and water), opens the possibility to explore whether the substitution of this anion could lead to a dynamic response of the network which could modify the magnetic properties. Moreover, the use of the flexible ligand btix, which provides adaptability properties to the framework, is an additional feature that may facilitate the occurrence of the anion exchange. For these reasons, anion exchange experiments have been performed as follows.

Crystalline powder samples of **12** were immersed at room temperature for 1 day in 3 M aqueous solutions containing $NaClO_4$, $NaPF_6$, $NaNO_3$, NaCl, or NaN_3. The BF_4^- anion in **12** is quantitatively exchanged with ClO_4^- (**13**), PF_6^- (**14**), NO_3^- (**15**), Cl^- (**16**) and N_3^- (**17**) accompanied with a colour change from purple to different blues for polymers **13**–**16** and a remarkably colour change to dark green in polymer **17**. All products **13**–**17** have been identified by elemental analysis (EA), infra-red

spectroscopy (IR) and X-ray powder diffraction (XRPD). Reversibility of the anion exchange was also examined by immersion of the exchanged products in 3 M $NaBF_4$ for 1 day. The ClO_4^-, PF_6^- and Cl^- anions in polymers **13**, **14** and **16** are quantitatively exchanged with BF_4^- and therefore reconverted into **12**. However, the NO_3^- anion in **15** is only partially exchanged even when the solid is immersed in a 3 M $NaBF_4$ solution for 3 days.

It is important to remark that this anion exchange could also be a solvent mediated process, as proposed by Khlobystov, Champness, Schröder and co-workers,[12] who have shown that the degree of reversibility of some solvent-induced anion-exchange transformations is determined by the ratio of the solubility product constants for the starting and resultant complexes.

Elemental analysis. EA provides information about the stoichiometry of the exchanged products. Table 5.2 summarizes the experimental EA for **12–17** in comparison with the theoretical expected values. Thus, although minor discrepancies are observed in some cases (*ca.* 1 %), compounds **13–16** show clearly a 1:2:2 ratio in Cu:btix:anion, whereas this ratio is 1:1:2 for compound **17**.

Table 5.2 Table of Elemental analysis for compounds **12–17.**

Compound		C [%]	H [%]	N [%]
12	exptl	38.59	3.32	22.92
	calcd	40.17	3.37	23.42
13	exptl	37.59	3.43	21.88
	calcd	38.30	3.26	22.62
14	exptl	36.91	3.18	21.54
	calcd	34.56	2.90	20.15
15	exptl	41.39	3.55	27.27
	calcd	43.15	3.62	29.35
16	exptl	46.21	3.90	26.94
	calcd	46.87	3.93	27.33
17	exptl	37.53	3.19	42.17
	calcd	37.16	3.12	43.34

IR studies. IR studies result of particular importance, since they afford valuable information of the exchange processes. This is mainly due to the large variations of the IR spectra of different structures but, most importantly, of different anions.

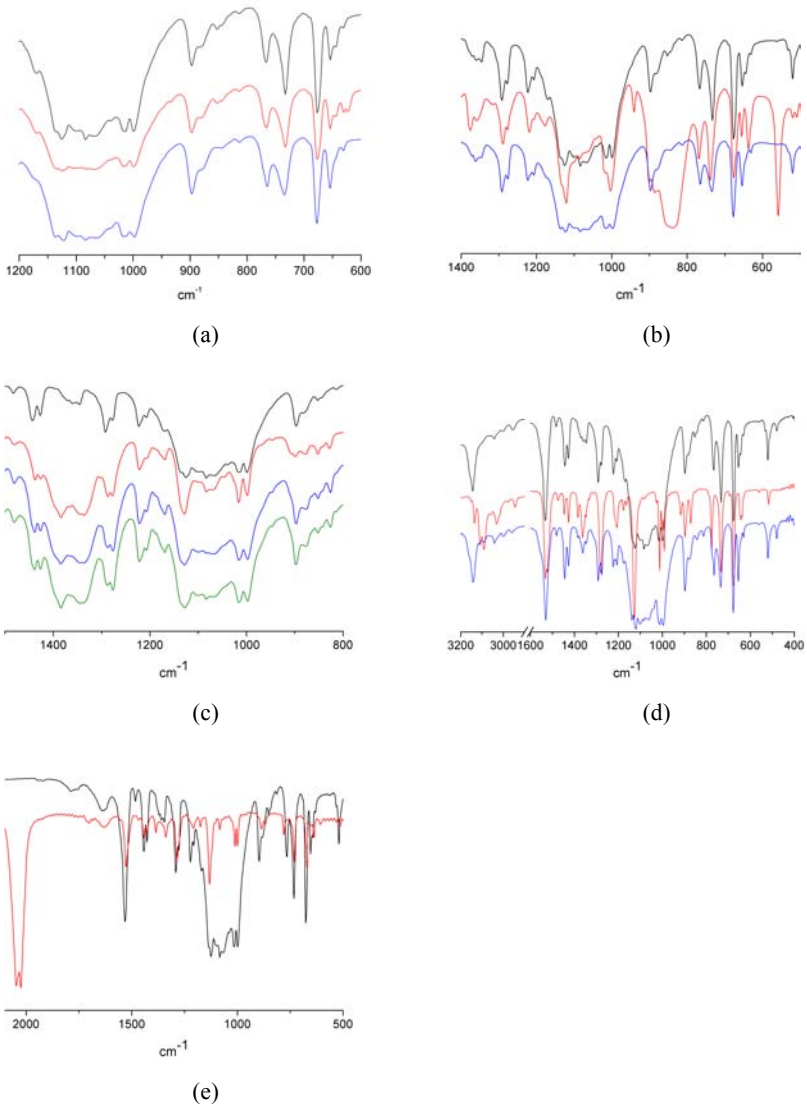

Figure 5.5 Infra-red spectra of the pristine materials (with BF_4^-), shown in black, after anion exchange, shown in red, and recovered materials (shown in blue and green after immersion for 1 day and 3 days, respectively): (a) ClO_4^- (**13**), (b) PF_6^- (**14**), (c) NO_3^- (**15**), (d) Cl^- (**16**) and (e) N_3^- (**17**).

The anion exchange processes and their possible reversibility have been monitored using IR spectroscopy by detecting the disappearance and further appearance of a strong IR peak at 1084 cm^{-1} (characteristic of the BF_4^- anion).

Basically, in the IR spectra of products **13–17**, new stretching vibrations corresponding to ClO_4^- (1105–1120 and 623 cm^{-1}), PF_6^- (839 and 558 cm^{-1}), NO_3^- (1384–1337 cm^{-1}), and N_3^- (2046 and 2025 cm^{-1}) clearly appear and then disappear upon reversibility of the process (figure 5.5)[13]. Of particular interest is the exchange process from **12** to **17** which is characterized by the appearance of two new strong peaks at 2046 and 2025 cm^{-1} (distinctive of the N_3^- anion). These peaks appear at lower frequencies than usually expected for $\mu_{1,1'}$-1,1-azido bridging anions in agreement with the highly asymmetrical nature of the azido bridge in the polymer.[14] The appearance of two bands instead of a single band should be related to the presence of two crystallographically independent N_3^- anions. However, only one type of azido can be found in the crystal structure of **17**. This suggests the existence of some degree of disorder in the azido bridging groups that is impossible to model in the Rietveld refinement from powder data.

5.2.3 Structural transformations upon anion exchange

The anion exchange processes studied can be described in terms of the structural transformation that takes place. Thus, depending on the modification occurred in the framework, the CPs obtained could be classified in three main groups:

Group I: Retention of the framework. This is the case of polymers **13** and **14,** which basically maintain the original crystal structure after anion exchange. Thus, immersion in 3 M solutions of $NaPF_6$ or $NaClO_4$ of **12** produces an anion exchange with retention of the crystal structure, as confirmed by XRPD studies (section 5.4.2.II). In this transformation, the ligands preserve their original conformation (see figure 5.6).

Group II: Reduction of the dimensionality. This group corresponds to the transformation in dimensionality from 3D to 2D given in polymers **15** and **16**. Upon exposure of **12** to NO_3^- and Cl^- anions, the anion exchange process induces a

conformational switch of half of the btix ligands from *syn*- conformation to *anti*- conformation, with the formation of a neutral two-dimensional grid with (4,4) topology (see figure 5.6). This transformation requires a rearrangement in the metal environment and implies the cleavage of coordination bonds between Cu^{II} ions and btix ligands, followed by the rotation of btix ligand through the methylene groups to adopt the *anti* conformation and subsequent re-formation of Cu–N bonds.

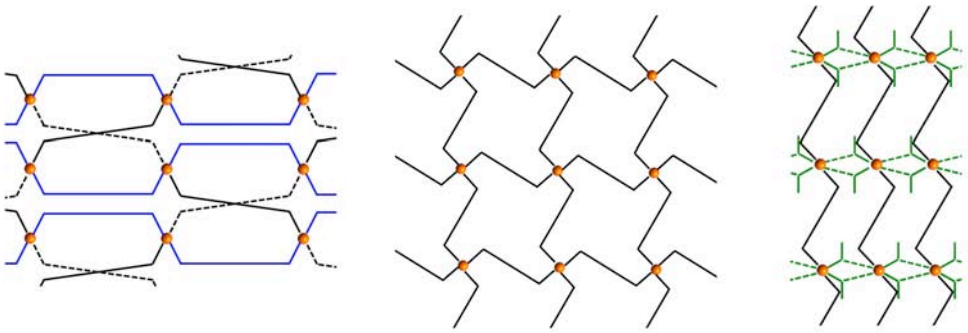

(a) (b) (c)

Figure 5.6 Schematic representation of the three different categories of CPs with the different conformations of the btix ligand: (a) 3D network of compounds **12**, **13** and **14** with I^0O^3 connectivity with half of the btix ligands in *anti*- conformation (represented in black) and half in *syn*- conformation (represented in blue); (b) 2D network of compounds **15** and **16** with I^0O^2 connectivity with all the btix ligands in *anti*- conformation; (c) 2D network of compound **17** with I^1O^1 connectivity with all the btix ligands in *anti*- conformation (green lines represent the inorganic connectivity).

Group III: Complete rearrangement of the network. The most remarkable anion exchange process is the transformation **12→17**, which modifies enormously the connectivity of the metal centres. When crystalline solid **12** is immersed in NaN_3 aqueous solutions, a remarkable colour change from purple to green is instantly observed. During this process a drastic rearrangement of the network occurs due to the exchange of the BF_4^- anions by N_3^- anions, accompanied by lose of one coordinated btix ligand which is transferred to the aqueous solution, whereas the remaining btix ligand remains in *anti*- conformation (see figure 5.6). This elimination of an organic ligand during anion exchange is not unprecedented and has recently been reported.[15] This is an interesting process since it could be applied for the elimination of toxic

azido ligands in aqueous solutions.[16] Nevertheless, given the change in Cu:btix ratio between **12** and **17**, and the gross structural changes, it is likely that the reaction occurs via dissolution of the precursor before (or simultaneously) with crystallization of the final product, analogous to that demonstrated for some anion exchange reactions involving crystalline solids.[12]

The different categories of the exchanged CPs are clearly differentiated following the classification introduced by Cheetham *et al.*,[17] where CPs are categorized by the dimensionality of their inorganic and organic connectivity as I^mO^n, where "I" and "O" refers to the connectivity through the inorganic and organic ligands, respectively, and "m" and "n" refers to the dimensionality of each type of connectivity. Compound **12** falls in the category of I^0O^3, quite common in MOFs. Upon exchange with ClO_4^- (**13**) and PF_6^- (**14**), the dimensionality of the exchanged CPs is maintained as I^0O^3. However, anion exchange to NO_3^- (**15**) and Cl^- (**16**) produces a change in the connectivity to I^0O^2, i.e. the dimensionality is reduced from 3D to 2D without involvement of the inorganic ligand. Furthermore, a conformational change of half of the ligands takes place during the anion exchange, as all btix ligands are found in *anti*-configuration for compounds **15** and **16**. Interestingly, upon exchange to N_3^- (**17**), the rare I^1O^1 topology is found, combining organic and inorganic ligands in the connectivity of the CP (see figure 5.7).

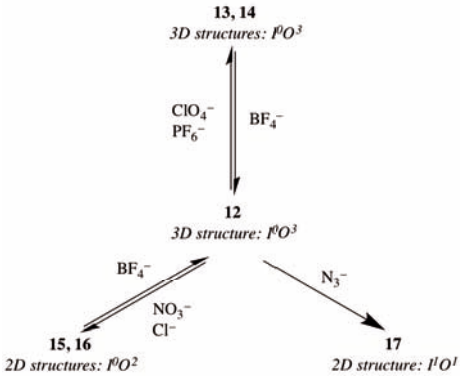

Figure 5.7 Schematic representation of the different transformation upon anion exchange following the dimensionality of their inorganic and organic connectivity as I^mO^n.

Although the number of used anions is limited and it is difficult to extract a definite conclusion, it seems that the modification of the framework upon anion exchange might be related to the coordinating ability of the different anions.[10] Thus, the exchange of the weak coordinating ligand BF_4^- (a^{TM} = –1.1) by the also weak coordinating ligands ClO_4^- (a^{TM} = –0.6) or PF_6^- (a^{TM} = –1.6) does not produce any structural change and the original structure is maintained. However, when more coordinating anions are used, as NO_3^- (a^{TM} = 0.1) and Cl^- (a^{TM} = 1.3) , the structure is slightly modified. Finally, when a highly coordinating ligand as N_3^- (a^{TM} = 2.1) is used, the structure is fully changed due to the strong coordinating tendency of the N_3^- ligand. This difference in coordination ability might also be related with the reversibility of the anion exchange. The less coordinating anions, ClO_4^- and PF_6^- are quantitatively exchanged with BF_4^- and therefore, CPs **13** and **14** easily reconvert into **12**. This idea implies that the more coordinating anions Cl^-, NO_3^- and N_3^- should not be quantitatively exchanged with BF_4^-, as observed in the case of compounds **15** and **17**. However, Cl^- anions are exchanged with BF_4^-, which could be due to the smaller size of the Cl^- anion (that would favour its exit through the channels) as compared with the NO_3^-. However, this could also be a result of differences in solubility of the CPs.[12] As expected, reversibility is unfeasible for polymer **17**, likely due to the strength of the coordinating anion, but also due to the different Cu:btix ratio which would require additional organic ligands in the media for the reverse reaction.

5.2.4 X-ray powder diffraction studies

Phase purity. The phase purity of polycrystalline samples of **12–16** has been investigated by XRPD. A Pawley refinement has been applied to the experimental powder patterns of polycrystalline samples **12–16** and the observed and calculated diffraction patterns are shown in figure 5.8. Pawley refinements revealed an excellent fit to a one-phase model and converged to R_{wp} = 0.0322 with a gof = 1.812 (**12**), R_{wp} = 0.0284 with gof = 1.606 (**13**), R_{wp} = 0.0368 and gof = 2.006 (**14**), R_{wp} = 0.0475 and gof = 2.751(**15**) and R_{wp} = 0.0235 and gof = 2.438 (**16**). In all cases the unit cell obtained from the Pawley refinement is consistent with those obtained for analogous

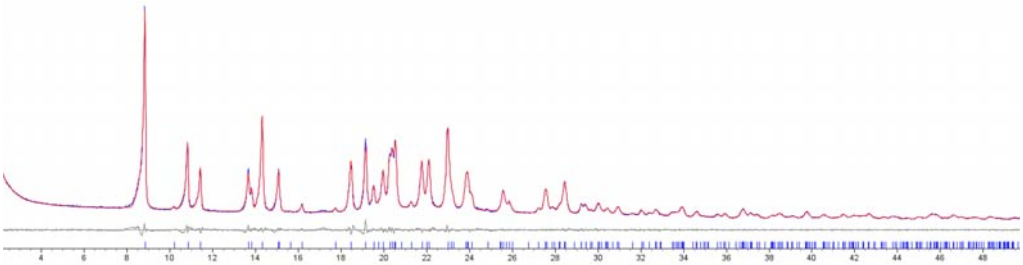

2θ

(a)

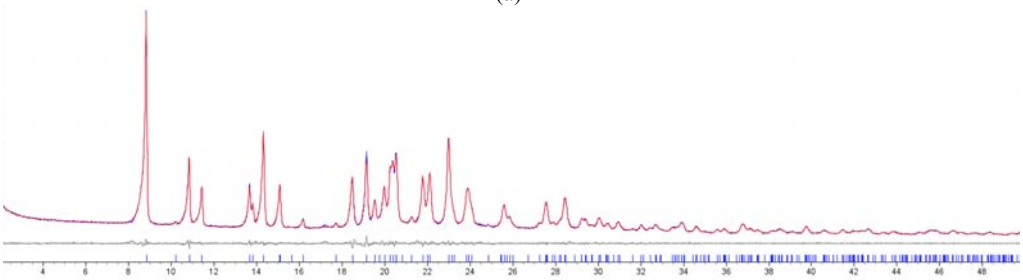

2θ

(b)

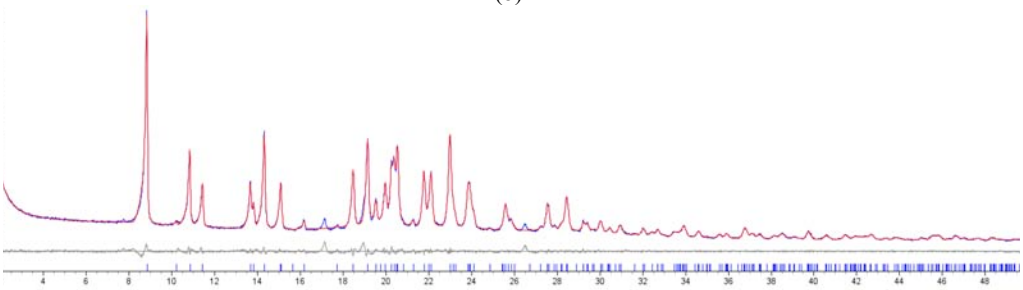

2θ

(c)

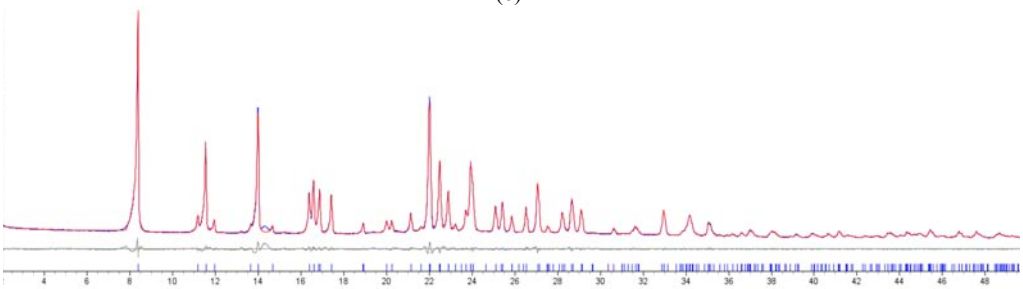

2θ

(d)

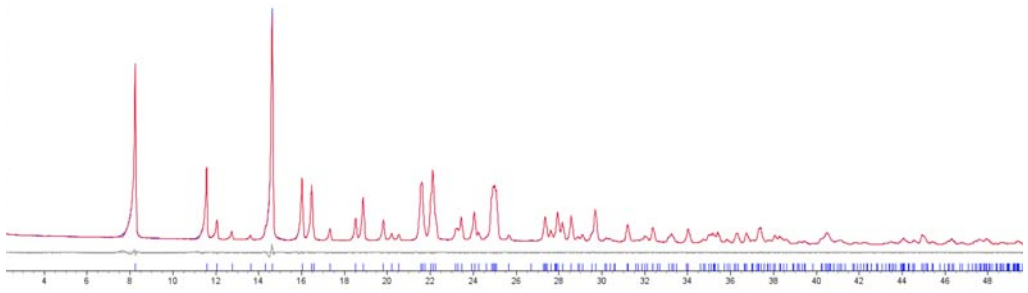

(e)

Figure 5.8 Observed (blue) and calculated (red) profiles and difference plot [($I_{obs} - I_{calcd}$)] (grey) of the Pawley refinements (2θ range 2.0–50.0°; maximum resolution 1.82 Å) for compounds **12** (a), **13** (b), **14** (c), **15** (d) and **16** (e).

structures by single crystal diffraction (see table 5.3). Phase purity and Pawley refinement of CP **17** are not presented here since they are implicit in its crystal structure solution fully described in section 5.4.2.III, which has been obtained *ab initio* from X-ray powder diffraction data and Rietveld refinement.

Table 5.3 Unit cell parameters from Pawley refinements for compounds **12**–**16** and those of analogous compounds from single crystal diffraction data.

	a (Å)	*b* (Å)	*c* (Å)	*α* (º)	*β* (º)	*γ* (º)
12	24.2369	9.5970	15.5184	90	124.50	90
$[Cu(btix)_2(BF_4)]_n$ [a]	23.820	9.5063	15.544	90	123.97	90
13	24.2443	9.5894	15.5118	90	124.46	90
$[Cu(btix)_2(BF_4)]_n$ [a]	23.820	9.5063	15.544	90	123.97	90
14	24.2372	9.5946	15.5158	90	124.45	90
$[Cu(btix)_2(BF_4)]_n$ [a]	23.820	9.5063	15.544	90	123.97	90
15	8.0338	21.0590	8.3511	90	100.46	90
$[Co(btix)_2(NO_3)_2]_n$ [b]	8.2019	20.7198	8.4751	90	105.60	90
16	7.6511	21.3942	8.5296	90	106.65	90
$[Cu(btix)_2Cl_2]_n$ [c]	7.6671	21.327	8.5287	90	106.559	90

a: Structure **12** presented in this *Chapter*; b: Structure **9** in *Chapter 4*; c: ref. 9

In addition to establish phase purity, XRPD has served to investigate how the type of anion substituted determines the final structure. Therefore, XRPD serves to classify the exchanged polymers **13**–**17** into one of the three different categories mentioned in section 5.2.3. Polymers **13** and **14** present XRPD patterns which match those of the original polymer **12**, indicating that the skeletal structure of the polymer remains stable upon anion exchange and correspond to the *group I: retention of the framework*. Polymers **15** and **16** show XRPD patterns similar to the 2D polymer *trans*-$[Cu(btix)_2Cl_2]_n$ previously reported, and are enclosed in the *group II: reduction of the dimensionality*.[9] Finally, polymer **17**, whose XRPD pattern suggests a totally different structure than the original network **12,** is classified in the *group III: complete rearrangement of the network*.

5.2.5 Magnetic properties

Magnetic susceptibility measurements were performed on polycrystalline powders of **12, 15, 16** and **17**. The products of the molar magnetic susceptibility times the temperature, $\chi_m T$ per Cu^{II} ion for **12** is presented in figure 5.9 At room temperature $\chi_m T$ has a value of 0.45 emu.K.mol^{-1}, close to the expected value for an isolated S = ½ Cu^{II} ion. When the temperature is decreased, $\chi_m T$ remains constant down to *ca.* 10 K where rapidly decreases reaching a value of 0.14 emu.K.mol^{-1} at 2 K. The decrease observed in $\chi_m T$ for compound **12** indicates the presence of very weak antiferromagnetic Cu···Cu interactions that, given the structure of this compound, may be attributed to the presence of btix bridges between the Cu^{II} ions. As explained in section 5.2.1, compound **12** is formed by regular chains where the Cu^{II} ions are connected through equivalent *syn*-btix ligands (blue undulating chains in figure 5.2). These chains are further connected with four equivalent chains via additional *anti*-btix ligands in an alternating way (one Cu atom is linked to chains A and B and the following Cu atom is linked to chains C and D). Accordingly, the magnetic data has been modeled as proposed by Hatfield *et al.*[18] (see expression in *Chapter 2*) considering a regular chain (J) of antiferromagnetically coupled S = ½ spins plus an

additional inter-chain interaction (z*J'*, with z = 4), modelled with the molecular field approximation.[19] This simple model satisfactorily reproduces the magnetic properties of the title compound in the whole temperature range with a Landé-factor g = 2.20, J = –4.1 cm^{-1} and J' = –1.1 cm^{-1} (with the spin Hamiltonian written as $H = -J \sum S_1 S_{1+N}$). As expected, both exchange constants are weak and antiferromagnetic, nevertheless, the *syn*-btix bridges are expected to yield a larger coupling constant whereas the *anti*-btix ligands should provide a weaker coupling, in agreement with the proposed model. Compounds **13** and **14** are expected to present similar magnetic properties due to their analogous connectivity to **12**, and, therefore, their magnetic properties have not been measured.

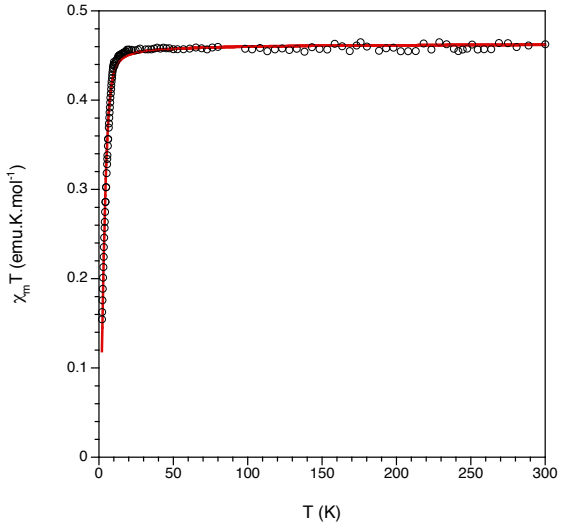

Figure 5.9 Thermal variation of the $\chi_m T$ product per Cu^{II} ion for compound **12**. Solid red line represents the best fit.

Compounds **15** and **16** present analogous magnetic behaviours. Their $\chi_m T$ products at room temperature present a value per Cu^{II} ion of *ca*. 0.45 emu.K.mol^{-1} and remains constant down to very low temperatures and then show a smooth decrease which is more abrupt in **16** than in **15** (figure 5.10). In particular, at 2 K the $\chi_m T$ values are 0.42 and 0.38 emu.K.mol^{-1} for **15** and **16**, respectively. The magnetic behaviour observed

for compounds **15** and **16** indicates that both compounds are essentially paramagnetic with a very weak antiferromagnetic interaction between the Cu^{II} ions.

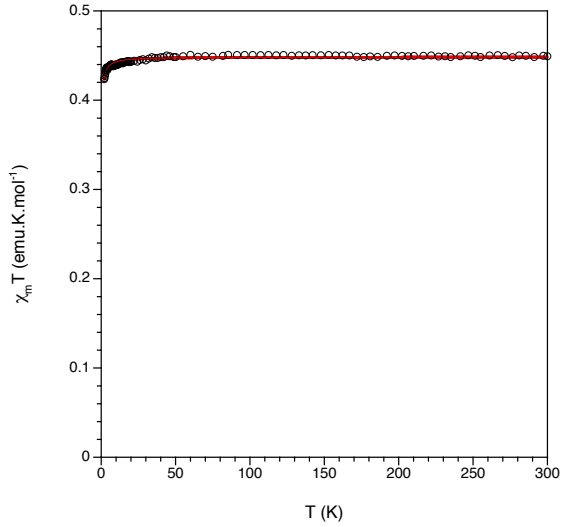

(a)

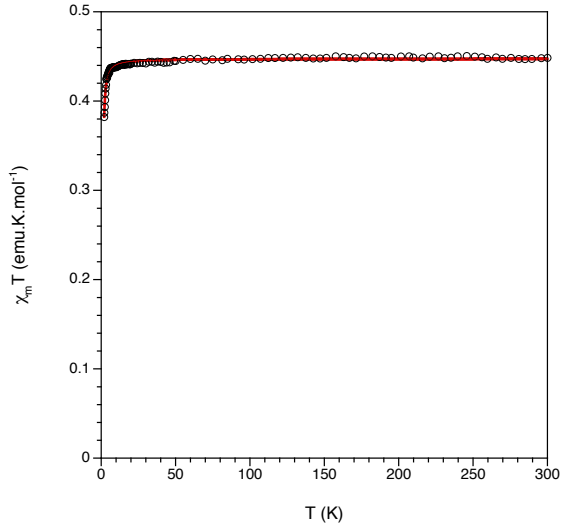

(b)

Figure 5.10 Thermal variation of the $\chi_m T$ product per Cu^{II} ion for compounds **15** (a) and **16** (b). Solid red lines represent the best fit to the models.

Since both compounds present 2D arrays of Cu^{II} ions with two equivalent bridges in both directions of the plane, a S = ½ 2D quadratic layer antiferromagnet model proposed by Lines (equation 5.1) has been used to fit the magnetic data.[20] This model reproduces the observed behaviour of both compounds in the whole temperature range with g = 2.19 and $J = -0.2$ cm^{-1} (for **15**) and g = 2.19 and $J = -2.9$ cm^{-1} (for **16**) (with the spin Hamiltonian written as $H = -J \sum S_1 S_{1+N}$).

$$\frac{Ng^2\mu_\beta{}^2}{\chi J} = 3\theta + \sum_{n=1}^{\infty} \frac{C_n}{\theta^{n-1}} \qquad \text{Eq. 5.1}$$

Where $\theta = kT/JS(S+1)$

and C_n are the coefficients of series for each value of spin, S.[20]

Compound **17** presents a completely different magnetic behaviour. The $\chi_m T$ product at room temperature shows a similar value (*ca*. 0.45 emu.K.mol^{-1}, figure 5.11) but when the temperature decreases below 100 K, $\chi_m T$ increases to reach a maximum of *ca*. 1.06 emu.K.mol^{-1} at 3 K (inset in figure 5.11). An increase in $\chi_m T$ indicates the presence of predominant weak ferromagnetic interactions between the Cu^{II} ions. At very low temperatures a decrease in $\chi_m T$ appears and may be attributed to the presence of weaker antiferromagnetic interactions. The structure of compound **17** shows that the asymmetric 1,1'–N_3 bridges form regular Cu^{II} chains which are further connected through the *anti*-btix ligands. Thus, given the presence of two kind of bridges, *anti*-btix and asymmetric 1,1'–N_3 bridges, it can be assumed that the observed ferromagnetic coupling is due to the asymmetric 1,1'–N_3 bridges whereas the weaker antiferromagnetic coupling is due to the presence of the *anti*-btix bridges, which is also consistent with the observed antiferromagnetic coupling in **12**, **14** and **16**. A simple regular (*J*) ferromagnetic chain model[21] with inter-chain interactions (z*J'*, with $z = 2$) modelled with the molecular field approximation[19] has been used to fit the data. This model reproduces very satisfactorily the magnetic properties of compound **17** in the whole temperature range, including the maximum at low temperatures, with a

Landé-factor g = 2.21, J = +5.9 cm^{-1} and J' = –0.2 cm^{-1} (with the spin Hamiltonian written as $H = -J \sum S_1 S_{1+N}$). As expected, the ferromagnetic coupling constant results larger than the absolute value of the antiferromagnetic coupling.

Although it is not very usual, the ferromagnetic coupling observed through the asymmetric 1,1'–N_3 bridge can be explained with the predictions based on DFT calculations performed for this kind of asymmetric double bridges.[22] These calculations show that in double asymmetric 1,1'–N_3 bridges the main parameter determining the sign and strength of the magnetic coupling is the long Cu–N bond length. The coupling is usually weak and antiferromagnetic when this long Cu–N bond is below *ca*. 2.8 Å but it may be ferromagnetic for Cu–N bond lengths above ca. 2.8 Å (antiferromagnetic < Cu–N bond lengths 2.8 Å < ferromagnetic). This is actually observed in compound **17**, where the long Cu–N distance is 2.886(10) Å, and the coupling between Cu^{II} results ferromagnetic.

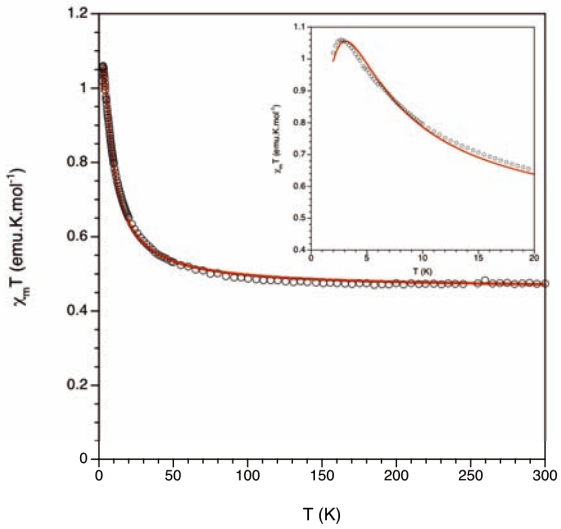

Figure 5.11 Thermal variation of the $\chi_m T$ product per Cu^{II} ion for **17** sowing the best fit (red line).

Table 5.4 Magnetic exchange parameters and Landé-factor values from best fits.

	J (cm^{-1})	J' (cm^{-1})	g
12	–4.1	–1.1	2.20
15	–0.2	-	2.19
16	–2.9	-	2.19
17	+5.9	–0.2	2.21

5.2.6 EPR studies

The solid X-band EPR spectra of **12** at room temperature (figure 5.12a) displays a slightly axially distorted spectrum with a peak at *ca*. 3300 G and a weak and broad signal at *ca*. 2950 G ($g_{\|}$ = 2.06 and $g_{\perp}$= 2.29 respectively, and $g_{average}$ = 2.14) which is in agreement with the value found in the susceptibility measurements. When the temperature is decreased, both an increase in intensity and a slight shift to lower fields of the main signal is observed (higher g values). These results support the tetragonally distorted coordination site, indicating that the unpaired electron of the Cu^{II} ion is situated in the $d_{x^2-y^2}$ orbital, located in the equatorial CuN_4 plane.

Compound **17** presents a more complex X-band EPR spectrum (Figure 5.12b). Thus, the EPR of **17** shows three signals at room temperature centred at *ca*. 3250 G (g = 2.08) that increase in intensity and split at low temperatures, leading in a g shift. The rhombic signal suggests a lower symmetry of the Cu^{II} centres. In addition, the splitting in the three signals may be not only due to a narrowing of the signals as the temperature is decreased but rather due to a shift of the two extreme components toward lower and higher fields in each case. Clearly, this behaviour does not correspond to isolated Cu^{II} sites but rather to that of the low-dimensional exchange-coupled formed in **17**.

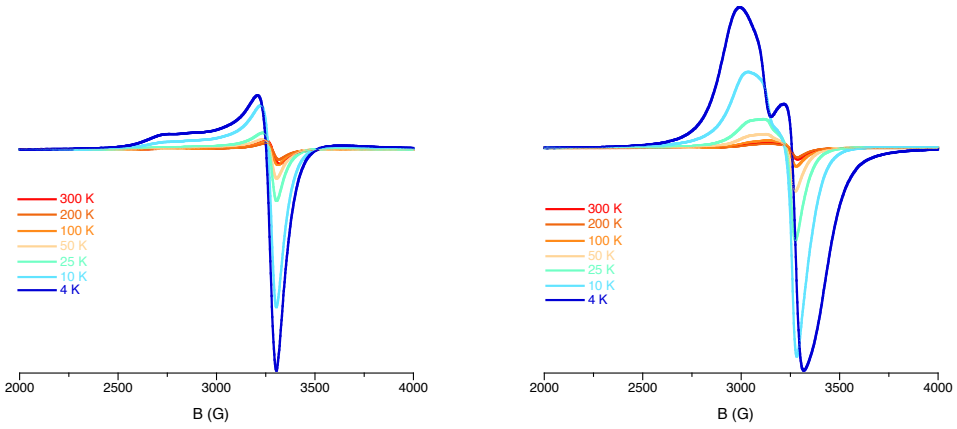

Figure 5.12 X-band EPR spectra at different temperatures for compounds **12** (a) and **17** (b).

5.3 CONCLUSIONS

In this *Chapter*, the effect provoked in a magnetic CP by an external chemical stimulus has been studied. In particular, the non-porous CP $[Cu(btix)_2(BF_4)_2]$ (**12**), which displays dynamic transformations in the solid state, has been studied in detail. This polymer reversibly exchanges the coordinated BF_4^- anion with PF_6^- and ClO_4^- maintaining its structure or with NO_3^- and Cl^- modifying the dimensionality of the network due to changes in the conformation of the flexible organic ligand. Moreover, this CP is capable of irreversibly convert into $[Cu(btix)(N_3)_2]$ (**17**) in the crystalline state when it is immersed in aqueous solution of NaN_3. These anion exchange processes have been monitored by IR spectroscopy.

The structural transformations that accompany the anion exchange processes have been intensely studied. These processes undergo a variety of structural modifications in CP **12** depending on the nature of the anion, which range from minor to severe transformations in the framework. In this sense, XRPD studies resulted essential for the comprehension of the modifications that take place. The main conclusion that can

be extracted from the structural study is that the nature of the anion exchanged has been proved to determine the final configuration adopted by the organic ligand. Thus, a classification of the exchanged CPs into three different groups has been conducted depending on the dynamic response developed in the framework: (i) a retention of the configuration of the organic ligand with no major structural changes; (ii) a switch of the configuration of the organic ligand with a reduction of the dimensionality of the network; and (iii) a switch of the configuration of the organic ligand with a complete rearrangement of the structure.

Interestingly, the structural changes provoked by the anion exchange affect the magnetic properties of the CPs due to changes in the connectivity between the metal centres. Magnetic susceptibility studies and EPR spectroscopy have been applied to study the anion exchange effect. Consequently, depending on the connectivity, three different types of frameworks with distinct magnetic properties are distinguished. CPs **12**–**14** present a 3D structure in which two different weak antiferromagnetic interactions are present. The magnetic behaviour for **15** and **16** also present antiferromagnetic interactions in a quadratic layer model. Finally, CP **17** is characterized by a ferromagnetic interaction a weaker antiferromagnetic interaction.

5.4 METHODS

5.4.1 Synthesis

All reagents and solvents were commercially available and used without further purification. The ligand btix (1,4-bis(triazol-1-ylmethyl)benzene) was prepared according to a literature method.[23]

Synthesis of *trans*-[Cu(btix)$_2$(BF$_4$)$_2$]$_n$ (12). A solution of btix (321 mg, 1.3 mmol) in 50 mL of MeOH was added dropwise into a methanolic solution of Cu(BF$_4$)$_2$·xH$_2$O (175 mg) without stirring. The mixture was left unperturbed at room temperature for crystallization. After several hours, light purple block-shaped crystals suitable for X-ray crystallography, were filtered off and washed with MeOH. Phase purity was

established by X-ray powder diffraction. Yield 87%. Anal. calc. $C_{24}H_{24}CuN_{12}B_2F_8$ (717.68): C, 40.17; H, 3.37; N, 23.42%. Found: C, 38.54; H, 3.42; N, 22.41%. FT-IR (KBr pellet, cm^{-1}): 3144(s), 1532 (vs), 1443 (m), 1427(s), 1346 (w), 1292 (m), 1125 (vs), 1083 (vs), 1115 (vs), 991 (vs), 897 (m), 766 (m), 732 (m), 676 (s), 520 (m).

Synthesis of anion exchanged solids 13-17. Powdered samples of **12** (50 mg) were each immersed in aqueous solutions of $NaClO_4$, $NaPF_6$, $NaNO_3$, NaCl or NaN_3 (3 M, 5 mL) for 1 day. The resulting anion-exchanged solids **13**-**17** (exchanged with ClO_4^- (**13**), PF_6^-(**14**), NO_3^- (**15**), Cl^-(**16**) and N_3^- (**17**)) were collected by centrifugation, washed several times with water, and then dried in vacuum. The products were characterized by EA, IR and XRPD. To verify the reversibility of the process, the anion-exchanged solids were immersed in 3 M $NaBF_4$ for 1 day, collected by centrifugation, washed several times with water, and then dried in vacuum. All solids were characterized by FT-IR spectra, and XRPD.

5.4.2 Structural characterization

5.4.2.I Single crystal X-ray diffraction of 12

A single crystal of compound **12** was mounted on glass fibre using a viscous hydrocarbon oil to coat the crystal and then transferred directly to the cold nitrogen stream for data collection. X-ray data was collected at 120 K on a Supernova diffractometer equipped with a graphite-monochromated Enhance (Mo) X-ray Source (λ = 0.71073 Å) at ICMol (University of Valencia). The program CrysAlisPro, Oxford Diffraction Ltd., was used for unit cell determinations and data reduction. Empirical absorption correction was performed using spherical harmonics, implemented in the SCALE3 ABSPACK scaling algorithm. Crystal structure was solved and refined against all F^2 values using the SHELXTL suite of programs.[24] Non-hydrogen atoms were refined anisotropically (except the disordered fragments) and hydrogen atoms were placed in calculated positions that were refined using idealized geometries (riding model) and assigned fixed isotropic displacement parameters except for those of water molecules, which were located and refined with distance restraints. In **1**, the

benzene moiety of the *syn*-btix ligand is disordered over two sites and has been modeled with a 50:50 ratio. A summary of the data collection and structure refinements is provided in table 5.5.

Table 5.5 Crystallographic data for compound **12**.

Compound	**12**
Empirical formula	$C_{24}H_{24}N_{12}B_2F_8Cu$
Formula weight	717.71
Crystal color	Purple
Crystal size (mm^3)	0.15 × 0.15 × 0.05
Temperature (K)	120(2)
Crystal system, Z	Monoclinic, 4
Space group	*C2/c*
a (Å)	23.820(9)
b (Å)	9.5063(15)
c (Å)	15.544(6)
α (°)	90.00
β (°)	123.97(6)
γ (°)	90.00
V ($Å^3$)	2918.8(16)
ρ_{calc} (Mg/m^3)	1.633
$\mu(Mo_{K\alpha})$ (mm^{-1})	0.840
θ range (°)	2.38 – 25.03
Reflns collected	6214
Independent reflns (R_{int})	2576 (0.1448)
Reflns used in refinement, *n*	2576
L. S. parameters, *p*/ restraints, *r*	212/0
$R1(F)$,[a] $I>2\sigma(I)$	0.0763
$wR2(F^2)$,[b] all data	0.1510
$S(F^2)$,[c] all data	0.973

[a] $R1(F) = \Sigma(||F_O| - |F_C||)/\Sigma|F_O|$; [b] $wR2(F^2) = [\Sigma w(F_O^2 - F_C^2)^2/\Sigma wF_O^4]^{1/2}$; [c] $S(F^2) = [\Sigma w(F_O^2 - F_C^2)^2/(n + r - p)]^{1/2}$

5.4.2.II X-ray powder diffraction

Phase purity of polycrystalline samples of **12**–**16** was established by XRPD (figure 5.7). Polycrystalline samples of **12**–**16** were lightly ground in an agate mortar and pestle and filled into 0.7 mm borosilicate capillaries. Data were collected at room temperature in the 2θ range 2 – 50 º on an Empyrean PANalytical powder diffractometer, using Cu K_α radiation (λ = 1.54177 Å) at ICMol (University of Valencia). Pawley refinements[25] were performed using the TOPAS computer program.[26]

5.4.2.III X-ray powder diffraction and Rietveld refinement

A polycrystalline sample of **17** was lightly ground in an agate mortar and pestle and filled into a 0.3 mm glass boron capillary prior to being mounted and aligned on a Empyrean PANalytical powder diffractometer, using Cu $K_{\alpha1}$ radiation (λ = 1.54177 Å). 35 repeated measurements were collected at room temperature (2θ = 3 – 70 º) and merged in a single diffractogram. The diffraction pattern was indexed using TOPAS[26] to a monoclinic cell and space group *C*2/*c* was assigned from volume considerations and a statistical consideration of the systematic absences. The dataset was background-subtracted and truncated to d = 2.885 Å (2θ = 31.00 º), for Pawley refinement[25] and structure solution using the simulated annealing (SA) global optimization procedure, described previously,[27] that is now implemented in the DASH computer program.[28] The SA structure solution involved the optimization of three independent fragments in the asymmetric unit (one half-Cu atom, one half-btix ligand and one azido ligand, considered from the composition of compound **17**), totalling 19 degrees of freedom. Z-matrices describing the molecular topology of the fragments were generated automatically within DASH using analogous moieties taken from the CSD. Global optimization of all external (rotational and translational) degrees of freedom against the extracted intensities was carried out with all DASH SA control parameters set to default values. 10 runs with 5×10^7 SA moves per run were implemented for each structure determination. The best SA solutions had a chemically reasonable packing arrangement, and exhibited no significant misfit to the data. The

solved structure was used as starting model for Rietveld refinement,[29] conducted using TOPAS. All atomic positions and displacement parameters, U_{iso}, of non-hydrogen atoms were refined (one for Cu atom and one for all C and N atoms; H atoms were fixed at idealized positions and the atomic displacement parameters were set as 1.2 times those of non-hydrogen atoms), subject to a series of restraints on bond lengths, bond angles and planarity of the aromatic rings. A March-Dollase correction of the intensities for preferred orientation was applied in the final stage of refinement. The observed and calculated diffraction patterns for the refined crystal structures are shown in figure 5.13. Rietveld refinement converged to R_{wp} of 0.0504, R_{wp}' = 0.14426 (R_{wp}' is the background subtracted R_{wp}).

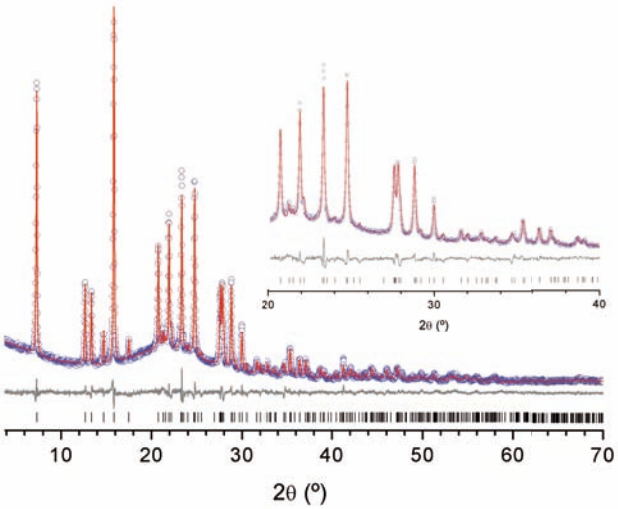

Figure 5.13 Observed (blue) and calculated (red) profiles and difference plot [(I_{obs} - I_{calcd})] (grey) of the Rietveld refinement of compound **17** (2θ range 3.0–70.0 °, maximum resolution of 1.34 Å). Rietveld refinement converged to R_{wp} of 0.0504, R_{wp}' = 0.14426 (R_{wp}' is the background subtracted R_{wp}).

Table 5.6. Data collection, structure solution and refinement parameters of **17**.

Compound	**17**
Empirical formula	$C_{12}H_{12}N_{12}Cu$
Formula weight	387.89
Specimen colour	green
Specimen shape (mm)	Cylinder
	12 × 0.7 × 0.7 mm
Wavelength, λ (Å)	1.54177
Crystal system	Monoclinic
Space group, *Z*	*C2/c*, 4
a (Å)	24.4913(10)
b (Å)	4.34232(12)
c (Å)	14.20752(55)
α (°)	90
β (°)	78.885(3)
γ (°)	90
V (Å^3)	1482.61(9)
ρ_{calc} (Mg/m^3)	1.737
Temperature (K)	298(5)
$\mu(Cu_{K\alpha})$ (mm^{-1})	2.329
2θ range (°)	3.0 to 70.0
Increment in 2θ (°)	0.014
Reflns measured, n	331
Specimen mounting	0.7 mm borosilicate capillary
Mode	transmission
Detector	PIXcel
Parameters refined, *p*	94
Restraints, *r*	36
R_p [a]	0.0386
R_{wp} [b]	0.0504
R_{exp} [c]	0.0377
GoF [d], all data	1.320

[a] $R_p = \Sigma|y_O - y_C|/\Sigma y_O$; [b] $R_{wp} = [\Sigma\omega(y_O - y_C)^2/\Sigma\omega(y_O)^2]^{1/2}$; [c] $R_{exp} = R_{wp}/GoF$; [d] $GoF = [\Sigma\omega(y_O - y_C)^2/(n - p + r)]^{1/2}$

5.4.3 Physical measurements

Carbon, nitrogen, and hydrogen contents were determined by microanalytical procedures using an EA 1110 CHNS-O elemental analyzer from CE Instruments. Infrared spectra were recorded in a FT-IR Nicolet 5700 spectrometer at ICMol (University of Valencia) in the 4000−400 cm^{-1} range using powdered samples diluted in KBr pellets.

Magnetic propoerties. Magnetic susceptibility measurements were performed on single-phased polycrystalline samples of **12**, **15**, **16** and **17** with a Quantum Design MPMS-XL-5 SQUID susceptometer at ICMol (University of Valencia). The susceptibility data were corrected from the diamagnetic contributions as deduced by using Pascal's constant tables. The d.c. data were collected in the range 2–300 K with an applied field of 0.1 T. Field dependences of the magnetization were measured at 2.0 K. Electron paramagnetic resonance spectroscopy was recorded with a Bruker ELEXYS E580 spectrometer operating in X-band (9.47 GHz).

5.5 REFERENCES

1. (a) Gütlich, P., Hauser, A. and Spiering, H. *Angew. Chem. Int. Ed*. **1994**, *33*, 2024; (b) Sato, O., Iyoda, T., Fujishima, A. and Hashimoto, K. *Science* **1996**, *272*, 704; (c) Coronado, E., Giménez-López, M. C., Levchenko, G., Romero, F. M., García-Baonza, V., Milner, A. and Paz-Pasternak, M. *J. Am. Chem. Soc*. **2005**, *127*, 4580; (d) Coronado, E., Giménez-López, M. C., Korzeniak, T., Levchenko, G., Romero, F. M., Segura, A., García-Baonza, V., Cezar, J. C., de Groot, F. H. F., Milner, A. and Paz-Pasternak, M. *J. Am. Chem. Soc.* **2008***, 130*, 15519; (e) Egan, L., Kamenev, K., Papanikolaou, D., Takabayashi, Y. and Margadonna, S. *J. Am. Chem. Soc.* **2006**, *128*, 6034.

2. (a) Coronado, E., Giménez-Marqués, M., Mínguez Espallargas, G. and Brammer, L. *Nature Commun.* **2012**, *3*, 828; (b) Navarro, J. A. R., Barea, E., Rodríguez-Diéguez, A., Salas, J. M., Ania, C. O., Parra, J. B., Masciocchi, N., Galli, S. and Sironi, A. *J. Am. Chem. Soc*. **2008**, *130*, 3978; (c) Ohkoshi, S., Arai, K., Sato, Y. and Hashimoto, K. *Nature Mater.* **2004**, *3*, 857; (d) Zhang, Y.-J., Liu, T., Kanegawa, S. and Sato, O. *J. Am. Chem. Soc*. **2009**, *131*, 7942; (e) Kurmoo, M., Kumagai, H., Chapman, K. W. and Kepert, C. J. *Chem. Commun*. **2005**, 3012.

3. (a) Cohen, S. R. *Chem. Rev.* **2012**, *112*, 970; (b) Wang, Z. and Cohen, S. R. *Chem. Soc. Rev.* **2009**, *38*, 1315; (c) Tanabe, K. K., Wang, Z. and Cohen, S. R. *J. Am. Chem. Soc.* **2008**, *130*, 8508; (d) Nagai, A., Guo, Z., Feng, X., Jin, S., Chen, X., Ding, X. and Jiang, D. *Nature Commun.* **2011**, *2*, 536. (e) Cohen, S. M. *Chem. Sci.* **2010**, *1*, 32

4. (a) Bradshaw, D., Warren, J. E. and Rosseinsky, M. J. *Science* **2007**, *315*, 977; (b) Beauvais, L. G., Shores, M. P. and Long, J. R. *J. Am. Chem. Soc.* **2000**, *122*, 2763; (c) Wu, C.-D., Hu, A., Zhang, L. and Lin, W. *J. Am. Chem. Soc.* **2005**, *127*, 8940; (d) Mínguez Espallargas, G., Brammer, L., van de Streek, J., Shankland, K., Florence, A. J. and Adams, H. *J. Am. Chem. Soc.* **2006**, *128*, 9584; (e) Mínguez Espallargas, G., Hippler, M., Florence, A. J., Fernandes, P., van de Streek, J., Brunelli, M., David, W. I. F., Shankland, K. and Brammer, L. *J. Am. Chem. Soc.* **2007**, *129*, 15606; (f) Mínguez Espallargas, G., van de Streek, J., Fernandes, P., Florence, A. J., Brunelli, M., Shankland, K. and Brammer, L. *Angew. Chem. Int. Ed.* **2010**, *49,* 8892; (g) Libri, S., Mahler, M., Mínguez Espallargas, G., Singh, D. C. N. G., Soleimannejad, J., Adams, H., Burgard, M. D., Rath, N. P., Brunelli, M. and Brammer, L. *Angew. Chem. Int. Ed.* 2008, **47**, 1693.

5. (a) Hoskins, B. F. and Robson, R. *J. Am. Chem. Soc.* **1990**, *112*, 1546; (b) Yaghi, O. M. and Li, H. *J. Am. Chem. Soc.* **1995**, *117*, 10401; (c) Yaghi, O. M. and Li, H. *J. Am. Chem. Soc.* **1996**, *118*, 295; (d) Noro, S.-i., Kitaura, R., Kondo, M., Kitagawa, S., Ishii, T., Matsuzaka, H. and Yamashita, M. *J. Am. Chem. Soc.* **2002**, *124*, 2568; (e) Aijaz, A., Lama, P. and Bharadwaj, P. K. *Inorg. Chem*. **2010**, *49*, 5883; (f) Fei, H., Bresler, M. R. and Oliver, S. R. J. *J. Am. Chem. Soc*. **2011**, *133*, 11110.

6. (a) An, J. and Rosi, N. L. *J. Am. Chem. Soc.* **2010**, *132*, 5578; (b) Calleja, G., Botas, J. A., Sánchez-Sánchez, M. and Orcajo, M. G. *Int. J. Hydrogen Energy*, **2010**, *35*, 9916.

7. Beer, P. D. and Gale, P. A. *Angew. Chem. Int. Ed*. **2001**, *40*, 486.

8. (a) Min, K. S. and Suh, M. P. *J. Am. Chem. Soc.* **2000,** *122,* 6834.

9. Ding, B., Liu, Y.-Y., Huang, Y.-Q., Shi, W., Cheng, P., Liao, D.-Z. and Yan, S.-P. *Cryst. Growth Des.* **2009**, *9*, 593.

10. Díaz-Torres, R. and Alvarez, S. *Dalton Trans*. **2011**, *40*, 10742.

11. (a) Liu, K., Shi, W. and Cheng, P. *Dalton Trans*. **2011**, *40*, 8475; (b) Li, B., Peng, Y., Li, B. and Zhang, Y. *Chem. Commun.* **2005**, 2333; (c) Meng, X., Liu, Y., Song, Y., Hou, H., Fan, Y. and Zhu, Y. *Inorg. Chim. Acta* **2005**, *358*, 3024.

12. (a) Khlobystov, A. N., Champness, N. R., Roberts, C. J., Tendler, S. J. B., Thompson, C. and Schröder, M. *CrystEngComm* **2002**, *4*, 426; (b) Cui, X., Khlobystov, A. N., Chen, X., Marsh, D. H., Blake, A. J., Lewis, W., Champness, N. R., Roberts, C. J. and Schröder, M. *Chem. Eur. J.* **2009**, *15*, 8861.

13. Nakamoto, K. *Infrared and Raman Spectra of Inorganic and Coordination Compounds, 4th ed.*

14. (a) Ray, M. S., Ghosh, A., Bhattacharya, R., Mukhopadhyay, G., Drew, M. G. B. and Ribas, J. *Dalton Trans*. **2004**, 252; (b) De Munno, G., Lombardi, M. G., Julve, M., Lloret, F. and Faus, J. *Inorg. Chim. Acta* **1998**, *282*, 82.

15. Supriya, S. and Das, S. K. *Chem. Commun.* **2011**, *47*, 2062.

16. Suzuki, A., Ivandini, T. A., Kamiyac, A., Nomurad, S., Yamanuki, I., Matsumoto, K., Fujishima, A. and Einaga, Y. *Sens. Actuators, B* **2007**, *120*, 500;

17. Cheetham, A. K.; Rao, C. N. R.; Feller, R. K. *Chem. Commun*. **2006**, 4780.

18. Brown, D. B., Donner, J. A., Hall, J. W., Wilson, S. R., Wilson, R. B., Hodgson, D. J. and Hatfield, W. E. *Inorg. Chem.* **1979**, *18*, 2635

19. O'Connor, C. J. *Prog. Inorg. Chem.* **1982**, *29*, 203.

20. Lines, M. E. *J. Phys. Chem. Solids* **1970**, *31*, 101.

21. Baker Jr., G. A., Rushbrooke, G. S. and Gilbert, H. E. *Phys. Rev.* **1964**, *135*, A1272.

22. Triki, S., Gómez-García, C. J., Ruiz, E. and Sala-Pala, J. *Inorg. Chem*. **2005**, *44*, 5501.

23. Meng, X., Song, Y., Hou, H., Han, H., Xiao, B., Fan, Y. and Zhu, Y. *Inorg. Chem*. **2004**, *43*, 3528.

24. Sheldrick, G. M. *Acta Crystallogr., Sect. A: Found. Crystallogr*. **2008**, *64*, 112.

25. Pawley, G. S. *J. Appl. Cryst.* **1981**, *14*, 357.

26. Coelho, A. A. TOPAS-Academic, Version 4.1, 2007, see: http:// www.topas-academic.net.

27. David, W. I. F., Shankland, K. and Shankland, N. *Chem. Commun*. **1998**, 931.

28. David, W. I. F., Shankland, K., van de Streek, J., Pidcock, E., Motherwell, S. and Cole, J. C. *J. Appl. Crystallogr*. **2006**, *39*, 910.

29. Rietveld, H. M. *J. Appl. Crystallogr*. **1969**, *2*, 65.

II

6

INTRODUCTION TO SPIN-CROSSOVER PHENOMENON

6.1 THE SPIN-CROSSOVER PHENOMENON

6.1.1 Ligand field considerations

Ligand field theory (LFT) describes the bonding, orbital arrangement, structural features and other characteristics of coordination complexes of transition metals (TMs). It represents an application of Molecular Orbital (MO) theory to TM complexes. In its pure electrostaci from namely crystal field theory (CFT), the metal centre is considered as a positive point charge, and the ligands are treated as negative point charges. According to CFT, electrons located in the d orbitals of TMs, which are energetically degenerated in a free ion, and break this degeneracy when placed into a non-spherical ligand field (figure 6.1a). Thus, in the case of an octahedral TM complex, the approach of the ligands towards the TM ion alters the energy of the orbitals, which split into two subsets, namely the e_g and t_{2g} irreducible representations.[1] If ligands are placed lying in the between the axes, the d_{xy}, d_{xz} and d_{yz} orbitals (t_{2g}) will be lowered in energy, while the $d_{x^2-y^2}$ and d_{z^2} orbitals (e_g) will be raised in energy as a result of electron–electron repulsion (figure 6.1b). However, the total energy of the system when all orbitals are fully occupied will not change. The resulting energy difference between the e_g and t_{2g} subsets is known as the ligand field splitting, Δ, and its magnitude ($10D_q$) depends on the type and oxidation state of the metal as well as the nature of the ligands and on metal-ligand distance (r).

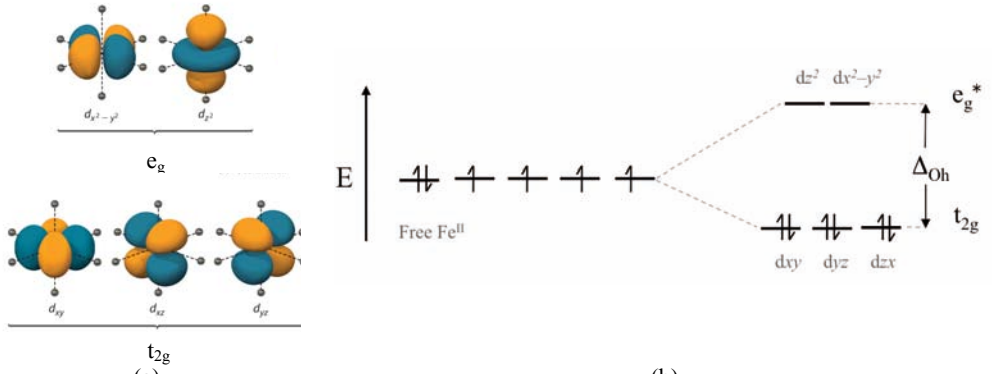

Figure 6.1 (a) Orientation of the d orbitals of a TM relative to a Cartesian coordinate system. (b) Effect on the relative energy of the d orbitals of placing a TM ion into an octahedral (O_h) ligand field (Δo_h).

The order of occupation of the d orbitals by electrons is determined by the magnitude of Δ and the energy required to spin-pair electrons within an orbital (the pairing energy, P).[1] If Δ < P, the d orbitals in both t_{2g} and e_g sets will become singly occupied prior to spin-pairing of electrons within the same orbital, in accordance with Hund's Rules. If Δ > P, the electrons will fill the d orbitals according to the Aufbau Principle, meaning that the lower energy t_{2g} subset will be completely filled before filling the higher energy e_g set. Thus, in the case of TM ions with a d^4 to d^7 electronic configuration in a ligand field with octahedral symmetry, two possible electronic terms with distinct spin states can exist. These are the high spin state (HS), which has the maximum spin multiplicity, and the low spin state (LS). For instance, the distribution of the d electrons in the d^6 Fe^{II} metal ion generates two possible spin states, $^1A_1$ [with an orbital occupation of $(t_{2g})^6$] and S = 0, and $^5T_{2g}$ [with an orbital occupation of $(t_{2g})^4(e_g)^2$ and S = 2] (figure 6.2a). Whether the ground state will be $^1A_1$ or $^5T_{2g}$ in a Fe^{II} complex depends on the ligand field strength, as shown in the so-called Tanabe-Sugano diagram,[2] which gives the dependence of the d orbital levels as a function of Δ (figure 6.2b). Weak ligand-field strengths produces small ligand field splitting Δ, and thus the electrons will fill up the orbitals following Hund's rule, affording the high-spin paramagnetic ground state $^5T_{2g}$. For higher values of ligand field splitting Δ, it is more favourable for the electrons to pair in the lower orbitals, resulting in the low-spin diamagnetic $^1A_1$ ground state. For compounds with a crystal field splitting value close to the critical value Δ_{crit}, where Δ ≈ P, a spin transition may be induced by causing a change in the $10D_q$ parameter through an external perturbation such as light, temperature, magnetic field or pressure. This process is known as spin-crossover phenomenon, and is possible when the difference in zero-point energy between the HS and LS states (ΔE^o_{HL}) is approximately equal to the thermal energy, i.e. $\Delta E^o_{HL} = E^o_{HS} - E^o_{LS} \approx k_B T$ (figure 6.3b).[3-5]

In Fe^{II} complexes the t_{2g} orbitals are of non-bonding character, whereas the e_g orbitals are anti-bonding. Therefore, the metal-ligand bond length, *r*, is significantly higher in the HS state than in the LS state, because in the former the anti-bonding orbitals are

populated and, additionally, less electrons for d_π–p_π back donation are available. Compounds with $Fe^{II}N_6$ core show typical values of $r_{HS} \approx 2.16 – 2.20$ Å and $r_{LS} \approx 1.96 – 2.00$ Å,[6] i.e. a difference of about 10 % in the metal-ligand distance.

Apart from Fe^{II}, other transition metal ions of the first row are also known to form spin-transition complexes. Examples for Co^{III},[7] Co^{II},[8] Fe^{III},[9] and Ni^{II},[10] are reported in the literature. In most of the cases, their stronger ligand field and their weaker spin pairing energy makes them rare. The cases for Ni^{II} are sometimes referred to as geometrical rearrangements, which are related to a change in spin multiplicity.

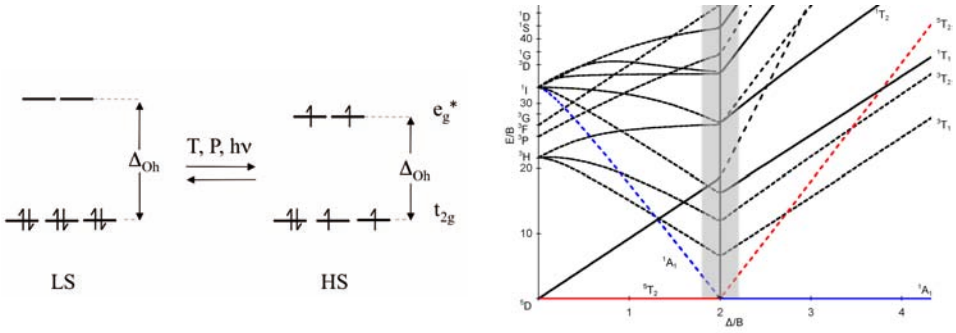

(a) (b)

Figure 6.2 (a) Scheme illustrating the SCO phenomenon for Fe^{II} provoked by different external stimuli in a Oh ligand field. (b) Tanabe and Sugano diagram for Fe^{II} with the $^5T_{2g}$ and the $^1A_1$ spin states shown in red and blue, respectively.

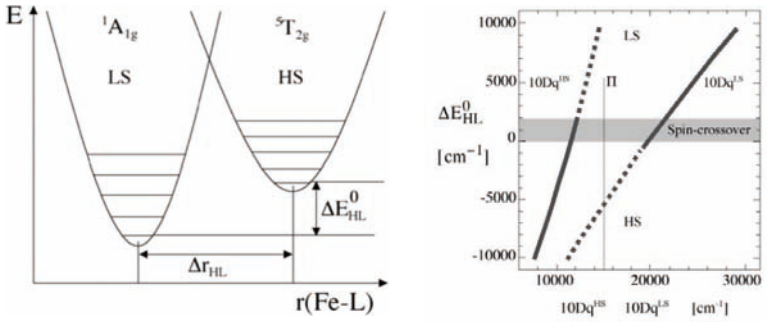

(a) (b)

Figure 6.3 (a) Configuration coordinate diagram for an Fe^{II} compound expressed along the totally symmetric metal-ligand stretch vibration, r(Fe-L). (b) Representation of the regions where each of the states (HS, LS or Spin Transition) is stable. Reproduced from reference 3.

6.1.2 Classification of Spin-Crossover systems

The first example of a spin crossover was reported by Cambi *et al.*[11] in 1931 on Fe^{III}-tris(dithiocarbamato) complexes. The first explanation of the phenomena arrived with Pauling, who initially explained the change in the magnetic properties of ferrihemoglobin hydroxide by the change in the bond type from covalent to ionic.[12] It took more than 20 years until Orgel suggested the correct explanation based on the change in the spin state of the ion.[13] The first Fe^{II} spin crossover system, namely $[Fe(phen)_2(NCS)_2]$ (phen = 1,10-phenanthroline), was found by Baker *et al.* 30 years after the discovery of Cambi.[14] This is very curious since SCO is much more common in Fe^{II} complexes than in Fe^{III}, but the latter were found 30 years before. Since then, the SC phenomenon and its mechanism has been studied extensively and reviewed by different authors.[15–18]

The temperature at which a spin crossover material has an equal ratio of high spin and low spin sites is called $T_{1/2}$.[5] Spin transition curves help to visualize the different type of spin crossover behaviour observed in the solid state. These curves consist of a plot of the molar fraction of the high spin component (γHS) as a function of temperature and can be derived from measurements of physical properties such as magnetism (susceptibility measurements), nuclear environment (Mossbauer spectroscopy), colour (UV-vis spectroscopy), bond lengths and other structural features (diffraction techniques). Figure 6.4 shows a series of spin transition curves that are most commonly observed in crystalline materials.[5,17] The simplest system to consider is that in which very few cooperative interactions between metal centres are present. The result is a very gradual spin transition (figure 6.4a), which may occur over several tens or hundreds of Kelvin, and may be considered as a Boltzmann distribution across the available spin states, randomly distributed throughout the crystal. It is possible for spin crossover processes to be incomplete, where only some of the TM centres undergo spin crossover, or stepped (figure 6.4b), where SCO centres undergo the spin transition at distinct temperatures, separated by an intermediate state that contains both HS and LS sites. When cooperative lattice interactions are present, abrupt transitions (figure 6.4c) are observed often accompanied by hysteresis (figure 6.4d).

This kind of hysteretic behaviour represents a form of molecular bistability and is important to potential applications as molecular switches or memory storage devices.

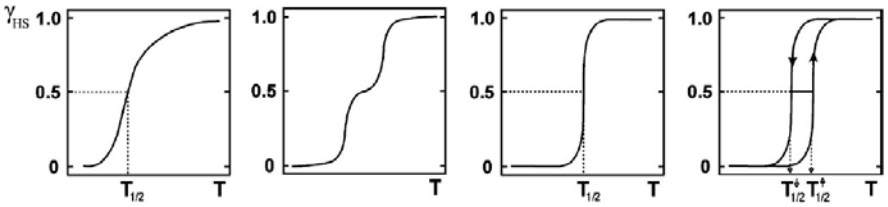

Figure 6.4 Spin transition curves for the most frequently observed types of transition represented in molar fraction of the high spin species (γ_{HS}) as a function of temperature (T). Reproduced from reference 3.

6.2 SPIN-CROSSOVER AT THE NANOMETER SCALE

Technological advances have moved electronic devices towards miniaturization (from μm to nm) and faster processing speed (from nanoseconds to femtoseconds). This has been at the origin of molecular electronics, which is a multidisciplinary field that has already resulted in exceptional examples of molecules acting as molecular-based functional units such as memories, modulators, rectifiers, switches, transistors or wires.[19-22]

Spin-crossover (SCO) systems represent one of the most promising systems as molecular switches or memory storage devices due to the molecular bistability associated with the SCO phenomenon.[23] Actually, our group has been involved in the fabrication of a molecular device exhibiting switching near room temperature. This device has been fabricated by contacting a bistable spin-crossover nanoparticle to two electrodes (figure 6.5).[24] By measuring the conductance, it has been shown that is possible to send current trough these particles, and that they show bistability in the conductance as a function of temperature. Interestingly, this device has also shown the possibility of controlling the spin state by applying an electric field. This discovery opens the possibility of using such devices in spintronics.

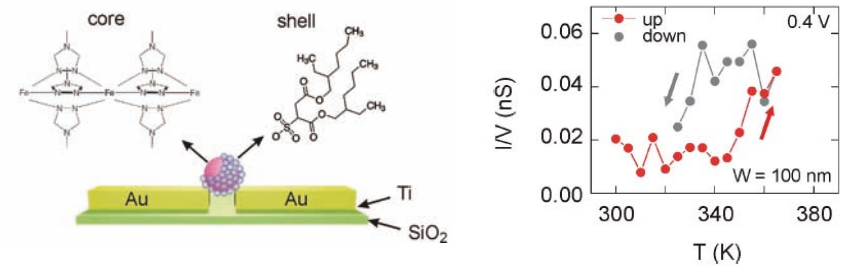

(a) (b)

Figure 6.5 (a) Schematic side view of the device geometry with the SCO-NP placed on top of the electrodes. (b) Conductance (I/V) as a function of temperature for the device with 100 nm wide electrodes. Each point represents the average of the conductance at 0.4 V of 30 individual current-voltage characteristics. Reproduced from reference 24.

Implementation of SCO materials in practical devices involves the design of nanoscale SCO systems which fulfil a number of requirements. In this sense, the SCO material may ideally present a complete, abrupt and hysteretic spin transition centered at room temperature, showing enhanced chemical stability.[25] An additional requirement involves the control on the miniaturization of the system. This is a challenging condition since cooperativity, which is responsible of the first-order transition necessary to obtain a memory effect, highly depends on the particle size. Accordingly, in order to obtain nanostructured SCO materials optimal for spintronic devices, it is essential to identify the critical particle size at which complete and hysteretic transition is preserved.

A convinient approach to synthesize a nanoscopic material is based on the use of water-in-oil (w/o) emulsions to confine the growth of the coordination network. The reverse micelle technique was first applied by Mann *et al*. to obtain NPs of Prussian Blue (NPs from 12 to 50 nm organized in domains of 200 nm),[26] and was further developed by the group of Mallah to obtain magnetic NPs of the Prussian blue type of 3 nm.[27] Concerning SCO materials, in 2004 the group of Létard reported preliminary results of SCO nanoparticles based on the Fe^{II}–NH_2-triazole system with a size comprised between 60 and 200 nm and a spin transition centred at room temperature, which was measured by optical reflectivity.[28] Later in 2007, thermal hysteresis was

first evidenced in our group for small nanoparticles of $[Fe(Htrz)_2(trz)](BF_4)$ with diameters around *ca*. 10 nm with a narrow distribution. This nanoparticles show a very abrupt transition above room temperature with a wide thermal hysteresis of *ca*. 40 K, thus preserving the properties of the bulk material.[29]

Since then, the number of publications dedicated to the study of SCO nanoparticles has been strongly enlarged. The vast majority of studies have focused in the synthetic procedures to gain control over the size and therefore physical properties of the SCO-NPs. Actually, all efforts have focused mainly in two systems: the 1D coordination polymers of the triazole family.[30-34] and the 2D and 3D coordination polymers of the family $[Fe(pz)\{M(CN)_4\}]$.[35-37] The first family will be discussed in detail in *Chapter 7*. Regarding the second family, nanoparticles were prepared by the reverse micelle technique by different groups, allowing the stabilization and size tuning of particles below 20 nm. Importantly, the particles have a magnetic behaviour different from that of the bulk (figure 6.6). Upon reduction in the size, the transition is smoother, the transition temperature shifts downward and the hysteresis loop is narrower, which is almost vanished for the smaller particles.

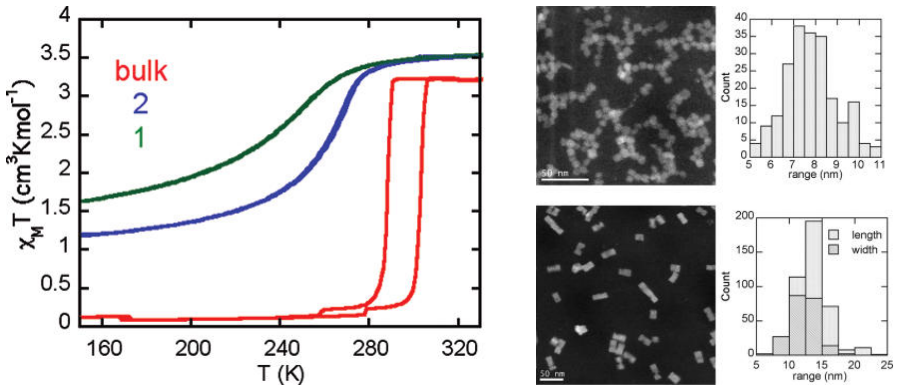

(a) (b)

Figure 6.6 (a) Magnetic behaviour of coordination nanoparticles of the 3D network $Fe(pyrazine)\{Pt(CN)_4\}$. (b) HAADF-STEM imaging and size distribution. Reproduced from reference 35.

AIM OF THE WORK

The following *Chapters* 7–9 are focused on the study of SCO-NPs, covering diverse aspects mainly based in the synthetic procedure, physical properties and processing.

In *Chapter 7*, a detailed description of the synthetic protocol used for the synthesis of SCO nanoparticles is presented. Extensive analyses have been developed in order to rationalize all parameters that exert an influence on the physical properties. In particular, a controlled reduction of the NP size and later analysis of this effect on the spin transition have been investigated.

In *Chapter 8* the effect of the ligand substitution in the transition temperature of SCO-NPs has been investigated. For this study, a family of SCO-NPs responding to the general formula $[Fe(Htrz)_{3-3x}(NH_2trz)_{3x}](ClO_4)_2$ has been synthesized, by successively substituting one ligand by another, with the resulting variation of the chemical composition. This chemical perturbation has shown to exert a dramatic effect in the spin transition of the NPs.

Chapter 9 considers the necessity to advance in the processing of nano-objects for nanodevices technologies. Different possibilities to organize the NPs onto surfaces are presented with the final aim of their direct addressing and manipulation.

6.3 REFERENCES

1. (a) Shriver, D. F.; Atkins, P. W., *Inorganic Chemistry*. Oxford University Press: Oxford, **1999**. (b) Cotton, F. A., Wilkinson, G., Gaus, P. L. *Basic Inorganic Chemistry*, Wiley, **1995**.
2. Tanabe, Y.; Sugano, S., *J. Phys. Soc. Japan* **1954**, *9*, 766.
3. Hauser, A., Gütlich, P., Goodwin, H. A. *Top. Curr. Chem*., **2004**, *233*,49.
4. Gütlich, P., Hauser, A., Spiering, H. *Angew. Chem. Int. Ed.* **1994**, *33*, 2024.
5. Gütlich, P., Goodwin, H. A. *Top. Curr. Chem*. **2004**, *233*, 1.
6. Wiehl, L., Kiel, G., Köhler, C. P., Spiering, H. and Gütlich, P. *Inorg. Chem.* **1986**, *25,* 1565.
7. Zarembowitch, J., *New J. Chem*. **1992**, 16, 255.
8. Létard, J.-F., Real, J. A., Moliner, N., Gaspar, A. B., Capes, L., Cador, O., and Kahn, O. *J. Am. Chem. Soc*. **1999**, *121*, 10630.
9. Real, J. A., Castro, I., Bousseksou, A., Verdaguer, M., Burriel, R. Castro, M., Linares, J. and Varret, F. *Inorg. Chem.* **1997**, *36*, 455.
10. Ksenofontov, V. Gaspar, A. B., Niel, V. Reiman, S., Real, J. A. and Gütlich, P. *Chem. Eur. J*., **2004**, *10*, 1291.
11. Cambi, L. and Cagnasso, A. *Atti Accad. Naz. Lincei* **1931**, *13*, 809.
12. Pauling, L. *J. Am. Chem. Soc.* **1937**, *59*, 633.
13. Orgel, L. E. 10th Chemical Conference, Brussels, **1956**, 289.
14. Baker, W. A. and Bobonich, H. M . *Inorg. Chem*. **1964**, *3*, 1184.
15. (a) Gütlich, P. *Struct. Bond*. **1981**, *44*, 83. (b) Beattie, J. K. *Adv. Inorg. Chem*. **1988**, *32*, 1.
16 Khan, S. U. M. and Zhou, Z. Y. *J. Chem. Soc. Faraday Trans*. **1991**, *87*, 535.
17. Gütlich, P., Spiering, H. and Hauser, A. *Angew. Chem*. **1994,** *106*, 2109.
18. Goodwin, H. A., Garcia, Y. and Gütlich, P. *Chem. Soc. Rev.* **2000**, *29*, 419.
19. Aviram, A. and Ratner, M. A. *Chem. Phys. Lett*. **1974**, 29, 277.
20. Gimzewski, J. K. and Joachim, C. *Science* **1999**, *283*, 1683.
21. Tour, J. M., Kozaki, M. and Seminario, J. M. *J. Am. Chem. Soc*. **1998**, *120*, 8486.
22. Raymo, F. M. *Adv. Mater*. **2002**, *14*, 401.
23. (a) Kahn, O. and Martinez, C. J. *Science* **1998**, *279*, 44. (b) Kahn, O., Kröber, J. and Jay, C. *Adv. Mater*. **1992**, *4*, 718.
24. Prins, F., Monrabal-Capilla, M., Osorio, E. A., Coronado, E. and van der Zant, H. S. J. *Adv. Mater*. **2011**, *23* 1545.
25. Kahn, O. and Launay, J. P. *Chemtronics* **1988,** *3,* 140.
26. Vaucher, S., Li, M. and Mann, S. *Angew. Chem., Int. Ed.* **2000**, *39*, 1793.
27. Catala, L., Gacoin, T., Boilot, J. P., Rivière, E., Paulsen, C., Lhotel, E. and Mallah, T. *Adv. Mat*. **2003**,15, 826.
28 (a) Fouché, O., Degert, J., Daro, N., Forestier, T., Deplanche, C., Létard, J. F. and Freysz, E.

presented at European Conference on Molecular Magnetism, Tomar, Portugal, October **2006**. (b) Létard, J.-F., Guionneau, P. and Goux-Capes, L. *Top. Curr. Chem.* **2004**, *235*, 221.

29. Coronado, E., Galán-Mascarós, J. R., Monrabal-Capilla, M., García-Martínez, J. and Pardo-Ibáñez, P. *Adv. Mater*. **2007**, *19*, 1359.
30. Forestier, T., Mornet, S., Daro, N., Nishihara, T., Mouri, S.-I., Tanaka, K., Fouché, O., Freysz, E. and Létard, J.-F. *Chem. Commun.* **2008**, *36*, 4327.
31. Forestier, T., Kaiba, A., Pechev, S., Denux, D., Guionneau, P., Etrillard, C., Daro, N., Freysz, E., Létard, J.-F. *Chem. Eur. J.* **2009**, *15*, 6122.
32. Thibault, C., Molnár, G., Salmon, L., Bousseksou, A. and Vieu, C. *Langmuir* **2010**, *26*, 1557.
33. Galán-Mascarós, J. R., Coronado, E., Forment-Aliaga, A., Monrabal-Capilla, M., Pinilla-Cienfuegos, E. and Ceolin, M. *Inorg. Chem*. **2010**, *49*, 5706.
34. Titos-Padilla, S., Herrera, J. M., Chen, X.-W., Delgado, J. J. and Colacio, E. *Angew. Chem. Int. Ed*. **2011**, *50*, 3290.
35. Volatron, F., Catala, L., Rivière, E., Gloter, A., Stéphan, O. and Mallah. T. *Inorg. Chem.* **2008**, *47*, 6584.
36. Boldog, I., Gaspar, A. B., Martínez, V., Pardo-Ibañez, P., Ksenofontov, V., Bhattacharjee, A., Gütlich, P. and Real. J. A. *Angew. Chem. Int. Ed.* **2008**, *47*, 6433.
37. Martínez, V., Boldog, I., Gaspar, A. B., Ksenofontov, V., Bhattacharjee, A., Gütlich, P. and Real, J. A. *Chem. Mat*. **2010**, *22*, 4271.

7

SYNTHESIS OF BISTABLE SPIN-CROSSOVER NPS BASED ON THE SYSTEM $[Fe(Htrz)_2(trz)](BF_4)$

7.1 INTRODUCTION

7.1.1 Generalities about the compound $[Fe(Htrz)_2(trz)](BF_4)$

Among the spin-crossover (SCO) materials, the family of polymeric one-dimensional (1D) SCO compounds of general formula $[Fe(Rtrz)_3](A)_2$ (Rtrz = 4-substituted-*4H*-1,2,4-triazole, and A = monovalent anion), is certainly one of the most intensely studied. These systems were first synthesized by Haasnoot and co-workers in 1977,[1] but it was not until 1992 that they gained worldwide attention due to its utilization as active elements of display devices.[2] Among these materials, $[Fe(Htrz)_2(trz)](BF_4)$ (Htrz = 1,2,4-triazole and trz− = triazolate) results particularly interesting since it presents an abrupt spin transition centred above room temperature ($T_{1/2}^{\uparrow}$ = 391 K and $T_{1/2}^{\downarrow}$ = 349 K) with a remarkable hysteresis loop of 42 K. In 1994, a more detailed work published by Kröber, Kahn and Haasnoot thoroughly described the synthesis and the magnetic properties of the $[Fe(Htrz)_2(trz)](BF_4)$ complex.[3] This compound presents an abrupt transition with $T_{1/2}^{\uparrow}$ = 385 K and $T_{1/2}^{\downarrow}$ = 345 K for the first cycle, with a progressive reduction of $T_{1/2}^{\uparrow}$ in the subsequent cycles, ending with a stable hysteresis of *ca*. 40 K (see figure 7.1). Similar work based in the $[Fe(Htrz)_2(trz)](BF_4)$ complex was published in 1994 by Sugiyarto and Goodwin.[4]

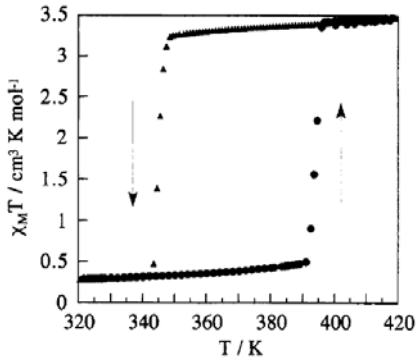

Figure 7.1 Temperature dependence of the molar magnetic susceptibility temperature product ($\chi_M T$) for $[Fe(Htrz)_2(trz)](BF_4)$.

Structural considerations were developed in parallel with the magnetic studies. Haasnoot *et al*.[1] enunciated the first hypothetic structure based on spectroscopic techniques, and referred to an octahedral environment of the Fe^{II} formed by two triazole and one triazolate ligands in a C_{2v} symmetry, charge balanced with a BF_4^- anion. Further investigations with Mössbauer and Diferential Scanning Calorimetry (DSC) confirmed this hypothesis.[3] This system is typically obtained as a microcrystalline powder. As a consequence, the sole structural data used for this compound during the last decades came from X-ray absorption spectroscopy.[5] This characterization gave a structural description of the close proximity of the metal centres (3.6–3.7 Å) and was used to corroborate the 1D polymeric structure, but gave no information on the crystal structure itself. Recently, a X-ray powder diffraction (XRPD) study on $[Fe(Htrz)_2(trz)](BF_4)$ led to a first structural hypothesis for both the HS and the LS species,[6] although a subsequent re-determination based on high resolution powder data has concluded with an advanced more precise crystal structure refinement.[7] The crystal structure is based on polymeric chains of Fe^{II} ions situated along the *b* axis with the three bridging triazoles in alternating invert positions, two Htrz ligands and one trz^- ligand (figure 7.2a), which gives the formula $[Fe^{II}(Htrz)_2(trz^-)](BF_4^-)$ (*Pnma* space group). Each BF_4^- ion is located in cavities formed by the triazole ligands (figure 7.2b) and no water molecules are found within the crystal structure. The distance between two neighbouring iron centres within a chain is exactly half of the *b* parameter. Each $[Fe(Htrz)_2(trz)]_n$ chain is surrounded by six identical adjacent chains (figure 7.3) with two different Fe···Fe interchain distances denoted d_1 and d_2 (figure 7.3). The crystal packing shows a pseudohexagonal structure, and it is the difference between d_1 and d_2 that mainly prevents **1** to adopt a hexagonal unit cell. The SCO produces a change of the intrachain Fe···Fe distance of 0.23 Å, with a variation of the *b* parameter of *ca*. 6.3 %, while the *a* and *c* parameters vary *ca*. 1.0 % and 4.0 %, respectively. The corresponding volume variation (11.5 %) appears larger than in other SCO materials (1–5 %).[8] This structural study confirms a chain architecture, that is formed by $[Fe(Htrz)_2(trz)]_n$ chains connected through short N–H···N contacts. Therefore, the unusually abrupt transition and large hysteresis of

40 K above room temperatures is consequently ascribed to this structural characterization.

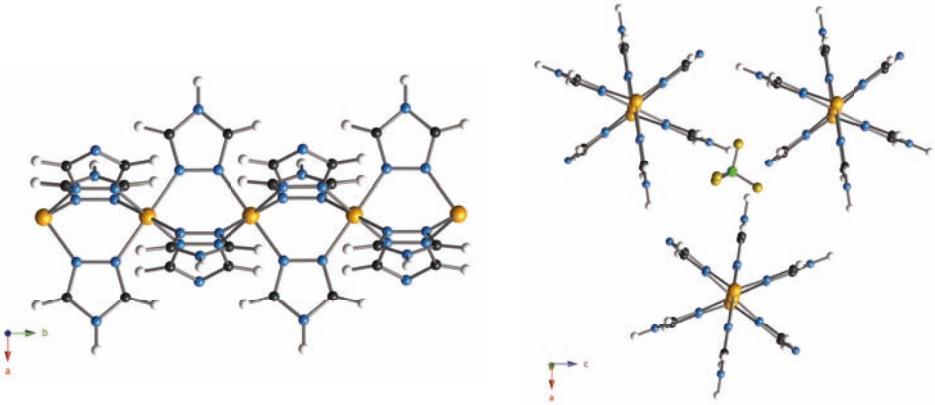

(a) (b)

Figure 7.2 (a) View of the cationic chains of $[Fe(Htrz)_2(trz)](BF_4)$ in which Fe^{II} are aligned parallel along the *b* axis with the three bridging triazoles in alternating invert positions (BF_4^- anions are omitted for clarity). (b) View of the BF_4^- anion cavities within the crystal packing of $[Fe(Htrz)_2(trz)](BF_4)$.

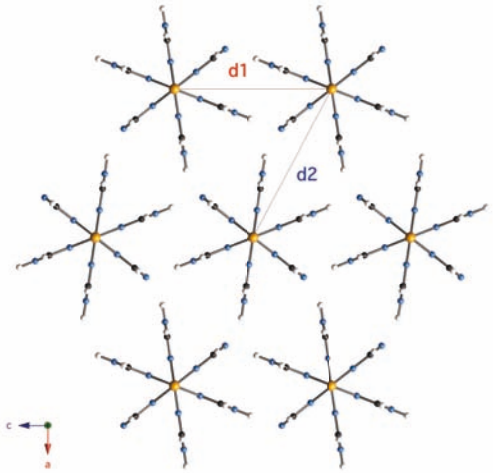

Figure 7.3 Crystal packing of $[Fe(Htrz)_2(trz)](BF_4)$ showing interchain distances d_1 (red) and d_2 (blue).

7.1.2 $[Fe(Htrz)_2(trz)](BF_4)$ at the nanometre scale

One of the most intriguing aspects of the SCO phenomenon concerns the critical size of the domain responsible of the SCO. This interest arises from the fact that SCO is a truly molecular phenomenon, and then, it is possible to reduce the size of SCO solid particles to reach the nanoscale while preserving the SCO phenomenon although reducing the cooperativity.[9] A plausible method to obtain SCO-NPs is based on the use of the reverse micelle technique.[10] This method was employed by Létard *et al.*[11] to produce spin-crossover NPs (SCO-NPs) of the system $[Fe(NH_2\text{-}trz)_3]Br_2$, Lauropal 205 as surfactant, and reaching sizes of 30 to 120 nm. The first NPs (NPs) based on the $[Fe(Htrz)_2(trz)](BF_4)$ system were synthesized by our group in 2007 following the same reverse micelle technique but using instead AOT as the surfactant (section 7.1.3).[12] These NPs were shown to exhibit abrupt transitions and large hysteresis very similar to the bulk material, but with a reduced size of *ca.* 11 nm (figure 7.4). Along this line, many studies have been developed and NPs ranging from only a few nanometres up to 100 nm have been obtained with reasonably polydispersity.[13] More recently, NPs of $[Fe(Htrz)_2(trz)](BF_4)$ have been synthesized in the presence of TEOS (tetraethoxysilane), and a hybrid SiO_2–SCO system that can incorporate multifunctionality (luminescence and SCO) has been obtained.[14]

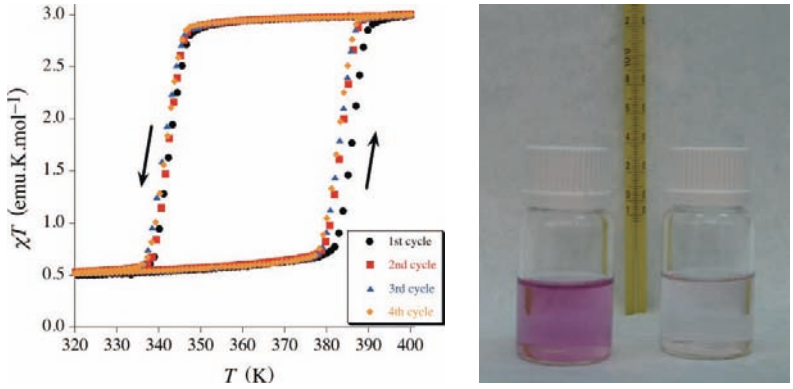

(a) (b)

Figure 7.4 (a) Magnetic thermal hysteresis for as-prepared $[Fe(Htrz)_2(trz)](BF_4)$ NPs. (b) Bistability of a suspension of the title NPs in octane: in the low-spin state (left) and in the high-spin state (right).

7.1.3 Generalities about the micellar systems

7.1.3.I Some relevant definitions

The word amphiphile comes from the Greek roots *amphi*, which means "double", and *philos,* which expresses affinity. An amphiphilic substance exhibits a double affinity, or, in terms of chemistry, a polar-apolar duality. A typical amphiphilic molecule is based on two parts: a polar group and an apolar group, which is in general a hydrocarbon chain. The polar part is often called hydrophilic or hydrophile since it exhibits a strong affinity for polar solvents, water among them. The apolar part is called hydrophobe or lipophile, from Greek roots *phobos* "fear" and *lipos* "grease".

A particular case of amphiphile molecules are the *surfactants* (short for surface-active-agent). These molecules exhibit superficial or interfacial activity due to their equilibrated hydrophilic and lipophilic tendencies. Surfactants performance consists on lowering the interfacial tension of the two phases in a microemulsion. An example of a surfactant molecule commonly used is sodium dodecyl sulfate.

7.1.3.II Reverse micelles as chemical reactors

As defined by Danielsson and Lindman[15] "*a microemulsion is a system of water, oil and amphiphile which is a single optically isotropic and thermodynamically stable liquid solution*". In other words, a microemulsion is a thermodynamically stable dispersion of two immiscible liquids in the presence of an emulsifier or surfactant.[16] These colloidal dispersions can be viewed as nanostructured chemical reactors confining the synthesis to the nanoscale. Consequently, they represent a very versatile reaction media that offers many applications in NP templating.[17] These particular dispersions have been widely used to fine control the particle size of many inorganic and organic materials due to their ability to solubilise insoluble materials. Boutonnet *et al*. in 1982 used for the first time reverse micelles as a template to synthesize metal NPs of Pt, Rh, Pd and Ir.[18] Later in 2000, Mann *et al*. used this *micellar* syntheses to control the growth of the Prussian Blue molecular magnet thus obtaining highly monodispersed magnetic NPs for the first time.[10]

This chemical reactor is also called a *micellar media* since the surfactant present in the solution tends to form aggregates of colloidal dimensions, which are known as *micelles*. Figure 7.5 shows different types of aggregates preferably formed by the surfactants in the microemulsions.

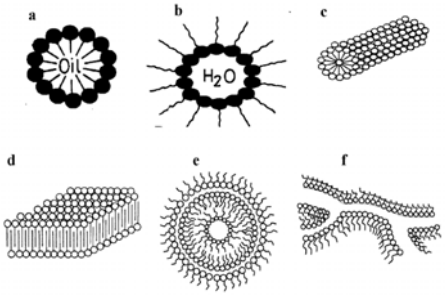

Figure 7.5 Schematic representation of organized aggregates of surfactants: (a) normal micelles, (b) reverse micelles, (c) cylindrical micelle, (d) planar lamellar phases, (e) onion-like lamellar phases and (f) interconnected cylinders. Reproduced from reference 16.

Microemulsions might be considered as a dynamic media, which means that the domains are not static, but are in continuous movement and collision with each other, thus permitting the interchange of material. This is the key point that enables this method for the synthesis of nanostructured coordination compounds. In a typical reverse micelle synthesis, the reactants, solubilised in individual reverse micelles (nanoreactors), come in close contact and undergo homogenous mixing. Micelles collide via random Brownian motion and coalesce to form dimers, which may exchange their contents and then break apart again. Therefore, the micellar exchange time depends directly on the collisions between micelles. This collision time (k_{ex} = exchange constant) is defined as $k_{ex} = (8/3)k_B T/\eta$, where k_B is the Boltzmann constant, T the temperature and η the viscosity.[19] The exchange process is fundamental to NP synthesis inside reversed micellar templates, allowing different reactants solubilised in separate micellar solutions to react upon mixing. Once intermicellar exchange of the reactants take place, nucleation starts with a specific growth rate leading to an increase of the size.[20] These reverse micelles favour the formation of small crystallites with a

narrow size distribution. In addition, at the latter stages of growth, steric stabilisation provided by the surfactant layer prevents the NPs from aggregating. A schematic diagram of the reaction dynamics for a binary system is given in figure 7.6.

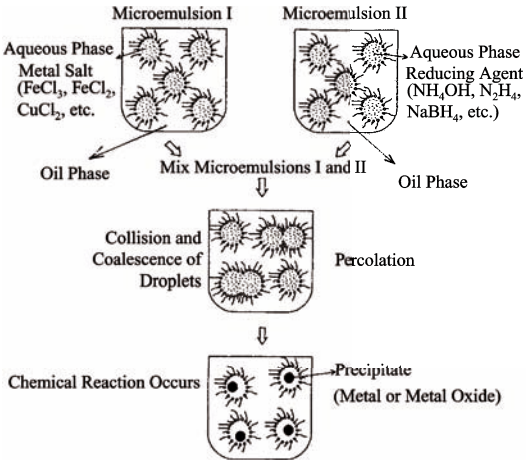

Figure 7.6 Mechanism proposed for the formation of NPs by the microemulsion approach. Reproduced from reference 20.

7.1.3.III The surfactant

The choice of the surfactant results a critical subject since it has a direct effect in the shape, size and stability of the NP. Surfactants can be classified depending in their dissociation in water as ionic or non-ionic:

Ionic Surfactants. This class encloses the anionic and the cationic surfactants, which are dissociated in water in an amphiphilic anion/cation respectively and its corresponding counterion. They are the most commonly used surfactants, although the cationic ones are in general more expensive and used as bactericides. The most common surfactants include, among others, alkylbenzene sulfonates, lauryl sulfate and di-alkyl sulfosuccinates for anionic surfactants and azo- compounds such as fatty amine salts and quaternary ammoniums as cationic surfactants.

Non-ionic Surfactants. They do not ionize in aqueous solution because their hydrophilic group is of a non-dissociable type, such as alcohol, phenol, ether, ester, or amide.

For the present study the surfactant of choice is the AOT sodium salt (sodium bis(2-ethylhexyl)sulfosuccinate) (figure 7.7). AOT is an anionic surfactant widely used in micellar systems. When a small amount of AOT is dissolved in organic solvents, thermodynamically stable reverse micelles are formed. These micelles consist of a hydrophilic core compartmentalized by the hydrophilic head group of the AOT, and with the hydrophobic alkyl tails extending into the nonpolar continuous phase solvent.

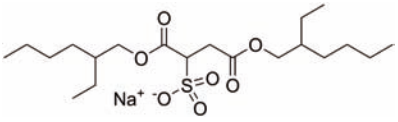

Figure 7.7 Chemical formula of AOT surfactant.

7.2 NANOPARTICLES OF $[Fe(Htrz)_2(trz)](BF_4)$

7.2.1 Experimental protocol

The experimental procedure follows the original protocol developed in our group in 2007[12] with some modifications that will be discussed in detail in the next paragraphs. The procedure has been divided in five different stages: (1) micellar composition; (2) micelle formation; (3) micellar exchange; (4) NPs precipitation; (5) NPs extraction.

I. *Micellar composition*. This first step involves the preparation of two separate micellar solutions incorporating the different reactants: an aqueous solution of $Fe(BF_4)_2.6H_2O$ (0.3 mL, 1 M) is added to a previously prepared solution of NaAOT (1 g) in *n*-octane (10 mL). Similarly, an aqueous solution of Htrz (0.3 mL, 3 M) ligand is added to a solution of NaAOT (1 g) in of *n*-octane (10 mL).

II. *Micelle formation.* The creation of the micelles is achieved by stirring the micellar solutions at room temperature. After *ca.* 30 min an optically isotropic and thermodynamically stable microemulsion is formed.

III. *Micellar exchange*. Once the microemulsions are stabilized, they are mixed at room temperature under Ar atmosphere. The microemulsion is stirred for 15 min to ensure the micellar exchange and thus the growth of the NPs. A characteristic pink colour appears immediately, indicating the occurrence of a nucleation process and the formation of the complex in an optically transparent suspension.

IV. *NPs precipitation*. Acetone is added to destabilize the microemulsion and therefore breaks the micelles. As a result, the NPs precipitate.

V. *NPs extraction*. NPs are collected by centrifugation (12000 rpm, 10 min) after several washing cycles with portions of acetone (x3) and ethanol (x3) to remove excess of water and surfactant. Finally, the powdered sample is dried under vacuum for 2 h to remove excess of solvent.

Hence, the presented protocol has been developed following a careful evaluation of the relevant parameters in each of the different stages of the procedure. The selection of these parameters has been the origin of controversial debates.[21] This is mainly due to the complexity in understanding all the energetic contributions existing in colloidal systems, but more importantly, given the different behaviour of each structure in a micellar system. However, the key parameters that have shown to influence size and polydispersity are the following: (i) the type of solvent employed, (ii) the surfactant or co-surfactants used, (iii) the concentration of reagents, and (iv) the molar ratio ω_0 = [water] / [surfactant]. In addition to these parameters, the physical properties of the NPs can be influenced by other external factors such as temperature, reaction time and method of precipitation and extraction. In this *Chapter*, a comprehensive analysis for the selection of parameters has been investigated and is presented in the following order: 1) the type of solvent used, 2) the ratio and concentration of reagents, 2) the surfactant employed, 3) the times necessary for micelle formation and 4) intermicellar exchange and finally, 5) the precipitation and extraction methods. The effect of these parameters on the final size of the NPs has been studied at each stage of the method with the aim to find a suitable value for each parameter to establish a general procedure (section 7.2.2). Table 7.1 summarizes the ensemble of parameters that have

been modified and will be discussed in detail in the following paragraphs. Finally, the effect of the molar ratio, ω_0, has been studied in detail and will be fully described in the separate section 7.3.

Table 7.1 Selection of parameters investigated at each stage of the procedure.

I	II	III	IV and V
Micellar composition	*Micelle formation*	*Micellar exchange*	*NP precipitation and extraction*
1) Solvent effect 2) Surfactant 3) Ratio and concentration of reagents 4) Molar ratio, ω_0	5) Time for micelle formation	6) Time for micellar exchange	7) Destabilization, centrifugation and washing.

7.2.2 Selection of synthetic parameters

7.2.1.I Micellar composition

1) Solvent effect. The type of solvent used is a relevant parameter to take into account since particle size is affected by the solvent type due to modulation of the growth rate. This is known as the "solvent effect". In all the experiments presented in this work, *n*-octane has been used as the continuous phase. Importantly, the same solvent to dissolve the two precursors (water) has been used in the two micellar solutions. This is a modification from the previous method in which different solvents were used in each microemulsion (water to dissolve the iron salt and ethanol to dissolve the ligand). With this variation, the two micellar systems present an equivalent composition in terms of solvents and surfactant, thus minimizing possible side effects derived from the use of different solvents such as variation in density or polarity.

For a given value of ω_0, [water] / [surfactant], the two micellar solutions only differ in the type of reagent, Fe^{II} or triazole. Especially relevant is the difference in pH of the

two micellar systems, which is between 1–2 for the Fe^{II} microemulsion and *ca.* 6 for the triazole microemulsion. This discrepancy is responsible of the different micelle formation, and will be discussed in section 7.2.II.

2) Surfactant and co-surfactant. As previously mentioned in section 7.1.3.III, the surfactant selected is the AOT, since it is the most studied surfactant and also affords the smallest NPs obtained for this system. The use of the behenic acid, which was initially proposed to perform as the co-surfactant, has been investigated. A simple experiment has been proposed in which three suspensions of NPs are synthesized in parallel keeping identical all the parameters, but containing different amounts of behenic acid: (1) stoichiometric amounts of behenic acid (AOT based), (2) catalytic amounts and (3) without behenic acid. The results obtained in the 3 systems present negligible differences in sizes. However, after 2 days without stirring a precipitate appears in sample 1. Several conclusions can be extracted from this experiment: first, colloidal stability is enhanced in the absence of this co-surfactant and, most importantly, contrary to previous studies, the synthesis of the SCO NPs is feasible in the absence of the behenic acid. For these reasons, and given the uncertain beneficial role of the behenic acid as a co-surfactant, it has been eliminated from the original synthetic procedure.

3) Ratio and concentration of reagents. In a first study, the appropriate molar ratio for the reagents Fe:Htrz has been investigated keeping constant all other factors. The stoichiometric relation from the general formula is 1:3 (Fe:Htrz). In a general procedure, different micellar systems with a fixed concentration of Fe^{2+}, [Fe], is used ([Fe] = 1), and a variable amount of Htrz has been used to obtain the corresponding relations 1:2.5, 1:3 and 1:5. For the three samples, the micellar solutions have been prepared normally and with a correct solubility of the reagents. Upon intermicellar exchange, a pink suspension indicative of the formation of NPs is obtained. The resulting suspensions are analyzed by dynamic light scattering (DLS) and the size of the NPs is given as number-based % (table 7.2). In the case of the triazole deficient system, ratio 1:2.5, a precipitate is formed during the intermicellar exchange, while

NPs of > 50 nm remain stable in the suspension. When an excess of triazole is used, ratio 1:5, a high polydespersity is observed with NPs of 8 and 42 nm. Finally, for the stoichiometric 1:3 ratio, NPs of 15 nm with a narrow distribution have been obtained. These results clearly indicate that the appropriate relation of reagents is the stoichiometric 1:3 ratio.

Table 7.2 Size for the NPs synthesized with different Fe:Htrz ratios.

[Fe]	[Htrz]	Size
1	2.5	>50 nm and >1μm
1	3	15 nm
1	5	8 and 42 nm

Then, once the ratio of reagents is established, it is time to study the optimal concentration. This parameter refers to the concentration of reagents *inside* the micelle. Several studies suggest that by increasing this concentration, the NP is reduced in size and in polydispersity.[22] An additional limitation is the solubility of the reagents in water, since high concentrations may result in poor solubility. With these two antagonic premises, in which higher concentrations afford smaller NPs with enhanced polydispersity but poor solubility, the optimal Fe^{II} concentration, [Fe], has been designed as the highest plausible concentration that permits a correct stabilization of the micellar solution. In order to find the appropriate concentration of reagents for this system, the following experiment has been performed. Different Fe^{II} concentration, [Fe] = 0.5, 1 and 1.5 M, have been tested by changing the quantity of $Fe(BF_4)_2.6H_2O$ while maintaining constant the water volume (0.3 mL) and the surfactant (1 g). As previously described, stoichiometric amounts of Htrz has been used in each case. For [Fe] < 0.5 M, the micellar solutions are prepared without noticeable difficulty, although upon mixture of the two micellar solutions a brown colour appears, indicating a partial or complete oxidation of the Fe^{II}. Similarly, a Fe^{II} concentration [Fe] = 1.5 M results to be an upper limit since the corresponding stochiometric amount of Htrz is not soluble in 0.3 mL of water ([Htrz] = 4.5 M). In all

cases the resulting suspensions have been analyzed by DLS and the size of the NPs is given as the hydrodynamic diameter based in number %. Elemental analysis of the precipitated NPs and mean size distributions are given in table 7.3.

Table 7.3 Size and elemental analysis for NPs synthesized with different [Fe].

[Fe]	Size (nm)	Elemental analysis	C [%]	N [%]	H [%]	S [%]	MW
0.5	25	experimental	33.57	22.39	4.49	3.21	
		$[Fe(Htrz)_2(trz)_1](BF_4)\cdot(AOT)_{0.7}$	36.39	19.10	5.18	3.46	660.03
1	15	experimental	16.87	29.31	3.13	0.22	
		$[Fe(Htrz)_2(trz)_1](BF_4)\cdot(AOT)_{0.02}$	17.55	28.79	2.01	0.15	437.95
1.5	11	experimental	19.08	27.85	2.39	0.41	
		$[Fe(Htrz)_2(trz)_1](BF_4)\cdot(AOT)_{0.04}$	18.29	28.22	2.14	0.29	446.84

From a general point of view, the three concentrations could be selected since they afford NPs with a suitable polydispersity and are in the optimal range for the proper solubility of reagents. However, and following the above-mentioned criteria, a Fe^{II} concentration [Fe] = 1 presents some advantages, which are the formation of NPs with a reduced size compared with Fe^{II} concentration [Fe] = 0.5 M, and an effective and rapid micelle formation as compared with a Fe^{II} concentration [Fe] = 1.5 M (see section 7.2.2.II for details). Consequently, the most suitable concentration of [Fe] and [Htrz] for this system are 1 M and 3 M, respectively.

4) Water to surfactant molar ratio (ω_0). The role of this parameter has been extensively reviewed in the past decades.[23] However, many studies have often afforded different conclusions. Generally, the final size of the NP depends on the water content, which is described by the water to surfactant molar ratio, ω_0. Effectively, micelles play a pattern effect and, in principle, it is possible to influence the NP size by fine-tuning these chemical reactors. It has been commonly established that an augment of the ω_0 parameter produces an increase of the droplets and therefore an augment of the NP size. It is also generally observed that the size of the

nanocrystals produced differs from that of the initial nanoreactors. Importantly, the variation in particle size with ω_0 is strongly dependent on the nature of the chemical reaction and this is mainly the reason why it is difficult to establish a clear tendency and. A detailed study regarding this effect is presented in section 7.3.

7.2.2.II Micelle formation

5) Time for micelle formation. Once the parameters concerning the micellar composition are fixed, it is necessary to establish the conditions in which the micelles are formed. The essential factor in this step is the time required for stabilization of the micelles upon stirring. The micelle formation occurs at room temperature and upon vigorous stirring. This agitation permits the mixture of the different components of the micellar mixture and thus the formation of the micelles resulting in a homogenous media. This phenomenon can be easily detected since a visually clear and translucent homogenous solution suggests the formation of the micelles (figure 7.8). The time required to obtain a homogenous optically isotropic and thermodynamically stable microemulsion depends on the ratio water/surfactant, ω_0. For instance, for $\omega_0 = 7$, the Fe^{II} microemulsion ([Fe] = 1 M) is stabilized in *ca.* 30 minutes, while is *ca.* 3 min for the triazole microemulsion ([Htrz] = 3 M). This difference is associated with the difference in pH of both micellar systems (between 1–2 for the Fe^{II} microemulsion and 6–7 for the triazole microemulsion). Several considerations can be finally discussed: i) for Fe^{II} microemulsions, the time required to stabilize the microemulsion shows a linear dependence with the concentration as seen in figure 7.9 in the 0.1–1.5 M range; ii) for Htrz microemulsions this time is constant in the 0.3–3 M range.

Figure 7.8 Pictures of the micellar solution (a) before and (b) after micelle formation upon stirring showing the difference in transparency.

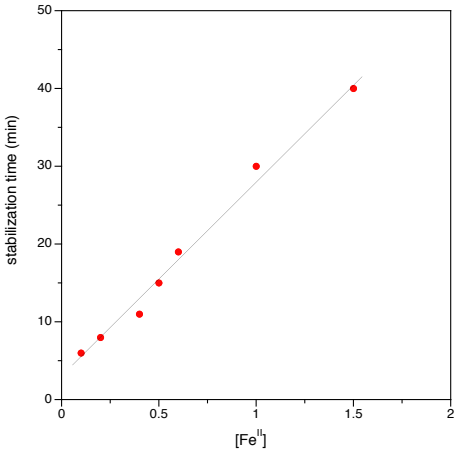

Figure 7.9 Representation of the stabilization time for the Fe^{II} microemulsions as a function of the metal concentration (0.1–1.5 M) with $\omega_0 = 5$ (the black line serves as a reference to linearity).

7.2.2.III Micellar exchange

6) Time for micellar exchange. In this part of the process the two microemulsions are combined and stirred to permit the micellar exchange. The parameters relevant in this step are the reaction time and the temperature. Typically, the appropriate temperature for the synthesis is at room temperature, temperature at which the system remains stabilized in the LS. There are several reasons for which this is an optimal temperature: first, micelles are easily stabilized due to the absence of temperature fluctuations, and in addition, the system in the LS state possesses an intense colour that serves as an indication of the completion of the reaction. The use of an argon atmosphere prevents Fe^{II} from oxidation. On the contrary, the reaction time has been reduced from 4 h to 30 min, for which completion of the intermicellar exchange is already reached. Further stirring has been proved to promote no effect on the final NP size.

7.2.2.IV NPs precipitation and extraction

7) Destabilization, centrifugation and washing. Finally, the reaction is stopped by destabilization of the micelles upon addition of acetone. This addition promotes the

precipitation of the NPs, which are then collected by centrifugation at 12000 rpm. By this method, the NPs are separated form the *n*-octane/surfactant mixture. Further treatment with acetone portions (x3) ensures elimination of the excess of reagents, water and above all, the excess of surfactant. By this new method of precipitation/extraction, the excess of surfactant in the final NPs has been highly reduced, although not completely. Unfortunately, total elimination of the surfactant excess still remains a question difficult to solve. This may be attributed to the ionic nature of the AOT, which favours the anionic exchange between the AOT^- and the BF_4^-. As a result, part of the AOT strongly interacts with the NP and difficults its elimination. In spite of this, compared with other surfactants AOT represents a clear advantage, which is the fact that micelles formed by AOT have undoubtedly afforded the smallest particle size ever obtained for this system. For instance, NPs based on the same system synthesized by the group of Létard with the non-ionic surfactant Lauropal, present a minimum size of 90 nm.

7.3 CONTROL OVER THE SIZE IN $[Fe(Htrz)_2(trz)](BF_4)$ NPS

7.3.1 Effect of ω_0 variation on the nanoparticle size

As previously mentioned in section 7.2.1.I, the study of the ω_0 (water to surfactant molar ratio) effect on the NP size has been at the origin of intense debate. This effect has been often studied in micellar systems containing AOT. General conclusions claim that an increase of the ω_0 parameter produces an increase of the droplets and therefore an increase of the NP size, although different results can be obtained depending on the system under study. For the system $[Fe(Htrz)_2(trz)](BF_4)$, this effect of the ω_0 on the particle size was already studied.[13c] In this preliminary work, the general trend was indeed observed for two different sizes, 11 and 6 nm NPs. However, given that the number of samples used is limited, it was difficult to extract a definite conclusion. Therefore, extensive analyses are required in order to establish a more

accurate tendency. At this point, and given the modifications of the synthetic parameters, a more detailed study has been proposed here. In this experiment, the concentration of surfactant has been modified while the water content remains constant, so that the concentration of reagents is not altered. Table 7.4 presents the contents of the micellar compositions used in each synthesis of this study, which strictly follows the first three steps of the protocol previously detailed.

Table 7.4 General parameters used in all the synthesis to study the ω_0 effect.

[Fe]	[Htrz]	V H_2O (mL)	V *n*-octante (mL)	mol AOT
1 M	3 M	0.3	10	variable

A series of NPs **1.1**–**1.13** has been synthesized in which each sample possesses a variable amount of AOT. Thus, from **1.1** to **1.13** a progressive increase of ω_0 (by a decrease of the AOT content) has been reached. The variable of control is the size of the NPs, which is given as the hydrodynamic diameter, obtained by measuring the suspension of the as synthesized NPs in octane by dynamic light scattering (DLS). To start with, the ω_0 range of study has been determined: for values of $\omega_0 < 5$ the micellar exchange becomes unstable and precipitation occurs; for $\omega_0 > 11.5$ the time for micellar formation is extremely large (> 5 hours). Consequently, the study has been located in the $5 < \omega_0 < 11.5$ range. Table 7.5 summarizes the NPs synthesized with the different ω_0 values and their corresponding NP size (DLS-number based).

By representing the particle size as a function of ω_0 (figure 7.10) three different zones with clearly diverse tendencies can be distinguished. The first region corresponds to the samples **1.1**–**1.4**, synthesized in the $5 < \omega_0 < 6.5$ range, for which an average particle size of *ca*. 3.8 (1.2) nm is obtained. Upon further increasing the ω_0 parameter (by decreasing the AOT content), a clear increase of the NP size is observed for samples **1.5**–**1.8**, synthesized in the $7 < \omega_0 < 9$ range, which present an average size of *ca*. 14.6 (1.8) nm. Finally, successive increase of ω_0 from 9 to 11.5 in samples **1.9**–**1.13** affords a new series in which the same particle size of *ca*. 10 nm is constantly obtained.

Table 7.5 Samples obtained as a function of the ω_0 parameter and corresponding size distribution measured by DLS (number-based).

Sample	ω_0	Size (nm)	Sample	ω_0	Size (nm)
1.1	5	4.5	**1.7**	8	13.5
1.2	5.5	3.8	**1.8**	9	15.7
1.3	6	3.6	**1.9**	9.5	10
1.4	6.5	3	**1.10**	10	10
1.5	7	13.5	**1.11**	10.5	10
1.6	7.5	15.7	**1.12**	11	11
			1.13	11.5	10

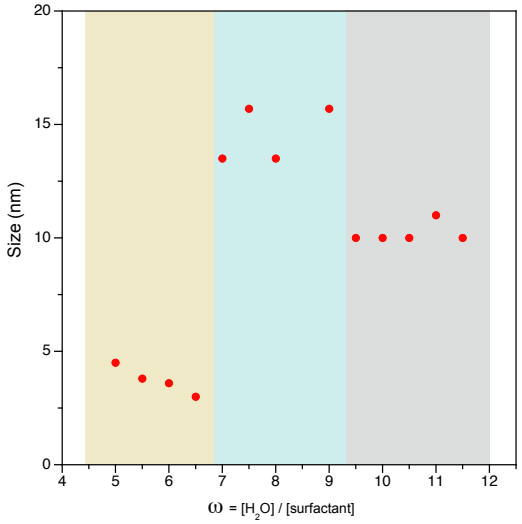

Figure 7.10 Representation of the NP size of **1.1**–**1.13** as a function of the ω_0.

This difference in tendencies can be explained as follows:

i) At low ω_0 ($\omega_0 < 5$, the water inside the reverse micelles can be considered "bound", since there is insufficient water available to solvate both the surfactant head group and

the counterion.[23e] With the water "bound", the micelle interface is said to be "rigid", lowering intermicellar exchange and therefore lowering as well the growth rates. Therefore, this ends with small NPs due to their difficulty in growing.

ii) As ω_0 is raised, the micelle interface becomes more fluid due to the presence of more water molecules, so the rate of growth increases until a given $\boldsymbol{\omega_0}$ range, promoting an increase of the particle size.[24,25]

iii) At this point, a further decrease of the amount of AOT added (increase of $\boldsymbol{\omega_0}$) causes the presence of extra of water in the micelles, which merely dilutes the reagents and decreases the reaction rates, leading to a decrease in the particle size.[24]

From the results obtained, several conclusions can be extracted for this system: *i)* the size of the NPs is noticeably affected by the ω_0 parameter; *ii)* three different ω_0 ranges with clear size tendencies can be differentiated; *iii)* manipulation of the particle size is possible upon accurate selection of the ω_0 parameter.

Complete characterization of particles has been developed for a representative sample of each group of sizes and will be discussed in the following paragraphs. In this sense, samples **1.6** (16 nm), **1.10** (10 nm) and **1.2** (4 nm) have been selected. Size distribution and EA of samples **1.6**, **1.10** and **1.2** are illustrated in figure 7.11 and table 7.6 respectively.

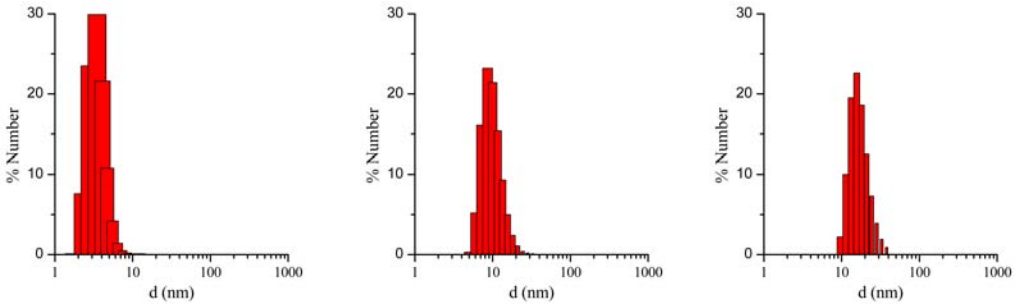

(a) (b) (c)

Figure 7.11 Number-based particle size distribution for the colloidal suspension **1.6** (a), **1.10** (b) and **1.2** (c) obtained by DLS analysis. (Parameters used for the data analysis: T = 293 K, refractive index = 1.450).

Table 7.6 Size and elemental analysis for samples **1.6**, **1.10** and **1.2**.

Sample	Size (nm)	Elemental analysis	C [%]	N [%]	H [%]	S [%]	MW
1.6	16	experimental	25.59	28.93	3.48	1.77	
1.10	10	experimental	26.24	28.82	3.38	1.66	
1.2	4	experimental	29.63	26.13	3.99	2.54	
Theoretical		$[Fe(Htrz)_2(trz)_1](BF_4)\cdot(AOT)_{0.2}$	27.43	28.78	3.86	1.46	437.75
Theoretical		$[Fe(Htrz)_2(trz)_1](BF_4)\cdot(AOT)_{0.3}$	29.88	26.14	4.00	1.99	482.21

The determination of the size of the NPs permits to estimate the number of Fe^{II} atoms that contains each single NP. This can be done by considering the structural parameters (unit cell: 17.35 Å, 7.33 Å, 9.19 Å, 90 °, 90 °, 90 °; space group *Pnma;* Z = 4).[7] The shape of the NPs plays an important role in this estimation since the number of Fe^{II} atoms varies depending on the direction of growth. Based on AFM studies (figure 7.12), it can be observed that these NPs are not spherical but possess an elongated shape, with one dimension approximately twice the other two dimensions. This larger direction can be assigned to the *b* parameter, which corresponds to the direction in which the cationic chains, $[Fe(Htrz)_2(trz)]^+$, are aligned. Table 7.7 summarizes the number of Fe^{II} atoms in relation with the NP size, and figure 7.13 illustrates the most likely composition of the 4 nm NPs.

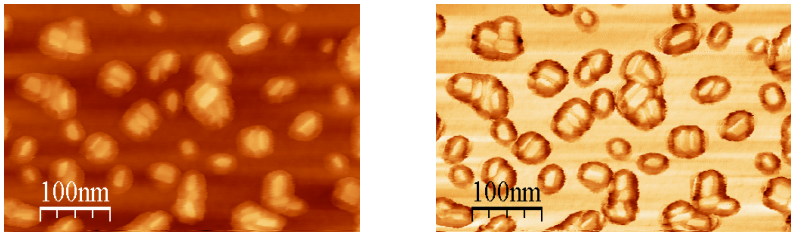

(a) (b)

Figure 7.12 AFM images measured in tapping mode of NPs on native SiO_2 (a), topography image; (b), phase image.

Table 7.7 number of Fe^{II} atoms in relation with the NP size for samples **1.6**, **1.10** and **1.2**.

Sample	Size (nm)	Number of Fe^{II} atoms
1.6	16	3960
1.10	10	840
1.2	4	40

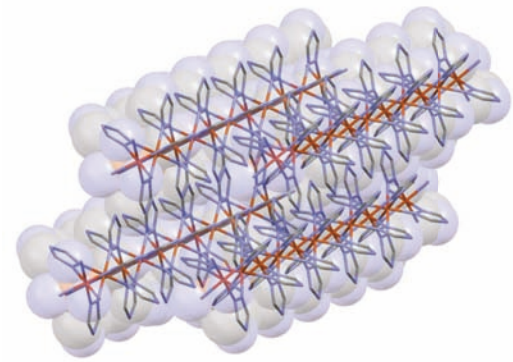

Figure 7.13 Cartoon representation of the most likely composition of the 4 nm NPs

7.3.2 Influence of the size on the spin transition

Once established the best synthetic parameters and the ω_0 size dependence for this system, the next step consists on the analysis of how the size variation affects the spin transition. For samples **1.6**, **1.10** and **1.2**, steps 4 and 5 of the synthetic protocol have been applied (precipitation and extraction). Solid dried samples have been used for magnetic measurements. The thermal dependence of $\chi_M T$ for the three samples is shown in figure 7.14, where χ_M is the molar magnetic susceptibility (in emu.K.mol^{-1}). Thermal spin transitions are characterized $T_{1/2}^{\uparrow}$ and $T_{1/2}^{\downarrow}$ which are defined as the temperatures for which 50% of both the LS and HS Fe^{II} centres is present in the sample in the cooling and warming modes, respectively. Finally, ΔT represents the

hysteresis width that appears in all the spin transitions. All these parameters are summarized in table 7.8.

NPs of **1.6** (*ca.* 16 nm) exhibit an abrupt spin transition centred above room temperature with a large hysteresis of 38 K ($T_{1/2}^{\uparrow}$ = 379 K and $T_{1/2}^{\downarrow}$ = 341 K), which is comparable to that of the bulk material ($T_{1/2}^{\uparrow}$ = 385 K and $T_{1/2}^{\downarrow}$ = 345 K). This behaviour is reproducible over successive thermal cycles. A relatively large HS remnant fraction of 20 % (higher than that found in the bulk) remains at low temperatures, which is indeed typical for these nanostructured chain compounds. This characteristic HS remnant fraction can be ascribed to the different coordination environment of the terminal Fe^{II} in the chains, which is coordinated to oxygen atoms from water ligands instead of the nitrogen atoms of the triazole ligand. Therefore, the terminal Fe^{II} in the chain presents a lower ligand field strength, which favours the HS state in all range of temperatures. In nanostructured materials, the number of terminal Fe is larger than in the bulk, and consequently the remnant fraction is also larger. When the particle size is reduced to 10 nm (**1.10**), the magnetic behaviour starts to deviate from the bulk (figure 7.14). A hysteresis of 31 K ($T_{1/2}^{\uparrow}$ = 374 K and $T_{1/2}^{\downarrow}$ = 343 K) is found in this case, with a similar remnant HS residue (~20 %). In addition, the sharpness of the hysteresis is maintained.

Magnetic measurements for a representative sample of the smallest particles obtained (**1.2**) show a reduced hysteresis loop of 24 K ($T_{1/2}^{\uparrow}$ = 367 K and $T_{1/2}^{\downarrow}$ = 343 K), which corresponds to a 40 % reduction of the hysteresis found in the macroscopic material. However, the occurrence of a hysteresis of 24 K is highly remarkable for 4 nm NPs since hysteresis is a consequence of elastic cooperativity, which seems to be still maintained for this small size. The HS residue is of *ca.* 23 %, slightly larger as expected for a smaller particle size. In addition, the sharpness of the transition is significantly maintained. This study confirms the tendency of reduced size NPs to gradually suppress the first-order phase transition in favour of a continuous spin

transition.[26]

Finally, the difference in the magnetic properties can be described in terms of the number of Fe^{II} atoms that form the NP (see table 7.7). Therefore, for the smallest NPs, (sample **1.2**) the occurrence of a hysteresis of 24 K is achieved by the cooperative interaction of 4 chains containing 10 Fe^{II} atoms each.

Table 7.8 Physical characteristics of the thermal spin transition $T_{1/2}\uparrow$ and $T_{1/2}\downarrow$ and particle sizes (see text for definitions).

Sample	Size (nm)	$T_{1/2}\uparrow$	$T_{1/2}\downarrow$	ΔT	%HS
1.6	16	379	341	38	23
1.10	10	374	343	31	20
1.2	4	367	343	24	20

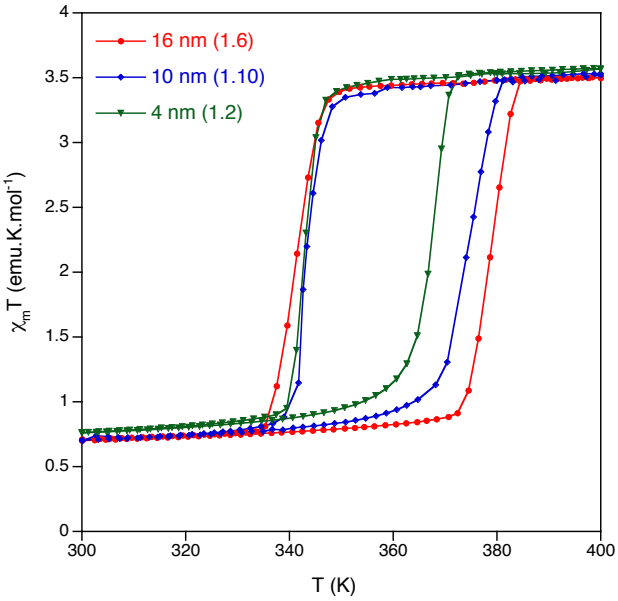

Figure 7.14 Temperature dependence of the molar magnetic susceptibility temperature product ($\chi_M T$) for samples **1.2**, **1.10** and **1.6** after several heating-cooling modes.

7.4 CONCLUSIONS

In this *Chapter*, a detailed description of the synthetic protocol used for the synthesis of SCO NPs is presented. In comparison with the previous method developed in our group, the protocol herein described considers all the relevant parameters that play a role in the physical properties of the NPs. To better rationalize and control the synthesis of $[Fe(Htrz)_2(trz)](BF_4)$ NPs by the reverse micelle technique, the key parameters responsible of the final physical properties have been modulated. The parameters investigated are: the type of solvent (*n*-octane and water) the ratio and concentration of reagents ([Fe] = 1 and [Htrz] = 3), the surfactant used (AOT in the absence of behenic acid), the times for micelle formation (which depends directly to ω_0) and intermicellar exchange (30 min) and finally the precipitation and extraction methods (addition of acetone followed by centrifugation processes with washing steps). Most of these parameters have a minor influence on the final physical properties by their own, but provide a robust and efficient approach when systematically adjusted in the overall procedure.

In addition, there is a specific parameter that plays a crucial role in the physical properties of the $[Fe(Htrz)_2(trz)](BF_4)$ NPs, which is the water to surfactant ratio, ω_0. As a matter of fact, the effect of ω_0 had been already investigated. In that preliminary work, the general trend was indeed observed for two different sizes, 11 and 6 nm NPs. However, given that the number of samples used was limited, it was difficult to extract a definite conclusion. Therefore, extensive analyses have been developed in order to rationalize a more accurate tendency. The results obtained over 13 samples, which only differ in the ω_0 used, show that there are three different ranges of ω_0 at which only one size is preferably obtained. It is then possible to synthesize NPs of 4, 10 or 15 nm with low polydispersity in a controlled manner, by only selecting the appropriate ω_0 value. Thus, this method provides an efficient approach to control the NPs size.

The effects of the reduction in size on the spin transition have been investigated by measuring the magnetic properties of 3 samples, a representative example of each size group. Importantly, all three NP samples exhibit the same abruptness characteristic of this system. However, noticeable changes are observed in the hysteresis width, which is significantly reduced with the progressive miniaturization of the NP length. It is important to note that this reduction of the hysteresis is produced by the decrease of $T_{1/2}\uparrow$ while $T_{1/2}\downarrow$ remains unaltered. This is, with the progressive decrease in size from 16 nm to 10 nm and then to 4 nm, $T_{1/2}\uparrow$ has decreased from 379 K to 374 and 367 K, respectively. Thus, modulation of the transition temperature is only possible upon chemical modification, for instance, by ligand replacement.

Importantly, for NPs with a particle size of 16 nm or below, the SCO behaviour starts to deviate from that of the system in bulk. It can be conclude that, for this system, the critical size at which the properties of the bulk are compromised is *ca*. 16 nm. This study was already effectuated on two samples of 11 and 6 nm synthesized by the previous method, and the conclusion extracted agrees with the present study. Finally, it is demonstrated that a relatively large hysteresis of 24 K is preserved for NPs of a few nm (3–4 nm). The fact that the SCO phenomenon is retained at such small sizes is a remarkable characteristic of this particular system, and may be attributed to the strong cooperativity and dimensonality of the system. In this sense, this nanostructured material is probably the most promising candidate for the implementation of SCO-NPs in magnetic devices.

7.5 METHODS

7.5.1 General synthesis

In a typical procedure, the first step involves the preparation of two separate microemulsions incorporating the different reactants. An aqueous solution of $Fe(BF_4)_2.6H_2O$ (0.3 mL, 1M) with *ca*. 10 mg of ascorbic acid is added to a previously prepared solution of NaAOT (1 g) in *n*-octane (10 mL) under vigorous stirring.

Similarly, an aqueous solution of the ligand Htrz (0.3 mL, 3M) is added to a solution of NaAOT (1g) in of *n*-octane (10 mL) under vigorous stirring. After 30 minutes of continuous stirring the two microemulsions become stable and are mixed at room temperature under Ar atmosphere. The resultant microemulsion is stirred for 30 min to ensure the intermicellar exchange and thus the growth of the NPs. Then, acetone is added to break the microemulsion and the NPs are collected by centrifugation after several washing cycles with acetone (x3) to remove excess of surfactant. Finally, the powdered sample is dried under vacuum for 2h to remove excess of solvent.

7.5.2 Physical measurements

Elemental analysis was carried out at the Centro de Microanálisis Elemental, Universidad Complutense de Madrid. Dynamic light scattering (DLS) measurements were performed on a Zetasizer Nano-S (Malvern Instrument, UK). A He-Ne laser at λ=632 nm was used as a light source and the scattering angle was 173º. The results of scattering data were analyzed via a non-negative least squares algorithm (GP) as implemented in the Zetasizer Nano software [ref: http://www.malvern.com].

Magnetic measurements. Magnetic susceptibility measurements were performed on single-phased polycrystalline samples with a Quantum Design MPMS-XL-5 SQUID susceptometer. The susceptibility data were corrected from the diamagnetic contributions as deduced by using Pascal's constant tables. The susceptibility data were collected at 1 $K \cdot min^{-1}$ with an applied field of 0.1 T.

7.6 REFERENCES

1. Haasnoot, J. G., Vos, G., Groeneveld and W. L*., Z. Naturforsch* **1977**, *32b*, 1421.
2. Kahn, O., Kröber, J. and Jay, C. *Adv. Mater*. **1992**, *4*, 718.
3. Kröber, J., Audière, J. P., Claude, R., Codjovi, E., Kahn, O., Haasnoot, J. G., Grolière, F., Jay, C., Bousseksou, A., Linarès, J., Varret, F. and Gonthier-Vassal, A. *Chem. Mater.* **1994**, *6*, 1404.
4. Sugiyarto, K. and Goodwin, H. *Aust. J. Chem.* **1994**, *47*, 263.
5. (a) Michalowicz, A., Moscovici, J., Ducourant, B., Cracco, D. and Kahn, O. *Chem. Mater.* **1995**, *6*, 1404; (b) Verelst, M., Sommier, L., Lecante, P., Mosset, A. and Kahn, O. *Chem. Mater*. **1998**, *10*, 980.
6. Urakawa, A., Beek, W. V., Monrabal-Capilla, M., Galán-Mascarós, J. R., Palin, L. and Milanesio, M. *J. Phys. Chem. C* **2011**, *115*, 1323.
7. Grosjean, A., Négrier, P., Bordet, P., Etrillard, C., Mondieig, D., Pechev, S., Lebraud, E., Létard, J.-F. and Guionneau, P. *Chem. Commun*. **2011**, *47*, 12382.
8. (a) Guionneau, P., Marchivie, M., Bravic, G., Létard, J.-F. and Chasseau, D. *Top. Curr. Chem.* **2004**, *234*, 97; (b) Halcrow, M. A. *Chem. Soc. Rev.* **2011**, *40*, 4119.
9. Bousseksou, A., Molnár, G., Salmon, L. and Nicolazzi, W.*Chem. Soc. Rev*. **2011**, *40*, 3313.
10. Vaucher, S., Li, M. and Mann*,* S. *Angew. Chem., Int. Ed.* **2000**, *39*, 1793.
11. (a) Fouché, O., Degert, J., Daro, N., Forestier, T., Deplanche, C., Létard, J. F. and Freysz, E. presented at European Conference on Molecular Magnetism, Tomar, Portugal, October 2006. (b) Létard, J.-F., Guionneau, P. and Goux-Capes, L. *Top. Curr. Chem*. **2004**, *235*, 221. (c) Létard, J. F., Daro, N., Nguyen, O. WO 2007/065996, 2007.
12. Coronado, E., Galán-Mascarós, J. R., Monrabal-Capilla, M., García-Martínez, J., Pardo-Ibáñez, P. *Adv. Mater*. **2007**, *19*, 1359.
13. (a) Forestier, T., Mornet, S., Daro, N., Nishihara, T., Mouri, S.-i., Tanaka, K., Fouché, O., Freysz, E. and Létard, J.-F. *Chem. Commun*. **2008**, 4327. (b) Forestier, T., Kaiba, A., Pechev, S., Denux, D., Guionneau, P., Etrillard, C., Daro, N., Freysz, E. and Létard, J.-F. *Chem. Eur. J.* **2009**, *15*, 6122. (c) Galán-Mascarós, J. R., Coronado, E., Forment-Aliaga, A., Monrabal-Capilla, M., Pinilla-Cienfuegos, E. and Ceolin, M. *Inorg. Chem.* **2010**, *49*, 5706. (d) Tokarev, A., Salmon, L., Guari, Y., Nicolazzi, W., Molnár, G. and Bousseksou, A. *Chem. Commun*. **2010**, *46*, 8011. (e) Gural´skiy, I. A., Quintero, C. M., Molnár, G., Fritsky, I. O., Salmon, L. and Bousseksou, A. *Chem. Eur. J.* **2012**, *18*, 9946.
14. Titos-Padilla, S., Herrera, J. M., Chen, X.-W., Delgado, J. J. and Colacio, E. *Angew. Chem. Int. Ed.* **2011**, *50*, 3290.
15. Danielsson, I. and Lindman, B. *Colloids Surf. A* **1981**, *3*, 391.
16. Ganguli, A. K., Ganguly, A. and Vaidya, S. *Chem. Soc. Rev.* **2009**, *39*, 474.
17. Lopez-Quintela, M. A., Tojo, C., Blanco, M. C., García Rio, L. and Leis, J. R. *Curr. Opin. Colloid.*

Interface Sci. **2004**, *9*, 264.

18. Boutonnet, M., Kizling, J., Stenius, P. and Maire, G. *Colloids Surf.* **1982**, *5*, 209.
19. Lopez-Quintela, M. A. *Curr. Opin. Colloid. Interface Sci.* **2003**, *8*, 137.
20. Capek, I. *Adv. Colloid Interface Sci.* **2004,** *110*, 49.
21. Eastoe, J. and Warne, B. *Curr. Opin. Colloid Interface Sci.* **1996**, *1*, 800.
22. (a) Lisiecki, I. and Pileni, M. P. *Langmuir* **2003**, *19*, 9486. (b) Maillard, M., Giorgio, S. and Pileni, M.-P. *J. Phys. Chem. B* **2003**, *107*, 2466. (c) Eastoe, J., Stebbing, S., Dalton, J. and Heenan, R. K. *Colloids and Surfaces A* **1996**, *119*, 123. (d) Lemyre, J.-L. and Ritcey, A. M. *Chem. Mat.* **2005**, *17*, 3040.
23. (a) Pileni, M.-P. *CR Chimie* **2003**, *6*, 965. (b) Pileni, M.-P. *Nature Mater.* **2003**, *2*, 145. (c) Pileni, M.-P. *Supramol Sci.* **1998**, 5, 321. (d) Pileni, M.-P. *Cryst. Res. Technol.* **1998**, *33*, 1155. (e) Pileni, M.-P. *Langmuir* **1997**, *13*, 3266. (f) Uskokovic, V. and Drofenik, M. *Surf. Rev. Lett*. **2005**, *12*, 239.
24. Bagwe, R. P. and Khilar, K. C. *Langmuir* **1997**, *13*, 6432.
25. Pileni, M.-P. *J. Phys. Chem.* **1993**, *97*, 6961.
26. Gütlich, P., Goodwin, H. A. *Top. Curr. Chem*. **2004**, *233*, 1.

8

TUNING THE TRANSITION TEMPERATURE IN SPIN-CROSSOVER NPS BY A SYSTEMATIC LIGAND SUBSTITUTION

8.1 INTRODUCTION

As previously detailed in *Chapter 7*, polymeric one-dimensional triazole-based Fe^{II} systems of general formula $[Fe(Rtrz)_3]X_2$, represent one of the most promising spin crossover (SCO) materials given its robustness and vast synthetic versatility.[1] Depending on the R substituent, the anion and the degree of hydration, a variety of thermal SCO can be observed ranging from extremely abrupt transitions with wide hysteresis to smoother transition with a few K hysteresis. These SCO systems can be synthesized as nanoparticles (NPs),[2] which implies their possible applicability into devices. However, a practical implementation of this family of SCO NPs into real applications involves requires to overcome several limitations: i) more stable colloidal suspensions are required to further process these materials; and ii) the control of the necessary fine-tuning of the transition temperatures. In terms of colloidal stability, a interesting approach to improve the synthesis and therefore the stability of NPs has been shown in *Chapter 7*. In addition, recent advances in the group of Bousseksou demonstrated that NPs of $[Fe(atrz)_3][ptol]_2$ and more recently $[Fe(C_7trz)_3][ptol]_2$ can be obtained in an homogeneous phase, thus avoiding the use of a surfactant.[3] A different approach consists on using silica as a matrix to attain colloidal stability while opening the possibility of surface functionalization affording multifunctional nanomaterials.[4] However, less attention has been paid to gain control over the transition temperatures, which are actually subjected to a trial and error approach. A rational method to modulate the transition temperature in spin crossover systems relies on the application of a chemical perturbation. This modification of the chemical composition has been proved to promote a variety of influences in the transition temperatures ranging from subtle changes (metal dilution and counterion/solvate effects) to drastic alterations (ligand substitution).[5]

Previous studies developed in our group demonstrated that the magnetic hysteresis of $[Fe(Htrz)_2(trz)](BF_4)$ NPs can be tuned with subtle modifications of the chemical composition.[6] This study was supported by the original concept of molecular alloy proposed by Kahn to obtain a family of coordination polymers of general formula

$[Fe(Htrz)_{3-3x}(NH_2trz)_{3x}](ClO_4)_2$ which show variable transition temperatures in the bulk as a function of the composition.[7] As illustrated in figure 8.1, for the molecular alloy with formula $[Fe(Htrz)_{2.85}(NH_2trz)_{0.15}](ClO_4)_2 \cdot H_2O$, a spin transition centred at room temperature was obtained.

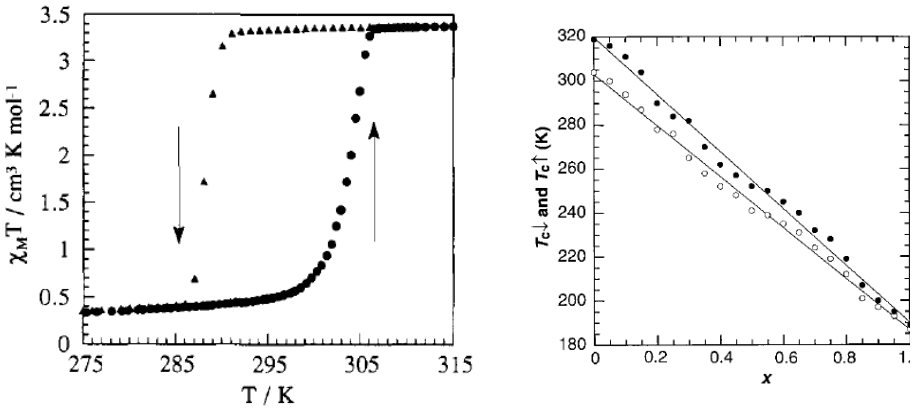

Figure 8.1 (a) Thermal spin transition centered at room temperature for the $[Fe(Htrz)_{2.85}(NH_2trz)_{0.15}](ClO_4)_2 \cdot H_2O$ allow. (b) Variation of the spin transition temperature for the system $[Fe(Htrz)_{3-3x}(NH_2trz)_{3x}](ClO_4)_2 \cdot H_2O$ as a function of alloy composition.

The possibility to obtain NPs showing bi-stability closer to room temperature was already established in our group.[8] The procedure consists on a systematically replacement of the ligand to promote minor changes in the chemical composition ($0.016 < x < 0.1$). For ligand substitutions of 2 %, 5 % and 10 %, the trend indicates that the thermal hysteresis moves to lower temperatures as the ratio of amino-triazole increases (figure 8.2). However, further ligand substitution (>10 %) resulted in macroscopic precipitates.

In this *Chapter* this idea has been extended with the aim of further explore the ligand effect in the spin transition when establishing not subtle but noticeable changes in the chemical composition. With this purpose, a family of SCO-NPs with a significant variation in the chemical composition has been synthesized, and therefore analyzed by means of UV-vis spectroscopy and magnetic susceptibility measurements.

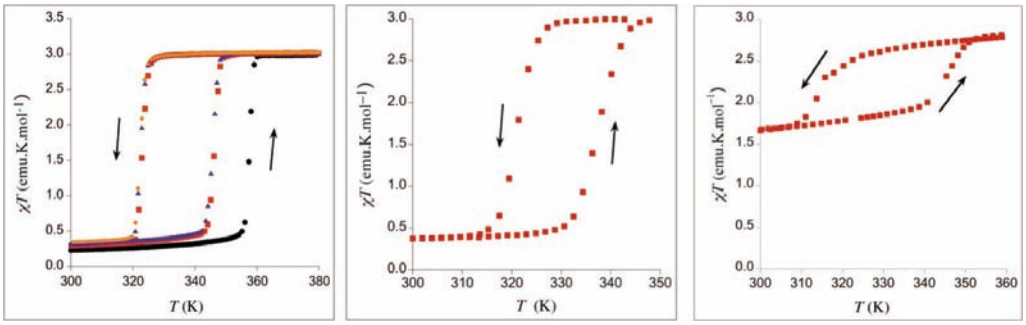

(a) (b) (c)

Figure 8.2 Magnetic properties of SCO-NP previously synthesized in our group with different compositions: (a) $[Fe(Htrz)_{2.95}(NH_2trz)_{0.05}](ClO_4)_2$, (b) $[Fe(Htrz)_{2.85}(NH_2trz)_{0.15}](ClO_4)_2$ and (c) $[Fe(Htrz)_{2.70}(NH_2trz)_{0.30}](ClO_4)_2$.

8.2 RESULTS AND DISCUSSION

The preparation of chemical mixtures or alloys of two different nanostructured SCO coordination polymers has been developed to obtain novel SCO NPs with different transition temperatures.

For the synthesis of the NPs with different chemical mixtures, two SCO coordination polymers of the family $[Fe(Rtrz)_3]X_2$ have been selected: $[Fe(Htrz)_3](ClO_4)_2 \cdot xH_2O$ and $[Fe(NH_2trz)_3](ClO_4)_2$. The two pure systems present considerably different spin crossover behaviour: while the hydrated triazole derivative shows abrupt spin bistability with $T_{1/2}\uparrow$ = 313 K and $T_{1/2}\downarrow$ = 296 K,[7a] the amino-triazole derivative presents an abrupt transition centred at 200 K with a reduced hysteresis.[9]

The family of SCO-NPs synthesized responds to the general formula $[Fe(Htrz)_{3-3x}(NH_2trz)_{3x}](ClO_4)_2$. Different chemical mixtures of NPs with x ranging between 0.066 and 0.5 and pure NPs (with x = 1 and x = 0) have been obtained (samples **2**–**6**). Notice that for values of x > 0.5 a macroscopic precipitate appears during the synthetic procedure, and, consequently, the maximum ligand substitution possible has been achieved in sample **5** and corresponds to the formula

$[Fe(Htrz)_{1.5}(NH_2trz)_{1.5}](ClO_4)_2 \cdot H_2O$. In addition, the use of aminotriazole as the unique ligand (i.e. x = 1) yields a gel.

The synthesis of the NPs is based on the same reverse micelle technique described in detail in *Chapter 7*. All parameters have been systematically fixed in the synthesis, aiming to obtain a comparable family of NPs with analogous size for a better relationship of the spin transitions. Table 8.1 summarizes the synthetic parameters used for all the samples.

Table 8.1 General parameters used in all the synthesis of samples **2**–**6**.

[Fe]	V H_2O (mL)	[L]	V *n*-octante (mL)	ω_0	T
1 M	0.3	3 M	10	7.4	293 K

Samples **2**–**5** are obtained as a clear suspension, while sample **6** is obtained as a gel (figure 8.3). Depending on the nature of the suspension in which the NPs are obtained, the size distribution of the NPs has been measured by DLS for clear suspensions of NPs in *n*-octane (samples **2**–**5**), or by TEM analysis in case of gel formation (sample **6**), as DLS is based on the Brownian motion of NPs in a suspension being thus unfeasible with gels. Table 8.2 summarizes the size distributions obtained for each sample (**2**-**6)** as a function of the mixture of ligands used. Small NPs of *ca*. 10 nm or less are obtained for all ligand mixtures (number-based mean size distribution).

Table 8.2 Chemical composition and mean size distribution for samples **2**–**5**.

Sample	Stoichiometry	3x	Size (nm)
2	$[Fe(Htrz)_2(trz)_1](ClO_4)$	0	4
3	$[Fe(Htrz)_{2.8}(NH_2trz)_{0.2}](ClO_4)_2$	0.2	8.7
4	$[Fe(Htrz)_2(NH_2trz)_1](ClO_4)_2$	1	8.7
5	$[Fe(Htrz)_{1.5}(NH_2trz)_{1.5}](ClO_4)_2$	1.5	11.7
6	$[Fe(NH_2trz)_3](ClO_4)_2$	3	3

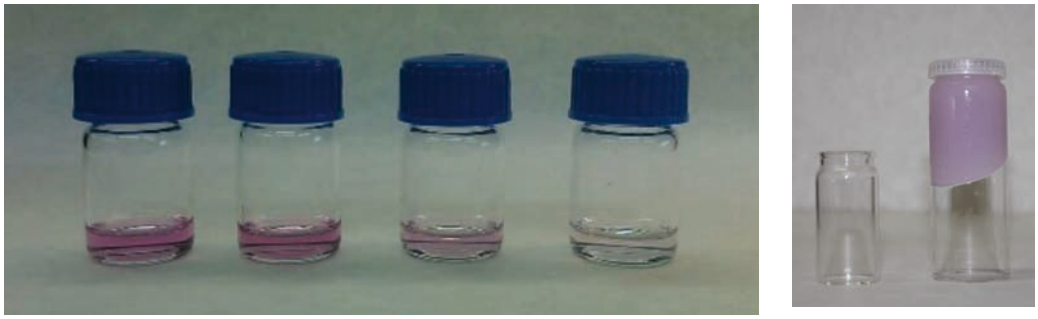

(a) (b)

Figure 8.3 (a) From left to right, NPs of **2**, **3**, **4** and **5** suspended in n-octane with the same concentration (b) Sample **6** is obtained as a SCO gel.

8.2.1 Optical properties

For equally concentrated samples **2**–**5** suspended in *n*-octane, it is possible to compare the gradual variation of the colour in optically transparent suspensions (see figure 8.3a). This could be attributed to a gradual modulation of the transition temperature, since NPs in the HS do not contribute to the colour. Therefore, a decrease in the colour intensity can be a simple proof of the stabilization of the HS species due to a ligand exchange.

The UV-visible absorption spectra have been recorded at 293 K for samples **2** and **3**. As an example, UV-visible absorption spectrum of **2** (20 mM) is shown in figure 8.4. The LS absorption peak is centred at 531 nm for sample **2** (for sample **3** this peak is centred at 532 nm), which can be assigned to the $^1A_1$ - $^1T_1$ transition.

The spin transition in these samples has been followed by the change in maximum optical absorbance that resulted from the (dis)appearance of the d–d transition band in the complex (centred at *ca*. 530 nm) that is characteristic of the low-spin (LS) state. Samples **2**–**3** have been cycled between 300 and 380 K and the absorbance was analyzed as a function of temperature. Optical absorption measurement on the stable, limpid, colloidal suspension can be properly executed, although the high temperature applied to reach a complete spin transition from the LS to the HS state results in minor

concentration changes in sample **2**, since the liquid medium is subjected to evaporation. Figure 8.5 displays the thermal dependence of the absorbance at 531 and 532 nm for **2** and **3**, respectively, in the heating (red) and cooling (blue) modes.

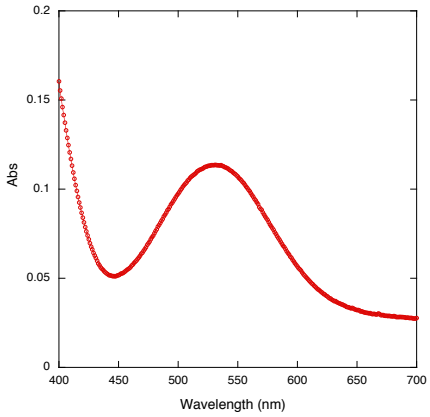

Figure 8.4 Absorption spectrum of **2** recorded at 298 K in the visible range showing the maximum absorption at 531 nm. The spectrum of **3** is essentially identical.

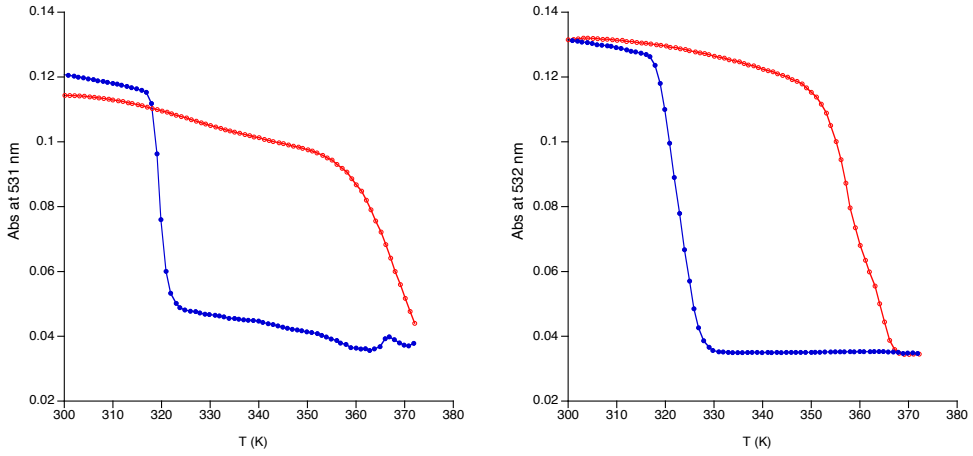

Figure 8.5 Thermal dependence of the absorbance at 531 and 532 nm for **2** and **3**, respectively, in the heating (red) and cooling (blue) modes, in the temperature range 300–380 K.

8.2.2 Magnetic properties

The SCO transitions have been addressed by recording the thermal variation of the $\chi_M T$ product of the different samples **2**–**6** under an applied external magnetic field of 0.1 T. Thermal spin transitions have been recorded at a constant rate of 1 K·min^{-1} in a different temperature range for each sample. Figure 8.6 shows the different thermal spin transitions recorded for each sample.

The evolution of the $\chi_M T$ product with temperature of the pure triazole-based NPs (**2**) (x = 0) suggests an extremely abrupt spin transition occurring above room temperature ($T_{1/2}^{\uparrow}$ = 371 K and $T_{1/2}^{\downarrow}$ = 328 K), showing a large hysteresis loop of 43 K. This large hysteretic behaviour of **2** has only been observed in the analogous compounds $[Fe(Htrz)_2(trz)](BF_4)$ and the anhydrous $[Fe(NH_2trz)_3](NO_3)_2$. Importantly, this behaviour contrasts with the spin transition of the corresponding bulk material $[Fe(Htrz)_2(trz)](ClO_4)$ which is characterized by an abrupt spin transition centred at *ca*. 304 K ($T_{1/2}\uparrow$ = 313 K and $T_{1/2}\downarrow$ = 296 K) and a much more reduced hysteresis of 17 K.[7]

Representation of he $\chi_M T$ product versus temperature of the pure aminotriazole–based NPs (**6**) (x = 1) shows a gradual thermal spin transition centred at *ca*. 270 K with a few Kelvin of hysteresis, which is reproducible over successive thermal cycles. This behaviour is different than the observed for the system synthesized in bulk,[9a] which presents a spin transition centred at 200 K. This discrepancy may be attributed to the formation of a gel during the synthetic procedure, although it could also be related to a different hydrated degree or the formation of some amino-triazolate bridges.

The magnetic properties for samples **3**–**5** corresponding to the mixtures of ligands display a progressive evolution of the transition temperatures from the pure triazole (Htrz) system to the pure amino-triazole (4-NH_2trz) system. As expected, by replacing the Htrz ligand by a mixture of Htrz and 4-NH_2trz ligands, the transition moves towards lower temperatures in both cooling and heating modes. Sample **3** exhibits a smooth spin transition occurring over 40 K centred above room temperature with a hysteresis of 16 K ($T_{1/2}\uparrow$ = 332 K and $T_{1/2}\downarrow$ = 316 K). This behaviour is reproducible

over successive thermal cycles. Sample **4** shows a rather smooth thermal spin transition, which occurs in more than 100 K. The gradual transition is centred closer to room temperature, with a small hysteresis of 10 K ($T_{1/2}\uparrow$ = 315 K and $T_{1/2}\downarrow$ = 305 K). Sample **5** exhibits a much smoother spin transition centred at 252 K with a reduced hysteresis of 4 K. A relatively large HS remnant fraction remains present at low temperatures for all samples, which is indeed typical for these nanostructured chain compounds, as explained previously in *Chapter 7* (section 7.3.2). The HS residues at low temperatures are slightly different depending on the sample and vary in the 25–35 % range. These differences may be attributed to minor disparities in NP size, although their difference in composition prevents further analysis and comparison.

Summarizing, these results are consistent with a gradual conversion from the pure triazole compound to the pure amino-triazole compound as a consequence of a systematic replacement of one ligand to another. This finding is in agreement with previous results performed on minor diluted samples in which the trend indicates that the thermal hysteresis moves to lower temperatures and becomes narrower as the ratio of amino-triazole ligand is increased.[6]

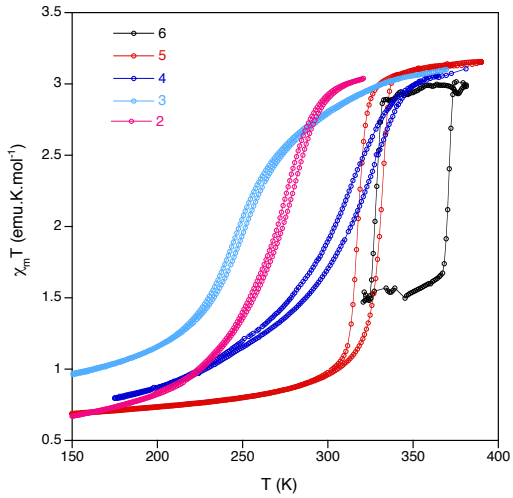

Figure 8.6 Temperature dependence of $\chi_M T$ for samples **2**-**6** in the temperature range 400-150 K.

Table 8.3 Physical characteristics of the thermal spin transition $T_{1/2}\uparrow$ and $T_{1/2}\downarrow$ and average particle sizes.

Sample	Stoichiometry	Size (nm)	$T_{1/2}\uparrow$	$T_{1/2}\downarrow$	ΔT
bulk	$[Fe(Htrz)_3](ClO_4)_2 \cdot xH_2O$ [7a]	-	296	313	17
2	$[Fe(Htrz)_3](ClO_4)_2$	4	328	371	41
3	$[Fe(Htrz)_{2.8}(NH_2trz)_{0.2}](ClO_4)_2$	8.7	316	332	16
4	$[Fe(Htrz)_2(NH_2trz)_1](ClO_4)_2$	8.7	305	315	10
5	$[Fe(Htrz)_{1.5}(NH_2trz)_{1.5}](ClO_4)_2$	11.7	254	250	4
6	$[Fe(NH_2trz)_3](ClO_4)_2$	3	273	270	3
bulk	$[Fe(NH_2trz)_3](ClO_4)_2$ [9]	-	207	200	7

8.3 CONCLUSIONS

A family of SCO-NPs with the general formula $[Fe(Htrz)_{3-3x}(NH_2trz)_{3x}](ClO_4)_2$ has been synthesized based in the parent compounds $[Fe(Htrz)_3](ClO_4)_2 \cdot xH_2O$ and $[Fe(NH_2trz)_3](ClO_4)_2$. The effect of the ligand substitution on the spin transition has been investigated and a gradual evolution from the nanostructured triazole system $Fe(Htrz)_3](ClO_4)_2 \cdot xH_2O$ to the nanostructured amino-triazole system $[Fe(NH_2trz)_3](ClO_4)_2$ has been achieved. All NPs have been obtained as stable colloidal suspensions except sample **6**, which has been obtained as a gel.

NPs based on the pure systems $[Fe(Htrz)_3](ClO_4)_2$ (**2**) and $[Fe(NH_2trz)_3](ClO_4)_2$ (**6**) have been synthesized for the first time. Magnetic measurements of both NPs show a thermal spin transitions that contrast with the spin transition of the corresponding bulk materials. Thus, NPs of **2** present an extremely abrupt spin transition with a large hysteresis loop, which is reminiscent of analogous compounds $[Fe(Htrz)_2(trz)](BF_4)$ and the anhydrous $[Fe(NH_2trz)_3](NO_3)_2$, and differs from the small hysteresis transition (and lower temperature) of the bulk. In addition, magnetic measurements of

6 show a gradual thermal spin transition that appears at higher temperatures than the bulk material.

Finally, magnetic measurements of the mixtures **3**–**5** reveal a gradual conversion from one system to another, which is accompanied of a suppression of the hysteresis. Further studies are in progress with the analogous family of compounds with BF_4 anion in order to corroborate this study.

8.4 METHODS

8.4.1 General synthesis

In a typical procedure, the first step involves the preparation of two separate microemulsions incorporating the different reactants. An aqueous solution of $Fe(ClO_4)_2.6H_2O$ (0.3 mL, 1M) with a.c. 10 mg of ascorbic acid is added to a previously prepared solution of NaAOT (1 g) in *n*-octane (10 mL) under vigorous stirring. Similarly, a particular amount (**2**, **6**) or mixture (**3**–**5**) of Htrz and NH_2trz ligands is dissolved in 0.3 mL of water and added to a solution of NaAOT (1g) in of *n*-octane (10 mL) under vigorous stirring (see table 8.2). After 30 minutes of continuous stirring the two microemulsions become stable and are mixed at room temperature under Ar atmosphere. A cha racteristic color appears immediately, which depends on the ratio Htrz/NH_2trz employed, indicating the occurrence of a nucleation process in an optically transparent suspension (see figure 8.3). The microemulsion is stirred for 15 min to ensure the intermicellar exchange and thus the growth of the nanoparticles. Then, acetone is added to break the microemulsion and the nanoparticles are collected by centrifugation after several washing cycles with portions of acetone (x3) and ethanol (x3) to remove excess of surfactant. Finally, the powdered sample is dryed under vacuum for 2h to remove excess of solvent.

8.4.2 Physical measurements

Dynamic light scattering (DLS) measurements were performed on a Zetasizer Nano-S (Malvern Instrument, UK). A He-Ne laser at **λ=**632 nm was used as a light source and the scattering angle was 173º. The results of scattering data were analyzed via a non-negative least squares algorithm (GP) as implemented in the Zetasizer Nano software [ref: http://www.malvern.com]. TEM analysis was done using a JEOL 1010 electron microscope operating at 100 keV. UV-vis was recorded in a Cary 100 spectrophotometer with a Cary temperature controller in the 20-100 ºC range.

Magnetic measurements. Magnetic susceptibility measurements were performed on single-phased polycrystalline samples with a Quantum Design MPMS-XL-5 SQUID susceptometer. The susceptibility data were corrected from the diamagnetic contributions as deduced by using Pascal's constant tables. The susceptibility data were collected at 1 $K \cdot min^{-1}$ with an applied field of 0.1 T.

8.5 REFERENCES

1. Roubeau, O. *Chem. Eur. J.* **2012**, *18*, 15230.
2. Coronado, E., Galán-Mascarós, J. R., Monrabal-Capilla, M., García-Martínez, J. and Pardo-Ibáñez, P. *Adv. Mater.* **2007**, *19*, 1359.
3. a) Tokarev, A., Salmon, L., Guari, Y., Nicolazzi, W., Molnár, G. and Bousseksou, A. *Chem. Commun*. **2010**, *46*, 8011. b) Tokarev, A., Salmon, L., Guari, Y., Molnár, G. and Bousseksou, A. *New J. Chem*. **2011**, *35*, 2081. c) Gural´skiy, I. A., Molnár, G., Fritsky, I. O., Salmon, L. and Bousseksou, A. *Polyhedron* **2012**, *31*, 245. d) Gural´skiy, I. A., Quintero, C. M., Molnár, G., Fritsky, I. O., Salmon, L. and Bousseksou, A. *Chem. Eur. J.* **2012**, *18*, 9946.
4. Titos-Padilla, S., Herrera, J. M., Chen, X.-W., Delgado, J. J. and Colacio, E. *Angew. Chem. Int. Ed*. **2011**, *50*, 3290.
5. Gütlich, P., Goodwin, H. A. *Top. Curr. Chem*. **2004**, *233*, 1.
6. Galán-Mascarós, J. R., Coronado, E., Forment-Aliaga, A., Monrabal-Capilla, M., Pinilla-Cienfuegos, E. and Ceolin, M. *Inorg. Chem.* **2010**, *49*, 5706
7. (a) Krober, J., Codjovi, E., Kahn, O., Groliere, F. and Jay, C. *J. Am. Chem. Soc*. **1993**, *115*, 9810. (b) Kahn, O. and Martinez, C. J. *Science* **1998**, *279*, 44.
8. Thesis of Maria Monrabal-Capilla **2011**.
9. Lavrenova, L. G.; Ikorskii, V. N.; Varnek, V. A.; Oglezneva, I. M.; Larionov, S. V. Koord. Khim. **1986**, *12*, 207. (b) Dirtu, M. M.; Rotaru, A.; Gillard, D.; Linares, J.; Codjovi, E.; Tinant, B. and Garcia, Y. *Inorg. Chem.* **2009**, *48*, 7838.

9

PROCESSING OF SPIN-CROSSOVER NANOPARTICLES

9.1 INTRODUCTION

The steady expanding of nanotechnology as a modern industrial technology supports the extended use of a technology capable of producing nanometer scale devices in one dimension over large areas through simple processes. In this sense, it is essential to advance and develop the processing of nano-objects for imminent nanodevices technologies, in which the physical size of components extends deep into the nanoscale. However, the fabrication of ordered nanoparticle (NP) films in large scale remains a major challenge. In this sense, the patterning of NPs on different substrates have been the focus of many investigations due to their unique potential for many applications, including nanophotonics,[1] molecular spintronics,[2,3] and biochemical sensing.[4]

The studies about the formation of monolayers based on magnetic NPs have been motivated by potential applications of the films in magnetic storage devices. Reasonable applications of NPs rely on fabrication techniques that are facile, rapid, and site selective.

In order to incorporate the spin-crossover nanoparticles (SCO-NPs) presented in the previous two *Chapters* into information storage devices, it is crucial to organize them onto surfaces for their direct addressing and manipulation. In addition, this should be done in a controllable manner and, if possible, into specific positions on the surface, with nanoscale accuracy. In our group, common processing techniques have been exploited to create thin films or patterned arrays of molecules or magnetic nanoparticles.[5–7]

As an example based on SCO-CP, Bousseksou and co-workers used a combined top-down/bottom-up approach for the nanoscale patterning of the 3D SCO system Fe(pyrazine)[Pt(CN)$_4$] achieving a high spatial resolution while retaining spin-crossover properties.[9] Later in 2012, also Bousseksou and co-workers elaborated good quality thin films, with thicknesses below 100 nm, of the [Fe(hptrz)$_3$](OTs)$_2$ SCO complex by soft lithographic approach.[10]

In this *Chapter*, efforts have been focused in understanding the preferential deposition on different substrates of the SCO-NPs with the aim of improving the processing for plausible implementation in electronic nano-devices.[8] In addition, we have studied their optimal patterning as thin films to obtain thicknesses of a few nm.

The work presented in this *Chapter* has been developed in collaboration with Dr. Alicia Forment-Aliaga.

9.2 PREFERENTIAL AND CONTROLLED DEPOSITION ONTO SURFACES

Previous studies developed in our group established the possibility of direct deposition of SCO-NPs onto gold and silicon surfaces by drop casting approach, i.e. without functionalization of the NP or the substrate.[9] Further investigations have been developed in order to improve understanding in the preferential deposition of this system. Nanoparticles of *ca*. 10 nm obtained with the reverse micelle technique developed in *Chapter 7* have been used for these studies (figure 9.1).

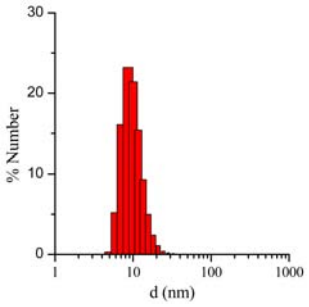

Figure 9.1 Number-based particle size distribution for the colloidal suspension of SCO-NP used in these experimets obtained by DLS. (Parameters used for the data analysis: T = 293 K, refractive index = 1.450).

The approximation used for the deposition follows a general drop casting methodology described in section 9.4. Figure 9.2 shows atomic force microscopy (AFM) images of SCO-NPs deposited on highly-ordered pyrolytic graphite (HOPG), Au(111) and silicon surfaces. AFM studies revealed that the highest NPs density is

reached on HOPG substrates, where the growth of compact NPs islands is observed. It may well be justified by the presence of van der Waals interactions between NPs alkylic chains and the HOPG surface. A preferential deposition of the SCO-NPs onto the surface defects is observed when gold surfaces were used, whereas a random deposition was observed in case of silicon substrates.

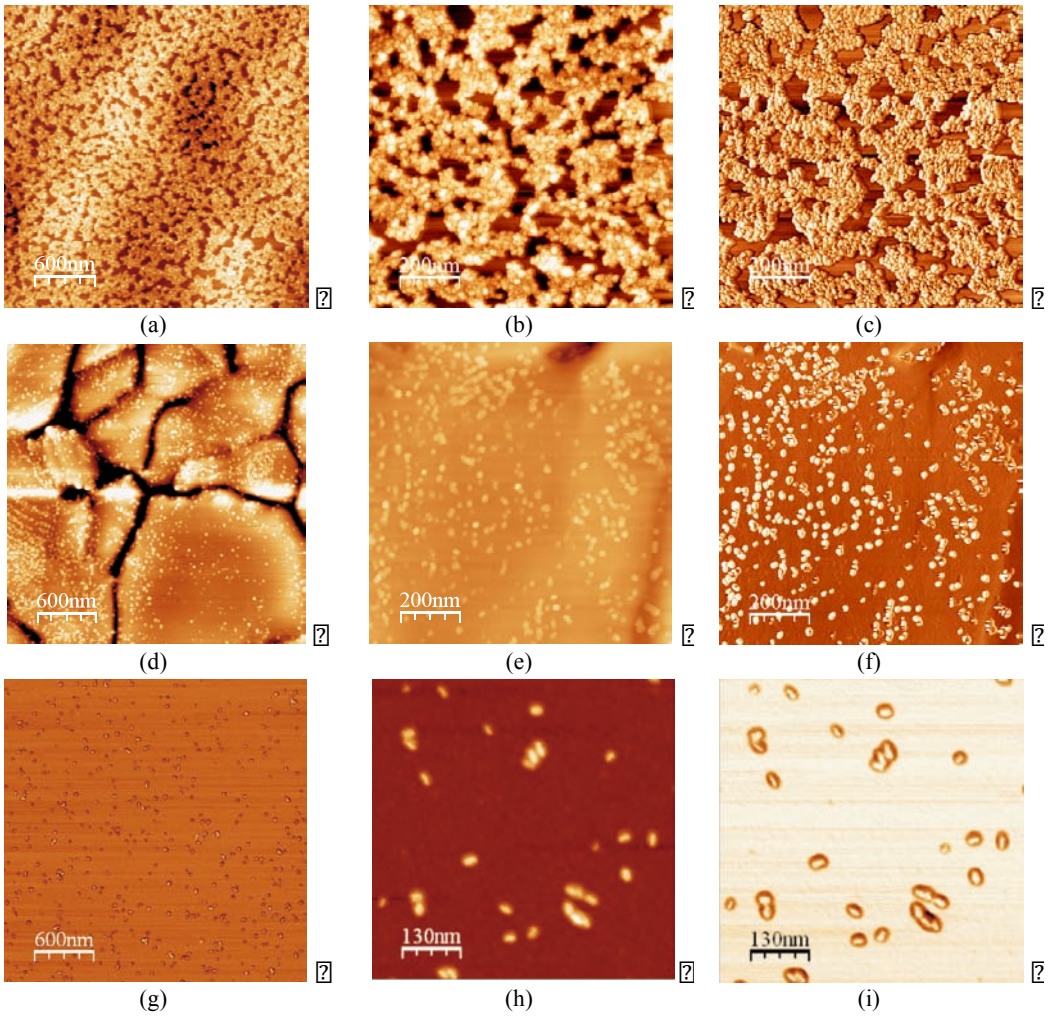

Figure 9.2 AFM images measured in tapping mode of nanoparticles on HOPG (top), Au(111) (middle) and native SiO_2 (bottom). (a,b,d,e,g,h), topography images; (c,f,i), phase images.

From these experiments, it can be concluded that the SCO-NPs are successfully deposited over silicon, although a limited and random deposition is obtained (figure

9.2). However, it is possible to improve this number of NPs deposited by modification of different parameters such as the concentration of the NPs and the deposition time.

Another possibility to improve surface coverage involves the use of a pre-functionalized surface to enhance the preferentiality of the SCO-NPs to be deposited. Thus, different functionalized silicon substrates can be used to subtle change the interaction with the SCO-NPs. This "bottom-up" approach consists on the surface functionalization by patterning self-assembled monolayers (SAMs) of different nature on the silicon surface. This method has already been successfully used in our group to deposit with nanometric accuracy magnetic molecules as well as magnetic nanoparticles.[5-7] The method exploits the long-range interactions established between the alkyl-terminated surfactant coating the NPs and the SAM grown onto the silicon substrate. In order to study the affinity of the SCO-NPs, two types of SAMs have been prepared with chemically distinct behaviour due to the nature of the terminating group: aminopropyltriethoxysilane (APTES) and octadecyltrichlorosylane (OTS). Whereas APTES possesses a $–NH_2$ hydrophilic terminating group, OTS has $–CH_3$ hydrophobic termination (see figure 9.3).

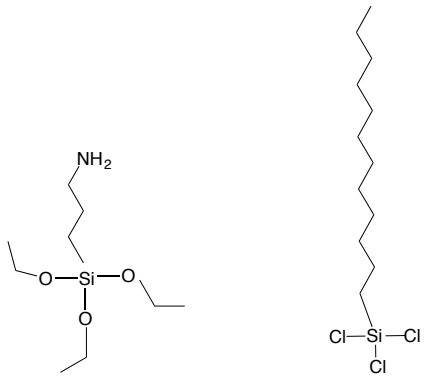

Figure 9.3 Chemical formulas of APTES (a) and OTS (b) molecules used for the preparation of SAMS.

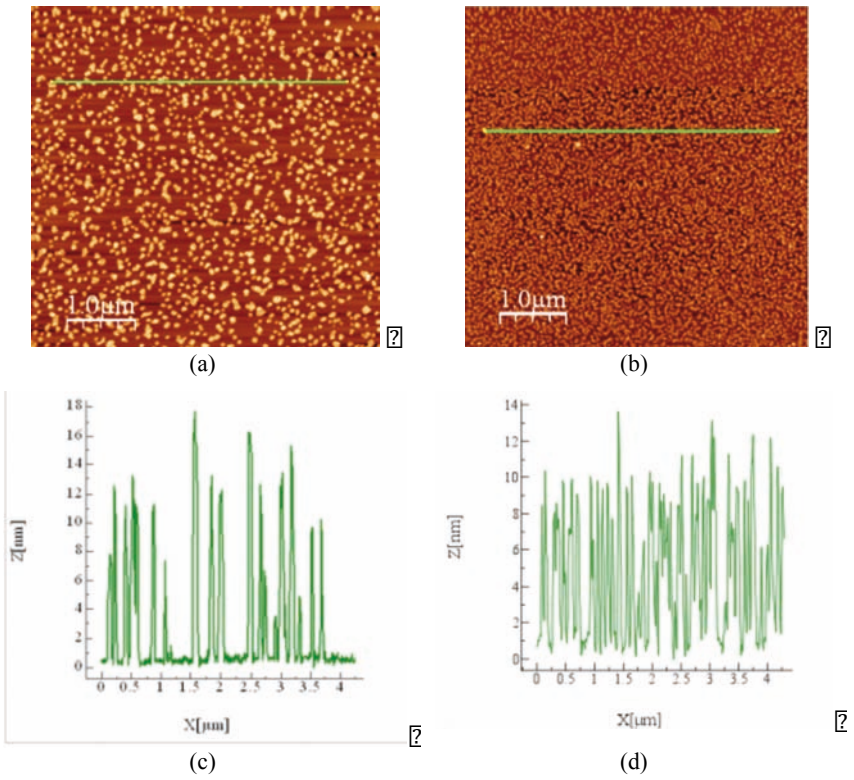

Figure 9.4 AFM images measured in tapping mode (a,b) and profiles (c,d) of the deposition of SCO-NPs of ~10 nm over two different functionalized silicon surfaces: (a) APTES grown on native SiO_2. (b) OTS grown on native SiO_2.

Considering these experiments of deposition over these different functionalized SAMs, several conclusions can be extracted. In a first stage, the number of SCO-NPs deposited considerably increases in both cases when compared with the non-functionalized native silicon substrate (figure 9.4). In addition, a remarkable preferentiality is observed when the NPs are deposited onto the OTS–SAM in comparison with the APTES-SAM. A plausible explanation may be the favoured van der Waals interaction promoted between the alkyl-terminated coating in the NPs and the hydrophobic alkyl-groups from the OTS-SAM.

9.3 CONTROLLED TWO-DIMENSIONAL DISTRIBUTION OF NP IN THIN FILMS

Drop-casting is an efficient technique to deposit SCO-NPs and study the binding ability to different substrates, although it has some drawbacks for the preparation of devices such as reproducibility and efficiency. In this sense, the use of spin-coating represent a possible solution to overcome these disadvantages. Spin-coating is a deposition technique that has been studied and used since the beginning of the 20th century. Basically, it consists on the deposition of a solution onto a horizontal rotating disc, resulting in ejection and evaporation of the solvent, thus leaving a solid film. Spin-coating is a unique technique in the sense that it is possible to apply a highly uniform film to a substrate over a large area (~ 30 cm) with a highly controllable and reproducible film thickness. The importance of spin-coating is manifested in its widespread use in science and industry and applies to inorganic, organic and inorganic/organic solution mixtures. The main application of this technique is the preparation of thin films on two-dimensional surfaces of wafers for microelectronics applications, such as in magnetic disks, flat screen displays, antireflection coatings and compact discs (CD, DVD).

Previous studies in our group were devoted to the preparation of thin films of SCO-NPs in a polymeric matrix.[11-12] However, these results were not very convincing. Thus, different polymers were tested as the matrix: polycarbonate (PC), polystyrene (PS) and polyvinyltrimethylsilane (PVTMS) and preliminary results established that when PC and PS were used as the polymer matrix films of *ca*. 150 and 220 nm were obtained, respectively, while PVTMS promoted instantaneous degradation of the NPs.

The following part describes the development of the preparation of thin films of SCO-NPs with the aim of achieving stable and homogeneous thin films of only a few nanometers thickness. In a first stage, both the solvent and the polymer used have been cautiously selected taking into account the stability of the NPs. The SCO NPs can be directly prepared either in hexane or octane, whereas they can be suspended, once prepared, in dichloromethane (DCM), chloroform or ethanol. Given the high boiling point of hexane and octane they are not appropriate for spin-coating technique,

and taking into account the solubility of the most common conducting polymers, ethanol can be discarded. Importantly, highly volatile solvents usually result in thicker films compared to low volatility solvents. For these reasons, the solvent of choice was DCM, with a very low boiling point of 39.6 ºC.

The polymer of selection has to prevent NPs from oxidation or decomposition and may be soluble in a compatible solvent. Different conducting polymers such as polypyrrole (PPY), polythiophene (PT) and polyaniline (PA) were tested, but combination with the NP resulted in either decomposition or incompatible solubilities. Similarly, polyvinylpyrrolidone (PVP) was discarded due to incompatibility of solubilities. The selected polymer resulted to be the commonly used polymethylmethacrylate (PMMA). This polymer fulfills the above-mentioned premises and also encloses some interesting properties such as transparency and thermal stability.

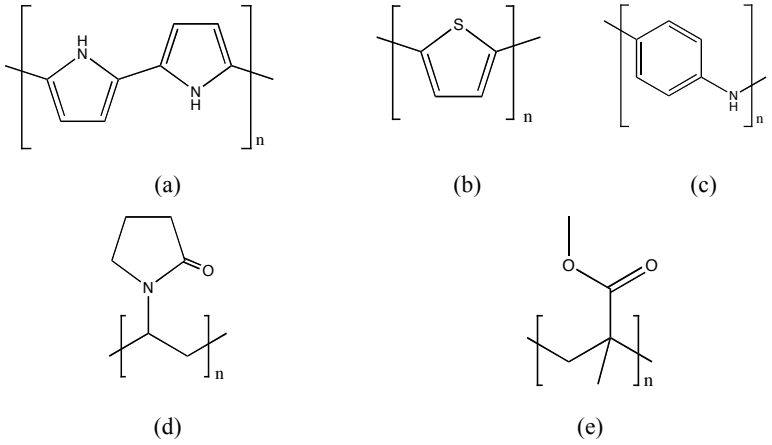

Figure 9.5 Chemical structure of PPY (a), PT (b), PA (c), PVP (d) and PMMA (e).

In a general procedure, films of PMMA-NP composite are prepared as described in section 9.4. In a first approximation, the NPs used for these experiments were synthesized in octane and presented a mean size distribution centered at 4 nm (figure 9.6). Films of these NPs dispersed in the PMMA matrix were prepared on silicon substrates. Preliminary results show the presence of an “oily” film, which can be attributed to the presence of octane in the sample. This possibility has been

circumvented by synthesizing the NPs in hexane, as this solvent presents a lower boiling point and is expected to be easily evaporated during the process.

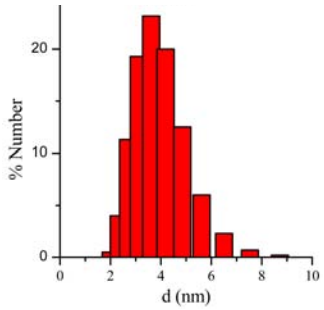

Figure 9.6 Number-based particle size distribution for the hexane colloidal suspension of SCO-NP used in spin-coating experiments obtained by DLS analysis. Parameters used for the data analysis: T = 293 K, refractive index = 1.370.

Thin films of the composite PMMA and SCO-NPs synthesized in hexane have been prepared on silicon substrates. The PMMA percentage (w/w %) present in the composite has been modulated in the 15-0.1 % range in order to study this effect on the thickness of the film. The thickness has been analyzed by perfilometry (for thicknesses > 30 nm) and atomic force microscopy (AFM) (for thicknesses < 30 nm). All the films are listed in table 9.1. Figure 9.7 illustrates how the thickness of the NP thin film can be controlled as a function of the PMMA added.

Table 9.1. Different thicknesses obtained as a function of the PMMA % used.

Sample	PMMA %	Thickness (nm)
1	15	65
2	10	49
3	5	35
4	2	18
5	1	12
6	0.2	10
7	0.1	10

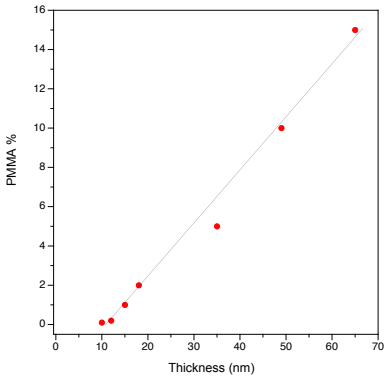

Figure 9.7 Representation of the different thin layer thickness obtained as a function of the PMMA added in the composite.

Interestingly, AFM analysis of three different samples of thin layers with the lowest thickness, reveal an interesting distribution of the NP in the film. In figure 9.8 a well-dispersed distribution of nano-objects is observed for the three samples. These nano-objects present a height of *ca*. 6 nm, which is in accordance with the hydrodynamic diameter (4 nm) observed in a suspension of NPs in hexane by DLS (dynamic light scattering). Thus, the nano-objects may well be seen as the SCO-NPs and minor differences in size may be attributed to a possible coating with PMMA. Another fascinating observation is the fact that in all three samples ultrathin layers of exactly 2 nm are clearly distinguished, which appear organized as islands of different two-dimensional sizes.

In order to check the origin of the nano-objects and the islands, the following experiment has been proposed. A sample of thin film has been prepared exactly in the same conditions, with the same amount of PMMA but in the absence of NPs. AFM analysis of this sample shows a totally different thin film in which neither the nano-objects nor the islands appear (figure 9.9). In this case, a highly porous PMMA thin film without layers is observed. Thus, the observed islands and nano-structures observed in the composite PMMA-NPs are clearly due to the presence of the NPs.

In conclusion, thin films of SCO-NP nanocomposite have been prepared in a reproducible and straightforward manner using the spin-coating technique. The NPs are well dispersed in the thin films immersed in the polymer matrix.

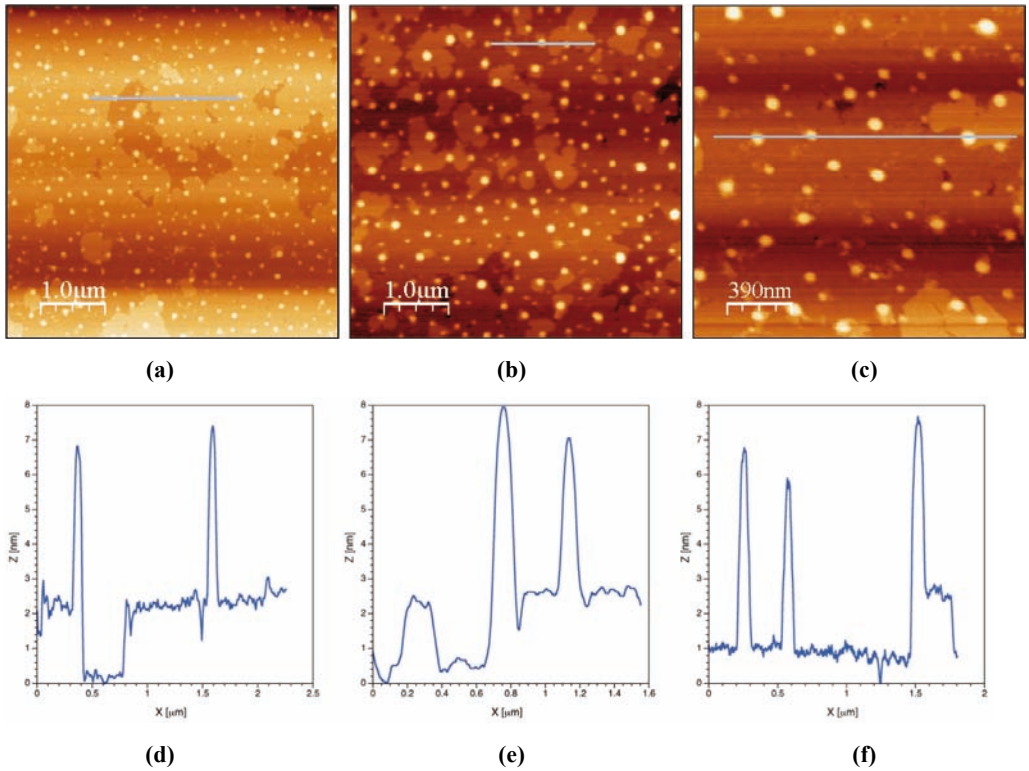

Figure 9.8 AFM images measured in tapping mode (a,b,c) and perfiles (d,e,f) of three different samples of thin films showing a well-dispersed distribution of nano-objects of *ca*. 6 nm and islands of 2 nm height.

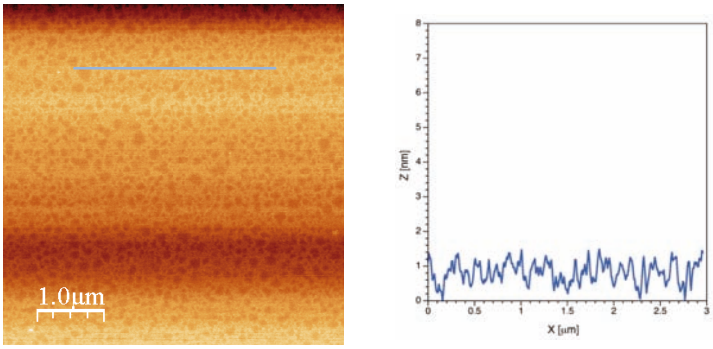

Figure 9.9 AFM image measured in tapping mode (a) and profile (b) of a thin film of PMMA showing a highly porous profile with roughness of 1 nm height.

9.4 SCO-NPs PATTERNED ON SiO_2 SURFACES

Another possibility to gain control over the deposition of SCO-NPs consists on taking advantage of the fabrication approaches of nanopatterning. In this section, efforts have been focused on the well-established micro contact printing technique.[11] This "top-down" approach, which has been extensively used in soft lithography, permits the controlled deposition of nano-objects through conformal contact. In this sense, a polydimethylsiloxane (PDMS) stamp has been patterned against a commercial master to form a relief pattern of arrays. Inking of the stamp occurs through the application of SCO-NPs solution. Applying the stamp to the substrate is easy and straightforward, which is one of the main advantages of this process. Typically, the stamp is brought into physical contact with the substrate under a controlled pressure and the NPs solution is transferred to the substrate (figure 9.10).

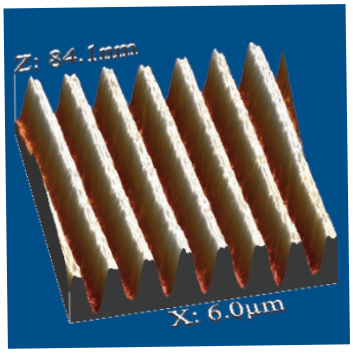

Figure 9.10 AFM illustration of the PDMS stamp used for patterning of the SCO-NP.

The SCO-NPs used for this method require specific treatment, since both the octane and hexane solvents employed in the synthesis are not compatible with the PDMS stamp. Therefore, precipitation and further re-dispersion steps have been necessarily included in the preparation protocol. Several solvents have been tested including, among others DCM, acetonitrile and different alcohols, and the best results have been obtained for NPs re-dispersed in ethanol.

Figure 9.11 illustrates the best results obtained so far, in which regular arrays of the SCO-NP are clearly distinguished. These results show that the controlled deposition of

SCO-NPs through conformal contact is indeed feasible, and opens the possibility to deposit the SCO-NPs in a controlled manner for further applications in nanodevices.

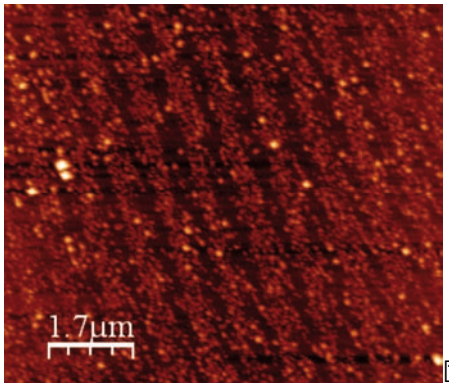

Figure 9.11 AFM image in tapping mode showing regular arrays of the SCO-NP onto silicon substrate.

9.5 CONCLUSIONS

SCO-NPs have been successfully deposited onto HOPG, Au(111) and silicon surfaces following the drop casting method. In addition, this deposition has been improved by surface functionalization. Then, SCO-NPs have been deposited on different self-assembled monolayers (SAMs) of different nature on silicon surfaces, OTS and APTES SAMs. In particular, a clear preferentiality is observed when the NPs are deposited onto the OTS–SAM.

In addition, stable and homogeneous thin films of SCO-NPs with a few nanometers thickness have been prepared following the spin-coating method. AFM studies reveal that the SCO-NPs are well dispersed in the thin films.

Finally, a proof of concept for the controlled deposition of SCO-NPs through conformal contact has been demontrated. This initial study opens the possibility for nano-organization in more sophisticated devices.

9.6 METHODS

Si cleaning process. Silicon surfaces of *ca*. 1 cm^2 are sonicated for 10 minutes in a freshly-prepared H_2O_2:NH_4OH:H_2O (1:1:2) solution (x3 times). Then, the substrates are rinsed with mili-Q water and then sonicated 5 minutes in mili-Q water (x2 times) and finally dried under a N_2 stream. *Ultrasonic cleaner*: BRANASONIC MTH-5510 ultrasonic cleaner (power 185 W).

Au(111) preparation. Gold substrate is first cleaned with ethanol and then annealed to ensure the formation of monoatomic terraces.

*Drop casting deposition***:** A drop of the corresponding SCO-NP suspension is dropped on top of the surface and left unperturbed for 30 second. Then, the substrate is rinsed with pure solvent (same solvent as used in the NP preparation) and finally the substrate is dried under a N_2 stream.

SAMs preparation. OTS monolayers are prepared inside the glove box in a controlled Ar atmosphere in the absence of oxygen and moisture. Clean silicon substrates are dipped in dry toluene solutions of OTS (2.8 mM) for three days. Then, the substrates are rinsed with toluene and sonicated in toluene, chloroform and 2-propanol to remove any physisorbed molecules. Finally, the samples are dried under N_2 stream. APTES SAMs are prepared by dipping the substrates in ethanolic solutions (absolute, reagent grade) of APTES (1 mM) for 45 minutes. Then, the samples are rinsed with ethanol and sonicated in this solvent for 5 minutes (x2 times). Finally, substrates are dried under N_2 stream. The quality of the SAMs are evaluated by water Advancing-Receding Contact Angle measurements in a Ramé-hart automatized goniometer and by AFM imaging.

Thin films of PMMA-NP. A specific amount of PMMA is dissolved in 10 mL of DCM. Then, 200 μL of the NP suspension (in hexane or octane) is added to the solution and sonicated until a homogeneous dispersion is obtained. The spin coating is performed by dropping 200 μL of the above composite solution on the clean silicon substrate,

and by rotating at 4000 rpm for 30 seconds in a DCM saturated atmosphere. The thickness of the thin film is evaluated by perfilometry and/or AFM.

AFMs: Nanoscope IIIa AFM (Veeco) and a Nanotec Cervantes Full Mode AFM (Nanotec Electrónica S.L.).

Typical tips for tapping mode: Sharp silicon probes without coating (Tapping Mode ~42 N/m, ~320kHz) PPP-NCH (Nanosensors).

9.7 REFERENCES

1. Cui, Y., Björk, M. T., Liddle, J. A., Sönnichsen, C., Boussert, B. and Alivisatos, A. P. *Nano Lett.* **2004**, *4*, 1093.
2. Rocha, A. R., García-Suárez, V. M., Bailey, S. W., Lambert, C. J., Ferrer, J. and Sanvito, S. *Nature Mater.* **2005**, *4*, 335.
3. Camarero, J. and Coronado, E. *J. Mater. Chem*. **2009**, *19*, 1678.
4. Dubertret, B., Skourides, P., Norris, D. J., Noireaux, V., Brivanlou, A. and Libchaber, A. *Science* **2000**, *298*, 1759.
5. Martínez, R. V., Martínez, J., Chiesa, M., García, R., Coronado, E., Pinilla-Cienfuegos, E. and Tatay, S. *Adv. Mater.* **2010**, *22*, 588.
6. Coronado, E., Forment-Aliaga, A., Pinilla-Cienfuegos, E., Tatay, S., Catala, L. and Plaza, J. A. *Adv. Funct. Mater.* **2012**, *22*, 3625.
7. Coronado, E., Martí-Gastaldo, C., Galán-Mascarós, J. R. and Cavallini, M. *J. Am. Chem. Soc.* **2010**, *132*, 5456.
8. Prins, F., Monrabal-Capilla, M., Osorio, E. A., Coronado, E. and van der Zant, H. S. J. *Adv. Mater.* **2011**, *23,* 1545.
9. (a) S. Cobo, Molnár, G., Real, J.A. and Bousseksou, A. *Angew. Chem. Int. Ed.* **2006**, *45*, 578. (b) Molnár, G., S. Cobo, Real, J.A, Carcenac, F., Daran, E., Vieu, C., and Bousseksou, A. *Adv. Mater.* **2007**, *19*, 2163
10. Quintero, C. M., Gural'skiy, I. A., Salmon, L., Molnár, G., Bergaud, C., and Bousseksou, A. *J. Mater. Chem.*, **2012**, *22*, 3745.
11. Galán-Mascarós, J. R., Coronado, E., Forment-Aliaga, A., Monrabal-Capilla, M., Pinilla-Cienfuegos, E. and Ceolin, M. *Inorg. Chem*. **2010**, *49*, 5706.
12. Doctoral thesis of Maria Monrabal-Capilla (2011).
13. (a) Cavallini, M., Albonetti, C. and Biscarini, F. *Adv. Mater*. **2009**, *21*, 1043. (b) Cavallini, M. *J. Mater. Chem*. **2009**, *19*, 6085. (c) Corradini, V., Menozzi, C., Cavallini, M., Biscarini, F., Betti, M. G. and Mariani, C. *Surf. Sci.* **2003**, *532*, 249. (d) Leclere, P., Surin, M., Lazzaroni, R., Kilbinger, A. F. M., Henze, O., Jonkheijm, P., Biscarini, F., Cavallini, M., Feast, W. J., Meijer, E. W. and Schenning, A. *J. Mater. Chem.* **2004**, *14*, 1959.

III

RESUMEN

El trabajo descrito en esta tesis se enmarca en el ámbito de los polímeros de coordinación (PC). Estos sistemas representan un área importante dentro de la Química de los Materiales, siendo principalmente interesantes sus aplicaciones en catálisis, electrónica y óptica. Su origen data de principios de los años 60, donde se produjo la primera revisión de estructuras de compuestos inorgánicos que formaban cadenas.[1] Los PC están formados por ligandos orgánicos y metales enlazados por enlaces de coordinación que se extienden infinitamente en 1, 2 o 3 dimensiones. En cuanto a su versatilidad química, las estructuras y propiedades varían en función de los metales o ligandos utilizados. Así pues, la variable naturaleza de los ligandos orgánicos junto con la diversidad de metales posibles dan lugar a un abundante número de potenciales topologías y arquitecturas que pueden ser ingeniadas mediante un diseño químico apropiado. Los PC dan lugar a redes regulares con una tremenda estabilidad química, aunque también pueden formar sólidos flexibles que responden a estímulos externos de interés.

Uno de los hallazgos más interesantes dentro de este campo de los PC ha sido el hecho de constatar que muchos PC con estructuras flexibles presentan cierto dinamismo[2] que está directamente relacionado con la flexibilidad del ligando[3] o con la habilidad que poseen los centros metálicos de coordinación para aceptar/intercambiar moléculas coordinadas. Estos materiales dinámicos son capaces de desarrollar cambios estructurales de forma reversible, siendo excepcionalmente útiles para la preparación de sofisticados materiales multifuncionales con propiedades físicas modulables. Esto resulta de particular interés en materiales magnéticos, ya que sus propiedades físicas son extremadamente sensibles a pequeños cambios estructurales provocados por un estímulo externo.

Los polímeros magnéticos de coordinación (PMC) son una clase de materiales magnéticos especialmente interesantes debido a sus potenciales aplicaciones en el desarrollo de materiales magnéticos de baja densidad, sensores magnéticos y

materiales inteligentes o multifuncionales.[4]

El magnetismo tiene su origen en los portadores de espín, que son centros metálicos paramagnéticos o ligandos orgánicos radicales. Dependiendo del origen del acoplamiento entre estos portadores, podemos distinguir entre dos tipos diferentes de PMC: i) los PMC que presentan ordenamiento magnético; y ii) los PMC basados en complejos de transición de espín.

En el primer caso el magnetismo proviene de las interacciones de canje cooperativas entre metales paramagnéticos por vías de supercanje a través de entidades (normalmente) diamagnéticas. Así pues, los centros magnéticos necesariamente deben estar organizados en topologías específicas y unidos por ligandos que promuevan eficientemente las interacciones de canje magnéticas. Por tanto, el diseño del ligando es crucial en la síntesis de estos materiales, resultando incluso un problema de delicada solución la fusión de porosidad y ordenamiento magnético. Para solventar este problema, una posible solución es el uso de ligandos orgánicos radicales, ya que los espines individuales que poseen pueden promover interacciones de canje efectivas, resolviendo así la necesidad de mantener cortas distancias entre los centros metálicos.[5] Es importante destacar que, en el mejor de los casos, las interacciones de canje son en general débiles y por tanto, la cooperatividad magnética sólo se observa a temperaturas muy bajas.

El segundo tipo de polímero magnético de coordinación se refiere a los sistemas basados en complejos de transición de espín. La transición de espín es un fenómeno en el que la configuración de iones de metales de transición puede intercambiarse entre bajo espín (BS) y alto espín (AE) en respuesta a un estímulo externo, como puede ser la temperatura, la presión o la irradiación de luz, produciendo cambios en el magnetismo, el color y la estructura. En particular, los compuestos de Fe^{II} exhiben un importante cambio magnético entre el estado paramagnético AE (S = 2) al estado diamagnético de BE (S = 0).[6–8] En este caso, las interacciones de canje entre centros magnéticos vecinos no son necesarias. No obstante, se necesitan efectos cooperativos para que el fenómeno de transición de espín sea útil. En este caso, la cooperatividad

tiene su origen en las fuerzas elásticas presentes en el sólido, y no en las interacciones de canje magnético. De este modo, esta aproximación resulta estar mejor adaptada a las exigencias para obtener polímeros magnéticos de coordinación que presenten las propiedades magnéticas a mayores temperaturas.

Los polímeros magnéticos de coordinación que responden a estímulo externo han sido objeto de gran atención en los últimos años, donde se han encontrado ejemplos con interesantes propiedades magnéticas incluyendo ordenamiento magnético,[9] materiales de transición de espín sensible a moléculas huésped,[10] y intercambio entre diferentes estados magnéticos inducido por moléculas huésped.[11] En estos sistemas, las propiedades magnéticas se ven dramáticamente afectadas por los cambios estructurales provocados por un estímulo externo ya sea físico, o químico.

El objeto de estudio de esta tesis es el desarrollo de nuevos polímeros magnéticos de coordinación que respondan a estímulos externos. Para ello se han explorado dos áreas, las cuales se refieren a la escala a la cual se han obtenido los sistemas. En este sentido. La tesis está dividida en dos partes: la primera parte trata la preparación de PMC cristalinos que responden a estímulos externos, mientras que la segunda parte aborda la preparación de nanopartículas magnéticas que responden a estímulos externos. De este modo, mediante diferentes metodologías se han obtenido PMC basados en cristales macroscópicos o nanopartículas.

La primera parte comprende los *Capítulos 1–5*, y aborda la preparación de PMC como sólidos cristalinos. El *Capítulo 1* desarrolla una introducción a los materiales que responden a estímulos externos. El *Capítulo 2* presenta un PC no poroso basado en un ligando imidazolato, que es capaz de modular sus propiedades físicas por quimisorción de moléculas gaseosas. Para ello es necesaria la reorganización de la red cristalina mediante rotura y formación de nuevos enlaces covalentes, que tiene lugar durante la quimisorción/desorción de gas, resultando en importantes cambios estructurales que provocan cambios en las propiedades magnéticas del sistema.

El *Capítulo 3* comprende la preparación de PC de transición de espín que resultan ser

sensibles a la fisisorción selectiva de CO_2. Estos sistemas son capaces de adsorber moléculas de gas a pesar de no poseer poros en su estructura. Esto es posible debido a la presencia de un ligando flexible que dota a la red de dinamismo. Medidas magnéticas realizadas antes y después de la fisisorción demuestran por primera vez la modulación de la transición de espín debido a la adsorbión de moléculas de gas.

Los *Capítulos 4* y *5* muestran ejemplos de PMC que son capaces de desarrollar cambios estructurales bajo el efecto de un estímulo externo físico y químico, respectivamente.

La segunda parte de la tesis se refiere al estudio de sistemas de transición de espín nanoestructurados. Esta sección comprende tanto la síntesis, caracterización como su posterior procesado, a lo largo de los *Capítulos 6–9*.

El *Capítulo 6* trata una pequeña introducción general a la transición de espín y, en concreto, al polímero de coordinación que se estudia en los siguientes capítulos.

En el *Capítulo 7* se describe el protocolo experimental para la obtención de nanopartículas bi-estables. En particular se describen los parámetros que ejercen una gran influencia sobre la propiedades físicas de las nanopartículas, así como también se desarrolla el estudio del efecto del tamaño de partícula en las propiedades magnéticas.

El *Capítulo 8* describe brevemente una familia de nanopartículas que presentan una modificación química, que consiste en una substitución gradual de ligando para modular así la temperatura de transición de las mismas.

Finalmente, en el *Capítulo 9* se trata el procesado de estas nanopartículas para su posible aplicación en espintrónica molecular. Para ello, las nanopartículas se han depositado con el fin de estudiar la preferencialidad frente a diferentes sustratos. Se presenta también la posibilidad de organizar estas nanopartículas en capas finas. Finalmente se ha procedido a la deposición de manera controlada en superficies mediante técnicas de contacto.

REFERENCIAS

1. Bailar Jr., J. C. *Preparative Inorganic Reactions*, ed. W. L. Jolly, Interscience, New York, **1964**,*1*,1.
2. (a) Kitagawa, S. and Uemura, K. *Chem. Soc. Rev*. **2005**, *34*, 109. (c) Férey, G. and Serre, C. *Chem. Soc. Rev*. **2009**, *38*, 1380.
3. (a) Kole, G. K. and Vittal, J. J. *Chem. Soc. Rev*. **2013**, 42, 1755. (b) Hawxwell, S. M., Mínguez Espallargas, G., Bradshaw, D., Rosseinsky, M. J., Prior, T. J., Florence, A. J., van de Streek, J. and Brammer, L. *Chem. Commun*. **2007**, 1532. (c) Pigge, F. C. *CrystEngComm* **2011**, *13*, 1733. (d) Fletcher, A. J., Thomas, K. M. and Rosseinsky, M. J. *J. Solid State Chem.* **2005**, *178*, 2491.
4. Coronado, E. and Mínguez Espallargas, G. *Chem. Soc. Rev.* **2013**, *42*, 1525.
5. Maspoch, D., Ruiz-Molina, D., Wurst, K., Domingo, N., Cavallini, M., Biscarini, F., Tejada, J., Rovira, C. and Veciana, J. *Nature Mat.* **2003**, *2*, 190.
6. Kahn, O. and Martinez, C. J. *Science* **1998**, *279*, 44.
7. "Spin Crossover in Transition Metal Compounds" (Eds: P. Gütlich, H. A. Goodwin), *Top. Curr. Chem*. **2004**, 233. (b) Spiering, H., Kohlhaas, T., Romstedt, H., Hauser, A., Bruns-Yilmaz, C., Kusz, J. and Gütlich, P. *Coord. Chem. Rev.* **1999**, *629*, 190. (c) Gütlich, P., Hauser, A. and Spiering, H. *Angew. Chem. Int. Ed*. **1994**, *33*, 2024. (d) Gütlich, P., Garcia, Y. and Woike, T. *Coord. Chem. Rev*. **2001**, 219, 839.
8. (a) Real, J. A., Gaspar, A. B., Niel, V. and Muñoz, M. C. *Coord. Chem. Rev.* **2003**, *236*, 121. (b) Hauser, A., Jeftic, J., Romstedt, H., Hinek, R. and Spiering, H. *Coord. Chem. Rev.* **1999**, *190-192*, 471. (c) Gaspar , A. B., Seredyuk, M. and Gütlich, P. *J. Mol. Struct*. **2009**, *9*, 924.
9. (a) Kaneko, W., Ohba, M. and Kitagawa, S. *J. Am. Chem. Soc.* **2007**, *129*, 13706. (b) Milon, J., Daniel, M. C., Kaiba, A., Guionneau, P., Brandes, S. and Sutter, J. P. *J. Am. Chem. Soc*. **2007**, *129*, 13872. (c) Navarro, J. A. R., Barea, E., Rodríguez-Diéguez, A., Salas, J. M., Ania, C. O., Parra, J. B., Masciocchi, N., Galli, S. and Sironi, A. *J. Am. Chem. Soc*. **2008**, *130,* 3978. (d) Sun, W. W., Tian, C. Y., Jing, X. H., Wang, Y. Q. and Gao, E. Q. *Chem. Commun*. **2009**, 4741. (e) Wang, Z. M., Zhang, B., Fujiwara, H., Kobayashi, H. and Kurmoo, M. *Chem. Commun*. **2004**, 416.
10. (a) Halder, G. J., Kepert, C. J., Moubaraki, B., Murray, K. S. and Cashion, J. D. *Science* **2002**, *298*, 1762. (b) Neville, S. M., Halder, G. J., Chapman, K. W., Duriska, M. B., Southon, P. D., Cashion, J. D., Létard, J. F., Moubaraki, B., Murray, K. S. and Kepert, C. J. *J. Am. Chem. Soc.* **2008**, *130*, 2869.
11. (a) Kurmoo, M., Kumagai, H., Chapman, K. W. and Kepert, C. J. *Chem. Commun.* **2005**, 3012. (b) Zhang, X. M., Hao, Z. M., Zhang, W. X. and Chen, X. M. *Angew. Chem., Int. Ed.* **2007**, *46*, 3456. (c) Cheng, X. N., Zhang, W. X., Lin, Y. Y., Zheng, Y. Z. and Chen, X. M. *Adv. Mater*. **2007**, *19*, 1494. (d) Motokawa, N., Matsunaga, S., Takaishi, S., Miyasaka, H., Yamashita, M. and Dunbar, K. R. *J. Am. Chem. Soc.* **2010**, *132*, 11943.

PART I

1	$[Cu(pyim)(Cl)(MeOH)]_n$
2	$(H_2pyimH)[CuCl_4]$
3	*cis*-$[CuCl_2(pyimH)]$
4	$[Fe(btzx)_3](ClO_4)_2$
5	$[Fe(btzx)_3](BF_4)_2$
6	$\{[Co(btix)_2(OH_2)_2]\cdot 2NO_3\cdot 2H_2O\}_n$
7	$\{[Zn(btix)_2(OH_2)_2]\cdot 2NO_3\cdot 2H_2O\}_n$
8	$\{[Zn_{(0.98)}Co_{(0.02)}(btix)_2(OH_2)_2]\cdot 2NO_3\cdot 2H_2O\}_n$
9	$[Co(btix)_2(NO_3)_2]_n$
10	$[Zn(btix)_2(NO_3)_2]_n$
11	$[Zn_{(0.98)}Co_{(0.02)}(btix)_2(NO_3)_2]_n$
12	*trans*-$[Cu(btix)_2(BF_4)_2]_n$
13	*trans*-$[Cu(btix)_2(ClO_4)_2]_n$
14	*trans*-$[Cu(btix)_2(PF_6)_2]_n$
15	$[Cu(btix)_2(NO_3)_2]_n$
16	$[Cu(btix)_2(Cl)_2]_n$
17	$[Cu(btix)(N_3)_2]_n$

PART II

1	$[Fe(Htrz)_2(trz)](BF_4)$
2	$[Fe(Htrz)_3](ClO_4)_2$
3	$[Fe(Htrz)_{2.8}(NH_2trz)_{0.2}](ClO_4)_2$
4	$[Fe(Htrz)_2(NH_2trz)_1](ClO_4)_2$
5	$[Fe(Htrz)_{1.5}(NH_2trz)_{1.5}](ClO_4)_2$
6	$[Fe(NH_2trz)_3](ClO_4)_2$